Valorization of different biomass ashes and sunflower particles in bio-based building materials : relation composition-structure-properties

Desire Ndahirwa

Normandie Université

THÈSE

Pour obtenir le diplôme de doctorat

Spécialité GENIE CIVIL

Préparée au sein de l'Université de Rouen Normandie

Valorization of different biomass ashes and sunflower particles in bio-based building materials : relation composition-structure-properties

Présentée et soutenue par
DESIRE NDAHIRWA

Thèse soutenue le 10/01/2023 devant le jury composé de		
M. BERNARD KUREK	DIRECTEUR DE RECHERCHE, UNIVERSITE REIMS CHAMPAGNE ARDENNE	Rapporteur du jury
M. MOHAMMED SONEBI	PROFESSEUR DES UNIVERSITES, QUEEN'S UNIVERSITY BELFAST	Rapporteur du jury
MME IRINI DJERAN-MAIGRE	PROFESSEUR DES UNIVERSITES, INSTITUT NATIONAL DES SCIENCES APPLIQUEES DE LYON	Membre du jury
MME HELENE LENORMAND	MAITRE DE CONFERENCES, UNILASALLE	Membre du jury
MME HAFIDA ZMAMOU	CHARGE DE RECHERCHE, UNILASALLE	Membre du jury
M. DANIEL LEVACHER	PROFESSEUR DES UNIVERSITES, Université de Caen Normandie	Président du jury
MME NATHALIE LEBLANC	MAITRE DE CONFERENCES HDR, UNILASALLE	Directeur de thèse

Thèse dirigée par NATHALIE LEBLANC (TRANSFORMATIONS ET AGRO-RESSOURCES)

UNIVERSITÉ DE ROUEN NORMANDIE

UniLaSalle Terre & Sciences

ED 497 NBISE Normande de Biologie Intégrative, Santé, Environnement

Transformations & Agro-Ressources UniLaSalle

Table of Contents

Abstract

The quantity of wood biomass ash produced from heating and power stations has recently increased. The disposal of this waste in landfills poses severe environmental concerns. On the other hand, sunflower particles (pith and bark) are by-products from the sunflower crop, which are renewable and locally available. The latter present a low bulk density and high porosity, which makes them an excellent alternative to hemp shiv in bio-based concrete. Therefore, this PhD research work aims to study the variability of wood ashes and valorize them along with sunflower particles (pith and bark) into eco-friendly lightweight bio-based building materials.

Eight batches of biomass ash, including wood fly ash, wood bottom ash and waste paper sludge ash were collected from three suppliers in the Normandy region. The sunflower particles were obtained from an agricultural cooperative located in the southwest area of France. First, the characteristics of all raw materials collected were investigated. Then, four batches of wood ashes (three wood fly ashes and one wood bottom ash) were selected and used to develop thirty different binding matrices. Natural hydraulic lime (NHL) and ordinary Portland cement (OPC) were incorporated as mineral additives to improve the mechanical properties of the pastes. Wood ashes accounted for 80 to 100 %, while NHL or OPC was added at 5, 10 and 20 % ratios.

Two wood ash pastes with higher 28-day compressive strengths were selected to prepare sunflower-based building materials. Due to the low density and high porosity of sunflower pith particles, the latter were used to elaborate six mortars for implementation by projection. On the other hand, sunflower bark particles were suitable for producing six mixtures of prefabricated building elements.

The results showed that the lightweight bio-based building materials produced in this study exhibited mechanical, thermal, hygroscopic properties and durability comparable to those of currently available bio-based materials. Hence, this study concludes that wood ashes and sunflower particles can be used as alternative raw materials in bio-based building materials.

Keywords: Wood ash, sunflower particles, bio-based mortar, microstructure, mechanical properties, durability.

Résumé

La quantité de cendres de biomasse produites par les centrales thermiques et électriques a augmenté au cours de ces dernières années. L'élimination de ces déchets dans les décharges pose de sévères problèmes environnementaux. D'autre part, les particules de tournesol (moelle et écorce) sont des co-produits issus de la récolte de tournesols. Renouvelables et disponibles localement, elles présentent une faible densité apparente et une porosité élevée, qui en font une excellente alternative à la chènevotte dans les bétons biosourcés. Cette thèse vise à étudier la variabilité des cendres de bois et à les valoriser avec des particules de tournesol (moelle et écorce) en matériaux biosourcés éco-responsables pour le bâtiment.

Huit lots de cendres de biomasse comprenant des cendres volantes de bois, des cendres sous-foyer de bois, cendres de boues de papiers ont été collectés auprès de trois fournisseurs en région Normandie. Les particules de tournesol ont été récupérées auprès d'une coopérative agricole située dans le sud-ouest de la France. Dans la première phase de l'étude, les caractéristiques de toutes les matières premières collectées ont été étudiées. Ensuite, quatre lots de cendres de bois (trois cendres volantes et un lot de cendres sous-foyer) ont été sélectionnés et utilisés pour développer trente matrices de liaison différentes. Afin d'améliorer les propriétés mécaniques, nous avons incorporé une petite quantité de chaux naturelle hydraulique (NHL) et du ciment Portland ordinaire (OPC). Dans les pâtes, les cendres de bois représentaient 80 à 100 %, tandis que NHL ou OPC étaient ajoutés dans des proportions de 5, 10 et 20 %.

Deux pâtes de cendres de bois présentant des résistances à la compression à 28 jours plus élevées ont été sélectionnées pour préparer des matériaux de construction à base de tournesol. En raison de la faible densité et de la porosité élevée des particules de moelle de tournesol, ces dernières ont été utilisées pour élaborer six mortiers destinés à être mis en œuvre par projection. D'autre part, les particules d'écorce de tournesol étaient adaptées à la production de six mélanges d'éléments de construction préfabriqués.

Les résultats ont montré que les matériaux de construction légers biosourcés produits dans cette étude présentaient des propriétés mécaniques, thermiques et hygroscopiques et de durabilité comparable à celles des matériaux biosourcés actuellement disponibles. Par conséquent, cette étude conclut que les cendres de bois et les particules de tournesol peuvent être utilisés comme matières premières alternatives dans les matériaux de construction biosourcés.

Mots-clés : Cendres de bois, particules de tournesol, mortier biosourcé, microstructure, propriétés mécaniques, durabilité.

Acknowledgements

The research work presented in this thesis has been carried out in the VAM^{2}IN (Valorization of Agro-resources in Innovative Molecules and Materials) team of the research unit "Transformations & Agro-resources" (T&A), at UniLaSalle Rouen, France.

The past three years I have devoted to this thesis have been intense and marked by learning, discovery, challenges and many emotions. The accomplishment of this project would not have been possible without the help of my family, friends, colleagues, industrial and academic collaborators. I greatly acknowledge the financial support by the Agency for the environment and energy management (ADEME) through the project "Démonstrateurs Industriels Valorisant des Agro-résidus" (DIVA).

First and foremost, I offer my sincerest gratitude to my family, my parents for their invaluable support and everything they have done for me to achieve this level, my siblings Victoire, Aimable, Clément and Yvonne, my cousin Deo, and mostly, Flora, my wife and Florie, my daughter for their unconditional love, advice and encouragement.

I would like to express my sincerest gratitude to my thesis supervisor Nathalie Leblanc and to my co-supervisors, Hélène Lenormand and Hafida Zmamou, for their guidance, support, encouragement and rewarding exchanges we had during the last three years.

Many thanks to Nathalie Leblanc for her precious advice, her kindness, the provision of the necessary facilities for the realisation of this thesis project and all the opportunities she offered me.

I would like to offer my most deep appreciation to Hélène Lenormand and Hafida Zmamou for sharing their passion for research, knowledge and skills in bio-based and cementitious construction materials. Thank you for their invaluable support, suggestions and generosity.

I would also like to thank the members of the individual follow-up committee (CSI): François Buyle-Bodin, Anne Daubresse, Baptiste Vivier and Pascal Favrel, for agreeing to follow this thesis work and their suggestions.

I convey my profound gratitude to the members of the defence jury: Bernard Kurek, Mohammed Sonebi, Irini Djeran-Maigre and Daniel Levacher for their interest in this research work and for reviewing this thesis manuscript.

Many thanks to Jean-Baptiste Besnier and Marianne Rosa for teaching me how to use different laboratory equipment and for their assistance during the experiments. I would like to thank Sébastien Potel and Elise Chenot (Geoscience platform, UniLaSalle Beauvais) for their help with XRD. Thank you to all UniLaSalle Rouen colleagues, particularly Elodie Cusset, Marie Vasseur, Alice Liguoro, Feriel Bacoup, Mariia Ostapchuk, and Laurence Alain, for their generosity.

Furthermore, I would not forget to thank all interns, PhD students and post-doctorate colleagues with whom I shared office and laboratory, particularly Maya Diakité, Angel Velasco Sanchez, Léo Saouti, Mazhar Hussein, Dylan Alavin, Morgan Lecoublet, Paul Burel, Santiago Arufe, Florian Martin, Théo Vinceslas, Mathilde Honoré and Clément Fosse, for enriching exchanges, encouragement, support and most importantly, their humour.

Lastly, thanks to all my friends, especially Constant Mahame, Jules Muhire, David Niyitegeka, Placide Uwizeyimana, Aimé Olivier Ngabonziza and Mwape Machula.

Abbreviations

SCMs	Supplementary cementitious materials	ICP-AES	Inductively coupled plasma-atomic emission spectroscopy
WA	Wood ash	W/D	Wetting and drying cycles
WFA	Wood fly ash	T	Temperature (°C)
WBA	Wood bottom ash	RH	Relative humidity (%)
WSA	Wastepaper sludge ash	MBV	Moisture buffer value (g/m^2. % RH)
SP	Sunflower pith	ρ	Bulk density (kg/m^3)
SB	Sunflower bark	λ	Thermal conductivity (W/m.K)
CFA	Coal fly ash	R_c	Compressive strength (MPa)
SF	Silica fume	R_f	Flexural strength (MPa)
GGBS	Ground granulated blast slag	Fmax	Maximum load (N)
LP	Limestone powder	AFm	Aluminate ferrite mono
MK	Metakaolin	AFt	Aluminate ferrite tri
NHL	Natural hydraulic lime	C_3A	Tri-calcium aluminate
OPC	Ordinary Portland cement	Mc	Calcium monocarboaluminate phase
ACC	Autoclaved aerated concrete	Hc	Calcium hemicarboaluminate phase
UHPC	Ultra-high-performance concrete	Hx	Calcium aluminate phase
UHPFRC	Ultra-high-performance fiber-reinforced concrete	C-S-H	Calcium-silica-hydrate
RCC	Roller compacted concrete	Mt	Million tonnes
LDS	Laser diffraction spectroscopy	RE 2020	Environmental regulation 2020
PSD	Particle size distribution	GHG	Greenhouse gas
DVS	Dynamic vapour sorption	IEA	International Energy Agency
TGA	Thermogravimetric analysis	ADEME	Agence de l'environnement et de la maîtrise de l'énergie (Agency for the environment and energy management)
TG	Mass loss	CODEM	Construction Durable et Écomatériaux Innovants (Sustainable construction and innovative eco-materials)
DTG	Differential mass loss	NOAA	National Oceanic and Atmospheric Administration
SEM	Scanning electron microscopy	USGS	United States Geological Survey
XRD	X-ray diffraction	SSD	Sortie de status de déchets (Removal from the waste status)
XRF	X-ray fluorescence spectrometry	CSI	Comité de Suivi Individuel (Individual follow-up committee)

Glossary

To facilitate the reading of this thesis manuscript, it is essential to define the following terms:

Cement paste

A cement paste can be defined as a mixture of cement and water. It serves as a glue that binds the fine and coarse aggregates to form a rock-like structure called concrete as a result of the progressive hardening of the paste due to the hydration reactions occurring between the cement phases and mixing water (Woodson, 2011).

Cement mortar

A cement mortar is a mixture of three ingredients, including a binder, generally cement, fine aggregates and water. Mostly, cement is used as a binder, while river or manufactured sand is used as fine aggregates (Li, 2011). Based on the nature of the binder, mortars can be classified into different groups. For example, lime mortar is a mortar made based on the lime binder. The application of lime mortars in building materials dates back to ancient time and persists until the 21st century (Nogueira et al., 2018; Ventolà et al., 2011). Since the late 19th century, the use of lime mortars started declining due to the invention of Portland cement, presenting better hardening and mechanical properties (Ventolà et al., 2011). Today, lime mortars are used in the restoration to restore historic buildings (Ventolà et al., 2011). Besides, lime binders are widely employed in the bio-based mortars/concrete production.

Concrete

Conventionally, concrete is a heterogenous mixture consisting of a mineral binder, water, and fine and coarse aggregates (Li, 2011). It is the second most used utility after water (Kang et al., 2020).

Bio-based building materials

In general, bio-based building materials may refer to all materials containing organic matter of plant and animal origin intended for the construction of buildings (Jones and Brischke, 2017).

Bio-based concrete

Bio-based concrete is typically a mixture of the lignocellulosic plant particles representing an important bulk volume, a mineral binder, and water (Amziane and Arnaud, 2013). The aggregates in bio-based concrete are usually the particles derived from the stem of plant cultivated for either their fibres (hemp, flax, cotton, bamboo, etc.) or for their seeds (sunflower, maize, rice, palm oil, etc.) (Amziane, 2016). It is important to note that the bio-based aggregates replace a portion or the totality of the sand. Furthermore, it is worth mentioning that the terms

"bio-based concrete", and "bio-based mortar and render" differ depending on their application, otherwise, both terms label materials of similar composition (Dutreix et al., 2017).

To conclude, Table 0-1 summarises the typical composition of the aforementioned materials.

Table 0-1. Main differences between cementitious and bio-based systems.

	Mineral binder	Fine mineral aggregates	Coarse mineral aggregates	Plant particles	Water
Paste	×				×
Mortar	×	×			×
Conventional concrete	×	×	×		×
Bio-based mortar/concrete	×	×*		×	×

**In addition to plant particles, bio-based mortars/concretes sometimes contain fine mineral aggregates.*

Valorization of the thesis

Review paper

1. **Ndahirwa D.**, Zmamou H., Lenormand H., Leblanc N., 2022. The role of supplementary cementitious materials in hydration, durability and shrinkage of cement-based materials, their environmental and economic benefits: A review. Cleaner Materials 5, 100123. https://doi.org/10.1016/j.clema.2022.100123.

Communications

1. **Désiré Ndahirwa**, Hafida Zmamou, Hélène Lenormand, Nathalie Leblanc, Durability performance and thermal conductivity of wood biomass ash and sunflower by-products-based mortar, 20th Global Joint Seminar on Geoenvironmental Engineering, GEE2022, Osaka University, 19-20 May 2022, Japan (oral and written).
2. **Désiré Ndahirwa**, Hélène Lenormand, Hafida Zmamou, Nathalie Leblanc, Mechanical properties of the biomass ash-based binder, 19th Global Joint Seminar on Geoenvironmental Engineering GEE2021, ESITC Caen, 20-21 May 2021, France (oral and written).
3. **Désiré Ndahirwa**, Hélène Lenormand, Hafida Zmamou, Nathalie Leblanc, Potential use of fly ashes from biomass blended with lime as hydraulic binder, 3rd Euromaghreb Conference "Sustainability and Biobased Materials on the road of Bioeconomy", 19-20 October, 2020, Rouen, France (oral).

Posters

1. **Désiré Ndahirwa**, Hélène Lenormand, Hafida Zmamou, Nathalie Leblanc, Mechanical and thermal properties of the lightweight mortar made of wood biomass ash and sunflower particles, XXIVème Journée de l'École Doctorale Normande de Biologie Intégrative, Santé & Environnent JED 2022, 01-02 June 2022 (online).
2. **Désiré Ndahirwa**, Nathalie Leblanc, Hélène Lenormand, Hafida Zmamou, High-volume use of wood biomass ash in cementitious materials, Journée des Jeunes Chercheurs 2021, 7-ème édition Wallonie/Hauts-de-France, 25 Novembre 2021, Dunkerque, France.
3. **Désiré Ndahirwa**, Nathalie Leblanc, Hélène Lenormand, Hafida Zmamou, Valorization of different biomass ashes and agricultural by-products in the production of concrete, Journée des doctorants 2021, 16 April 2021, UniLaSalle Rouen, France.

List of figures

List of Tables

Introduction

1.1 General context

1.1.1 Wood ash and sunflower particles

While the drawbacks of greenhouse gas emissions have become more evident in the recent years, various economic sectors including construction have recognized their implications and have embarked on the search for sustainable pathways for their activities. One of the most promising approaches is the recycling and reuse of different industrial and agricultural by-products in the building materials.

The concrete industry has been using a wide range of industrial by-products as supplementary cementitious materials (SCMs) for many years. However, owing to heavy environmental impact of the industrial processes generating some of these SCMs, there is a growing interest in alternative materials with lower carbon footprints, particularly those derived from biomass. Wood ash is one of emerging biomass by-products that has attracted a significant research attention in the recent years. It is obtained from the combustion of a variety of wood products such as chips, sawdust, etc., from heating and power biomass plants. Figure 0-1 shows a typical thermal and heating biomass plant diagram.

There are generally two types of wood ash: bottom ash and fly ash. “Bottom ash is an ash fraction generated from the grate and in the primary combustion chamber. It usually contains mineral impurities from biomass fuel, such as sand particles (mostly quartz), soil, small stones and unburnt biomass fraction. On the other hand, fly ash is classified into cyclone fly ash and filter fly ash. The cyclone fly ash refers to fine mainly organic ash particles transported with the flue gas and precipitated in the secondary combustion zone, in the boiler and particularly in the cyclones placed behind the combustion unit. The finer fraction of fly ash, which precipitates in electrostatic filters, fibrous filters or as condensation sludge in flue gas condensation units, is called filter fly ash” (Modolo et al., 2013; Van Loo and Koppejan, 2008).

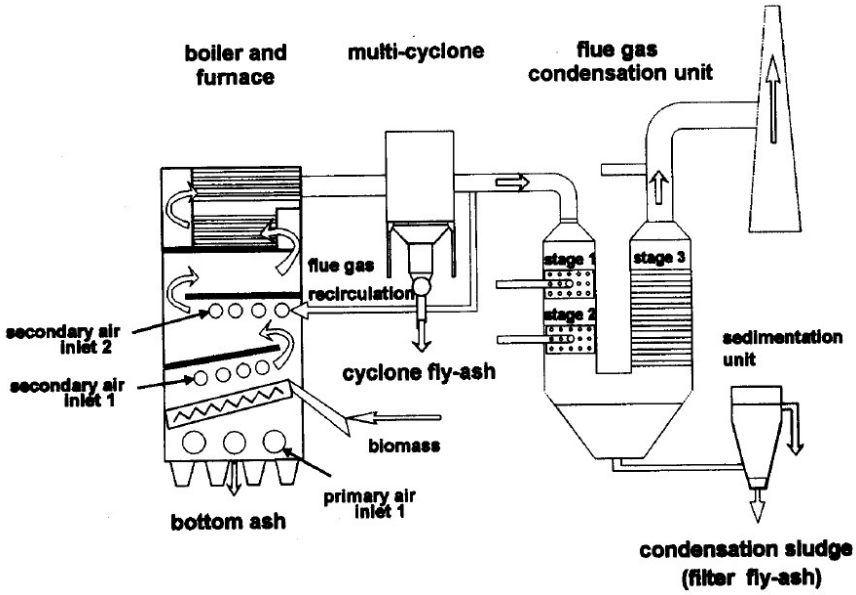

Figure 0-1. Diagram illustrating a typical thermal and heating biomass plant (Obernberger et al., 1997).

The aforementioned by-products can be used as a filler or a substitute for cement and aggregates in cement blends, pastes, mortars and concretes. The characteristics of the wood fly ash are comparable to those of cement and other recognised SCMs. Wood ash is mostly composed of angular, spherical and irregular shaped particles (Ohenoja et al., 2016; Omran et al., 2018a). Its bulk density typically ranges between 300 and 950 kg/m^3 (Abdullahi, 2006; Chowdhury et al., 2015; Naik, 2002; Van Loo and Koppejan, 2008).

Other than that, the use of plant particles in the production of lightweight building insulation materials has increased considerably recently. As the demand in bio-based concrete keeps increasing, the industry is looking for new agricultural wastes to valorize as aggregates. The by-products from sunflower crop, especially pith and bark are among the most suitable alternatives to hemp shiv that have already been identified. They are characterised by high porosity, low density and excellent insulation properties. The bulk density of the sunflower pith and bark is in the range of 14-37 kg/m^3 and 120-180 kg/m^3, respectively (Abbas et al., 2020; Lagouin et al., 2019; Mahieu et al., 2019; Yin et al., 2007). The thermal conductivity has been reported to be about 0.035-0.051 W/m.K for sunflower pith and 0.053-0.070 W/m.K for sunflower bark (Brouard et al., 2018; Lenormand et al., 2014; Magniont, 2010; Magniont et al., 2012; Vandenbossche et al., 2012).

1.1.2 Impact of the construction sector on the environment

Since the 20th century have been marked with rapid population growth and urbanization. According to recent the statistics, the global population increased from 1 billion in 1800 to about 8 billion today (Roser et al., 2013). In general, population growth directly correlates with urbanization. At the beginning of the 20th century, nearly 10 % of the population lived in the cities; today roughly 55 % of the world's population which is the equivalent of 4.2 billion inhabitants live in the cities (Mehta, 2002; The World Bank, 2020). The demographic growth and urbanization have led to the extensive use of natural resources, energy, and the quick industrial development. Consequently, this has resulted in serious environmental concerns such as global warming, drought, flooding, etc.

From 1980s, the trend in the global surface temperature has been increasing along with carbon dioxide emissions (Global Monitoring Laboratory NOAA, 2022; Ritchie et al., 2020). Since the pre-industrial era, the global average temperatures have increased by more than 1ºC (Ritchie et al., 2020). Greenhouse gas (GHG) emissions are perceived as one of the major causes of the climate crisis. The most common GHG include carbon dioxide (CO_2), methane (NH_4), nitrous oxide (N_2O), etc. The cement industry and buildings represent a large part of carbon dioxide (CO_2) emissions from the overall construction sector. For example, the French building sector generates more than 123 million tonnes of CO_2 per year and accounts for 44 % of energy consumption (Ministère de la Transition écologique, 2021a).

The Portland cement production is a high energy-intensive process that emits massive amounts of CO_2 emissions into the atmosphere. The clinker is a product of limestone and clay calcination in the kiln at 1450 ºC. After grinding the clinker into a fine powder, a small amount of gypsum is added. The resulting product is ordinary Portland cement (OPC). The decomposition of limestone into calcium oxide represents two-third while the combustion of fuels accounts one-third of the total CO_2 emissions generated from the cement production (International Energy Agency IEA, 2018; Skibsted and Snellings, 2019). The production of 1 tonne of OPC releases about 0.87-1 tonne of CO_2 into atmosphere, making the entire cement industry responsible for 6-8 % of anthropogenic CO_2 emissions and the third largest energy consumer, representing 7 % of the total industrial energy use (International Energy Agency IEA, 2018; Li et al., 2020b; Skibsted and Snellings, 2019).

Over the last few years, the global demand in cement, thus concrete has significantly increased (Muduli and Mukharjee, 2019). In 2002, the annual demand in concrete was estimated at around 2.7 billion m^3 and it is expected to reach 7.5 billion m^3 by 2050 (Rafieizonooz et al., 2016). The

United States Geological Survey (USGS) data show that the global cement production increased from 1660 Mt in 2000 to 4200 Mt in 2020 (Hatfield, 2022; van Oss, 2001). According to the IEA Technology Roadmap projections, the cement production could reach 4682 Mt/year by 2050 (International Energy Agency IEA, 2018). Apart from cement, the concrete industry also requires extreme quantities of natural resources. Actually, the concrete industry reportedly uses up about 12.6 billion tons of raw materials including cement, water, sand and rock per year (Mehta, 2002).

1.2 Scope of research

Generally, the bio-based mortar/concrete is composed of three main components. The binding material which usually of mineral origin, the aggregates which are plant derived particles and the mixing water. Lime is the most common binder in bio-based concrete. However, other binders like cement and geo-sourced materials such as earth, are also used. The production of lime and cement consumes significant quantities of natural non-renewable resources and energy, as well as emits massive amounts of carbon dioxide into the atmosphere. Replacing lime and cement with the maximum possible amount of wood ash could significantly reduce the environmental burden and cost of the binders in bio-based mortars/concretes.

On the other hand, hemp concrete is the most predominant bio-based building material today. However, owing to the attention that has been paid to the bio-based building materials, there is a concern that the available hemp shiv supply might not be able to satisfy the market demand in the next few years. In addition to industrial hemp, plenty other annual lignocellulosic crops are grown in France and around the world. The harvesting of these crops generates tons of by-products which could be applied as a new source of aggregates in bio-based mortars/concretes.

The aim of this thesis work is to study the variability of wood ashes and valorize them with sunflower particles into lightweight bio-based building materials. Wood ash is used as the main component of the binding matrix while sunflower particles are added separately in the mixtures as aggregates. Two applications are proposed:

i. Sunflower pith is used to produce the lightweight mortars for implementation by projection;
ii. Sunflower bark is employed to elaborate the mixtures for the production of prefabricated building elements, respectively.

The main idea is to find a good compromise between mechanical and thermal properties while incorporating larger quantities of wood ash and sunflower particles in the mixtures.

The main objectives of this research are to:

- Valorize biomass by-products in bio-based lightweight insulation mortars;
- Study potential binding matrices made of wood ashes mixed with 5-20 % natural hydraulic lime and ordinary Portland cement contents;
- Investigate the effect of natural hydraulic lime and ordinary Portland cement on the mechanical and microstructural properties of the wood ash-based pastes;
- Prove the feasibility of using a binder made of higher than 80 % wood ash content (by mass) as a binder of bio-based building materials;
- Examine the mechanical, microstructural, thermal and hygroscopic properties of the sunflower pith mortars and sunflower bark mixtures;
- Understand the reaction mechanisms that occur between the wood ash binder and sunflower particles in the mixtures;
- Contribute to the available skills and know-how in the field bio-based building materials.

1.3 Thesis funding: DIVA project

The French environmental and energy management agency (ADEME) funded this work, which is part of the project DIVA (Démonstrateur Industriels Valorisation des Agro-résidus en écoconstruction et bio-rénovation). The DIVA project aims to:

- Manufacture and commercializing insulating mortars incorporating sunflower and maize piths that can be easily prepared on site to be sprayed by conventional façade machines. These products are intended for the renovation of buildings, in particular old buildings (dating from before 1949);
- Study the feasibility of prefabricating insulation materials in factories based on barks and possibly piths, mainly destined for new buildings, in collaboration with industrial actors of the prefabrication for a validation on an industrial scale (proof of concept only);
- Study other ways of valorization of the piths in the realisation of lightweight and/or insulating screeds (new and renovation) and filling of hollow walls and construction voids (renovation);
- Study and developing the harvesting process and transformation of sunflower and maise stems;
- Studying and defining the modalities and logistic processes allowing to ensure the constancy of the characteristics and performance of the plant materials throughout the chain (packing, controls, etc.);

- Defining the economic and commercial relations between producers, processors, manufacturers of building materials and craftsmen.

This project assembles a number of industrial and academic institutions such as PAREXGROUP subsidiary of the SIKA group, which is the coordinator of the project, UNILASALLE, three agricultural cooperatives (Groupe La Dauphinoise, OVALIE, GDA Loches-Montresor), ENTPE and Groupe F.L.D.I.

1.4 Organization of the chapters

This thesis manuscript consists of six chapters.

The introduction introduces two biomass by-products that this work intends to study and valorize. Then, the impact of the construction sector, particularly cement and concrete industry, is outlined. At last, the scope and objectives of this research are highlighted.

Chapter 1 summarises the literature on the supplementary cementitious materials (SCMs), plant derived particles and their applications. At the beginning, the five commonly used SCMs were discussed and presented in form of a review paper.

In Chapter 2, the procurement of the wood ash and its applications were reviewed. Subsequently, the reported physical and chemical properties of the wood biomass ash, and its environmental behaviour were provided. Furthermore, the previous publications on the applications of the wood ash in cement-based and bio-based materials have been summarised. Finally, the literature on sunflower by-products, their applications, development and properties of the bio-based concretes was examined.

Chapter 3 presents the raw materials and experimental methods used in the characterization of the biomass ashes, natural hydraulic lime, ordinary Portland cement and sunflower particles. The physical and chemical properties of these raw materials are evaluated. The obtained results are presented and discussed. As a result, four wood ashes are selected to be used in the preparation of the binding matrices.

In Chapter 4, thirty binding matrices are elaborated based on four wood ashes chosen in the previous chapter. Then, the mechanical and microstructural properties of these wood ash pastes are investigated. The influence of natural hydraulic lime and ordinary Portland cement on the overall performance of the pastes is also highlighted. Lastly, two wood ash pastes with the highest compressive strengths at 28 days, are selected to be used in the preparation of the sunflower mixtures.

In Chapter 5, six sunflower pith mortars are designed and elaborated. At the desired curing age, the mechanical, microstructural, thermal and hygroscopic properties of the hardened samples are examined. In addition, the effect of the sunflower particles on the overall properties of the developed lightweight mortars is also highlighted.

In Chapter 6, six sunflower bark mixtures are developed. At the required curing age, the mechanical, microstructural, thermal and hygroscopic properties of the samples are investigated. Furthermore, like in the previous chapter, the impact of sunflower bark on the properties of the resulted mixtures is underlined.

Chapter 1: Overview of most popular supplementary cementitious materials

This chapter presents a summary of the previous publications on the applications of most commonly used industrial by-products in construction materials.

At first, five different industrial by-products, namely coal fly ash, silica fume, ground granulated blast furnace slag, limestone powder and metakaolin are selected. Then, a survey on their impact on the hydration, durability and shrinkage of cement-based materials, as well as their social and environmental advantages is presented. It is noteworthy that, this section is a lightly modified version of the review paper that I co-authored, published in Cleaner Materials 5(2022) 100123; https://doi.org/10.1016/j.clema.2022.100123. It has been reused here with the authorisation of the copyright holder.

Furthermore, a synthesis of the literature on the intrinsic physico-chemical properties and applications of the wood biomass ash and sunflower particles in different building materials such as pastes, mortars and concretes, is provided. In addition, the available findings on bio-based mortars/concretes in general are also examined. In conclusion, important points to retained are highlighted.

1.1 The role of supplementary cementitious materials in hydration, durability and shrinkage of cement-based materials, their environmental and economic benefits: A review

1.1.1 Abstract

Due to strict environmental regulations, the construction sector has observed extensive use of supplementary cementitious materials (SCMs) in recent years. As a result, new alternative SCMs have emerged and research in this particular area has considerably developed. Although a great deal of research has been conducted on cement-based materials blended with SCMs, their characteristics, effects on the hydration, and the durability of cement pastes, mortars and concrete are still the subject of debate. Therefore, this review summarized the most widespread methods for SCMs characterization, main characteristics, and the role of each of the five widely used SCMs including coal fly ash, silica fume, ground granulated blast furnace slag, limestone powder, and metakaolin in the hydration and durability of cement-based materials. Ultimately, their environmental and economic advantages were also reviewed.

A huge variation in the SCMs physical and chemical characteristics has been highlighted as the major concern when it comes to the establishment of standards and characterization methods. The literature has also shown that the hydration, compressive strength and durability of cement-based materials blended with SCMs typically depend on the replacement ratios, fineness and synergic effect of the SCMs' reactivity mechanisms. Owing to their high specific surface area and pozzolanic activity, partial cement replacement with a suitable amount of silica fume and metakaolin considerably accelerates the hydration and increases the heat of hydration of cement-based materials. Besides, limestone powder and ground granulated blast slag reportedly present better environmental and economic benefits compared to metakaolin and silica fume.
Keywords: Supplementary cementitious materials, cement-based materials, hydration, durability, chloride binding ability, shrinkage.

1.1.2 Introduction

The trend in the supplementary cementitious materials (SCMs) applications in cement and concrete have drastically increased over the last few decades (Kocak, 2020; Yang et al., 2016). Based on the origin, SCMs can be distinguished in organic and inorganic admixtures. Moreover, depending on their nature, SCMs can be classified into natural pozzolans and industrial by-products. Natural pozzolans such as limestone powder (LP), volcanic rock ashes, etc. have been widely used in construction for many years. The most commonly used industrial by-products

in cement and concrete manufacturing include coal fly ash (CFA), ground granulated blast furnace slag (GGBS), silica fume (SF), and calcinated clays like metakaolin (MK).

The cement industry poses a great threat to the environment. Indeed, the production of 1 tonne of OPC releases about 0.87-1 tonne of carbon dioxide (CO_2) into the atmosphere, making the entire cement sector responsible for 6-8 % of anthropogenic CO_2 and the third-largest energy consumer, representing 7 % of the total industrial energy use (International Energy Agency IEA, 2018; Li et al., 2020b; Skibsted and Snellings, 2019). At present, the construction sector considers the use of SCMs and industrial by-products as a relevant approach to minimize its burden on the environment. Skibsted and Snellings (2019) reported that replacing OPC clinker with SCMs can reduce CO_2 emissions by 30-40 % without considerably compromising the main properties such as the strength and durability of cement-based materials. Thanks to this method, the clinker proportion in the cement has been declining since early 2000 (Schneider et al., 2011). The IEA technology roadmap claimed that the clinker to cement ratio in 2014 was 0.65 and predicted that it will reach 0.60 by 2050. Meanwhile, the thermal energy intensity of clinker, being accounted for 3.5 GJ/tonne clinker in 2014, is expected to attain 3.1 GJ/tonne clinker by 2050 (International Energy Agency IEA, 2018).

Additionally, the SCMs are broadly employed as cement replacement in a variety of cement-based materials, in particular, pastes (Antoni et al., 2012; Moghaddam et al., 2019; Munjal et al., 2021), mortars (Ni et al., 2021; Shaikh et al., 2014; Wianglor et al., 2017), and all types of concrete including lightweight concrete (Ahmad et al., 2019; Shafigh et al., 2016), high-performance concrete (Alaskar and Hooton, 2020; Iqbal Khan et al., 2017) and ultra-high-strength concrete (Huang et al., 2017; Shi et al., 2015). In the USA more than 60 % of ready-mixed concrete incorporates SCMs (Juenger and Siddique, 2015).

Tightening environmental regulations has led to extensive utilization of SCMs in cement and concrete. To meet the demand and requirements of the market, lots of research efforts have been made, resulting in the expansion of the SCMs applications scale in construction materials and the emergence of new supplementary alternative cementitious materials. A great deal of research in this area focuses on optimizing the quantity of SCMs that can substitute the clinker in blended cement and ordinary Portland cement (OPC) in concrete without compromising its properties (Kang et al., 2019a; Pacewska and Wilińska, 2013; Skibsted and Snellings, 2019; Wang et al., 2018; Yang et al., 2016; Li et al., 2020b).

The presence of SCMs in cement-based materials affects the properties of cement-based materials including the hydration process, microstructure, strength development, and durability (Kadri et al., 2011; Kocak, 2020). In a hydrous cementitious system, depending on the type of the SCM, four reactivity mechanisms such as filler, dilution, nucleation, and chemical effects can be observed. These actions play a major role in the formation of hydration products, microstructure refinement, densification, porosity, etc. In addition to the pozzolanic reactions, other parameters influencing the properties of cement-based materials include particle size distribution, specific surface area, replacement ratios and etc. (Liu et al., 2018; Zhang et al., 2016a, 2016b).

It is generally accepted that replacing cement with SCMs at low content (below 50 %) can positively affect the mechanical and durability properties of cement-based materials (ElNemr, 2020; Juenger and Siddique, 2015; Li et al., 2020b; Medjigbodo et al., 2018; Sigvardsen and Ottosen, 2019; Xu et al., 2020; Zhang et al., 2016a). On the contrary, when added at higher levels (above 50%), they can have a detrimental influence on the overall performance of the material (Kayali and Sharfuddin Ahmed, 2013; Li et al., 2020b; Wianglor et al., 2017). Nevertheless, high-volume SCMs have been confirmed to enhance some concrete properties such as shrinkage resistance (Li et al., 2020b; Medjigbodo et al., 2018) and resistance to chemical attacks (such as expansion due to chloride, sulphate, and alkali-silica reaction) (Bondar et al., 2019; Zhang et al., 2019) and frost (Shon et al., 2018).

Although a large number of research works (De Weerdt et al., 2011; Lothenbach et al., 2014; Medjigbodo et al., 2018) and reviews (Özbay et al., 2016; Wang et al., 2018; Panesar and Zhang, 2020) have investigated the role of SCMs in the hydration and durability of cement-based materials, these aspects are still not entirely understood mostly due to their complexity and large disparities in SCMs characteristics. Besides, very few review papers have attempted to compile in one summary the aspects covered within this present work considering the five most widespread SCMs.

Therefore, the aim of this review is to provide an overview of the recent research developments (from 2010 to 2021) mainly focusing on coal fly ash (CFA), silica fume (SF), ground granulated blast slag (GGBS), limestone power (LP) and metakaolin (MK). At first, the major physical and chemical characteristics of SCMs with their respective characterization methods were reviewed. Afterward, the contribution of each of the five earlier-mentioned SCMs to the cementitious materials hydration, microstructure, compressive strength, chloride binding capacity, and shrinkage resistance was summarized. Finally, the environmental and economic

benefits of the considered SCMs were outlined. This review intends to support scholars and researchers seeking to upgrade their knowledge in treated aspects while enabling them to save a considerable amount of time.

1.1.3 Common supplementary cementitious materials used in cement-based materials

Fly ash (FA) is an industrial by-product obtained from the combustion of pulverized coal and/or biomass as fuels at electrical power stations (Omran et al., 2018; Park, 2020). FA particle size distribution has been reported to be comparable to that observed on OPC. The physical, chemical and morphological properties of FA may vary depending on a wide range of factors such as the composition of raw coal and/or biomass, degree of pulverization, combustion temperatures, methods of collection and storage conditions (Aïtcin, 2016; Omran et al., 2018; Panesar and Zhang, 2020).

Regarding the calcination temperatures, Cheah and Ramli (2011) reported that carbonates and bicarbonates particularly calcite ($CaCO_3$) abundantly available in wood ash can be obtained at low temperatures (below 500 °C). However, the amount of $CaCO_3$ decreases with increase in furnace temperatures up to greater than 1000 ºC. The pronounced reduction in the above-mentioned chemical compounds can be attributed to the decomposition of $CaCO_3$ into calcium oxide (CaO). This chemical transformation simultaneously releases carbon dioxide (CO_2) at temperatures beyond 550 °C (Sigvardsen et al., 2021). Both coal fly ash (CFA) and biomass fly ash (BFA) are considered as SCMs. However, this paper explored coal fly ash (CFA) due to its widespread applications in cement-based materials.

Silica fume (SF) can be defined as an ultrafine, extremely reactive powder generated in electric arc furnaces during the production of silicon and ferrosilicon alloys. SF is collected at around 800 °C and is mainly composed by amorphous silicon oxide (Aïtcin, 2016; Zhang et al., 2016b). Owing to the carbon and iron content, SF can have either whitish-grey or dark grey colour (Aïtcin, 2016). SF has been used in the production of cementitious materials especially high and ultra-high-performance concrete thanks to its pozzolanic reactions and microstructure refinement capacity (filler effect), which thereby contribute to the improvement of the overall concrete density, strength, and durability (Aïtcin, 2016; Wang et al., 2020a; Wu et al., 2016; Zhang et al., 2016b).

Ground granulated blast furnace slag (GGBS) is a by-product from the pig iron manufacturing, obtained at temperatures about 1170-1500 °C (Aïtcin, 2016; Panesar and Zhang, 2020; Samad and Shah, 2017). On the other hand, limestone powder (LP) is a by-product of limestone quarry

obtained after the process of grinding limestone. Owing to its availability and high content in calcium oxide, LP has been used in the production of cement-based materials for many years (Tang et al., 2019; Wang et al., 2018). Thanks to the filler, nucleation, and dilution effects, LP favourably contributes to the hydration, densification of pore structure and mechanical properties of cement-based materials (Li et al., 2020b; Panesar and Zhang, 2020; Scrivener et al., 2019; Tang et al., 2019; Wang et al., 2018).

Metakaolin (MK) is an amorphous aluminosilicate fine, white powder obtained as a result of kaolinitic clay calcination at high temperatures from 450 °C to 900 °C depending on the purity and crystallinity of the precursor clay. MK is mostly used in several architectural applications and high-performance concrete (Aïtcin, 2016; Meddah et al., 2018; Panesar and Zhang, 2020). MK complies with ASTM C618 class N chemical requirements (ASTM C618, 2003; Kadri et al., 2011).

1.1.4 Characterization of supplementary cementitious materials (SCMs)

The characterization of SCMs is generally recommended prior to their application in cement-based materials (Cheah and Ramli, 2011). According to Arvaniti et al. (2015a), the characterization techniques initially designed for Portland cement can also be utilized on SCMs. However, there could occur some limitations due to the different physical and chemical characteristics of these two types of materials. In this section, the techniques that are widely applied to characterize the supplementary cementitious materials have been discussed. Moreover, the main physical and chemical properties of SCMs have been summarized.

(a) Physical properties of SCMs

Sieve analysis and laser diffraction spectroscopy (LDS) are the most widely used techniques to determine the particle size distribution (PSD) of the SCMs. The sieve analysis also called the gradation test is usually applied on particles diameter greater than 2 mm. It consists on mechanically shaking the sieves column thereby allowing the material to pass through a set of sieves from bigger mesh to the smaller mesh size and weighing the quantity of material that is stopped by each sieve as a portion of the entire mass. Basically, the sieve analysis is carried out according to the European standard EN 196-6 or ASTM C136 (Arvaniti et al., 2015a; ASTM C136, 2003). On the contrary, the laser diffraction spectroscopy (LDS) technique is often used to measure the PSD of ultrafine powders. The latter is able to determine the particles size ranging from 0.01 to 3500 µm (Arvaniti et al., 2015a). Although LDS has been validated by the International Organization for Standardization (ISO 13320:2020, 2020), the analysis should be carried out with precaution to avoid potential errors that may occur from the mathematical

models used, agglomeration of SCMs particles, etc. (Arvaniti et al., 2015b; Juenger and Siddique, 2015).

Besides, bulk density, skeletal density, specific gravity, and specific surface area have been also among the commonly investigated physical characteristics of SCMs. Generally, the density and specific gravity of cement can be measured with the Le Chatelier flask as per (ASTM C188-95, 2003). The protocol consists on placing the liquid (for example: kerosine) into an empty dry flask. After taking the initial reading, a sample can be added. At this point, the final reading should be registered. The sample density is eventually obtained by dividing the sample mass by the volume of displaced liquid ($\rho = \frac{M}{V}$), where ρ is the density (g/cm^3), M, the mass of cement (g) and V, the volume of displaced liquid after adding the sample (cm^3). The flask temperature fluctuations should be kept under 0.2°C until the test is completed (ASTM C188-95, 2003). On the other side, the specific gravity is obtained by dividing cement density by water density at 4°C ($S_p = \frac{D_c}{D_w}$), where S_p, D_c, D_w are respectively the specific gravity of cement, cement density (kg/m^3), water density (kg/m^3) that is equal to 1000 kg/m^3 (1g/cm^3) at 4 °C. The skeletal density is computed using the helium pycnometer (Arvaniti et al., 2015b; ASTM C188-95, 2003; Brewer et al., 2014; Helsel et al., 2016).

Furthermore, the Blaine air-permeability and Brunauer, Emmett and Teller (BET) methods have been widely used to determine the cement and SCMs specific surface area (SSA). The Blaine air-permeability consists on measuring the resistance of air movement through a well-loaded powder bed under a specific air pressure (Arvaniti et al., 2015b; ASTM C204, 2003; Mantellato et al., 2015). On the other hand, the BET essentially uses the nitrogen adsorption principle but other inert gas can also be applicable. The principle relies on computing the nitrogen molecules volume required to form a single layer on the surface of the sample (Arvaniti et al., 2015b; Mantellato et al., 2015). The comparative study by Arvaniti et al. (2015a) devoted to SCMs characterization approaches concluded that apart from the technical limitations that may occur, in most cases the techniques designed for cement characterization may not be explicitly suitable for SCMs due to the irregularity of their shapes and sizes.

Throughout the process of collecting data on the SCMs physical characteristics, it has been noticed that some challenges could emerge due to not only limited protocol descriptions but also inappropriate use of some expressions particularly density and bulk density. Thus, providing detailed information in research reports could contribute to efficient knowledge transmission and interpretation of the results.

The major physical properties of the SCMs discussed in the present review are listed in Table 1-1. Generally, CFA, SF and GGBS consist of spherical particles while, LP and MK are made up of angular-shaped particles. The average particle size distribution D_{50} of CFA, SF, GGBS, LP and MK largely vary from 5.89 to 23.4 μm, 0.1 to 58.2 μm, 10.8 to 14.4 μm, 3.7 to 8.5 μm and 1 to 31 μm, respectively. SF and MK particles have been reported to be finer while GGBS tends to have coarser particles. On the other side, the density of five selected SCMs is in the range of 2000 and 3000 kg/m^3 whereas, the reported bulk density of CFA, SF, GGBS and MK varied from 921.7 to 2000 kg/m^3, 130 to 2400 kg/m^3, 600 to 1300 kg/m^3 and 852.3 to 2300 kg/m^3, respectively. Besides, treatments such as grinding, densification, etc. can alter the bulk density of SCMs. For example, the bulk density of non-densified and densified SF can attain 130-430 kg/m^3 and 200-650 kg/m^3, respectively (Juenger et al., 2012; Panesar and Zhang, 2020; Zhang et al., 2016b).

Table 1-1. Physical properties of common SCMs reported in literature.

SCMs	Particle size distribution D_{50} (μm)	Density (kg/m^3)	Specific gravity	Blaine specific surface area (m^2/kg)	Shape	Reference
CFA	5.89-23.40	2190-2310 922*- 2000*	1.30-2.90	250-600	Spherical	(Bourchy et al., 2019; Elahi et al., 2010; Hany et al., 2020; Ipavec et al., 2013; Iqbal Khan et al., 2017; Kayali and Sharfuddin Ahmed, 2013; Li, 2016; Megat Johari et al., 2011; Nežerka et al., 2019; Panesar and Zhang, 2020; Yang et al., 2016)
SF	0.10-58.20	208-2400 130*- 2400*	2.10-2.50	150-30000 290**- 30000**	Spherical	(Bourchy et al., 2019; Elahi et al., 2010; Hany et al., 2020; Huang et al., 2017; Ipavec et al., 2013; Iqbal Khan et al., 2017; Juenger et al., 2012; Kayali and Sharfuddin Ahmed, 2013; Li, 2016; Meddah et al., 2018; Medjigbodo et al., 2018; Megat Johari et al., 2011; Nežerka et al., 2019; Panesar and Zhang, 2020; Zhang et al., 2016b)
GGBS	10.80-14.40	2800-2960 600*- 1300*	2.67-2.91	340-600	Spherical	(Bourchy et al., 2019; Hany et al., 2020; Ipavec et al., 2013; Li and Jiang, 2020; Megat Johari et al., 2011; Saluja et al., 2019; Shariq et al., 2010; Yang et al., 2016)
LP	3.70-8.50	2640-2700	2.61-2.70	380-1211 800**-2200**	Angular	(Huang et al., 2017; Ipavec et al., 2013; Li and Jiang, 2020; Medjigbodo et al., 2018; Panesar and Zhang, 2020; Shi et al., 2016)
MK	1.00-31.00	852*- 2300*	2.20-2.64	370-15000 16000**- 19000**	Angular	(Bucher et al., 2017; da Silva Andrade et al., 2018; Hany et al., 2020; Li, 2016; Meddah et al., 2018; Medjigbodo et al., 2018; Megat Johari et al., 2011; Muduli and Mukharjee, 2019; Nežerka et al., 2019; Panesar and Zhang, 2020; Ramezanianpour and Bahrami Jovein, 2012; Shi et al., 2016; Wianglor et al., 2017)

**Bulk density (kg/m^3); **BET specific surface area (m^2/kg).*

As presented in Table 1-1, the specific gravity of CFA, SF, GGBS, LP and MK is in the range of 1.30-2.90, 2.10-2.50, 2.67-2.91, 2.61-2.70 and 2.20-2.64, progressively. The slight disparities have been perceived in the specific gravity of all selected SCMs except CFA. The specific surface area (SSA) varied from one SCM to another. The Blaine SSA ranges between 250-600 m^2/kg for CFA, 150-30000 m^2/kg for SF, 340-600 m^2/kg for GGBS and 380-1211 m^2/kg for LP. On the other hand, the BET SSA of SF, LP and MK has been reported to be in the range of 290-30000 m^2/kg, 800-2200 m^2/kg and 16000-19000 m^2/kg, respectively. Obviously, the SSA is primarily influenced by the SCMs particle size distribution. In fact, the finer SCM particles are, the higher SSA becomes.

(b) Chemical composition of SCMs

The chemistry of cementitious materials including SCMs is usually studied using numerous quantitative and qualitative techniques. The oxide compounds can be quantified with X-ray fluorescence spectrometry (XRF) (Arvaniti et al., 2015a; Rafieizonooz et al., 2016). The thermogravimetric analysis (TGA) can be used to determine the loss on ignition (LOI) and thermally unstable phases. On the other hand, X-ray diffraction (XRD) enables to study the mineralogical composition of the cementitious materials (Anjos et al., 2020; Yang et al., 2017). Scanning electron microscopy (SEM) offers a wide range of possibilities to evaluate the microstructure (pore structure, particle shape, etc.). However, when equipped with the energy dispersive X-ray spectrometry (EDS), it can be used to detect chemical elements and their respective contents in a given cementitious material (Kocak, 2020; Wianglor et al., 2017).

Based on previous publications, the chemical composition of supplementary cementitious materials has been recapitulated in Figure 1-1. The data has been collected taking into account different geographical locations including Europe, America, Asia, Australia and Africa.

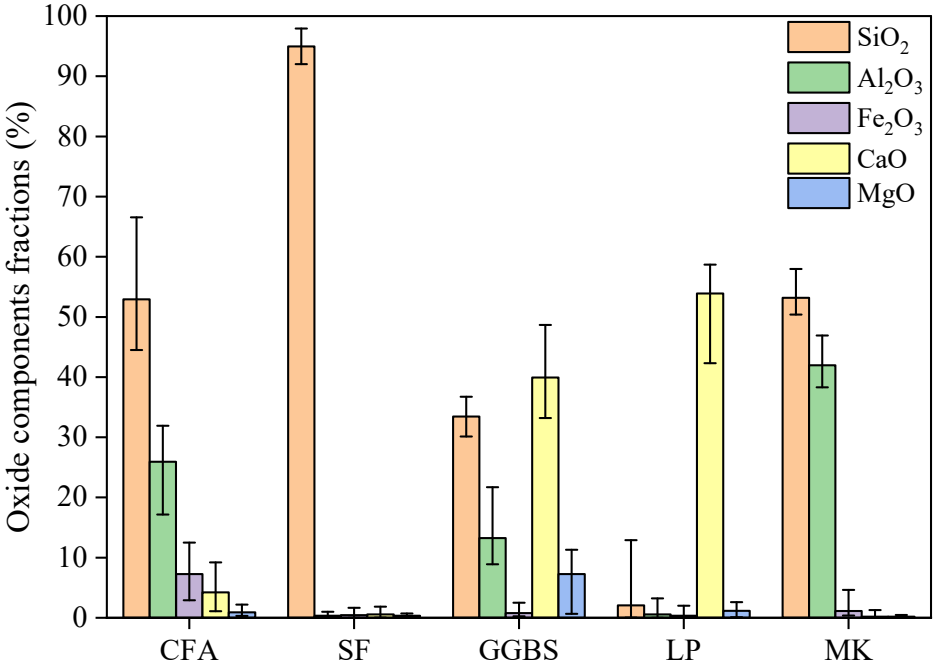

Figure 1-1. SCMs chemical composition.

Figure 1-1 presents the fractions of major oxides in CFA, SF, GGBS, LP and MK. The top end of the bar chart indicates the average whereas, the upper and lower error bars represent maximum and minimum ranges, respectively. Actually, CFA is mainly composed by SiO_2 and Al_2O_3. Moreover, oxides such as Fe_2O_3, CaO, MgO can also be found in CFA but, their proportions remain minimal (less than 10 % each). On the contrary, SF is almost entirely composed by SiO_2 representing about 95 %. At the same time, the average amounts of Al_2O_3, Fe_2O_3, CaO and MgO in SF have been reported to be rather insignificant (lower than 1 % each).

The GGBS chemical composition tends to be well-balanced compared to other SCMs. In fact, the major oxides in GGBS include CaO, SiO_2, Al_2O_3 and MgO, typically accounting for 40 % ,33 %, 13 % and 7 %, respectively. Furthermore, LP is mainly composed by CaO, representing more than 50 % of its overall oxide compounds. It is worth mentioning that, unlike other SCMs, LP exhibits extremely high loss on ignition (LOI) estimated at about (35-45) % while CFA, SF, GGBS and MK account for up to 5.5 %, 5 %, 2 % and 4 %, respectively. As far as MK is concerned, the major oxides in MK include SiO_2 and Al_2O_3, representing 53 % and 42 %, respectively. Additionally, MK can contain slight amounts of Fe_2O_3, CaO and MgO (below 2 % each).

The ternary diagram shown in Figure 1-2 illustrates the positions of CFA, SF, GGBS, LP and MK according to their CaO-Al_2O_3-SiO_2 contents. As it can be seen, the chemistry of SCMs

widely varies from one to another, which is in agreement with the boundaries suggested by (Lothenbach et al., 2011; Panesar and Zhang, 2020).

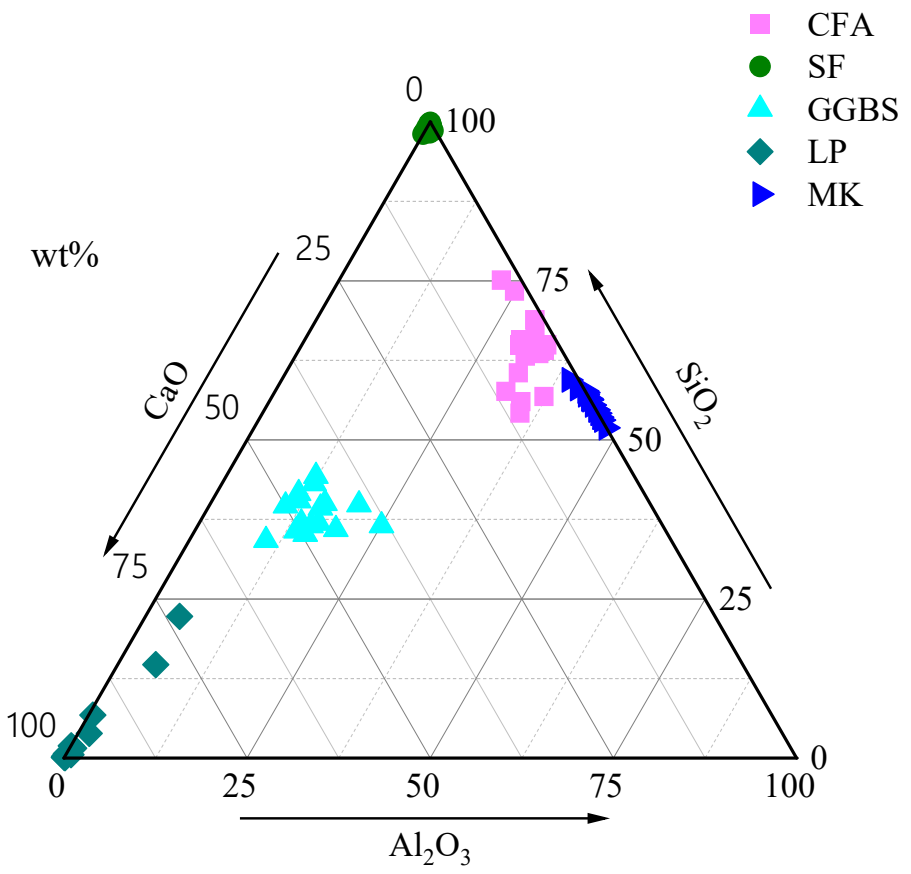

Figure 1-2. Ternary diagram of SCMs CaO, Al_2O_3 and SiO_2 reported in the literature.

All results presented in Figure 1-1 and Figure 1-2 were collected from the following literature:

- CFA: (Castel and Foster, 2015; Indukuri et al., 2019; Ipavec et al., 2013; Islam et al., 2017; Li, 2016; Mironyuk et al., 2021; Nežerka et al., 2019; Sigvardsen and Ottosen, 2019; Thomas et al., 2012; Xu et al., 2017; Yang et al., 2016; Moghaddam et al., 2019; Zhang et al., 2016a; Indukuri et al., 2019; Yang et al., 2020; Megat Johari et al., 2011).
- SF: (Ahmad and Chen, 2018; Arvaniti et al., 2015a; Huang et al., 2017; Indukuri et al., 2019; Ipavec et al., 2013; Iqbal Khan et al., 2017; Li, 2016; Meddah et al., 2018; Megat Johari et al., 2011; Nežerka et al., 2019; Thomas et al., 2012; Wu et al., 2016; Xu et al., 2020; Zhu et al., 2020; Xin Wang et al., 2020).
- GGBS: (Castel and Foster, 2015; Li and Jiang, 2020; Saluja et al., 2019; Thomas et al., 2012; Xu et al., 2017; Yang et al., 2016; Yuan et al., 2017; Arvaniti et al., 2015a; Megat Johari et al., 2011; Elahi et al., 2010; Jiang et al., 2018; Alaskar and Hooton, 2020; Elyamany et al., 2018; Kang et al., 2019b; Qin et al., 2019).

- LP: (Alyousef et al., 2019; Antoni et al., 2012; De Weerdt et al., 2011; Hu and He, 2020; Huang et al., 2017; Ipavec et al., 2013; Kang et al., 2019a; Li et al., 2020a; Li and Jiang, 2020; Schankoski et al., 2017; Shi et al., 2016; Tang et al., 2019; Tennich et al., 2015; Yang et al., 2020; Yuan et al., 2017).
- MK: (Antoni et al., 2012; Cai et al., 2021; Harbi et al., 2017; Hu and He, 2020; Li and Xiao, 2021; Li, 2016; Meddah et al., 2018; Megat Johari et al., 2011; Muduli and Mukharjee, 2019; Nežerka et al., 2019; Pavlík and Užáková, 2016; Qin et al., 2020; Shi et al., 2016; Tang et al., 2019; Wianglor et al., 2017).

The physical characteristics and chemical composition of SCMs influence the properties of cement-based materials in which they are incorporated. The main hydration products such as the calcium-silicate-hydrate (C-S-H) phase play a key role in the strength development of cement-based materials. Since the compressive strength is not only correlated with the hydration but also, with the durability of cement-based materials, it is hard to discuss one of these three aspects without mentioning others. Therefore, prior to highlighting the role of SCMs in hydration, their influence on the compressive strength of different cement-based materials was briefly discussed.

1.1.5 Reported compressive strength of several cement-based materials blended with SCMs

Mechanical performance is perceived as one of the most important and investigated properties of cement-based materials. The compressive strength of cement-based materials blended with SCMs is influenced by different parameters including the nature, amount of SCMs added and curing conditions. Besides that, the water to binder ratio is another important parameter that needs to be considered. An adequate amount of water in the mixture can trigger the pozzolanic reactions. On the contrary, a high w/c ratio increases the porosity and thus, reduces the mechanical properties of the cement-based materials (He et al., 2018).

Most studies have acknowledged that the addition of high amounts of SCMs (above 50 %) leads to a reduction of the compressive strength of the cement-based materials. Kayali and Sharfuddin Ahmed (2013) indicated that partial OPC replacement by 50 % and 70 % of class F fly ash led to a drastic reduction in elastic modulus, tensile and compressive strengths of the concrete. In their recent study, Li et al. (2020b) concluded that partial replacement of cement with LP content exceeding 60 % (by mass) significantly decreased the pore structure density and strength of the ultra-high-performance concrete (UHPC). Shariq et al. (2010, 2016) observed a

similar trend in the early and long-term compressive strength of concrete containing 20-60 % GGBS as partial OPC replacement. Wianglor et al. (2017) used high-volume MK as OPC replacement in the production of six different cement mortars. As a result, the compressive strength of the mortars containing 70 % and 100 % MK decreased from 25 MPa to 6 MPa, respectively. Additionally, Table 1-2 recapitulates the compressive strength at 28 days of several cement-based materials containing CFA, SF, GGBS, LP, and MK reported in the literature.

Table 1-2. Reported compressive strength of different cement-based materials containing SCMs.

	SCM (%)	OPC (%)	R_c at 28 days (MPa)	Curing conditions	Dimensions (mm)	Application	Reference
CFA	30	70	125.3 ± 2.39 (105.9 ± 1.98)*	22 ± 1°C; (90 ± 2% RH)	100×100×100	Concrete**	(Nežerka et al., 2019)
	40	60	40-60 (80)*	Soaked in lime saturated water	50×50×50	Blended cement paste	(Moghaddam et al., 2019)
	50	50	30; (44.5)*	29 ± 3°C; (67-82% RH)	100×100×100	Concrete**	(Shafigh et al., 2016)
	60	40	27 (32.5)*	n.a.	100×100×100	Concrete** fly ash activated with Na_2SO_4	(Nawaz et al., 2020)
	70	30	9; (35)*	25°C	50×50×50	Cement mortar	(Shaikh et al., 2014)
SF	5	95	60; (58)*	20 ± 2°C; (95% RH)	40×40×40	Blended cement paste	(Li et al., 2020c)
	6	94	31; (35)*	25°C	50×50×50	Cement mortar**	(Shaikh et al., 2014)
	20	80	60; (50)*	20°C	n.a.	Cement mortar	(Ni et al., 2021)
	30	70	97.7 ± 6.77 (105.9 ± 1.98)*	22 ± 1°C; (90 ± 2% RH)	100×100×100	Concrete**	(Nežerka et al., 2019)
	80	20	20 (n.a)*	n.a.	40×40×40	High-volume fly ash paste activated with Na_2SO_4	(Yang et al., 2021)
GGBS	15	85	43.9; (40)*	20 ± 2°C; (98% RH)	100×100×100	Coral sand concrete* *	(Cheng et al., 2017)
	20	80	52; (59)*	20 ± 3°C; (60 ± 5% RH)	20×20×20	Blended cement paste	(Qin et al., 2019)
	45	55	79; (70)*	25°C	50×50×50	Blended cement paste	(Bhojaraju et al., 2021)
	70	30	36.39 ± 0.88 (43.17 ± 0.45)*	25 ± 3°C; (100% RH)	50×50×50	Blended cement paste	(Munjal et al., 2021)
	80	20	35; (51)*	20°C; (≥95% RH)	40×40×40	Blended cement paste	(Xu et al., 2022)
LP	15	85	46; (49)*	n.a.	40×40×40	Blended cement paste	(Antoni et al., 2012)
	15	85	32 (32.5)*	Soaked in calcium hydroxide solution at 23±2°C	40×40×40	Cement mortar	(Celik et al., 2019)
	20	80	45; (59)*	20±3°C; (60±5%RH)	20×20×20	Blended cement paste	(Qin et al., 2019)
	25	75	20; (64)*	20±1°C; (≥98%RH)	40×40×160	Blended cement paste	(Du et al., 2021)
	50	50	28 (n.a)*	Soaked in calcium hydroxide solution in a standard curing room	40×40×40	Blended cement paste	(Wang et al., 2019a)
MK	5	95	47.3; (40)*	20 ± 2°C; (98% RH)	100×100×100	Coral sand concrete**	(Cheng et al., 2017)
	25	75	82; (64)*	20±1°C; (≥98%RH)	40×40×160	Blended cement paste	(Du et al., 2021)
	30	70	96.7 ± 4.04 (105.9 ± 1.98)*	22 ± 1°C; (90 ± 2% RH)	100×100×100	Concrete**	(Nežerka et al., 2019)
	30	70	56; (49)*	n.a.	40×40×40	Blended cement paste	(Antoni et al., 2012)
	40	60	30; (32)*	n.a.	n.a.	Concrete	(Al Menhosh et al., 2018)
	100	0	4-6 (n.a.)*	23 ± 2°C; (55% RH); 60°C; (95%RH)	50×50×50	Cement mortar; alkali-activation with NaOH and Na_2SiO_3	(Wianglor et al., 2017)

*n.a.: not available; *R_c at 28 days of the control mixtures; **Superplasticizer was added.*

As shown in Table 1-2, regardless of the curing conditions and specimen dimensions, the compressive strength (R_c) diminished with the increase in SCMs replacement ratios. The R_c of the mixtures with CFA was in the range of 9-125 MPa, SF (20-97 MPa), GGBS (35-79 MPa), LP (20-46 MPa), and MK (4-96 MPa). This severe reduction in compressive strength can be attributed to multiple raisons: 1) excessive quantity of certain chemical compounds that do not find other essential compounds to interact with and therefore form hydrates, 2) increased porosity in the material's matrix, 3) retarded pozzolanic activity and 4) less amount of hydration products.

1.1.6 Effects of SCMs on hydration of cement-based materials

The ordinary Portland cement (OPC) phases consist of similar oxides as those found in the supplementary cementitious materials (SCMs). It is well known that the chemical composition, particle size distribution and specific surface area are the main factors influencing the pozzolanic activity of the SCM. Indeed, in most scenarios, SCMs with finer particles, often have higher specific surface area and possess a high level of reactivity. From chemistry standpoint, the SCMs pozzolanic reactions produce the same hydration products as OPC depending upon the amount of available calcium hydroxide ($Ca(OH)_2$) also known as portlandite (CH) (Skibsted and Snellings, 2019). Normally, when cement comes in contact with water the hydration process occurs, resulting in the dissolution of cement soluble ions into the water to form hydration products such as ettringite $Ca_6Al_2(SO_4)_3(OH)_{12} \cdot 26H_2O$ (C-S-H), aluminate ferrite tri (AFt), aluminate ferrite mono (AFm), hydrogarnet, etc. Whilst, from physical point of view, the hydration of cementitious materials plays a fundamental role in the refinement of pore structure and porosity reduction (Cai et al., 2021; Li, 2011). For example, the diagram shown in Figure 1-3, illustrates the hydration process for cement paste incorporated with MK in the early age (Cai et al., 2021).

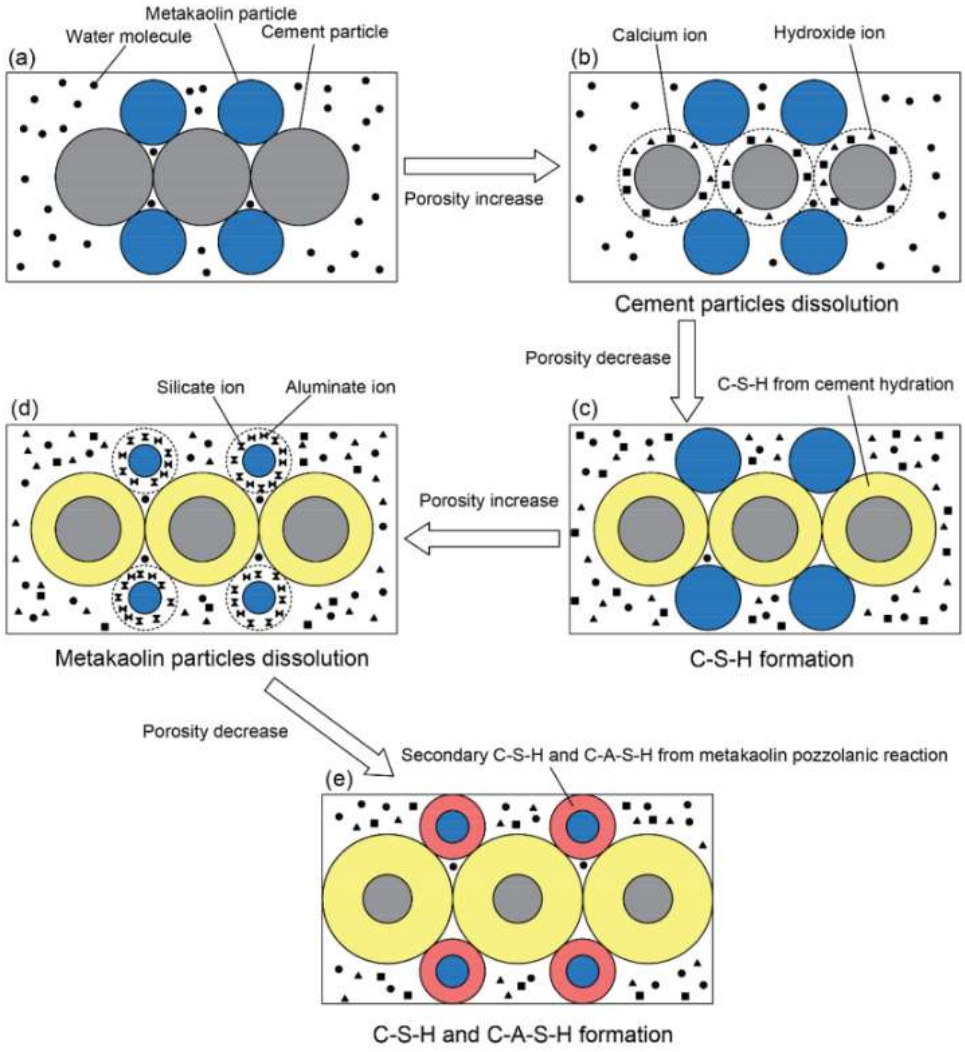

Figure 1-3. Typical diagram of the early age hydration process for cement paste containing MK (Cai et al., 2021).

According to previous studies, there seems to be a general agreement on the SCMs implication in the hydration of cement-based materials, hydration heat evolution and pozzolanic activity. Medjigbodo et al. (2018); Wang et al. (2018) pointed out that the SCMs reactivity mechanisms can be classified into four main effects: filler effect, nucleation effect, dilution effect and chemical effect. The particle size distribution has been argued to be the principal factor influencing the filler effect in cementitious materials. Li and Jiang (2020); Moon et al. (2017) indicated that fine SCMs particles fill the voids between cement particles, thus densifying the concrete microstructure and simultaneously, reducing porosity. In addition to that, the filler effect also contributes to the strength development of the cement-based materials (Tang et al., 2019; Wang et al., 2018; Zhang et al., 2016a).

The nucleation effect of limestone powder (LP) is pronounced when LP reacts with aluminates to generate the additional nucleation sites on which hydrates such as C-S-H can be formed during the cement hydration (Li and Jiang, 2020; Scrivener et al., 2019; Wang et al., 2018). In the hydrated cement-MK system, MK dissolution products namely aluminate and silicate, consume the CH which is OPC hydration product, thereby leading to the production of extra C-S-H gel (Kadri et al., 2011; Muduli and Mukharjee, 2019; Panesar and Zhang, 2020). Furthermore, Tang et al. (2019) claimed that the consumption of CH by MK and LP refined the pore structure in a ternary system consisting of OPC, MK and LP, where MK and LP together account for 30 % of the weight of the system. The study also added that the symbiotic effect between MK and LP encouraged the formation of carboaluminates at all ages of hydration (Tang et al., 2019). Replacing cement with a suitable amount of LP can favourably influence the cement and concrete properties (Zajac et al., 2014). Given that LP is rich in $CaCO_3$, representing beyond 90 % (by weight), it reacts with tri-calcium aluminate (C_3A) and CH to produce new hydration products namely hemi-carboaluminate, mono-carboaluminate phase and thereby ettringite (Kang et al., 2019a; Tang et al., 2019; Zajac et al., 2014).

The chemical effect depends on the particle size distribution and interactions between SCMs and OPC (Wang et al., 2018). In this regard, Wang et al. (2018) have shown that the incorporation of ultrafine LP into cement-based systems improved the $CaCO_3$ dissolution and chemical reactions between $CaCO_3$ and aluminate. Moreover, numerous studies have indicated that SF exhibits similar behaviour as MK and LP in cement-based materials. Zhang et al. (2016a, 2016b) observed a diminution in CH, following the incorporation of SF in the concrete. It was also revealed that SF contributes to the refinement of pore structure, as shown in Figure 1-4.

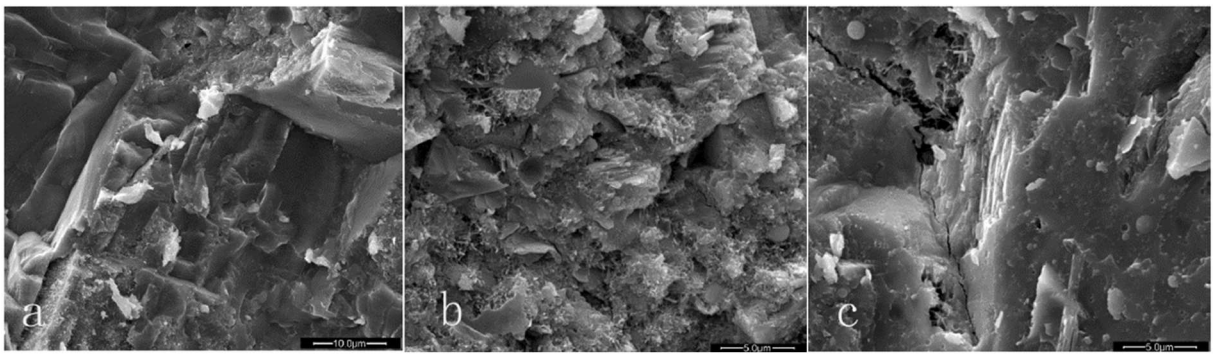

Figure 1-4. SEM micrographs of cement pastes (w/c = 0.29) after 28 days of curing: (a) reference sample without SF, (b) paste containing densified SF, (c) paste incorporating raw SF (Zhang et al., 2016b).

Rong et al. (2014) declared that SF accelerated the hydration of SF-OPC paste whereas, CFA hindered the hydration of CFA-OPC paste. The comparative study about the impact of densified SF fineness on cement hydration conducted by Ni et al. (2021) confirmed that replacing OPC with densified SF of particle size <150 μm by 10 % and 20 % improved the heat of hydration and hydration process of the cement paste. It was also revealed that coarser densified SF (particle size >150 μm) delayed the acceleration period of cement hydration and simultaneously decreased the hydration heat. Li et al. (2020c) used the SF as partial OPC replacement by 5 % in blended cement. The water-to-cement binder (W/B) ratio was fixed at 0.4 and a temperature of 20 °C. The study reported that the cumulative heat of hydration of pure cement after 12 h, 24 h and 72 h was around 117.79 J/g, 176.60 J/g and 250.18 J/g, respectively whereas for blended cement with SF, it has increased to 120.72 J/g, 178.92 J/g and 256.88 J/g at the same age.

On the other hand, Moghaddam et al. (2019) pointed out the impact of CFA fineness on the heat of hydration. The OPC was partially replaced with 20 % and 40 % CFA and three different types of CFA have been selected. The results obtained after 48 h revealed that the heat of hydration was approximately 250 J/g for the control mixture whereas, for the pastes blended with 20 % and 40 % CFA, it dropped to 200 J/g and 150 J/g, respectively. The cumulative heat of hydration decreased with increase in CFA content and with increased CFA particle sizes.

Besides, Xu et al. (2017) observed an increased hydration rate of OPC-GGBS-CFA system at early age. Nonetheless, if the CFA proportion exceeds 55 % in the OPC-CFA binary system, the hydration process was hindered. Kang et al. (2019a) showed that adding LP up to 50 % as OPC replacement boosted the initial hydration of ultra-high-performance fiber-reinforced concrete (UHPFRC). Furthermore, Huang et al. (2017) also declared that the incorporation of LP up to 54 % as OPC replacement increased the hydration rate of the ultra-high-performance concrete (UHPC) from 39% for plain UHPC to 66 % for limestone UHPC. While a large majority of studies tend to agree that high-volume SCMs accelerate the hydration of cement-based materials, few research works (Liu et al., 2017; Moghaddam et al., 2019; Xu et al., 2017; Yang et al., 2016) have pointed out that in some circumstances the addition of great amounts of SCMs especially GGBS, CFA in the concrete can decrease the heat and rate of hydration.

Regarding the pozzolanic activity, SF and MK are well known for their higher reactivity compared to CFA, GGBS and LP. Further, SF tends to exhibit higher pozzolanic activity than MK (Kadri et al., 2011). Since the pozzolanic reactions are exothermic (Zhang et al., 2016a),

the reactions between high reactive SCMs such as MK and SF, and CH from OPC hydration, increase the hydration heat (Kadri et al., 2011). Moreover, the aluminate phase in OPC's C_3A and C_4AF, and in SCMs stimulates the hydration heat (Wang et al., 2018). Note that, the greater the content of C_3S and C_3A in OPC, the higher the rate and heat of hydration becomes (Yang et al., 2016).

The heat of hydration can be greatly affected by the amount of SCMs added to the mixture and their particle size distribution. Finer SCMs generally fill the pores between the particles, which leads to the densification of the microstructure. Thanks to the pozzolanic activity, SCMs react with portlandite to produce the hydration products such as calcium silicate hydrate gel. Moreover, SCMs can also provide additional nucleation sites on which the hydration products can be formed. The presence of a high amount of SCMs in the matrix of the cement-based materials results in a dilution effect which therefore delays the pozzolanic activity, decreases the heat of hydration and hydration peaks, reduces the amount of hydration products and increases the capillary porosity (Medjigbodo et al., 2018; Moghaddam et al., 2019; Wang et al., 2018). Eventually, the hydration of cement-based materials relies on the replacement ratios, fineness and synergic effect of the SCMs reactivity mechanisms.

1.1.7 Impact of SCMs on the durability of cement-based materials

Li (2011); Mehta and Monteiro (2006) defined "the durability of Portland cement concrete as its ability to resist weathering action, chemical attack, abrasion, or any other degradation process while preserving its original shape, quality, and serviceability when exposed to its intended service environment" (Li, 2011; Mehta and Monteiro, 2006). Carbonation, chloride binding capacity, corrosion, and frost are among common phenomena inducing the deterioration of cement-based materials. Hence, this section highlights the effect of these previously-mentioned phenomena on the durability of cement-based materials containing CFA, SF, GGBS, LP, and MK.

The carbonation and porosity present a major threat to the durability of cement-based materials because they can promote the ingress of moisture, harmful ions, gas, etc. into the material's structure (He et al., 2018). The study by Wu and Ye (2017) evaluating the carbonation and porosity of cement paste blended with CFA and GGBS, revealed that the 70 % GGBS, 10 % CFA + 54 % GGBS, and 30 % CFA + 30 % GGBS blended cement pastes had superior carbonates originating from the carbonation of low calcium C-S-H than the control paste (100 % OPC) and the cement paste blended with 30 % CFA. Apart from that, the study also noticed an

increment in the total and effective porosity of 70 % GGBS, 10 % CFA + 54 % GGBS, and 30 % CFA + 30 % GGBS cement pastes after the carbonation while, for the control paste and 30 % CFA blended cement paste, decreased after carbonation. The augmentation of porosity observed on SCMs blended mixtures was attributed to the carbonation of the majority of C-S-H gel varieties whereas, the reduction of porosity in the control and 30 % CFA contained cement pastes was due to the carbonation of portlandite.

Additionally, Papadakis (2000) studied the impact of SCMs on concrete resistance when exposed to carbonation and chloride ingress. The results indicated that the carbonation depth increased with increase in either cement or aggregate replacements by SCMs. In addition, the chloride ions penetration was higher in the concrete blended with high or lower calcium CFA compared to the SF contained concrete. On the other hand, the combined use of CFA and MK has been revealed to improve the chloride binding capacity of alkali-activated CFA-MK geopolymers compared to hardened OPC pastes (Fu et al., 2020).

The chloride binding capacity of cement-based materials containing SCMs was reported to be dependent on the alumina or aluminium oxide (Al_2O_3) proportion in SCMs, alkalinity of the environment and water to cement (w/c) ratio (Bondar et al., 2019; Ipavec et al., 2013; Li et al., 2020a; Thomas et al., 2012). Owing to Al_2O_3 content in MK and SF being equal to 45 % and less than 0.5 %, respectively, Thomas et al. (2012) suggested that the better chloride binding capacity of the MK cement paste was attributed to the Al_2O_3 content in MK. Thus, concluding that Al_2O_3 significantly controlled the chloride binding capacity of the cement-based materials.

Furthermore, Zhu et al. (2020) claimed that incorporation of high-volume CFA improved the concentrations of bound chlorides of the cement mortar, while the presence of SF resulted in lower chloride binding ability. Apart from Al_2O_3 content in SCM, the study also revealed that the pH of pores solution substantially influenced the chloride binding capacity of the cement mortars. Additionally, a recent study by Li and Xiao (2021) also indicated that the addition of MK decreased the alkalinity of pore solution while improving the chloride resistance and chloride binding capacity, which resulted in hindrance of the reinforcement bars corrosion initiation.

The study on the chloride binding capacity of blended cement taking into account the limestone impact and alkalinity carried out by Ipavec et al. (2013), showed that the chloride binding capacity of limestone blended cement was relatively lower compared to plain cement mainly due to different Al_2O_3 content in each material and solution alkalinity. Generally, the increment

in alkalinity prevents the chloride binding capacity at lower chloride concentrations. Whilst, at high chloride concentrations, the impact becomes negligible.

The behaviour of cement-based materials blended with SCMs exposed to sulphate attacks, corrosion and frost has also been previously reported (Hu and He, 2020; Li et al., 2020a; Shen et al., 2020). Kayali and Sharfuddin Ahmed (2013) have shown that, although replacing OPC with CFA (class F) up to 50 % led to improvement of the concrete resistance to chloride caused by corrosion, it thereafter weakened the mechanical properties. Furthermore, the study by Jianming et al. (2020) reported that the long-term water and sulphate corrosion resistance of magnesium potassium phosphate cement (MKPC) paste can be improved by incorporating a suitable amount of CFA. The addition of GGBS and SF up to 30 % and 6 % respectively as OPC replacements, improved the frost resistance and reduced the porosity in foam concrete (Gong and Zhang, 2019). Shen et al. (2020) reported that the combined use of LP and SF considerably improved the frost resistance of the roller compacted concrete containing CFA. In contrast, when similar SF content was added with a great amount of CFA, the frost resistance was adversely affected due to high content of CFA.

1.1.8 Shrinkage resistance

The shrinkage deformation is responsible for the diminution of cross-sectional dimensions and cracks in cement-based materials. The shrinkage extent can be determined by considering the variations in volume and length of the sample (Salimi et al., 2020; Wu et al., 2017). Taking into account the origin and start time, shrinkage can be classified into autogenous, drying, plastic, carbonation and chemical shrinkage. The autogenous and drying shrinkage simultaneously occur in cement-based materials. The autogenous shrinkage arises due to macroscopic volume decrease produced by self-desiccation and cement hydration (Rezvani and Proske, 2017; Wu et al., 2017). In contrast, the drying shrinkage occurs during the hardening of cement-based materials and is caused by volumetric changes due to evaporation of capillary water (Wu et al., 2017; Zhang et al., 2013). In most cases, cement-based materials are cured in air, hence, the probability that autogenous and drying shrinkage can occur is very high. Therefore, the following paragraphs sum up various studies addressing these two aforementioned phenomena in cement-based materials incorporating CFA, SF, GGBS, LP, and MK.

Yang et al. (2020) reported that autogenous shrinkage emerges at the early age from 0 to 7 days whereas, drying shrinkage occurs between 3 and 7 days, and persists until the long-term age. Usually, the highest drying shrinkage increase rate occurs at early age (up to 7 days after casting) and then gradually declines as the age increases. According to Singh et al. (2016), over 85 %

of the total shrinkage can be achieved within the first 28 days. The drying shrinkage resistance is one of the important properties considered in the long-term durability assessment of concrete.

A large number of studies have evaluated the influence of SCMs on the shrinkage of cement-based materials (Alaskar and Hooton, 2020; Li, 2016; Ling et al., 2019; Rafieizonooz et al., 2016; Salimi et al., 2020; Singh et al., 2016; Zhang et al., 2015). Replacing sand with 50 %, 75 % and 100 % coal bottom ash, and OPC with 20 % coal fly ash reduced the drying shrinkage compared to plain concrete (Rafieizonooz et al., 2016). Shariq et al. (2016) revealed that high-volume GGBS can increase the creep and shrinkage strains in concrete. At 150 days of persistent loading, the average creep coefficients of concrete containing up to 20 %, 40 %, and 60 % GGBS as OPC replacement, were 16.3 %, 33.3 %, and 55.3 % higher than the control concrete.

Moreover, Liu et al. (2017) have indicated that incorporating SCMs in association with internal curing significantly alleviates autogenous shrinkage deformations in UHPC. In another study by Singh et al. (2016), it was revealed that the concrete comprising of a ternary cementitious binder (FA-GGBS-cement) experiences 4-10 times less drying shrinkage than the OPC concrete.

Previous publications on the shrinkage revealed that the drying shrinkage in cement-based materials can be developed due to a variety of factors including curing conditions, fineness, and capillary stress resulting from refinement of pore microstructure. Alaskar and Hooton (2020) indicated that increased fineness of the SF blended cement led to a growth in compressive strength, drying shrinkage, and cracking potential. Saluja et al. (2019) reported that the refinement of pore structure in roller compacted concrete (RCC) with GGBS influences the capillary action, leading to self-desiccation and development of autogenous shrinkage. The RCC containing high amounts of GGBS as cement replacement exhibited greater shrinkage strain. The least shrinkage strain was observed in RCC that contained limestone aggregates and 20 % GGBS. In addition, the presence of GGBS in concrete has been also reported to increase chemical shrinkage, thus autogenous shrinkage (Liu et al., 2017).

In their study, Kang et al. (2019a) declared that partial replacement of cement with LP up to 25 % did not modify the total volume of the capillary pores. Nevertheless, the total porosity increased by about 2 % when LP content reached 50 %. Eventually, the partial cement replacement with LP ranging between 25 % and 50 % contributed to reduction of autogenous shrinkage in ultra-high-performance fiber-reinforced concrete (UHPFRC). Besides, Xu et al. (2017) reported that GGBS and FA can reduce the risks of cracking by controlling the heat

release during hydration. On the other hand, substituting cement with LP up to 40 % (by weight) led to reduction of the total free shrinkage (Li et al., 2020b).

The study conducted by Medjigbodo et al. (2018) illustrated that the MK-based mixtures exhibited lower ultimate shrinkage than that spotted on the reference mortar (100 % OPC). Additionally, when the w/c ratio was 0.42, the ultimate drying shrinkage decreased with increasing SCMs fractions in both binary mortars containing metakaolin (15 % MK, 30 % MK) as OPC partial replacements and ternary mortar comprising of OPC and MK + LP (30 % MK+15 % LS). When the w/c ratio equalled to 0.5, a similar trend was observed except for the mortar containing 45 % (30 % MK +15 % LS) substitution of Portland cement.

The addition of CFA in geopolymer mortar resulted in a reduction of drying shrinkage whereas autogenous shrinkage increased (Yang et al., 2017). Several authors have reported identical behaviour. For instance, Hu et al. (2017) have shown that autogenous shrinkage increased alongside with increase of GGBS and CFA content in cement mortar. Similarly, Zhao et al. (2017) showcased that the simultaneous addition of CFA and GGBS in HPC increases autogenous shrinkage but reduces total shrinkage. However, binary use of CFA-OPC significantly reduced autogenous shrinkage compared to that of GGBS-cement.

Furthermore, Jiang et al. (2018) noted that partial cement replacement with GGBS up to 40 % prevented the drying shrinkage of concrete. In their recent study, Qin et al., (2020) concluded that magnesium phosphate cement (MPC) mortar blended with 30 % MK exhibits considerably lower drying shrinkage compared to unmodified MPC mortar. This tendency conforms to the study by Li (2016) who reported that the presence of MK in the concrete reduces the rate of water loss and thus, drying shrinkage. Cheng et al. (2017) indicated that the partial replacement of OPC with FA, GBBS, MK remarkably mitigates the drying shrinkage of coral sand concrete (CSC).

The attempt by Li (2016) to predict the drying shrinkage of the paste containing MK, SF and CFA as cement replacement, revealed that when the binary system MK-OPC was considered, the results indicated that the increment of ratio MK/cement from 0 to 0.2 led to a decrease of the drying shrinkage by 36 % at 147th day of exposure. In contrast, the binary use of SF-OPC or CFA-OPC resulted in an increase in the drying shrinkage at similar age of exposure. The drying shrinkage expansion was also studied by (Yuan et al., 2017). The study showed that the rate of drying shrinkage remarkably increased with the increase in LP content. On the contrary,

the autogenous shrinkage increased when LP content was reduced to less than 30 % (Yuan et al., 2017).

1.1.9 Environmental and economic benefits of SCMs

The advantages of applying SCMs in the production of cement-based materials from environmental and economic standpoint have been investigated by many researchers. In the United Kingdom (UK), the use of CFA (400 000 tonnes) in concrete contributes to annual reduction of nearly 250 000 tonnes of CO_2 emissions (Samad and Shah, 2017). The supplementary cementitious materials including CFA, SF, GGBS are obtained from industrial energy intensive processes, involving greenhouse gases emissions. However, the environmental impact of the above-mentioned processes, is less pronounced compared to cement manufacturing, as shown in Table 1-3 below. The production of one tonne of MK consumes energy of 2.2 MJ/tonne, which is 80 % lower than the energy required to manufacture a tonne OPC (Medjigbodo et al., 2018).

Table 1-3. Temperature ranges, embedded CO_2 emissions and costs of cementitious materials.

Cementitious materials	Temperature (°C)	CO_2 emission (kg/tonne)	Cost (€/tonne)	Reference
OPC	1400-1500	930	208-340	(Comores En Ligne, 2022; Li and Jiang, 2020; Li, 2011; Muduli and Mukharjee, 2019; Tout sur le béton, 2020)
NHL	850-1200	335-568	320-430	(Travaux-maçonnerie, 2019; Válek et al., 2014; Ciments Vigier SA, 2014; Agence de l'environnement et de la maîtrise de l'énergie (ADEME), 2014)
SF	2000	0**	130*-870*	(Luoyang Minghong import and export trade Co., Ltd, 2022; Mindess, 2019; Tuffe, 2018)
GGBS	1170-1500	143	115-180	(Aïtcin, 2016; ECOCEM, 2011; Özbay et al., 2016; Panesar and Zhang, 2020)
LP	0	17	14*-45*	(Li and Jiang, 2020; Li et al., 2020b)
MK	450-900	175	1920-3400	(Aïtcin, 2016; CERADEL, 2022; Kenzai, 2022; Meddah et al., 2018; Medjigbodo et al., 2018; Muduli and Mukharjee, 2019; Panesar and Zhang, 2020)

*NHL: natural hydraulic lime; *Cost in China; **Embedded CO_2 emissions excluding transport effect.*

The costs reported by (Li and Jiang, 2020) were converted into Euros (€) based on the current exchange rate which is about 1€ = 7.25 RMB. It is quite challenging to compare the cementitious materials costs due to several factors such as the quality of the product (or purity), fineness, quantity to be purchased, applications, geographical location, etc. Therefore, the

comparison of prices shown in Table 1-3 was achieved by mainly considering pricing information from the French and European markets. The prices per kilogram as well as per tonne were taken into account in order to obtain the approximate price range (taxes included).

As can be seen in Table 1-3, OPC is produced at the temperature range of 1400-1500 °C whereas NHL and MK are obtained at lower temperatures approximately (850-1200) °C, and (450-900) °C, respectively. However, some SCMs could be obtained at almost similar or higher temperatures compared to OPC. This is the case of GGBS and SF which are usually produced at (1170-1500) °C and 2000 °C, correspondingly. Regarding carbon footprint, the embedded CO_2 emissions of OPC accounts about 930 kg/tonne while NHL, GGBS, LP and MK represent 335-568 kg/tonne, 143 kg/tonne, 17 kg/tonne and 175 kg/tonne, respectively. The low LP carbon footprint can be attributed to its manufacturing process which unlike other cementitious materials does not involve the calcination at high temperatures. Given that SF is an unavoidable by-product generated by default in the ferrosilicon alloys production, its embedded CO_2 emissions without taking into account the transportation effects have been reported to be zero (Tuffe, 2018). On the other hand, one tonne of silicon metal releases about 4.1 tonnes CO_2 equivalent during its life cycle (Ernst & Young s.r.l./S.E.N.C.R.L., 2015).

From economic point of view, the cost of OPC is relatively higher than LP and GGBS. Actually, the cost of the reviewed cementitious materials (expressed in € per tonne) varies from 208 to 340 for OPC, 320 to 430 for NHL, 130 to 870 for SF, 115 to 180 for GGBS, 14 to 45 for LP and 1920 to 3400 for MK. By comparing SCMs, LP is the most affordable whereas MK and SF are the most expensive SCMs. The high cost of MK and SF can be attributed to the high demand and low quantity of those materials available on the market.

The recent study by Bajpai et al. (2020) on the life cycle of three geopolymer concrete mixtures versus conventional cement concrete concluded that CO_2 emissions of concrete were reduced up to 148, 135 and 133 kg CO_2-equivalent for geopolymer concrete without SF, geopolymer with SF and geopolymer concrete without Na_2SiO_3 respectively, compared to 597.54 kg CO_2-equivalent for plain concrete. Additionally, the application of FA and SF in geopolymer concrete can also reduce the cost from 10.87 % to 17.77 % per volume.

Li et al. (2020b) replaced cement with high-volume LP ranging from 20 % to 80 % in the production of the ultra-high-performance concrete (UHPC). The results showed that OPC replacement with LP up to 50 % in UHPC can reduce the embedded CO_2 emissions by about 47 % (474 kg/m^3), as shown in Figure 1-5 and the cost by about 25.5 €/m^3, without

compromising compressive strength. Yang et al. (2015) performed a study on the effectiveness of GBBS and FA in the reduction of CO_2 emissions from OPC concrete, based on Korean lifecycle inventory from cradle to preconstruction. The results showed that the GGBS and CFA replacement ranging from 15 % to 20 % promptly decreased CO_2 emissions, while a slight regression has been observed when greater amounts of GGBS and FA have been added. Ultimately, at similar replacement ratios, GGBS was more effective than FA in reducing CO_2 emissions of concrete.

Elchalakani et al. (2014) indicated that OPC replacement with GGBS reduced CO_2 emissions from 386 kg/m^3 in 100 % OPC concrete to 184 kg/m^3 and 154 kg/m^3 for 60 % and 80 % GGBS-contained concrete, respectively. Additionally, the concrete comprising of 50 % GGBS, 30 % FA and 20 % OPC as a binding ternary system, exhibited much lower CO_2 emissions estimated at 147 kg/m^3. Moreover, Zhang et al. (2019) have also reported that the addition of either FA or SF as cement replacement lessened the CO_2 emissions of the FA or SF concrete compared to the conventional concrete. The CO_2 emissions calculations carried out by Yang et al. (2020) showed that concrete samples consisting of the binding systems: FA-SF-LP-OPC and FA-SF-BP-OPC, experienced a significant reduction in CO_2 emissions. However, in terms of mechanical performance, the study revealed that concrete mixtures containing LP exhibited higher compressive strength than basalt powder (BP).

He et al. (2019) produced two kinds of recycled cement (RC-450 and RC-800) by calcinating old OPC pastes (age: >2 years) pieces (size <10 mm) in an oven at temperatures 450 °C and 800 °C. Once the burnt old OPC pastes cooled down, they were ground using a ball mill into powder to achieve a particle diameter <300 μm. It was found that to produce one tonne of cement, CO_2 emissions were 0.78 tonne, 0.05 tonne and 0.19 tonne for OPC, RC-450 and RC-800, respectively. On the other hand, the compressive strength of RC-450 paste was comparable to OPC paste while, for RC-800 paste, it significantly decreased.

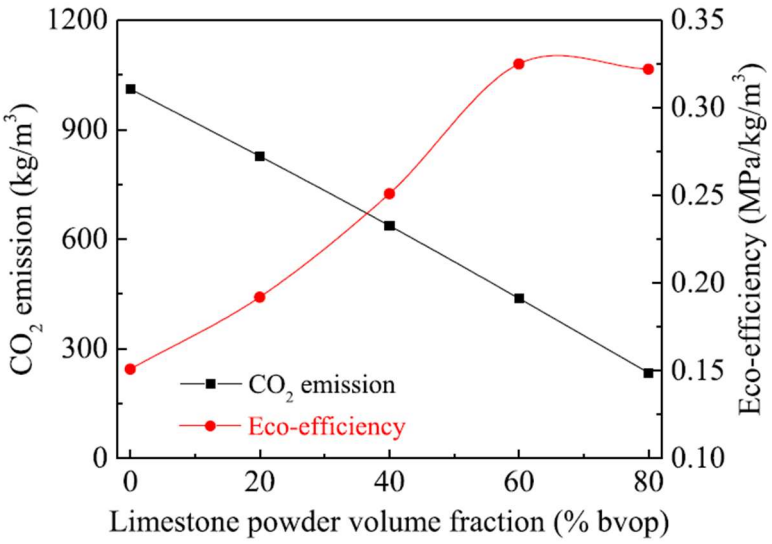

Figure 1-5. Limestone powder content as function of CO_2 emissions and Eco-efficiency in UHPC. Note: bvop: by the volume of total powder (Li et al., 2020b).

Owing to the presence of heavy metals in SCMs, particularly GGBS and CFA, they should be applied with precaution and conformably to the standards. Otherwise, they can pose critical environmental problems (Xu et al., 2017). The directive 2010|75|EU of European Parliament and Council on industrial emissions restricts the total emissions of antimony (Sb), arsenic (As), lead (Pb), chromium (Cr), cobalt (Co), copper (Cu), manganese (Mn), nickel (Ni) and vanadium (V) to 0.5 mg/Nm^3, cadmium (Cd) and thallium (Tl) together to 0.05 mg/Nm^3 while, mercury (Hg) emissions must not exceed 0.05 mg/Nm^3 at a sampling period of at least 30 minutes to 8 hours maximum. Moreover, the leachability test is generally recommended prior to the application of SCMs in cement-based materials (Cheah and Ramli, 2011; Czech et al., 2020; European parliament and council, 2010).

1.1.10 Conclusions

This review summarized over 150 research articles and reports from genuine international institutions discussing mainly the impact of the five widespread SCMs on the hydration and durability of cement-based materials. The characterization methods along with major characteristics, environmental and economic benefits of CFA, SF, GGBS, LP and MK were also discussed. Based on the literature, the following conclusions were drawn:

1) In most cases, the incorporation of greater amounts of SCMs (beyond 50 %) in cement-based materials accelerates the cement hydration at early age thanks to dilution and filler effect. In fact, the cement-based materials containing LP experience more consistent trend than those comprising of MK, CFA, SF and GGBFS. Besides, it is worth noting

that SCMs do not identically affect the cement hydration mainly due to their differences in terms of particle size distribution, fineness and pozzolanic activity;

2) The porosity resulting from the carbonation is reportedly higher in cement-based materials blended with SCMs than in cement-based materials without SCMs;
3) The chloride binding capacity in cement-based materials containing SCMs strongly depends on the alumina (Al_2O_3) content in SCM and the alkalinity (pH) of the pore solution. The addition of SCMs rich in Al_2O_3 (>10 %) increases the concentration of the bound chloride ions in the cementitious materials. The decrease in pore solution pH value has been reported to improve the chloride binding capacity of the mortars and concrete. In other words, the chloride binding capacity is most likely to be weakened in a high alkaline pore solution;
4) A considerable number of research works have indicated that the partial OPC replacement with SCMs up to 40 % can reduce and even prevent the shrinkage in cement-based materials. Mostly, the combined application of OPC and SCMs reduces the drying shrinkage along with autogenous shrinkage. However, the use of SCMs in a ternary system (OPC + two different SCMs) decreases the drying shrinkage, while the autogenous shrinkage of concrete increases;
5) The application of SCMs in concrete does not only improve its performance but also provides potential environmental and socio-economic benefits including the adequate use of natural resources, efficient waste management, reduction of energy consumption, cost of production and CO_2 emissions. Given that SCMs (for example: CFA, GGBS) may contain heavy metal concentrations, the leachability analysis should be carried out prior to any application of SCMs in cement-based materials.

1.1.11 Recommendations and future research perspectives

The contradicting conclusions in the literature are often due to the lack of relevant documentation and disparities between SCMs characteristics. Despite the already existing standards and recommendations, important questions regarding the applications of SCMs remain unanswered. Therefore, designing the standard specifications for all recognized SCMs that do not meet the requirements of ASTM C618, (2003), for example, would be a great achievement.

Inadequate use of some technical terms and the lack of clearly described protocols could sometimes mislead the readers. Therefore, a rigorous description of all experimental procedures

adopted in a research study could eventually facilitate the reading and thereby make the research outcome well understood.

The hydration and durability of cement-based materials blended with SCMs remain the aspects of research interest due to their importance and complexity. In addition to that, the variability of the SCMs properties makes these above-mentioned research areas much harder to control. For those reasons, further investigations will be necessary to deepen the existing knowledge.

To date, little research has been done on coal and biomass fly ash blended cementitious systems. Consequently, further studies are necessary to understand the synergic effects resulting from the combined use of the earlier-mentioned SCMs. It would also be interesting to study the compatibility of SF, GGBS, LP, and MK with newly emerged SCMs from biomass origin. This practice would not only expand the applications of the SCMs in construction materials but also, substantially decrease the cost of production.

Chapter 2: Literature review on the valorization of wood ashes, plant-based particles in construction materials

2.1 Supply and applications of wood biomass ashes

At present, about 17 million hectares, meaning that 31 % of the French metropolitan territory is occupied by forest, ranking France in the 4th position in the European Union. Generally, wood is used in a variety of applications such as energy production, construction, packaging, furniture, carpentry, composite materials, papermaking, and chemical industries (Ministère de la Transition écologique, 2021b).

In 2021, the wood construction sector represented 6 % of the total construction. Given the implementation of the new environmental regulation RE 2020, the applications of wood-based materials in buildings are expected to increase (Ministère de la Transition écologique, 2021b). Additionally, as part of the promotion of green energies, most heating and power plants have heightened their interest in renewable resources. As a result, the trend in heat and electricity production from biomass (wood and agricultural wastes) has increased, leading to an increment in ash output. The estimates predict that biomass ash production will continue increasing in the future. Actually, biomass combustion generates approximately 170 Mt of ash per year and at some point in the future, the latter could possibly attain roughly 1000 Mt/year (Zhai et al., 2021).

Regarding the energy sector, biomass represents a large part of renewable sources used in heat production worldwide. Indeed, it accounts for beyond 95 % of the heat produced in power plants and heat consumed in end sectors. On the other hand, the production of an average electricity of 1.5 MWh/tonne of biomass generates an average ash content of 3 %. Hence, the electricity (from biomass origin) output of 483 TWh results in producing nearly 10 Mt of ashes around the globe (IEA Bioenergy, 2018). According to Zhai et al. (2021), the global ash production from wood fuel, wood chips, particles, residues, charcoal, and recovered wood is estimated at about 18.5 Mt per year, including about 2.42 Mt of wood biomass ash (WBA) produced in Europe.

In France, biomass represents about 80 % of renewable heat production and over 55 % of the energy generated from renewable resources (Tenerrdis, n.d.). About 7150 bioenergy installations with a boiler power beyond 50kW have been identified in 2021 (CIBE, 2021). The estimates show that the annual gross biomass ash production in 2015 was 200 000 tonnes and that was expected to reach 300 000 tonnes by 2020 (Boulday and Marcovecchio, 2016).

During the combustion of biomass, the larger particles that fall beneath the boiler grate are referred to as bottom ash. On the other hand, the very fine particles that are transported in the flue gas are called fly ash (Forest Research, 2022). Generally, a large amount of WBA (70 %) is discharged in landfills while 20 % is valorized in agriculture and the remaining 10 % is employed in other applications (Fořt et al., 2021; Milovanović et al., 2019). Typical examples of wood ash applications reported in (Etiégni and Campbell, 1991; IEA Bioenergy, 2018; Mivière, 2008; Obernberger and Supancic, 2009) include:

- As mineral admixture in mortars and concretes (filler and cement replacement);
- As fine or coarse aggregate substituent material;
- Road construction (asphalt filler, pavements, etc.);
- Landscaping;
- Soil stabilization and fertilizer. Owing to the high alkalinity of WBA (pH = 10 to 13.5), they can be valorized in agriculture and forestry to reduce the acidity of the soil. Besides, WBA are in rich in nutrients which are vital for plant development, therefore they can be applied as a fertiliser;
- For the neutralisation of wastes;
- As a substitution material in ceramics, etc.

2.2 Physical and chemical properties of the wood ashes

The characteristics and applications of biomass fly ash as an alternative cementitious material in the production of mortars and concretes have been investigated since the late 90s (Omran et al., 2018). The physicochemical characteristics of biomass ash vary depending on several factors namely the type of feedstock, treatment applied on feedstock, thermal technology, temperature, combustion techniques, ash extraction method (dry or humid), ash treatment, etc. (Boulday and Marcovecchio, 2016; Cheah and Ramli, 2011). For instance, the combustion of wood waste at temperatures below 500 ºC resulted in wood ash rich in carbonates such as calcite ($CaCO_3$) while at temperatures beyond 1000 ºC, the carbonate content drastically decreased. This decline in carbonates is ascribed to the chemical decomposition of calcite at this range of temperatures (Cheah and Ramli, 2011).

Regarding the physical characteristics, biomass fly ash usually consists of porous particles with angular and spherical shapes. These particles can also have rough and smooth surfaces (Omran et al., 2018). Naik (2002) investigated the physical properties of 15 different wood ashes and found that the average bulk density of wood fly ash and wood bottom ash was 490 kg/m^3 and 827 kg/m^3, respectively. The BET specific surface area was reported to be in the range of 1.74-

40.29 m^2/g (Esteves et al., 2012; Omran et al., 2018; Rajamma et al., 2009). The average particle size may vary enormously depending on the initial size of raw WBA particles, the desired granulometry after grinding and intended use. As far as WBA is used as a filler or cement replacement, many researchers tend to use very fine WBA with a maximum particle size not exceeding 1000 µm.

The chemical composition of wood biomass ash is mainly composed of calcium, silicon, potassium, sodium, magnesium, and sulphur (Hassan et al., 2019; Obernberger and Supancic, 2009) as shown in Table 2-1.

Table 2-1. Reported chemical composition (expressed in %) of wood biomass ash.

Reference	CaO	SiO_2	Al_2O_3	Fe_2O_3	K_2O	Na_2O	MgO	MnO	P_2O_5	SO_3	TiO_2	Cl	LOI	$SiO_2+Al_2O_3+Fe_2O_3$
(Rajamma et al., 2009)	11.4	41.00	9.30	2.60	3.90	0.90	2.30	0.30	0.9	-	0.40	-	-	52.9
	25.4	28.00	6.20	2.20	3.20	3.30	5.00	0.70	0.9	-	0.30	-	-	36.4
(Berra et al., 2015)	33.13	29.88	9.58	5.79	3.64	1.32	3.50	0.77	2.33	2.90	-	1.07	4.50	45.25
	23.76	36.44	8.96	6.39	6.70	1.49	3.52	0.52	1.9	4.68	-	1.90	3.64	51.79
	20.76	40.38	9.54	6.09	2.08	3.04	3.00	0.15	0.68	9.30	-	1.74	3.13	56.01
(Xing et al., 2016)	21.24	26.45	4.47	2.79	6.42	2.31	4.27	2.08	1.847	-	0.68	-	-	33.708
	26.27	19.32	2.78	2.48	5.68	1.48	2.75	4.06	2.786	-	0.66	-	-	24.589
	14.57	21.57	3.61	2.63	4.92	0.86	2.82	1.57	1.537	-	0.65	-	-	27.81
(Omran et al., 2018)	39.77	27.82	16.55	1.95	1.05	0.74	2.26	-	-	1.92	-	-	5.12	46.32
	34.80	33.40	21.50	1.50	0.60	0.10	1.90	-	-	1.70	-	-	1.0	56.4
	46.50	21.30	11.70	1.80	0.80	0.70	2.40	-	-	7.80	-	-	3.2	34.8
(Hassan et al., 2019)	44.81	0.98	1.51	1.19	6.89	1.64	3.81	-	1.72	1.07	0.29	-	35.9	3.68
	43.38	2.30	1.41	1.75	4.80	2.46	2.91	-	2.35	3.48	0.87	-	34.06	5.46
	40.85	4.40	2.34	2.59	7.17	1.22	2.56	-	2.32	5.54	0.33	-	30.64	9.33
	37.68	5.54	2.93	2.54	6.45	4.04	3.95	-	3.44	3.33	0.43	-	29.6	11.01
	35.32	6.53	2.39	2.67	7.54	3.75	5.98	-	3.4	3.56	0.98	-	27.68	11.59
	41.65	4.44	1.54	1.95	6.56	6.54	1.65	-	2.54	1.10	0.28	-	31.56	7.93
	29.36	21.86	7.29	2.56	3.89	2.54	2.55	-	1.65	4.76	0.97	-	22.51	31.71
	27.98	19.65	8.21	2.98	5.68	1.43	3.82	-	5.67	2.28	0.89	-	21.39	30.84
(Sigvardsen et al., 2021b)	48.90	8.60	1.90	2.30	16.80	2.20	3.80	-	-	5.40	-	-	15	12.8
	45.20	21.80	4.90	2.70	7.20	0.80	4.00	-	-	5.80	-	-	16.2	29.4
Average	32.99	20.08	6.60	2.83	5.332	2.04	3.27	1.27	2.2481	4.04	0.59	1.57	17.821	-
Minimum	11.40	0.98	1.41	1.19	0.60	0.10	1.65	0.15	0.68	1.07	0.28	1.07	1	-
Maximum	48.90	41.00	21.50	6.39	16.80	6.54	5.98	4.06	5.67	9.30	0.98	1.9	35.9	-

As seen in Table 2-1, the sum of three oxides namely silica, alumina and iron oxide, that play a major role in pozzolanic reactions of wood ash is in the range of 3-60 %. The loss on ignition (LOI) varies from 1 to 36 %. The total amount of alkalis ($Na_2O_{eq.}$) in wood biomass ashes ranges between 0.5 and 6 % (Berra et al., 2015; Omran et al., 2018). Therefore, this proves that some biomass wood ashes meet the chemical requirements for Class C pozzolans as prescribed in (ASTM C618, 2003).

2.3 Environmental behaviour of the wood ashes

The combustion of untreated wood waste produces WBA containing important concentrations of zinc (Zn), copper (Cu), lead (Pb), chromium (Cr), nickel (Ni), arsenic (As), molybdenum (Mo), and cadmium (Cd) (Mivière, 2008). Given that most biomass power plants use a wide range of wood particles (barks, chips, sawdust, etc.), there is a high probability that the resulted ash may contain hazardous elements. Indeed, this have been proven by several researchers. Table 2-2 recapitulates the amount of hazardous elements present in the wood biomass ashes reported in (Berra et al., 2015; Mivière, 2008; Rajamma et al., 2009; Siddique, 2012).

Table 2-2. Reported heavy metals concentrations (expressed in mg/kg) present in wood biomass ash.

As	Cd	Cr	Cu	Hg	Ni	Pb	Zn	Mo	Se	Source
2.99	1.71	33.90	287.00	0.10	26.5	15.95	181.00	1.10	0.59	forestry chips
5.20	2.06	51.10	101.00	0.08	25.00	79.40	168.00	0.87	0.79	wood fuel
44.00	9.00	405.00	743.00	0.36	112.50	680.00	2332.00	9.20	1.80	untreated wood waste
10.10	1.02	115.00	193.00	0.02	59.80	249.00	935.00	0.05	0.22	wood aggregates
6.60	3.80	91.80	175.00	0.13	56.60	125.60	745.00	2.80	0.80	wood bark
-	1.00	47.00	99.00	<1.00	35.00	191.00	376.00	-	-	wood waste
-	1.30	73.00	27.00	<1.00	27.00	12.00	34.00	-	-	
18.00	9.00	101.00	175.00	0.20	41.00	177.00	2274.00	-	-	chestnut or poplar
15.00	7.60	18.00	48.00	0.30	50.00	39.00	636.00	-	-	virgin wood chips
45.00	60.00	124.00	920.00	0.40	102.00	5318.00	17470.00	-	-	scraps of treated wood
42.00-53.00	5.50-6.10	12.00-14.00	41.00-46.00	0.05-0.08	6.00-8.00	29.00-35.00	380.00-420.00	-	0.53-0.64	normal wood fuel
22.50-26.90	7.30-7.90	12.00-15.00	50.00-59.00	0.06-0.10	6.00-7.00	73.00-78.00	530.00-610.00	-	0.55-0.64	wood particles/ plywood
78.00-98.00	7.10-8.10	34.00-39.00	71.00-93.00	0.36-0.52	7.00-10.00	920.00-1010.00	1420.00-1520.00	-	0.84-0.97	construction/demolition wood

As is evident in Table 2-2, the heavy metal concentrations in the wood biomass ashes vary from one ash to another. It appears that the most dominant hazardous elements in wood ashes include zinc, lead, and copper. The estimates show that zinc account for 34-17 470 mg/kg, lead for 12-5318 mg/kg and copper for 27-920 mg/kg. The highest heavy metal concentrations were observed on ashes obtained from untreated wood waste (Mivière, 2008) and two batches of ashes from chestnut or poplar virgin wood chips and scraps of treated wood investigated by (Berra et al., 2015). On the other hand, it is noteworthy to mention that mercury (<1 mg/kg) and selenium (<2 mg/kg) are the detected heavy metals with the lowest concentrations.

While heavy metal concentrations remain the primary limiting factor to the wood ash recycling, recent advances in cementitious materials have shown that the latter can be employed in mortars and concrete as an alternative supplementary cementitious material. In fact, the physical and chemical characteristics of WFA are close to those of cement and recognised SCMs. Furthermore, it is important to note that the valorization of the biomass ash should be implemented in accordance with the existing recommendations for heavy metal leaching. For example, the European parliament and council 2003/32/CE describes the limit values of leachate recommended for the waste to landfill (Table 2-3).

Table 2-3. Waste landfill conditions in terms of heavy metal traces according to the European parliament and council 2003/32/CE (Conseil de l'Union Européenne, 2003).

Element	Inert waste landfill	Non-hazardous waste landfill	Hazardous waste landfill
	mg/kg dry mass		
Arsenic (As)	0.5	2	25
Barium (Ba)	20	100	300
Cadmium (Cd)	0.04	1	5
total Chromium (Cr)	0.5	10	70
Copper (Cu)	2	50	100
Mercury (Hg)	0.01	0.2	2
Molybdenum (Mo)	0.5	10	30
Nickel (Ni)	0.4	10	40
Lead (Pb)	0.5	10	50
Antimony (Sb)	0.06	0.7	5
Selenium (Se)	0.1	0.5	7
Zinc (Zn)	4	50	200
Chloride	800	15000	25000
Fluoride	10	150	500
Sulphate	1000	20000	50 000
COT on eluate	500	800	1000
Soluble fraction	4000	60000	100000

COT: total organic carbon.

2.4 Influence of wood ashes on the mechanical properties and durability of cement-based materials

A great deal of research has examined the possibilities of using wood ashes as fillers or as replacements for cement and aggregate in the production of different cement-based materials including pastes, mortars and concretes. Wood ashes have been used in cement-based materials for more than 20 years. The addition of wood ash in the cement-based materials has been reported to influence the mechanical and durability properties.

Omran et al. (2018) noticed that the presence of biomass fly ash improved the mechanical properties of the concrete. The compressive strength, flexural strength, splitting-tensile strength, and elasticity modulus. Moreover, the incorporation of 20 % biomass fly ash densified the microstructure, reduced the permeability and improved the resistance to freezing-thawing and de-icing salt scaling degradation of the concrete. Biomass fly ash can be used in cement mortars to mitigate the alkali-silica reactions (ASR). In the study conducted by Esteves et al. (2012), cement was partially replaced with 20-30 wt.% biomass fly ashes. The results showed that the presence of biomass fly ash decreased the ASR expansion in cement mortar under accelerated curing conditions. However, the addition of biomass fly ash along with metakaolin (20 % WFA+10 % MK) allowed to significantly mitigate the ASR expansion in the cement mortar.

On the other hand, as shown in Table 2-4, the use of biomass ash induces a reduction in mechanical performance. The flexural strength and compressive strength decrease with the increase in biomass ash ratios.

Table 2-4. Typical compressive and flexural strengths of wood ash-contained pastes and mortars at 28 days.

WFA (%)	OPC (%)	Other SCM (%)	R_f (MPa)	R_c (MPa)	Produced material	Reference
100	0	-	-	≈ 0.6	Paste	(Ohenoja et al., 2016)
100	0	-	-	≈ 0.7		
100	0	-	-	3		
100	0	-	-	6		
0	100	-	9.5 ± 0.6	61.7 ± 2.3	Mortar	(Fořt et al., 2021)
10	90	-	8.8 ± 0.7	58.2 ± 2.4		
20	80	-	8.7 ± 0.8	54.3 ± 3.2		
30	70	-	8.1 ± 0.6	49.1 ± 2.7		
40	60	-	8.1 ± 0.3	42.7 ± 3.4		
50	50	-	6.4 ± 0.5	24.4 ± 1.8		
60	40	-	4.9 ± 0.3	19.4 ± 2.3		
70	30	-	4.2 ± 0.4	13.1 ± 1.3		
20	80	-	3.63-4.16	42.45-46.08	Mortar A Glenium 26 SCC superplasticizer was used	(Esteves et al., 2012)
30	70	-	3.57-4.50	32.20-50.19		
20	70	MK: 10	6.34-7.28	36.36-41.81		
0	100	-	-	≈ 46	Mortar	(Berra et al., 2015)
15	85	-	-	≈ 39-40		
30	70	-	-	≈ 38-39		
0	100	-	-	78 ± 4	Mortar cured in water at room temperature	(Maschio et al., 2011)
5	95	-	-	71 ± 5		
10	90	-	-	62 ± 8		
20	80	-	-	49 ± 4		
30	70	-	-	42 ± 4		
WBA (%)						
0	100	-	11.1 ± 1.3	49.5 ± 1.8	Mortar	(Garcia and Sousa-Coutinho, 2013)
5	95	-	10.4 ± 0.4	47.5 ± 1.3		
10	90	-	10.1 ± 1.0	44.3 ± 2.1		
5	95	-	-	82 ± 4	Mortar cured in water at room temperature	(Maschio et al., 2011)
10	90	-	-	74 ± 4		
20	80	-	-	66 ± 4		
30	70	-	-	57 ± 4		
PFA (%)						
90	10	-		2.6	Paste	(Zmamou, 2015)
95	5	-		2.6		
100	0	-		2.1		

Note: WFA: wood fly ash; WBA: wood bottom ash; OPC: ordinary Portland cement; SCM: supplementary cementitious materials; MK: metakaolin; PFA: paper fly ash.

Furthermore, Lessard et al. (2017a, b) studied the mechanical performance of a dry cast concrete (DCC) containing 10-30 % biomass fly ash (BFA) as cement substitution. The results showed that the DCC mixtures (w/b = 0.37) incorporating 0, 10, 15, 25, and 30 % BFA had the compressive strength of 71, 63, 56, 47, and 44 MPa, respectively at 28 days. This strength loss was ascribed to:

- The huge difference between the reactivity of both powders. Indeed, the reactivity of cement is relatively higher than that of biomass fly ash;
- The voids resulted from the low compactness of the DCC mixtures and the expansive nature of hydration products of biomass fly ash.
- Similarly, the study conducted by Chowdhury et al. (2015) also revealed a slight decrease in strength properties namely compressive strength, splitting tensile strength, and flexural strength as the content of wood ash increased in the concrete mixtures, at both 7 and 28 days.

From the literature above, it appears that the application of high contents of biomass ashes negatively affects the strength development of the materials. Nevertheless, when used at lower contents, their influence on the mechanical properties is minimal. Furthermore, a number of studies have shown that biomass ashes can be used effectively in the production of non-structural and low strength building materials, including lightweight wall board and bricks with particular properties (Gómez-Barea et al., 2009), low-density clay bricks with good thermal insulation ability (Fernández-Pereira et al., 2011), etc.

In addition, the applications of alternative cementitious materials have expanded in bio-based building materials. A number of researchers have demonstrated that industrial by-products, such as coal fly ash, ground granulated blast furnace slag, silica fume, metakaolin can be blended with cement or lime in the preparation of bio-based mortars/concretes (Alengaram et al., 2011; Caldas et al., 2021; de Bruijn and Johansson, 2013; Kinnane et al., 2016; Lagouin et al., 2019; Vo and Navard, 2016; Walker et al., 2014). On the contrary, by-products from thermal and heating biomass plants, particularly wood ash, have been overlooked.

2.5 Valorization of sunflower by-products in bio-based lightweight mortars

2.5.1 History of bio-based insulation materials

The materials of biomass origin have been used in construction since the paleolithic period. The latter were typically applied in the construction of temporary shelters associated with other local resources (Dupre, 2014). In the Middle Ages, the use of plant-based materials gradually declined due to the discovery of new techniques and materials. The plant-derived materials were replaced by mineral ones such as stone, clay, and wood since the latter offered better properties that were essential to constructing buildings (Dupre, 2014; Jones and Brischke, 2017). The fibres from plant or animal origins such as straw and horse hair were being integrated to reduce the brittleness of building materials, particularly mud bricks. In the early 20^{th} century, the scientific community started investigating the suitability of mineral and synthetic fibres as reinforcement in cement-based materials (Brandt, 2008; Nozahic et al., 2012).

In the 1880s, the first buildings made of straw bale were constructed in Nebraska (USA) (Bozsaky, 2010). Then, in the 1920s, thanks to the in-fill wall system technique, the first industrial and residential buildings were built in France by filling the timber frame walls with straw bales (Dupre, 2014). Later, at the end 19^{th} century, owing to the significant development of heating and ventilation appliances, the first thermal insulation materials emerged. Initially, people were using natural insulation products, then, they developed a new technique which consisted of bricklaying elements. Afterward, the latter was replaced by the first artificial insulation materials. The summary of thermal insulation materials history from the paleolithic era to today is shown in Figure 2-1 (Bozsaky, 2010). It is worth mentioning that the causes for altering materials in the five grouped periods have been highlighted in blue colour.

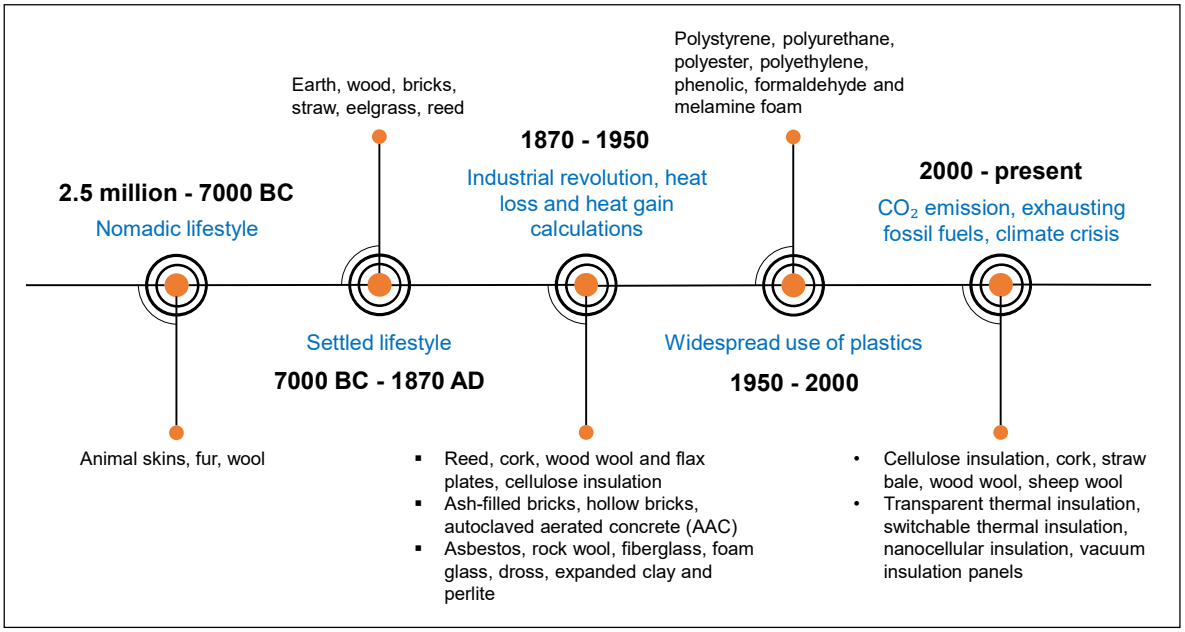

Figure 2-1. Development of thermal insulation materials (Bozsaky, 2010).

2.5.2 Evolution of the thermal regulations in France

Residential and industrial buildings constructed before 1940 had no heating or air conditioning systems. However, after the first oil shock in 1973, there was an urgent need to make buildings (new and renovated) thermally efficient (Dupre, 2014). As a result, in 1974, France initiated the first thermal regulation aiming at reducing at least 25 % of building energy consumption compared to the standards adopted in the 1950s. A new environmental regulation RE 2020 which was introduced on 01 January 2022 focuses on three major points:

- Reduction of the energy demand of new building until achieving almost a zero annual energy consumption;
- Mitigation of the CO_2 emissions originated from heating and air conditioning equipment;
- Improvement of the indoor comfort during the summer.

A considerable effort has been made to improve the energy efficiency of the buildings, as shown in Figure 2-2. The annual energy consumption limits recommended by thermal regulations decreased from 225 KWh/m^2/year in 1974 to 50 KWh/m^2/year in 2012. The year 2020 is the time of passive and low-energy buildings. According to RE 2020, new buildings should be able to produce the energy that they consume and if the building is able to generate higher energy than its demand, the latter should be stored and used in case of necessity.

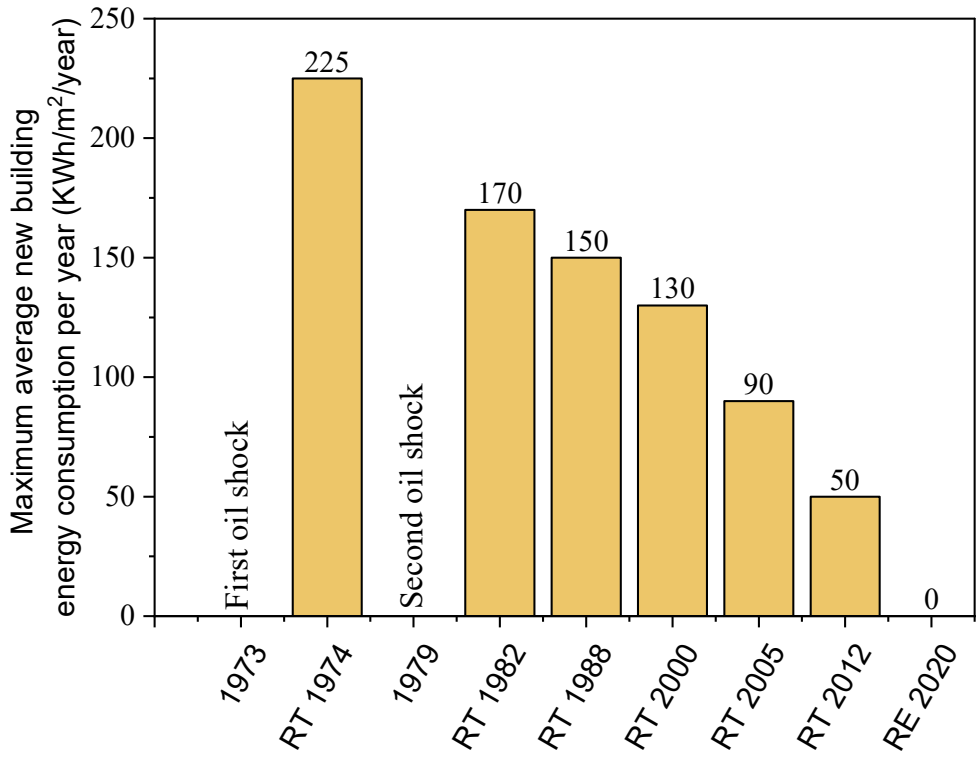

Figure 2-2. Evolution of thermal regulations regarding new buildings energy consumption from 1974 to 2022 (Harmonie, 2017; Lalanne, 2021).

2.5.3 Agricultural by-products: a case study of the sunflower particles

The agriculture sector plays a fundamental role in the economic growth of many countries around the globe. Agriculture occupies 50 % of the habitable land, which is 51 million km^2 (Ritchie and Roser, 2013). In France, the agricultural land represented 52.3 % (286 601 km^2) in 2018 (The World Bank, 2022). The cereals, industrial crops, and forage plants all combined accounted for 28 % of the average French agriculture output between 2018 and 2020 (European Commission, 2021). France ranks at the first position in terms of cereals production in the EU (Eurostat, 2022a). In addition, it also generates important quantities of maize, grapes, sugar cane, a variety of oilseed and industrial crops. The sunflower, rapeseed, linseed and hemp are few examples of common oilseeds and industrial crops widely available across the EU, including France. The total oilseed crops production of the European Union's 28 regions was 36.1 million tonnes in 2017. Rape seeds (rape and turnip rape) represented 60.7 % whilst, sunflower seeds accounted 28.9 % of the total harvested production (Eurostat, 2019).

The harvest of the above-mentioned crops generates massive amounts of waste. A part of these wastes is used as animal feed and bedding, burned in the agricultural lands, or at heating and power plants to produce energy. Recently, the use of crop post-harvest remaining in building materials is one of the emerging techniques enabling the building sector to minimize its

environmental impact. Today, the concrete industry already accommodates a wide range of agricultural wastes. Plant-derived particles can be used in a bulk to fill the walls and insulate the buildings. On the other hand, they can also be employed in the production of a wide range of bio-based building materials including mortars/concrete and particleboard panels. The bio-based mortars/concrete may exist in different forms such as shuttered concrete, prefabricated concrete, sprayed concrete, coatings, etc. (Dutreix et al., 2020; Pichon and Naumovic, 2018). Generally, these materials are used in the insulation of newly constructed buildings or renovated buildings (Dutreix et al., 2020). Apart from that, they are also utilized as sound absorbers at the edges of highways and railways (Dupre, 2014), and facade coating from inside or outside (Dutreix et al., 2020). Furthermore, due to a low compressive strength (less than 3 MPa), bio-based concrete can also serve as a non-load-bearing material (Pichon and Naumovic, 2018; Sonebi et al., 2015).

In France, the most popular lignocellulosic and fibrous plant by-products in bio-based building materials include hemp, sunflower, flax, rapeseed, maize, miscanthus, etc. (Construction Durable et Écomatériaux (CODEM), 2021). Hemp concrete or hempcrete is unarguably the most widespread bio-based material nowadays. It plays a key role in the market of bio-based building insulation materials thanks to its high porosity, low bulk density, and low thermal conductivity. As the demand for hemp concrete continues to grow, the availability of hemp shives could become a critical concern preventing further development of hemp concrete and bio-based materials hemp in the near future. In 2021, industrial hemp occupied only 33 410 ha while sunflower seed represented 4 345 380 ha across the EU. Regarding France, hemp and sunflower crops accounted 18 280 ha and 698 330 ha, respectively (Eurostat, 2022b).

The growing demand for bio-based building materials has led to the pursuit of new plant-derived particles that could be applied as alternatives to hemp shives. A number of research studies devoted to the characterization and suitability of the by-products obtained from sunflower, rice, maize, barley, etc in bio-based mortars/concrete have been carried out (Abbas et al., 2020; Arufe et al., 2021; Chabannes et al., 2014; Laborel-Préneron et al., 2018a; Lagouin et al., 2019). This will not only allow the sector to meet the market demand but also, will contribute to expansion of the bio-based materials applications. In this context, this section provides insights on the recent developments in bio-based lightweight mortars/concrete. Since one of the objectives of this thesis project is the valorization of sunflower stem (pith and bark), sunflower by-products and residues will be the main discussion topic in this part.

(a) History of sunflower crop

The sunflower (Helianthus annuus) is an annual plant with a daisy-like flower face, originally from North America, brought to Europe by Spanish people in the 16th century (Berglund, 2007; TerresOléoPro, 2014). Today, the sunflower plant is cultivated in over 267 countries worldwide (Ritchie and Roser, 2020). Typically, the sunflower plant can grow up to 4-12 feet (1.22-3.66 m) tall and its blooms diameter varies from 4 to 12 inch (10.16 to 30.48 cm) (Gilmour, 2018). The sunflower seeds are usually sowed in April-May to be harvested in August-September (TerresOléoPro, 2014). Despite the fact that a large part of the sunflower harvest serves as animal feed, the sunflower crop is grown for human consumption in form of seeds and vegetable oil (Eurostat, 2019). Indeed, the sunflower seed is primarily composed of oil, representing 38-50 %, and proteins, accounting for up to 20 % (Berglund, 2007). The oil extracted from sunflower seeds could further be applied in several industrial applications including the production of biodiesel, inks, and paint (Eurostat, 2019).

In 2018, the European Union produced 9.97 million tonnes of sunflower seeds, making it the second-largest sunflower producer after Russia (Ritchie and Roser, 2020). France currently ranks at the third place in the EU after Romania and Bulgaria (Eurostat, 2022b). According to the statistics, the French sunflower seed output has been increasing since the early 1960s. Indeed, it has grown from 12 201 tonnes in 1961 to 1.9 million tonnes in 2021 (Eurostat, 2022b; Ritchie and Roser, 2020). The evolution of sunflower seed along with hemp, rape and turnip rape seeds, and linseed (oilflax) production in France over the past 20 years is shown in Figure 2-3.

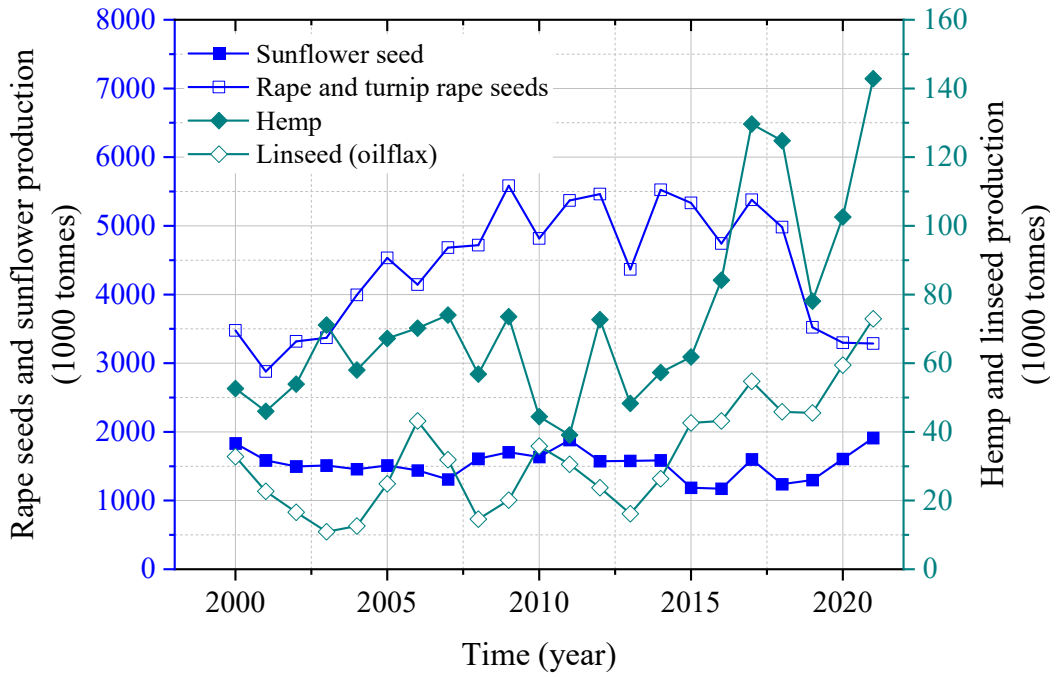

Figure 2-3. Production of sunflower seed, hemp, rape and turnip rape seeds, linseed (oilflax) in France from 2000 to 2021 (Agreste, 2022; Eurostat, 2022b).

As can be seen in Figure 2-3, since 2000, the trend in the production of sunflower, hemp, and linseed has been somehow stable with slight fluctuations, in contrast to rapeseed which has significantly increased with slight alterations until 2017. From 2018 to 2021, the production of sunflower seed has been gradually increasing. However, at the same time, the production of hemp and linseed slightly increased while rapeseed significantly dropped. Despite that, the production of rapeseed is still higher compared to those three selected crops. In 2021, the rapeseed, sunflower, hemp, and linseed productions accounted for up to 3.3 Mt and 1.9 Mt, 142 840 tonnes, and 72 940 tonnes, respectively.

(b) Sunflower by-products and their applications

The yield straw of sunflower is approximately 2 tonnes per hectare (Lenormand et al., 2014). Given that the by-products and residues resulting from the sunflower harvest are regarded as waste, a part of the latter is valorized in livestock farming as animal feed and bedding while the remaining portion is incinerated and dumped in the agricultural lands. The incineration of the sunflower by-products and residues represents a serious threat to the environment and ecosystem as it emits CO_2 emissions in the atmosphere and can contribute to soil contamination, etc.

Owing to their availability and similarity to hemp shiv, sunflower particles have received a lot of research attention in bio-based building materials in recent years. For instance, hemp and

sunflower-based materials exhibit comparable morphological and mechanical properties (Nozahic et al., 2012). In addition, the increasing demand for bio-based insulation materials especially hemp concrete has led to the search for new alternative lignocellulosic particles that could be applied in case available hemp by-products fail to keep up with the market demand. The crops such as flax, rapeseed, sunflower, miscanthus, and maize are among the most investigated alternative particles in the production of bio-based lightweight insulation mortars/concretes.

From a physical standpoint, the sunflower stem mainly consists of two main parts: bark, which is the external woody part, and pith, which is the internal sponge-like part, as shown in Figure 2-4. Sunflower particles are usually characterised by high porosity, malleability, permeability, flexibility, low apparent density, and thermal conductivity. The sunflower pith is reportedly more porous, lighter, and permeable than the sunflower bark. The typical bulk density of the sunflower pith varies from 15 to 34 kg/m^3 while that of the sunflower bark is within the range of 120 and 170 kg/m^3 (Arufe et al., 2021; Brouard et al., 2018; Chabriac et al., 2016). On the other hand, the sunflower bark has better mechanical properties (compressive strength, Young's modulus) than that of the sunflower pith (Sun et al., 2013).

Figure 2-4. (a) Sunflower crop in the field and (b) cross-section of a dry sunflower stem (Abbas, 2021).

The thermal conductivity the lignocellulosic particles used in bio-based mortars/concrete is comparable to that of conventional building insulation materials. As a matter of fact, the thermal conductivity of loose sunflower pith, bark and hemp shiv is about 0.036-0.051 W/m.K, 0.053-0.074 W/m.K, 0.055-0.07 W/m.K, respectively (Abbas et al., 2020; Brouard et al., 2018; Lenormand et al., 2014; Magniont et al., 2012). On the other side, the thermal conductivity of 0.034-0.05 W/m.K has been reported for rock wool, 0.035-0.06 W/m.K for glass wool, and

0.02-0.03 W/m.K for polyurethane (Jelle, 2011; Jones and Brischke, 2017). Furthermore, sunflower pith observes a significantly higher water uptake ability than that of sunflower bark and hemp shiv. The water absorption rate of the sunflower pith and bark after 60 min of immersion in water (at temperature of 20 ºC) was estimated at 223 % and 154 %, correspondingly (Brouard et al., 2018).

Regarding biochemical composition, sunflower pith contains considerable amounts of soluble compounds and mineral matter. Besides, cellulose, hemicellulose, and lignin are dominant in the particles derived from lignocellulosic plants such as sunflower, industrial hemp and flax, as can be seen in Table 2-5 (Arufe et al., 2021; Chabriac et al., 2016; Glé et al., 2021; Vandenbossche et al., 2012; Viel et al., 2018).

Table 2-5. Biochemical composition of some lignocellulosic particles determined by Van Soest and Wine method.

Biochemical composition (%)	Sunflower bark	Sunflower pith	Hemp shiv	Flax shiv
Soluble	6.0 - 10.6	38.6 - 50.2	8.1 - 17.7	5.2 - 9.1
Hemicelluloses	16.0 - 18.1	4.0 - 7.0	16.8 - 21.6	17.6 - 24.4
Cellulose	28.0 - 46.1	23.0 - 45.0	49.0 – 60.8	43.0 - 44.6
Lignin	18.6 - 46.0	3.0 - 22.0	8.1 – 12.3	21.0 - 32.3
Ash	3.8 - 4.9	11.7 - 17.0	0.7 - 4.1	1.48 - 2.7

2.5.4 Typical binders for bio-based mortars/concretes

The choice of binder in bio-based mortars/concrete may depend on several factors including intended applications, geographical location, etc. Lime binders have been widely used in the production of bio-based concrete for many years.

Lime-based binders can be classified into air and hydraulic lime. The air or aerial lime (or quicklime) is obtained from the calcination of limestone rocks in the kiln at the temperature of 900 ºC. Afterward, quicklime can be quenched in water to form slaked lime (or hydrated lime). The setting and hardening of the mixtures incorporating air lime occur thanks to the carbonation reaction, during which calcium hydroxide $Ca(OH)_2$ reacts with carbon dioxide CO_2 present in the atmosphere to form calcite $CaCO_3$ (Cérézo, 2005; Lagouin et al., 2019).

Besides, natural hydraulic lime is another form of lime that is obtained from the combustion of siliceous limestone with clay impurities at high temperatures. After the decomposition of clay at the temperatures of 400-600 ºC, it links up with certain quantities of lime at 950-1250 ºC to form silicates and aluminates which are the main compounds contributing to the hydraulic

behaviour of NHL (Callebaut et al., 2001; Válek et al., 2014). The setting of NHL takes place because of hydration process whereat free lime and silica reacts with water to form calcium hydroxide and hydrates.

Prior to the discovery of hydraulic binders, aerial lime was widely used in the production of mortars. At the beginning of the 19th century, it was replaced by NHL which ultimately became the principal binder in masonry mortars until the 20th century. In the past, these two binders were utilized in the construction of architectural structures such as buildings, museums, monuments, etc. However, the invention of Portland cement has led to a significant drop in lime-based binders' applications. Today, the latter are broadly applied in the production of bio-based lightweight mortars/concrete and also in rendering and coating mortars for the restoration of historic structures (Callebaut et al., 2001; Pavlík and Užáková, 2016; Válek et al., 2014).

Ordinary Portland cement (OPC) is the second most widespread binder in bio-based mortars/concrete. Compared to lime-based binders, OPC has better mechanical performance, interesting hydraulic properties, quick setting time, and better resistance to frost and chemical attacks, etc. However, it is less ecological due to its high carbon footprint. Lime-based binders are preferred over OPC due to their availability, low environmental impact, and compatibility with plant particles (Jami et al., 2019). Apart from that, other common binders for bio-based mortars/concrete include earth, commercial binders, supplementary cementitious materials, etc. Ultimately, lime-based binders are more preferred in the production of bio-based mortar/concrete thanks to their low density, good compatibility with vegetal particles, low cost and less environmental impact compared to OPC.

2.5.5 Properties of biobased mortars/concretes

(a) Physical properties

Owing to the high porosity of plant aggregates, bio-based mortars/concrete are very light and possess a porous structure. Numerous data from the literature on the physical properties of bio-based concretes have been summarised in Table 2-6. As can be seen, the typical dry density of bio-based concrete ranges from 150 to 900 kg/m^3 whereas, the total porosity varies between 60 and 95 %. This rate of porosity is comparable to that of cellular concrete (75-82 %) and is significantly higher than that of wood concrete 52 % (Cérézo, 2005).

Table 2-6. Reported porosities of different building materials.

Material	Dry density (kg/m^3)	Skeletal density (kg/m^3)	Total porosity (%)	Reference
Lime-sunflower bark concrete	-	-	68.6 ± 1.7*	(Lagouin et al., 2019)
Metakaolin-sunflower bark concrete	-	-	71.5 ± 5.3*	
Metakaolin-maize bark concrete	-	-	69.2 ± 0.7*	
Hemp concrete	-	-	60-80	
Hemp concrete	-	-	80	(Arnaud and Gourlay, 2012)
Formulated lime sunflower pith concrete	550 ± 5	2390	77 ± 1**	(Abbas et al., 2020)
Formulated lime sunflower pith and hemp concrete	590 ± 6	1970	70 ± 2**	
Cement-additive based sunflower pith concrete	150 ± 4	2500	94 ± 1**	
Hemp lime concrete	478 ± 7	-	76.4 ± 0.1	(Rahim et al., 2015)
Flax shiv lime concrete	598 ± 4	-	70.6 ± 0.3	
Hemp lime plaster	723-881	-	65.9-72.0	(Mazhoud et al., 2016)
Hemp clay concrete	347-523	-	73.1-81.1	(Mazhoud et al., 2021)
Hemp cement concrete	-	1200 - 1500	70-80*	(Gourlay et al., 2017)
Hemp lime concrete	-	-	71.5	(Benmahiddine et al., 2020)

*Note: *: open porosity; **: skeletal porosity.*

The skeletal density is another parameter that can be determined during the microstructural characterization of bio-based materials. The latter refers to the ratio of the material's dry mass to the skeletal volume of the material. Where the skeletal volume is defined as the volume of the material including the closed pores but excluding accessible pores and interparticle spaces (ASTM, 2002; Nguyen et al., 2019). The skeletal density of bio-based materials is usually computed with a gas pycnometer using helium or argon. According to Table 2-6, the skeletal density of bio-based concrete was found to be within the range of 1200 and 2500 kg/m^3. The comparison between porosity and skeletal density results indicates that both parameters

correlate. As the matter of fact, the skeletal density of bio-based materials increases with the increase in the porosity rate.

(b) Mechanical properties

The mechanical behaviour is unarguably the most investigated property of bio-based mortars/concrete. Depending on the intended application, bio-based mortars/concrete should meet the minimum strength requirements described in the standards. For instance, according to professional rules for hemp construction, the hemp mortar for coating, cured in the standard conditions (20 ºC; 50 % RH) should have at minimum the Young's modulus of >20 MPa and compressive strength of >0.3 MPa at 60 and 90 days (SEBTP - Société d'édition du bâtiment et des travaux publics, 2012). The compressive strength and Young's modulus of a wide range of bio-based mortars/concrete reported in the literature were recapitulated in Table 2-7.

Table 2-7. Reported compressive strength and Young's modulus of different bio-based lightweight concretes.

Material	Binder	Aggregate	Compressive strength (MPa)	Young's modulus (MPa)	Reference
Hemp concrete	commercial lime-based binder: Tradical PF70	hemp shiv	0.46 - 0.94	-	(Benmahiddine et al., 2020)
Unfired earth bricks	earth	barley straw	3.30 - 3.80	-	(Laborel-Préneron et al., 2018a)
		hemp shiv	1.80 - 2.40	-	
		corn cob	1.80 - 3.20	-	
Hemp concrete	aerial calcic lime (CL90) and natural hydraulic lime (NHL3.5)	hemp hurd	0.48 ± 0.02	16	(Chabannes et al., 2014)
Rice husk concrete		rice husk	0.33 ± 0.03	28	
Lime hemp concrete	NHL3.5	hemp shiv	0.18	9	(Arnaud and Gourlay, 2012)
	NHL3.5 with pozzolans		0.31	36	
	NHL2		0.10 - 0.22	5 - 24	
Lime hemp concrete	commercial lime-based binder: Tradical PF70	hemp shiv	1.36	43	(Tronet et al., 2016a)
Lime hemp concrete	hydrated lime+ hydraulic lime (NHL5)	hemp shiv	0.15 - 0.20	3.34 - 4.05	(de Bruijn et al., 2009)
Lime and cement hemp concrete	hydrated lime+NHL5+ cement (CEMII/A-L)		0.44 - 0.83	1.48 - 1.80	
Cement hemp concrete	cement (CEMII/A-L)		0.55	12.2	
Lime hemp concrete	70% hydrated lime, 20% NHL3.5 and 10% PC	hemp shiv	0.37	-	(Walker et al., 2014)
	70% hydrated lime, 30% GGBS		0.41	-	
	80% hydrated lime, 20% metakaolin		0.34	-	
Lime hemp concrete	commercial lime-based: T70 and Tradichanvre	hemp shiv	0.25 - 1.15	4 - 160	(Cérézo, 2005)
Sunflower concrete	a mixture of cement, lime and additives	sunflower pith	0.10 - 0.27	-	(Abbas et al., 2020)
Lime sunflower concrete	aerial lime	sunflower bark	0.20	26.6 ± 1.2	(Lagouin et al., 2019)
Metakaolin sunflower concrete	metakaolin	sunflower bark	0.33	55.1 ± 6.7	
Metakaolin maize concrete	metakaolin	maize bark	-	14.7 ± 2.7	
Sunflower concrete	a fast-setting hydraulic binder obtained from argillaceous limestone	sunflower stem	0.57 ± 0.04	29.20 ± 0.61	(Chabannes et al., 2015)
Sunflower concrete	pre-formulated lime-based: 75% aerial lime, 15% hydraulic lime, 10% pozzolanic binder	sunflower stem	0.43 ± 0.06	26.50 ± 0.02	
Rapeseed straw concrete	Vicat prompt natural cement	rapeseed straw	0.70 - 2.00	10.00 - 90.00	(Sheridan et al., 2020a)

As described in Table 2-7, bio-based mortars/concretes can be produced using a wide range of binders (lime, earth, cement, pozzolans, etc.) and a variety of plant by-products such as hemp shiv, sunflower stem (bark and pith), maize particles, barley straw, etc. The compressive strength of bio-based concrete was found in the range of 0.1-4 MPa while the Young's modulus varied from 1.5 to 160 MPa. The huge disparities between the strength properties of bio-based mortars/concrete can be attributed to multiple factors. As an example, Arnaud and Gourlay (2012) investigated the mechanical performance of hemp concretes under different curing conditions. It has been noted that at lower RH (30 %), air lime hemp concrete exhibits better compressive strength and Young's modulus than the hemp concrete made with hydraulic lime. In contrast, at higher RH (beyond 75 %), both hemp concretes observed a significant decrease in mechanical performance. Considering all curing conditions evaluated in this study, the optimum mechanical performance was obtained at a temperature of 20 ºC and relative humidity of 50 % (Arnaud and Gourlay, 2012).

Furthermore, several studies suggest that the chemical composition of the lignocellulosic particles delays and may hinder the setting and hardening mechanisms of mineral binders, thus weakening the mechanical properties of the mortars/concrete. Aggarwal and Singh (1990) investigated the effect of plant fibre extractives on the properties of cement. The authors concluded that the presence of water-soluble compounds in coir and sisal fibres did not only augment the initial and final setting times of cement but also reduced its the compressive strength, depending on the nature and quantity of fibres added in the mixture. Miller and Mosleni (1991) reported that glucose, quercetin, xylan and acetic acid extracted from wood particles lowered the tensile strength of the wood-cement composites. However, unlike glucose which contributed to about 50 % decrease in tensile strength, the influence of quercetin, xylan, and acetic acid was less pronounced.

Further, Bilba et al. (2003) affirmed that lignin increased the setting time of the sugar cane bagasse-cement composites. Sobral (2004) also claimed that the hemicellulose, sugar, starch, tannins, phenols and lignin contents in plant fibres hinder the setting and strength development in cement matrix. The water-soluble extractives also inhibit the cementitious system incorporating plant fibres to achieve its full strength and durability properties.

The low flexural and compressive strength obtained from three hemp concretes was ascribed to hemp shiv water extracts, namely ash, protein, phenolic compounds and sugar. Besides that,

these hemp shiv extracts also contributed to the retardation of the setting time and reduction of the amount of portlandite $Ca(OH)_2$ in the cement pastes (Diquélou et al., 2015).

More typical chemical compounds present in lignocellulosic plant aggregates that interfere with the hydration and strength development of bio-based mortars/concrete, are listed in Table 2-8 (Aggarwal and Singh, 1990; Amziane and Collet, 2017; Bilba et al., 2003; Diquélou et al., 2015; Miller and Mosleni, 1991; Sobral, 2004; Wang et al., 2019c).

Table 2-8. Some biochemical components in lignocellulosic particles.

Monosaccharides	Polysaccharides	Phenolic compounds	Organic acids	Terpenes
Glucose	Sucrose	Tannins	Fatty acid	
Galactose	Hemicellulose	Quercetin	Acetic acid	
Mannose	Pectin	Lignin		
Rhamnose	Starch	Teracacidin		
Arabinose	Arabinogalactan			
Xylose	Xylan			

Hemp concrete exhibits a low elasticity modulus which means that it is flexible and can be easily deformed without developing cracks (Pichon and Naumovic, 2018). On the contrary, conventional concrete has high brittleness, low tensile strength, and high risks to develop cracks and shrinkage (Vo and Navard, 2016). On the other side, it is generally agreed that the strength of bio-based materials strongly correlates with their densities. For instance, Florentin et al. (2017) indicated that hemp concrete with densities varying from 430 and 600 kg/m^3 exhibited the compressive strength of 0.25-1.2 MPa, correspondingly.

As for the impact of the binder content, the comparison of the mechanical performance of hemp concrete made by incorporating two different lime-based binders: T70 and Tradichanvre revealed that the density, compressive strength, and Young's modulus increased with an increase in the binder's fraction in the concrete mixtures. For instance, the hemp concrete containing the lime-based binder designated T70 in the range of 10 %, 19 % to 29 %, and 40 % exhibited the compressive strength of 0.25 MPa, 0.35 to 0.80 MPa, and 1.15 MPa, correspondingly (Cérézo, 2005).

Except for the aforementioned factors, according to (Aggarwal and Singh, 1990; Pichon and Naumovic, 2018), the setting and strength development of bio-based mortars/concrete can also be influenced by:

- pH of the fresh mixture;

- decomposition of hemicellulose and lignin due to alkalis generated from cement hydration;
- water-to-binder ratio;
- binder-to-aggregate ratio;
- type and nature of the binder;
- nature and quantity of plant aggregate used;
- manufacturing methods, etc.

(c) Thermal properties

Thermal conductivity (λ) refers to the ability of a material to conduct heat. In the steady-state, the thermal conductivity can be measured according to Fourier's law of heat conduction, as illustrated in Equation 2-1 (Zhao et al., 2016):

$$\lambda = \frac{Q * L}{A * \Delta T} \qquad \text{Equation 2-1}$$

where, λ: thermal conductivity (W/m.K), Q: quantity of heat passing through the material (W), L: distance between two temperature sensors in contact with the material; A: cross-sectional area of the material (m^2), ΔT: the temperature difference between the hot side and cold side of the material.

The thermal conductivity of the bio-based mortars/concrete can be determined using steady-state or transient methods. According to Zhao et al. (2016) and Palacios et al. (2019), "in the steady-state techniques, the thermal conductivity and interfacial thermal conductance are determined by measuring the temperature difference (ΔT) under the steady-state heat flow (Q) through the sample (thickness). Whereas, in the transient methods, the heat sources are supplied either periodically or as a pulse, resulting in periodic (phase signal output) or transient (amplitude signal output) temperature changes in the sample, respectively."

The steady-state methods include the heat flow meter and guarded hot plate. On the other hand, among the transient methods, we may cite transient hot-wire, transient plane source (TPS), temperature modulated differential scanning calorimetry (TM-DSC), laser flash, 3ω method, and thermocouple method (Palacios et al., 2019; Zhao et al., 2016).

A number of studies have shown that bio-based building materials incorporating lignocellulosic plant aggregates have a similar thermal conductivity as that of conventional mineral and synthetic insulation materials. As given in Table 2-9, the thermal conductivity of bio-based concrete is in the range of 0.055 to 0.35 W/m.K with dry densities of 235 and 1671

kg/m^3, respectively. It is worth mentioning that the thermal conductivity of cement mortar and plain concrete is estimated at 1.186 W/m.K and ≈ 3.0 W/m.K, respectively (Demirboğa, 2003; Reddy et al., 2020). On the other hand, the thermal conductivity of sunflower concretes oscillates between 0.055 and 0.19 W/m.K which is almost identical to cellular concrete (0.16-0.33 W/m.K) (Cérézo, 2005) and autoclaved aerated concrete AAC (0.11 W/m.K) (Florentin et al., 2017).

Table 2-9. Reported thermal conductivity and density of different bio-based lightweight concretes.

Material	Binder	Aggregate	Thermal conductivity (W/m.K)	Dry density (kg/m^3)	Reference
Hemp concrete	Tradical PF70	hemp shiv	0.094 - 0.101	-	(Benmahiddine et al., 2020)
Unfired earth bricks	earth	barley straw	0.14 - 0.28	1100 - 1537	(Laborel-Préneron et al., 2018a)
		hemp shiv	0.20 - 0.30	1271 - 1519	
		corn cob	0.26 - 0.35	1565 - 1671	
Hemp hurd concrete	aerial calcic lime (CL90) and natural hydraulic lime (NHL3.5)	hemp hurd	0.108 ± 0007	364 - 600	(Chabannes et al., 2014)
Rice husk concrete		rice husk	0.10 - 0.14	509 - 734	
Hemp concrete	lime	hemp shiv	0.11	450	(Florentin et al., 2017)
Sunflower concrete	a mixture of cement, lime and additives	sunflower pith	0.065 ± 0.002	150 ± 4	(Abbas et al., 2020)
Sunflower and hemp concrete	calcic lime-based binder	sunflower pith + hemp shiv	0.14 ± 0.008	590 ± 6	
Sunflower concrete	formulated lime: hydraulic lime + calcareous charges, hydrophobic and rheological admixtures	sunflower pith	0.19 ± 0.007	550 ± 5	
Sunflower concrete	aerial lime	sunflower bark	0.127 ± 0.008	539.64 ± 51.56	(Lagouin et al., 2019)
Metakaolin-sunflower concrete	metakaolin	sunflower bark	0.128 ± 0.009	511.07 ± 61.86	
Metakaolin-maize concrete	metakaolin	maize bark	0.112 ± 0.006	534.08 ± 82.30	
Sunflower concrete	a fast-setting hydraulic binder obtained from argillaceous limestone and pre-formulated binder: 75% aerial lime, 15% hydraulic lime, 10% pozzolanic binder	sunflower stem	0.096 - 0.105	469 - 473	(Chabannes et al., 2015)
Sunflower concrete	50% natural hydraulic lime (NHL5) + 50% flash calcined metakaolin	sunflower pith	0.115	576.4	(Magniont et al., 2012)
Sunflower concrete	clay	sunflower pith	0.055	235	(Brouard et al., 2018)
Sunflower concrete	clay	sunflower bark	0.1578	714	
Sunflower concrete	clay	sunflower bark and pith	0.0878	512	
Rape-straw concrete	clay	rape-straw	0.0712	438	
Hemp concrete	clay	hemp shiv	0.089 – 0.12	-	(Mazhoud et al., 2021)

Based on summarized data in Table 2-9, there is a good relationship between the thermal conductivity and density of bio-based concrete. Actually, the thermal conductivity of the selected bio-based materials increases with an increase in dry density. Apart from that, the thermal conductivity of the bio-based materials may vary depending on the type and proportion of the binder, quantity of plant aggregate, porosity, moisture content, temperature, etc. (Collet and Pretot, 2014; Construction Durable et Écomatériaux (CODEM), 2021; Lagouin et al., 2019).

Aiming at highlighting the influence of water content and density on thermal performance of hemp concrete, Collet and Pretot (2014) revealed that the moisture content has a less pronounced effect than density on the thermal conductivity of the hemp concrete. In fact, the hemp concrete λ value in a dry state and at 90 % RH increased from 15 to 20 %, respectively. Besides, the increment of density by up to 2/3 resulted in an increase in thermal conductivity by 54 %. The λ value of all studied hemp concrete mixtures varied between 0.09 and 0.16 W/mK at 23 ºC and 50 % RH. Moreover, Rahim et al. (2016) also observed that the thermal conductivity (λ) of bio-based concretes was significantly affected by the water content and temperature. Indeed, at free saturation, λ increased by about 25 % for hemp concrete and flax concrete whilst, 37 % for rape straw concrete compared to the results obtained in the dry state. It was also noticed that the thermal conductivity of bio-based concrete samples at free saturation increased with an increase in temperature.

Additionally, many studies agree that adding plant aggregates improves the thermal conductivity of bio-based materials. For example, the study on the effect of plant aggregates (barley straw, hemp shiv and corn cob) on unfired earth bricks conducted by Laborel-Préneron et al. (2018a) concluded that λ decreased from 0.57 W/m.K for plain earth bricks to 0.14 W/m.K for earth bricks containing 6 % (by mass) barley straw. Recently, Chen et al. (2020) concluded that the use of miscanthus fibres along with cement and expanded waste glass (EWG) considerably improved the thermal and acoustic performance of the lightweight bio-based concrete. The thermal conductivity decreased from 0.12 W/m.K for the reference (containing cement and EWG) to 0.09 W/m.K for the concrete incorporating 30 % miscanthus fibres (by volume). Moreover, miscanthus fibres (length = 2-4 mm) proportion greater than 20 % (by volume) led to a high sound absorption beyond 0.5 at frequencies of 600-1200 Hz. Apart from that, the thermal conductivity of bio-based mortars/concrete can also be affected by the manufacturing method adopted.

(d) Hygroscopic properties

Bio-based building materials present excellent hygroscopic properties compared to conventional building materials (Pichon and Naumovic, 2018). The capacity of bio-based building materials to store and release water or moisture is plotted thanks to the sorption isotherm curves. Sorption isotherm (adsorption and desorption) portrays the correlation between the water content of a material and equilibrium relative humidity at a constant temperature (Amziane and Collet, 2017; Laborel-Préneron et al., 2018a).

The study by Sing et al. (1984) reported that the moisture adsorption of a porous material can appear in two main steps: physisorption in micropores and mesopores or macropores. The main physisorption process is referred to micropore filling. The latter describes the adsorption of water by the entire accessible volume in micropores (pore width < 2 nm). However, the physisorption in mesopores (2 nm < pore width < 50 nm) may occur in three different stages:

- Monomolecular adsorption (when the molecules of water on the external surface are adsorbed in mesopores to form a monolayer).
- Multimolecular adsorption (when the adsorption space in mesopores accommodates many layers of water molecules).
- Capillary condensation (when the liquid-like material separated from the gas phase by menisci fills the adsorption space in mesopores that remained after multimolecular adsorption).

Additionally, the deviation between adsorption and desorption curves is known as adsorption hysteresis. The latter is very common among bio-based building materials. The sorption isotherm curves of these aforementioned materials are classified as type II according to the IUPAC's classification, as shown in Figure 2-5 (Sing et al., 1984).

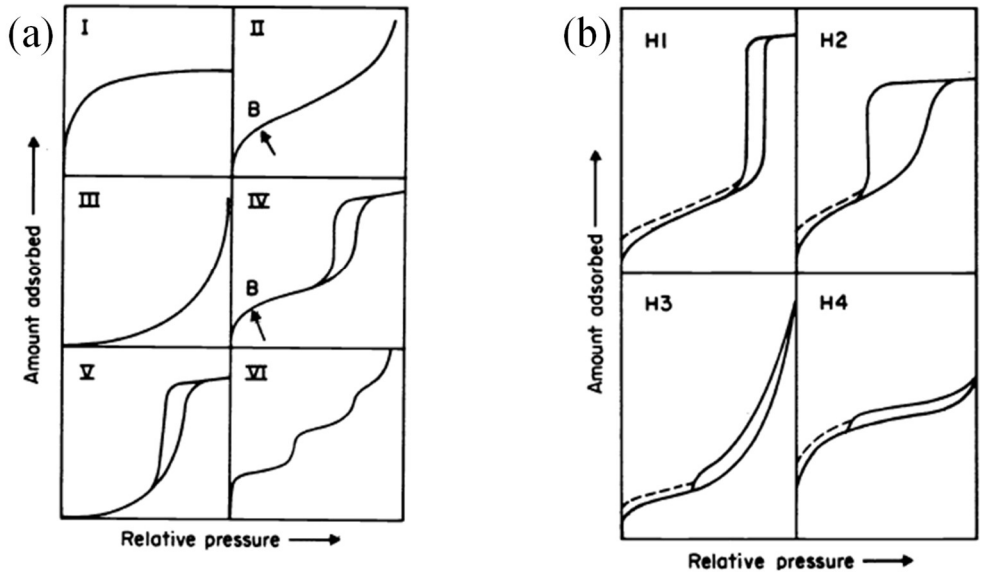

Figure 2-5. (a) Types of sorption isotherms and (b) hysteresis loops (Sing et al., 1984).

Several methods such as dynamic vapour sorption (DVS), climatic chambers, desiccator and saturated salt solution, etc. have been used by many researchers to evaluate the water sorption ability of bio-based materials (Brouard et al., 2018; Collet et al., 2013; A. Laborel-Préneron et al., 2018; Lagouin et al., 2019).

The hygroscopic behaviour of bio-based mortars/concrete depends on the nature of the binder and aggregates (Laborel-Préneron et al., 2018a; Lagouin et al., 2019). Typically, loose plant aggregates have a relatively higher water uptake and release ability than that of mineral binding matrix and bio-based mortar/concrete. For example, the use of barley straw, hemp shiv and corn cob as aggregates marginally increased the sorption capacity of unfired earth bricks (Laborel-Préneron et al., 2018a).

Lagouin et al. (2019) compared the sorption isotherms of sunflower and maize bark particles with that of lime and metakaolin pastes. The results showed that the moisture content of these particles at 95 % RH was 2 to 5 times higher than that of the binding matrices. Moreover, when these materials were associated together, the resulted concrete formulations exhibited comparable sorption isotherms. However, the water absorption capacity of metakaolin-sunflower concrete appeared to be slightly higher compared to lime-sunflower and metakaolin-maize concretes, as shown in Figure 2-6.

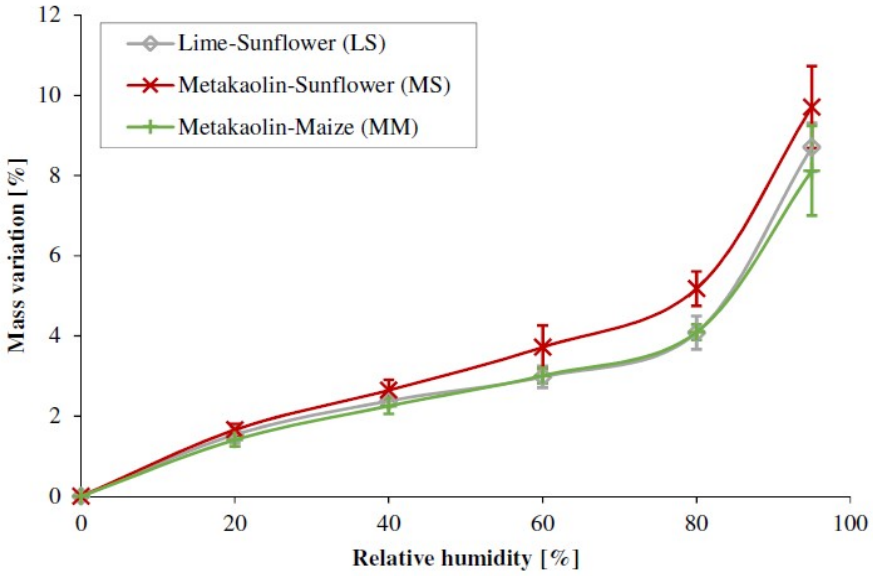

Figure 2-6. Sorption isotherms of sunflower and maize barks concretes (Lagouin, 2020; Lagouin et al., 2019).

Moreover, the moisture buffering capacity expressed as moisture buffer value (MBV) is another hygroscopic parameter that is widely evaluated among bio-based building materials. MBV is usually determined according to the NORDTEST project protocol. The latter classified building materials into five classes depending on their practical MBV ranges, as given in Table 2-10 (Rode et al., 2005).

Table 2-10. Classes of building materials and their respective practical MBV ranges according to (Rode et al., 2005).

Class	Negligible	Limited	Moderate	Good	Excellent
Practical MBV [g/(m^2 .% RH)]	0 – 0.2	0.2 – 0.5	0.5 – 1.0	1.0 – 2.0	> 2.0

Many studies have attempted to investigate the moisture buffering capacity of the bio-based building materials made of aggregates derived from lignocellulosic plants such as sunflower, maize, hemp, flax, and barley (Abbas et al., 2021; Dubois et al., 2012; Laborel-Préneron et al., 2018a; Lagouin et al., 2019; Mazhoud et al., 2016; Rahim et al., 2015; Rode et al., 2005). The practical MBV of the sunflower pith and hemp shiv is equal to 2.60 g/m^2. % RH and 2.90 g/m^2. % RH, respectively (Abbas et al., 2021). Rahim et al. (2015) studied the moisture buffering capacity of two bio-based concretes made of a similar binder. The study showed that both concretes exhibited comparable moisture storage capacity with an ideal MBV of 2.7 g/m^2. % RH for hemp lime concrete and 2.9 g/m^2. % RH for flax lime concrete.

Another comparative study conducted by Laborel-Préneron et al. (2018a) reported a slight variation of MBV with addition of plant aggregates in unfired bricks. The earth pastes exhibited an ideal MBV of 3 g/m^2. % RH while the earth bricks incorporating barley straw, hemp shiv and corn cob observed the ideal MBV in the ranges of (2.3-2.9) g/m^2. % RH, (2.6-3.1) g/m^2. % RH, (3.0-3.3) g/m^2. % RH, respectively. Figure 2-7 presents some practical MBV of different building materials reported in (Abbas et al., 2021; Dubois et al., 2012; Lagouin et al., 2019; Rode et al., 2005).

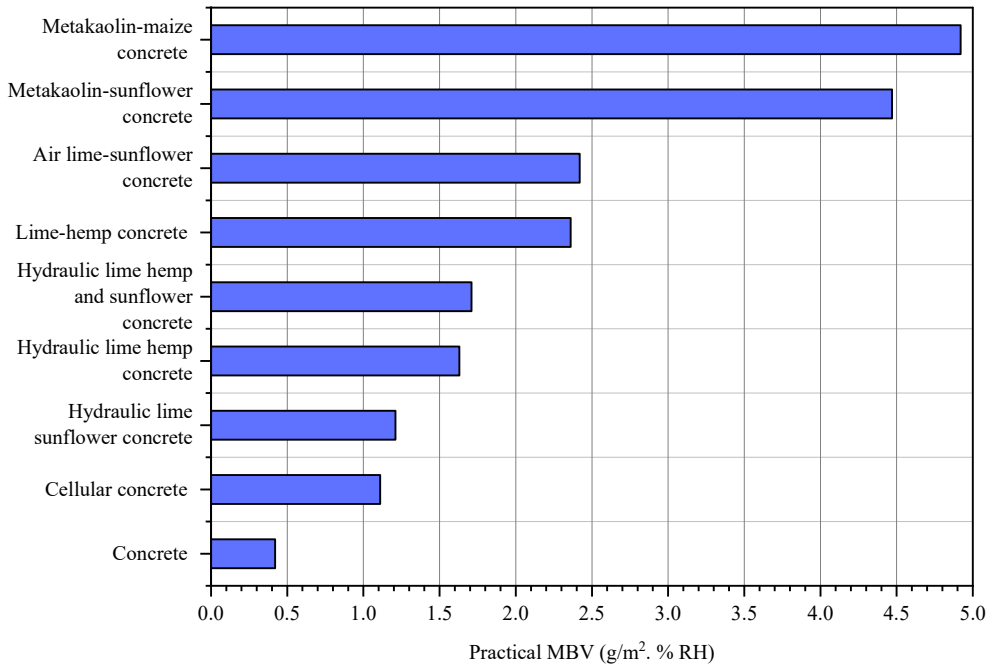

Figure 2-7. Reported MBV of different bio-based concretes and other building materials.

Furthermore, the nature of the binder can also affect the moisture buffering capacity of the bio-based mortars/concretes. The comparison between two sunflower concretes comprising two different binders revealed that the metakaolin-sunflower concrete showed higher MBV than air lime-sunflower concrete. The practical and ideal MBV of metakaolin-sunflower concrete was about 4.5 and 5.7 g/m^2. % RH, respectively, while for air lime-sunflower concrete, it was approximately 2.4 and 3.6 g/m^2. % RH, correspondingly (Lagouin et al., 2019).

Apart from that, the MBV of bio-based concretes may also vary depending on the production method. A comparative study on hygroscopic properties of sprayed, moulded and precast hemp concretes revealed that the sprayed and moulded hemp concretes had almost similar average moisture buffering values (2.15 and 2.14 g/m^2. % RH, respectively) whilst, the precast hemp concrete had an average MBV of 1.94 g/m^2. % RH (Collet et al., 2013).

Briefly, the moisture buffering capacity of the bio-based mortars/concretes depends on various factors including the nature of the binder, intrinsic properties of plant aggregates and implementation methods.

(e) Durability

Bio-based materials are very sensitive to the environment to which they are exposed. Previous studies have shown that the durability of bio-based mortars/concrete may depend on various factors including the environmental conditions (temperature, relative humidity, moisture content, etc.), nature of the binder and plant aggregates (Amziane and Collet, 2017; Delannoy et al., 2020). The experiments such as cyclic wetting and drying (Sonebi et al., 2015), freeze-thaw cycles, salt exposure and biological degradation are among a wide range of scenarios considered by researchers during the durability assessment of bio-based materials.

The submission of bio-based mortar and concrete to wetting and drying cycles has been reported to negatively influence their overall properties. The cyclic wetting and drying of bio-based mortar and concrete lead to a substantial decrease in mechanical properties and slight changes in thermal and acoustic properties. This falls in line with the study conducted by Sonebi et al. (2015) which reported a reduction of 50 to 80 % in compressive strength of three different hemp concrete formulations after 10 cycles of wetting and drying. Similarly, Benmahiddine et al. (2020) have also discovered that hemp concrete dropped about 51 % of its compressive strength whereas its water vapor permeability has increased by 38 %.

As for thermal and acoustic behaviours, Marceau et al. (2015) have indicated that exposing hemp concrete mixtures to wetting and drying cycles for 75 days slightly affected their thermal and acoustic properties. The thermal conductivity before and after wetting and drying cycles varied from 0.102 to 0.105 W/m.K. and 0.103 to 0.112 W/m.K., correspondingly. It was also concluded that the environment with high relative humidity (98 % RH) and low pH (less than 10) contributed to the biological aging. Furthermore, Delannoy et al. (2020) observed a significant augmentation of the lime and cement hemp-based concretes densities and thermal conductivity due to hydration of carbonation reactions of the binding matrices. After 2 years of wetting and drying cycles, the thermal conductivity of lime hemp-based concrete has increased by about 19 % and 7 % for cement hemp-based concrete. On the contrary, the acoustic performance has declined owing to the mineralization of vegetal aggregates porosity by portlandite.

The above-cited studies attributed the drastic strength reduction to weight loss, the weaker interfacial area between plant aggregates and mineral binders, and increased porosity in the bio-based mortar/concrete. Whilst the alterations observed in the thermal and acoustic properties have been ascribed to the changes that occurred in the microstructure of bio-based mortar/concrete due to increased density, continued hydration and carbonation of the binders over time, mineralization of plant aggregates, deterioration of particles cell walls, etc.

2.5.6 Some examples of methods to improve the compatibility of plant aggregates and mineral binders

The incompatibility of lignocellulosic plant particles with mineral binders is one of the major causes of the weaker mechanical and durability performance observed among bio-based mortars/concrete. To improve the interaction between plant aggregates and mineral binders, several methods such as physical and chemical treatment of plant aggregates, compaction, modification of the binding matrix, application of mineral and chemical admixtures, etc. have been proposed (Amziane and Collet, 2017; Vo and Navard, 2016).

For instance, the immersion of lignocellulosic plant particles in water enables the removal of some soluble compounds, therefore easing the hardening of the bio-based mortars/concretes. Moreover, the study conducted by Nozahic and Amziane (2012) revealed that treating sunflower stem particles in 1) a water bath for 5 minutes, 2) a solution of calcium hydroxide, and 3) coating the surface with paraffin wax ($C_{25}H_{52}$) notably improved the hygroscopic properties of sunflower aggregates and their adhesiveness with a mineral binder. In fact, the shear stress increased by 33 %, 66.3 %, and 67 %, respectively.

On the other side, heat treatment is another effective technique that has been used to improve the strength and durability of bio-based concrete. For example, the comparison between the concrete containing untreated and heat-treated apricot shells revealed that heat-treated apricot shells improved the compressive and flexural strength by 50.2 % and 87.7 %, respectively at 28 days. The study also indicated that heat-treatment on aggregates contributed to the reduction of concrete drying shrinkage by 29.2 % to 36.1 % at 108 days, micro-cracks and porosity, consequently ameliorating the resistance to freeze-thaw cycles (Wu et al., 2021).

The compaction process in the casting of bio-based mortars/concretes has been reported to favourably affect their mechanical behaviour. Nguyen et al. (2010) reported that the compaction process improves the mechanical properties of the hemp concrete thanks to the reduction of volume voids in the mortar/concrete and increment of the weight-to-volume ratio

as well as density. Besides that, they also observed a slight increase in thermal conductivity due to increased density and less amount of air trapped within the hemp concrete. Similarly, Nozahic et al. (2012) also concluded that casting by compaction contributes to the rearrangement of plant aggregates in layers, consequently enabling the production of bio-based mortars/concretes with orthotropic and improved mechanical performance.

In addition, the application of viscosity modifying agents (VMAs) such as microsilica, nanosilica slurry, polysaccharides, cellulose ethers, acrylic emulsions, acrylic acids and welan gum, remarkably improves the flowability, rheology and stability, cohesion and water retention capacity of the mortar and concrete mixtures (Khayat, 1998; Leemann and Winnefeld, 2007; Sheridan et al., 2020a, 2020b). In fact, Sheridan et al. (2020a, 2020b) noted that using polyacrylic acid led to a substantial decrease in the capillary water absorption capacity of hemp and rapeseed straw concretes. Moreover, it also enhanced the compressive strength, modulus of elasticity and durability of these materials.

Furthermore, it has also been reported that mixing lime with industrial by-products improves the strength and durability of bio-based mortars/concretes. The comparison of the mechanical properties of hemp concrete incorporating pozzolans namely GGBS and MK, and those without them revealed slight fluctuations in the kinetics of strength development. At 28 days, the hemp concrete containing a commercial binder displayed superior compressive strength compared to others. However, after 1 year, all hemp concretes eventually achieved comparable compressive and flexural strengths (Walker et al., 2014). Besides that, Aggarwal and Singh (1990) showed that the addition of an accelerator, for example, calcium chloride, can offset the retardation effect of plant extractives on the setting and hardening of the cement pastes.

2.5.7 Environmental benefits of bio-based materials

Bio-based materials present substantial environmental advantages compared to conventional building materials. For example, the median whole-life (50 years) embodied carbon emissions for a reinforced concrete frame and steel frame are estimated at 185 kg $CO_{2eq.}/m^2$ and 228 kg $CO_{2eq.}/m^2$, respectively (Hart et al., 2021). On the contrary, the literature has proved that lime-hemp concrete is a carbon-negative material as it does not only offset all CO_2 emissions generated during its lifetime but also, sequestrates a significant amount of CO_2 from the atmosphere. Boutin et al. (2006) reported that a load-bearing hemp concrete wall of 260 mm thickness, made by spraying lime-hemp concrete on the timber frame can sequestrate 14-35 kg of $CO_{2eq.}/m^2$ over a lifetime of 100 years. Moreover, the study conducted by Ip and Miller

(2012) has also claimed that a non-load bearing wall of 300 mm thickness, built based on timber frame supports and lime-hemp concrete poured between temporary shuttering enables the storage of 36.08 kg $CO_{2eq.}/m^2$ at a similar lifespan.

2.5.8 Current market situation of bio-based materials as building insulation materials

Despite lots of endeavours to promote bio-based building materials, there are still many barriers limiting their development. The Nomadéis report published in 2017 indicated that bio-based insulation materials accounted for about 8 % of the French market of insulation materials while mineral wool, glass fibres, and expanded polystyrene represented 38.5 %, 32 %, and 22 %, respectively (Dutreix et al., 2017). This low share of bio-based materials in the insulation materials market can be explained by their high cost (the price of raw materials and implementation included), lack of skilled labourers, and clients' attitudes. For instance, the comparison between hemp mortar and polystyrene panels as building insulators by the exterior shows that the cost for both materials can be estimated at about 30-90 and 15-35 €/m^2, correspondingly (Baecher et al., 2012).

In relation to implementation, the average cost for the sprayed hemp concrete is estimated at around 150 € (tax excluded) /m^2 which is comparable to that of conventional solutions with exterior insulation or distributed insulation. However, the aforementioned price is higher than that of the concrete block insulated by the interior with mineral wool and plasterboard, which is about 100 €/m^2 (Floissac et al., 2016). With regard to technical properties, the particularity of bio-based mortars/concrete lies in their interesting thermal, acoustic, and hygroscopic properties. Nevertheless, the latter exhibit low mechanical performance.

2.6 Conclusion

In this chapter, an overview on the application of supplementary cementitious materials (SCMs) in construction materials has been made. The use of SCMs has been acknowledged by the research community as a relevant way to mitigate the impact of the cement and concrete industry on the environment. In addition, SCMs also provide economical and technical advantages. Most studies in this field have approved that the use of low amounts (< 50%) of SCMs as cement replacement can benefit the mechanical and durability properties of cement-based materials. On the contrary, the addition of greater amounts (> 50 %) of SCMs can have negative effects on the overall concrete performance.

At the same time, there has been a growing interest in alternative cementitious materials of biomass origin recently. These materials are the by-products resulting from the combustion of

wood (chips, sawdust, etc.) or agricultural wastes at heating and power biomass plants. Wood ash is one of these biomass by-products which is widely available and that has been used for many years in the preparation of various construction materials production, including cement-based materials. It is noteworthy that, when wood biomass ash is used as a replacement for cement or aggregate, it is mostly added at lower percentages (below 50 % by mass). Other than that, it is also apparent that, to date, scant attention has been paid to the applications of wood biomass ash in bio-based mortars/concrete.

Apart from SCMs, the literature on the recent advances in bio-based building materials has also been reviewed. In this regard, it appears that the increased awareness of building energy consumption did not only lead to the establishment of thermal regulations but also, promoted the development of bio-based building insulation materials. Since the presentation of the first hemp concrete in 1986, bio-based materials have received significant research attention. Most research studies have confirmed that bio-based mortars/concretes do not only present excellent thermal insulation and hygroscopic properties but also, offer considerable environmental benefits.

On the contrary, the bio-based materials sector faces multiple challenges such as weak mechanical and durability performance, and low attractiveness in the market of building insulation materials due to their high production cost. Therefore, numerous recent research works in this area focus on improving the strength development and durability and lowering the manufacturing cost of bio-based materials. In this regard, the use of supplementary cementitious materials has emerged and there is a growing interest in lignocellulosic plant particles other than hemp shiv in bio-based building materials sector.

Chapter 3: Characteristics of wood ashes, mineral additives and sunflower particles

This chapter presents the materials, experimental methods, and main results of raw materials characterization. First, the collected raw materials, their quantities and notation are presented. Then, the main characterization methods used to investigate the physical, chemical, microstructural and hygrothermal properties of the raw materials will be described. After evaluating the major characteristics of the raw materials, the results will be presented, discussed and the main conclusions are drawn.

3.1 Description of the raw materials

The industrial by-products used in this study as the main constituents of the binding matrices were of biomass origin. Eight different batches of biomass ash were collected from various locations in the Normandy region. Indeed, the biomass ashes denoted as WFA1, WFA2, WFA8, and WFA9 were supplied from Coriance (Mont-Saint-Aignan) Energie Verte (MAEV), a local biomass heating plant. According to the supplier, the plant uses boilers with a power input of 6 and 8 megawatts (MW). The biomass fuels used include a wide range of wood chips (forestry wood chips, bocage wood chips, removal from the waste status (SSD) wood chips class A, pallet shavings), wood bark, etc., mostly from the departments of Orne and Calvados, France. The distance between the collection site and the heating plant does not exceed a radius of 150 km to ensure financial reliability.

The wood chips and barks are burnt in the furnace at high temperatures, in the range of 900-1100 ºC. The wood fly ash generated at this biomass heating plant is discharged into the landfill whereas wood bottom ash is valorized in agricultural applications (for example spreading). Moreover, the biomass ashes designated as WFA3, WBA and WSA were obtained from Veolia, a multinational company providing diverse services including waste management and valorization, etc. Lastly, the biomass ash named WFA7 was obtained from the Engie branch in Caen.

In addition to the supplier information, Table 3-1 provides more details about the collected biomass ashes, such as the quantity, colour, wood origin, physical state and nature of waste.

Table 3-1. Description of the collected biomass ashes.

Notation of biomass ash	WFA1	WFA2	WFA3	WBA	WSA	WFA7	WFA8	WFA9
Supplier	Coriance MAEV		Veolia Rouen			Engie Caen	Coriance MAEV	
Colour	light grey	dark grey	dark	dark	white	grey	light grey	dark grey
Quantity	6 buckets (32L)	2 buckets (32L)	1 big bag (≈1 m^3)	1 big bag (≈1 m^3)	2 buckets (5.5L)	1/2 bucket (5.5L)	1 big bag (≈1 m^3)	1 big bag (≈1 m^3)
Physical state	ultra-fine powder		coarse sludge		fine powder	coarse sludge	ultra-fine powder	
Condition	dry		wet		dry	wet	dry	
Origin	wood chips		wood pallets		paper sludge	wood	wood chips	

Note: WFA1: wood fly ash 1; WFA2: wood fly ash 2; WFA3: wood fly ash 3; WBA: wood bottom ash; WSA: wastepaper sludge ash; WFA7: wood fly ash 7; WFA8: wood fly ash 8; WFA9: wood fly ash 9.

These above presented biomass ashes and two types of hydraulic binders, namely ordinary Portland cement and natural hydraulic lime, selected to be used as mineral additives in biomass ash-based pastes, are shown in Figure 3-1.

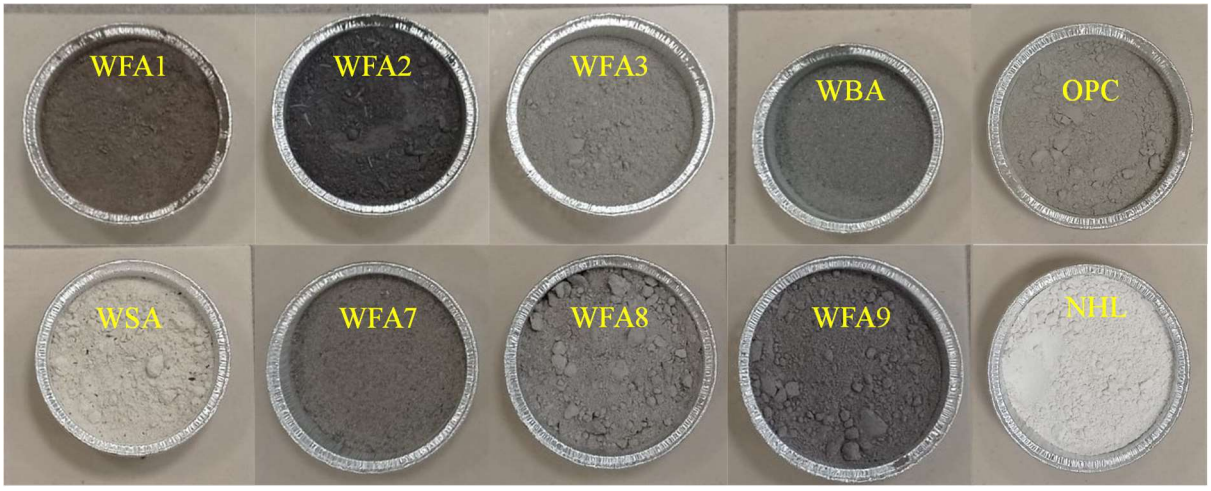

Figure 3-1. Mineral raw materials used in this study.

3.1.1 Hydraulic binders

In the beginning of this study, two types of hydraulic binders were chosen to improve the mechanical performance of the binding matrices. The first choice was the natural hydraulic lime (PRB hydraulic lime of Saint-Jacques NHL 3.5) (NHL), which complies with the French standards NF EN 459-1. The second option was the multi-purpose ordinary Portland cement

CEM II/B-LL 32.5N (OPC), commercially known as Cement Pro, conforming to the French standards (NF EN 197-1, 2011). According to the manufacturer's data sheet, the minimum compressive strength of OPC and NHL at 28 days is 32.5 and 3.5 MPa, respectively. These hydraulic binders were purchased from a local construction materials supplier.

3.1.2 Sunflower particles

The agricultural by-products employed as aggregates in this project, were the sunflower pith and bark, provided in 2017 by Groupe Oxyane (formerly known as La Dauphinoise, an agricultural cooperative located in the Auvergne-Rhone-Alpes region in the South East of France. The quantity of sunflower pith and bark that was made available to the study was approximately 1/2 big bag (≈1 m^3) and 1 big bag (≈1 m^3), respectively. Both materials were stored in a room at ambient temperature and relative humidity. The sunflower particles used in the production of the lightweight insulation mortar are shown in Figure 3-2.

Figure 3-2. Sunflower particles: (a) ground sunflower stem, (b) pith and (c) bark.

As is evident, the morphology of sunflower pith (SP) is different than that of sunflower bark (SB). SP particles tend to be more spherical or circular, while SB particles are typically parallelepipedal or rectangular in shape.

3.2 Characterization methods for wood ashes, mineral additives and sunflower aggregates

3.2.1 Particle size distribution

A laser diffraction spectroscopy (LDS) method was adapted for determining the particle size distribution (PSD) of the wood ashes, lime and cement. The instrument used was a Malvern Mastersizer 2000 equipped with a hydro 2000 MU dispersion unit. The laser diffraction measures the light scattered by the particles and then a mathematical model (for example: Fraunhofer diffraction model, Mie theory) converts the light scattering data to particle size

distribution (Arvaniti et al., 2015b). This technique has been validated by the International Organization for Standardization (ISO 13320:2020, 2020) and is often used to measure the PSD of ultrafine powders. It is capable of determining the particle sizes ranging from 0.01 to 3500 µm (Arvaniti et al., 2015a; Ndahirwa et al., 2022).

For the sunflower particles, the particle size distribution of the pith and bark was determined using two methods: 2D image processing and mechanical sieve analysis. The ImageJ software was used to determine the dimensions (length and width) of the sunflower particles that were randomly picked. The major benefit of this method is that it enables the characterization of intricate particles morphology, as well as their heterogeneity (Nozahic et al., 2012). Furthermore, the mechanical sieve analysis was also performed to make the cumulative PSD by considering the mass of particles retained on different sieves and also determine the dust content in sunflower pith and bark. The image processing and sieve analysis were carried out according to (Amziane and Collet, 2017).

3.2.2 Bulk density

In the case of the raw mineral materials, the bulk density was measured using a glass cylinder and weighing scale (accuracy: ± 0.01 g). The sample was filled to half of the cylinder (inner diameter of 7.5 cm and height of 15 cm). The cylinder containing the sample was then shaken before marking the level and taking the mass. Once the sample was removed, the same cylinder was filled with water to the same level as the sample to measure the volume. Finally, the bulk density of the sample was obtained by dividing the sample mass (g) by the volume occupied by the water (cm^3). It should be mentioned that three repetitions were made for each sample.

On the other hand, for the sunflower particles, the bulk density of pith and bark was determined, following the protocol established by RILEM Technical Committee 236 recommendations on bio-based materials (Amziane and Collet, 2017). The detailed protocol is described as follows: the sunflower bark and pith particles were first dried in a ventilated oven at 60 °C until constant mass (mass variation < 0.1% between two weighing in 24h). The dry sunflower bark and pith were placed into a dry cylindrical glass mould (inner diameter of 12 cm and height of 24 cm) without applying compaction. Then, the glass mould containing the loose sunflower particles was inverted 10 times and gently agitated. Once a horizontal surface was obtained, the mass was recorded and the level of sunflower particles was marked. After the sample was removed from the mould and the latter was cleaned, and dried using a compressed air pump. The mould was then filled with tap water to the levels marked and the corresponding masses were taken.

Finally, the bulk density was obtained by dividing the mass of sunflower particles (g) by the volume occupied by water (mL). The reported bulk density results are average values obtained from twenty-seven measurements made on different sunflower pith and bark samples.

3.2.3 Skeletal density

A Pycnomatic Evo operating under argon, an alternative gas to helium, was used to for measuring the skeletal densities of the biomass ashes, ordinary Portland cement and natural hydraulic lime. The pycnometer vessel with a volume of 21.4 cm^3 was packed with a dry powder sample to about two-thirds of its volume. The ratio between the mass of the sample and its volume without counting open porosity was referred to as skeletal density. Note that three repetitions were made for each sample.

Moreover, the skeletal density of the sunflower particles was measured using a similar method. The pycnometer vessels employed for the sunflower pith and bark had a volume of 61.5 cm^3 and 21.4 cm^3, respectively. The vessels were filled with dry ground (maximum particle diameter < 1 mm) and unground samples to about two-thirds of its volume. The skeletal density was computed by dividing the mass of the sunflower particles sample by its volume excluding open porosity. The skeletal density reported herein represents the average values of the results obtained from nine measurements on different sunflower pith and bark samples.

3.2.4 Porosity

The open and closed porosities of sunflower particles were calculated based on their bulk and skeletal densities according to (Arufe et al., 2021). Note that Equation 3-1 and Equation 3-2 were employed:

$$\theta_{\text{open}} = 1 - \frac{\rho_{\text{b unground}}}{\rho_{\text{s unground}}} \qquad \text{Equation 3-1}$$

$$\theta_{\text{closed}} = 1 - \frac{\rho_{\text{s unground}}}{\rho_{\text{s ground}}} \qquad \text{Equation 3-2}$$

where θ_{open} is open porosity (%); θ_{closed} is closed porosity (%); $\rho_{b\ unground}$ is bulk density of unground particles (kg/m^3); $\rho_{s\ unground}$ is skeletal density of unground particles (kg/m^3); $\rho_{s\ ground}$ is skeletal density of ground particles (kg/m^3).

3.2.5 Relative humidity

The moisture content of the biomass ashes was determined using three instruments including a weigh scale (accuracy: ± 0.01 g), a Memmert ventilated oven and a desiccator. A 1g biomass

ash sample was weighed, dried in an oven at 105 °C for 48 h. Afterwards, the sample was cooled down for 1 h in a desiccator. The difference between the mass before and after oven drying was designated as the moisture content of the biomass ashes. For each sample, three repetitions were made. For sunflower particles, the relative humidity was measured on ground sunflower pith and bark samples, using an infrared dryer (Sartorius). It should be mentioned that the tested samples were previously stored in a ventilated oven at 40 °C.

3.2.6 Chemical composition

The chemical composition of the mineral raw materials was assessed using two methods: inductively coupled plasma-atomic emission spectroscopy (ICP-AES) and X-ray fluorescence spectroscopy (XRF). The ICP-AES was chosen because it was affordable and it has been used by researchers such as (Delannoy et al., 2020; Ragoug et al., 2019) in order to identify the oxide compounds in mineral powders. On the other hand, due to the limited budget, XRF analysis was performed on only three samples (OPC, WFA8, and WFA9) that were randomly picked, to validate the relevance of the ICP-AES results.

Furthermore, the chemical composition of sunflower pith (SP) and bark (SB) was determined with a FibertecTR 8000 Foss machine, as shown in Figure 3-3, according to the Van Soest and Wine method. This technique consists on extracting non-water-soluble compounds from the plant particles using detergent solutions such as Acid Detergent Fiber (ADF) and Neutral Detergent Fiber (NDF).

Figure 3-3. Fibertec 8000 equipment used to study the biochemical composition sunflower particles.

Prior to experiment, the sunflower particles were milled using a high-speed rotor mill (Fritsch Pulverisette 14) until achieving a particle diameter passing through a 0.5 mm sieve mesh. The

obtained SP and SB powders were kept in two plastic containers and dried in a Memmert ventilated oven at 40 ºC until constant weight. On the test day, SP and SB samples had a relative humidity of 5.5 ± 1.5 % and 2.9 ± 0.5 %, respectively. Owing to the high volume of SP, the analysis was carried out on 0.5 g of sunflower pith. For the sunflower bark, a sample of mass 1 g was used. All measurements were conducted in triplicate.

3.2.7 Pozzolanic activity

This characteristic is particular for mineral materials. Due to time constraints, this analysis was only performed on the WFA8. It appeared that the pastes containing WFA8 displayed better strength development than other pastes. Thus, it was interesting to study its pozzolanic activity.

The pozzolanic activity of the WFA8 was investigated using the modified Chapelle test according to NF P18-513 (Avet et al., 2016; Esteves et al., 2012; Ferraz et al., 2015; Fořt et al., 2021). The test protocol was as follows: a high accuracy scale was used to weigh the materials. 1g of WFA8 was mixed with 2 g of calcium oxide (CaO) and 250 mL of distilled water. The solution was then boiled at 90 ºC for 16 h with continuously stirring (400 rpm) in a glass Erlenmeyer flask connected to a reflux condenser to prevent water loss. After 16 h, the Erlenmeyer containing the solution was cooled down at ambient temperature in tap water.

Moreover, a solution of 61.65 g of sucrose 0.7 mol/L and 250 mL of distilled water was added to the cooled WFA8 and CaO solution. The newly formed solution was agitated for 15 minutes and filtrated with help of a Buchner filter. A filtrate of 200 mL was taken and each 25 mL of this filtrate was titrated with hydrochloric acid (HCl 0.1(N)) using 2-3 drops of phenolphthalein as an indicator. Ultimately, the amount of fixed calcium hydroxide $Ca(OH)_2$ was calculated based on the volume of HCl solution added, as seen in Equation 3-3.

$$P = 2 \times \frac{V_{1-} V_2}{V_1} \times \frac{74}{56} \times 1000 \qquad \text{Equation 3-3}$$

where P is pozzolanic activity of wood fly ash, expressed in mg $Ca(OH)_2$ fixed by g wood fly ash; V_1 is volume of HCl 0.1N required to titrate 25 mL of the filtrate obtained without wood fly ash (blank test); V_2 is volume of HCl 0.1N required to titrate 25 mL of the filtrate obtained with wood fly ash.

3.2.8 Potential of hydrogen (pH)

Among the classical methods for determining the pH of concrete, an ex-situ leaching method was chosen (Behnood et al., 2016; Haque and Kayyali, 1995). This method does not require

special equipment or pre-conditioning, the pH measurement is performed with an electrode. The samples of all biomass ashes collected and ground bio-based mortars were suspended in distilled water with a solid/liquid ratio of 1/4. The suspension was stirred for 5 minutes then, sealed and stored for 24 hours. Finally, after a vigorous agitation, the mixture was filtered using a Buchner filter. The pH of the filtrate was afterward measured using WTW and Mettler Toledo SevenMulti pH-meters.

On the other hand, the pH of the sunflower pith and bark (unground and ground) was also evaluated using a Mettler Toledo SevenMulti pH-meter. Due to the high-water absorption capacity of the plant materials, the above-mentioned ratio of 1/4 was not considered. However, care was taken to ensure that the sunflower pith and bark samples were completely immersed in distilled water. Three measurements were made for each sample.

3.2.9 Water absorption capacity

It should be pointed out that this analysis is specific for bio-based materials. The water absorption capacity of sunflower pith and bark was determined according to RILEM Technical Committee 236 recommendations on bio-based materials (Amziane and Collet, 2017). The sunflower pith and bark samples were dried in a ventilated oven at 60 °C until the constant mass (mass variation less than ±0.1 g in 24 h). 15 g of sunflower pith and 50 g of sunflower bark were weighed and packed into water permeable synthetic tissues. Then, the samples were immersed in a water bath until the desired time. The water absorption kinetics were obtained from weight measurements (in triplicate) at 1, 5, 15, 30, 45, 60 minutes, 24 h and 48 h, according to Equation 3-4 (Nozahic and Amziane, 2012):

$$W(t) = \frac{M(t) - M_0}{M_0} \times 100 \qquad \text{Equation 3-4}$$

where W(t) is water absorption capacity of sunflower particles at time t (%); M(t) is mass of soaked sunflower particles at time t (g); M_0 is initial mass of oven-dried sunflower particles (g).

3.2.10 Water sorption isotherms

This analysis was performed on the wood fly ash WFA8, cement and sunflower particles. Water sorption isotherms namely adsorption and desorption, represent the relationship between the water content of the material and the ambient relative humidity (RH) at a constant temperature (Amziane and Collet, 2017; Lagouin et al., 2019). The water sorption isotherms of the samples were measured with a ProUmid Dynamic Vapour Sorption (DVS) machine

fitted with SPS-sorption test system, under nitrogen gas, at a temperature of 23 °C. Numerous relative humidity conditions were selected. The relative humidity of 0, 35, 50, 75, 85, and 92 % was chosen for adsorption tests while the relative humidity of 92, 85, 75, 50, 35, and 0 % was set for desorption tests. The default weight limit and equilibrium condition were set at 500 % and 0.01 % (15 minutes), respectively. At least a triplicate was made for each sample.

3.2.11 Thermal conductivity

There exist several methods to determine the thermal conductivity of building insulating materials. The most commonly employed methods include guarded hot plate, fluxmeter, hot wire and hot disk methods (Dupre, 2014). The fluxmeter method does not only allow to achieve a certain level of accuracy but also save a significant amount of time. Note that the latter complies with ISO 8301 and NF EN 12667 (Dupre, 2014).

A Heat Flow Meter HFM 446 small/lambda NETZSCH was used to evaluate the insulation capacity of the raw materials and lightweight mortar elaborated in this study. The thermal conductivity (λ) measurements were conducted on the dry sunflower bark and pith. Both samples were previously dried in a ventilated oven at 60 °C until the constant mass (variation less than 0.1 g between two mass measurements in 24 h) (Amziane and Collet, 2017). Also, before the test, the mass of the sample was measured. The mould used was made of expanded polystyrene with the bottom side covered by aluminium foil. The temperatures of the upper and lower plates were set at 30 °C and 10 °C, respectively. The temperature gradient (ΔT) between the hot and cold plate was 20 °C. The measurements were carried out at temperature of 23 °C on the loose sunflower particles at least in triplicate.

3.2.12 Scanning electron microscopy

A JEOL JSM-IT100 scanning electron microscopy was used to observe the microstructure of the OPC and biomass ashes. The analysis was performed on a small amount of the powder sample dispersed on a carbon double-sided sticker that covered the sample support. The observations were made in a high-vacuum (HV) model, using a secondary electron detector (SED) with an energy of 5kV and a distance (WD) of 12 mm. As for sunflower particles, the scanning was performed by a backscattered electron detector (BSE), with an energy of 15 kV and a distance (WD) of 19 mm for sunflower pith 12 mm and for sunflower bark.

3.2.13 Thermogravimetric analysis

The thermogravimetric analysis (TGA) was carried out at a heating rate of 10 °C/minute under an argon atmosphere from a dynamic heating interval ranging from 25 to 1000 °C on the

mineral raw materials, using a NETZCH-TG 209 F1. The measurements were performed on powder samples of mass varying from 20 to 40 mg. The samples were in alumina crucibles and at least a duplicate was considered for each powder. Regarding sunflower particles, a similar test set up was used, except for the heating interval that was shifted from 25 to 600 °C.

3.2.14 Microstructure composition

X-ray diffraction (XRD) was employed to identify the main crystalline phases in the OPC, NHL and biomass ashes. This qualitative and semi-quantitative method has been widely used for evaluating the mineralogical composition of cementitious materials. In the present study, a Bruker D8 Advance X-ray diffractometer was employed to identify the crystalline phases in the mineral raw materials, some binding matrices and sunflower-based mortars. The XRD had 2 Theta (θ) configuration using copper anode Cu Kα radiation generator (λ = 1.540 Å) and was equipped with LynxEye OD detector. The double diffraction angle (2θ) ranged from 3 to 70 with step size of 0.015° and acquisition speed of 0.5 seconds per step. The scanning graphs were treated using DIFFRAC.EVA software.

3.3 Results and discussion

3.3.1 Mineral raw materials

(a) Pre-treatment and preparation of the raw materials

The ashes denoted as WFA1, WFA2, WSA, WFA8, WFA9 were delivered in a dry and very fine state. For this reason, these powders did not require any pre-treatment prior to their characterization and use in the blended pastes and mortars. In contrast, biomass ashes received as wet sludge required thermal and physical pre-treatments. The treatments consisted of oven drying WFA3, WBA, and WFA7 at 105 °C for 48 h to remove excess moisture. Due to the wide range of particle sizes from 0.05 mm to 15 mm, the freshly dried WFA3, WBA, and WFA7 were manually ground with a hammer to obtain fine particles. The ground powder passing through a 0.5 mm sieve was placed in clean containers. All batches of collected biomass ash were kept in sealed plastic buckets and stored in the laboratory at room temperature and relative humidity.

(b) Particle size distribution

The particle size distribution (PSD) of mineral raw materials was determined with the laser diffraction technique as described in section 3.2.1. The analysis was performed on the powder samples of WFA3, WBA, WF8, WFA9, OPC, and NHL soaked in milli-Q water under

agitation (wet method). Note that at least three measurements were performed for each sample. As shown in

Figure 3-4, OPC and NHL particles were finer than biomass ashes. The WFA3 and WBA consisted of coarser particles compared to WFA8 and WFA9. Generally, almost all particles of the mineral raw materials used in this study ranged between 0.1 and 500 µm.

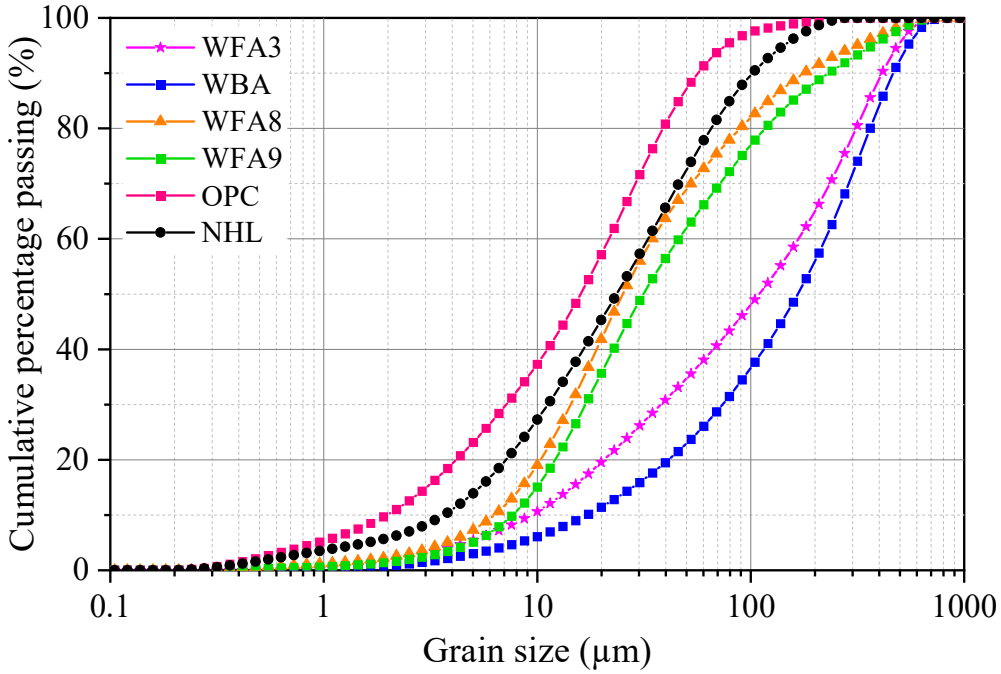

Figure 3-4. Particle size distribution of WFA3, WBA, WFA8, WFA9, OPC and NHL.

(c) Bulk density

It should be noticed that the bulk density measurements were performed on the raw materials that were selected for the use in preparing the binding matrices. These materials included four wood ashes, natural hydraulic lime (NHL) and ordinary Portland cement (OPC). The bulk density results obtained from the above-mentioned powders are presented in Table 3-2.

Table 3-2. Bulk density of some biomass ashes, OPC, NHL.

Sample	OPC	NHL	WFA3	WBA	WFA8	WFA9
Bulk density (kg/m^3)	1303	715	631	1035	374	379

It is evident that the average bulk densities of OPC and NHL are higher than those of the wood fly ashes, namely WFA3, WFA8, and WFA9. The higher bulk density obtained from the wood bottom ash WBA can be explained by its morphology as it consists of large and rock-like particles. The bulk density of WFA8 and WFA9 was lower than the values found in previous

studies. As an example, the bulk density of wood ash has been reported to be in the range of 490-760 kg/m^3 (Chowdhury et al., 2015; Naik, 2002; Siddique, 2012). With respect to natural hydraulic lime, it varies from 700-846 kg/m^3 (Arnaud and Gourlay, 2012; Grilo et al., 2014). It is important to mention that the bulk density of OPC (1303 kg/m^3) used in this study was slightly lower than the values reported in the literature.

(d) Skeletal density

The skeletal density results of the mineral raw materials are given in Figure 3-5. Accordingly, the average skeletal densities of the biomass ashes, OPC, and NHL vary from 2 to 4.5 g/cm^3. The lowest skeletal density values were obtained from WFA3 (2.0 g/cm^3) and WBA (2.3 g/cm^3) while the highest values were observed on WFA8 (3.6 g/cm^3) and WFA9 (4.5 g/cm^3).

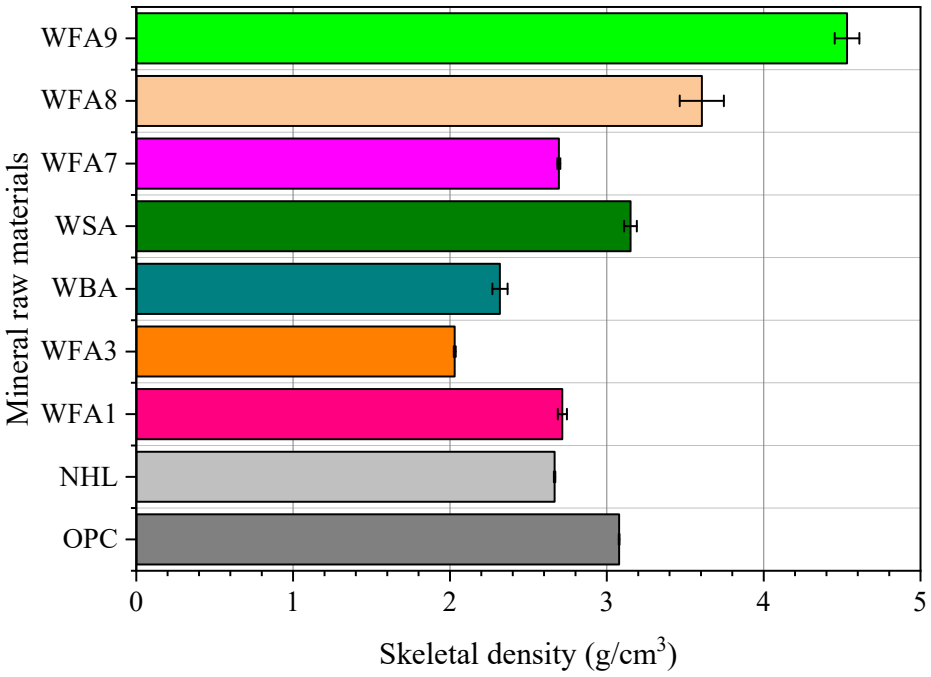

Figure 3-5. Skeletal density of the biomass ashes, OPC and NHL.

(e) Moisture content

The moisture content of seven tested biomass ash samples was below 2 % by weight, as can be seen in Figure 3-6. The lowest average moisture content, being 0.02 % was observed on WSA whilst, WFA3 exhibited the highest average water content (1.43 %). The higher moisture content in wood biomass ashes notably WFA1, WFA2, WFA3, WBA, WFA8, and WFA9 can be attributed to the porosity and unburned wood particles, which absorb ambient humidity.

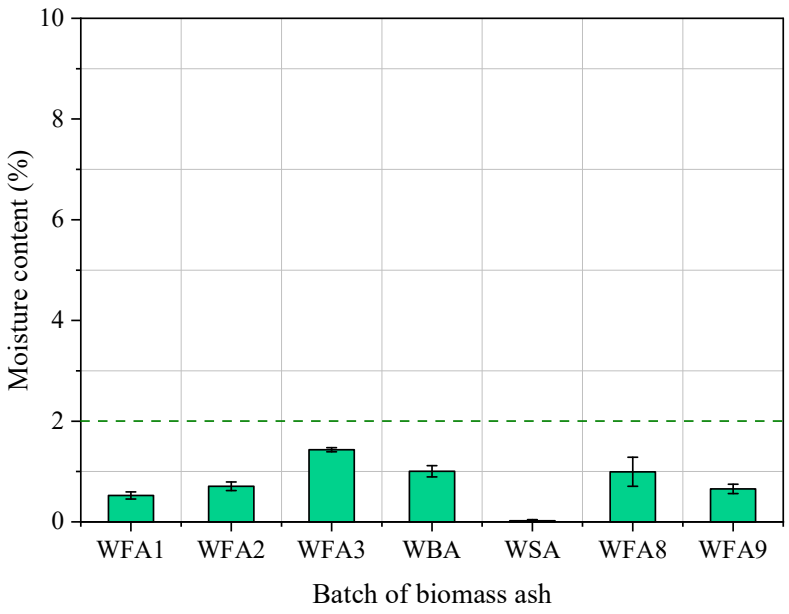

Figure 3-6. Moisture content of the biomass ashes.

(f) Chemical composition

It was important to determine the oxide compounds comprising in the raw materials, in order to understand the effect of the chemical composition of each material on the properties of the pastes and mortars that will be developed in the next chapters. The chemical composition of eight biomass ashes, NHL and OPC was determined using an inductively coupled plasma-atomic emission spectroscopy (ICP-AES) at analytical laboratory in organic, inorganic and materials chemistry (FILAB), Dijon, France.

In addition, X-ray fluorescence spectroscopy (XRF) analysis was performed on three randomly selected samples OPC, WFA8 and WFA9 at another external laboratory. As previously mentioned in section 3.2.6, the main objective of using two methods was to check the consistency of the results obtained by these two methods. The identified oxide compounds and their contents are given in Table 3-3 and Table 3-4.

Table 3-3. Chemical composition of OPC, NHL and biomass ashes determined by ICP-AES.

Compounds	OPC	NHL	WFA1	WFA2	WFA3	WBA	WSA	WFA7	WFA8	WFA9
SiO_2	15.90	15.00	0.95	5.05	7.48	17.30	14.30	15.30	4.96	3.48
Al_2O_3	3.27	0.30	0.26	1.60	1.98	3.77	5.51	4.61	1.25	1.14
Fe_2O_3	3.02	0.18	0.51	2.03	1.01	2.30	1.03	3.95	1.39	2.28
CaO	43.30	44.30	20.20	18.40	22.50	18.20	44.20	16.30	17.70	19.50
MgO	1.00	0.50	2.94	3.30	2.63	2.33	2.09	3.19	2.68	2.97
TiO_2	0.20	0.02	0.04	0.15	0.14	0.33	0.69	0.37	0.12	0.10
MnO	0.05	0.01	0.50	1.54	0.35	0.38	0.06	0.73	0.95	1.59
P_2O_5	0.23	0.03	3.08	3.02	2.28	1.77	0.37	2.00	2.73	2.76
K_2O	0.82	0.06	13.00	7.04	5.80	4.31	0.81	4.00	8.14	9.26
SO_3	3.01	0.66	18.20	13.20	7.36	1.52	2.00	0.75	15.40	14.00
$SiO_2 + Al_2O_3 + Fe_2O_3$	22.19	15.47	1.72	8.68	10.47	23.37	20.84	23.86	7.60	6.90

As shown in Table 3-3, the major oxide compounds in analysed samples vary from powder to powder. As expected, calcium oxide (CaO) and silicon oxide (SiO_2) are predominant oxides in OPC and NHL. In the case of biomass ashes, CaO is present and dominant in all analysed samples. It is noteworthy that, the wood ashes (WFA3, WBA, WFA7) received in the wet state and wastepaper sludge ash (WSA), were rich in SiO_2 and had lower levels of alkalis. In contrast, the wood fly ashes, including WFA1, WFA2, WFA8 and WFA9 contained significant amounts of sulphur trioxide (SO_3) and potassium oxide (K_2O) while their SiO_2 contents were below those of the other samples.

Furthermore, the XRF data for OPC, WFA8 and WFA9 provided in Table 3-4 confirmed that CaO and SiO_2 were the major oxides in OPC. Regarding WFA8 and WFA9, the most prominent oxides were CaO, SiO_2 and K_2O. Apart from that, the Fe_2O_3 content was notably higher in WFA8 than in OPC and WFA9. It should be noticed that the loss on ignition (LOI) of the OPC was slightly lower than those of WFA8 and WFA9.

Table 3-4. Chemical composition of OPC, WFA8 and WFA9 determined by XRF.

Compounds	OPC	WFA8	WFA9
SiO_2	15.72	15.54	14.98
Al_2O_3	3.91	2.3	2.15
Fe_2O_3	2.85	7.19	2.39
CaO	58.18	37.24	40.54
MgO	1.22	2.55	3.02
TiO_2	0.22	0.18	0.18
MnO	0.06	0.82	1.34
P_2O_5	0.21	1.95	2.4
K_2O	1.1	12.82	15.01
SO_3	2.96	2.9	1.38
NaO_2	0.04	0.08	0.09
LOI	13.44	15.69	15.52
$SiO_2 + Al_2O_3 + Fe_2O_3$	22.48	25.03	19.52

The results of WFA8 and WFA9 given in Table 3-4 are coherent with the findings reported by (Ragland et al., 1991). These authors have claimed that wood ash generally comprises 40-70 % calcium oxide and 10-30 % potassium oxide (Ragland et al., 1991). The comparison of the ICP-AES and XRF results revealed remarkable differences in terms of oxides percentages. Furthermore, in contrast to ICP-AES, XRF allowed the determination of the sodium oxide (Na_2O) content and LOI in the samples.

The sum of $SiO_2 + Al_2O_3 + Fe_2O_3$ for each biomass ash analysed was lower than 30 %, whereas SO_3 varied from 0.75 to 18.20 %. The loss on ignition (LOI) also referred to as quantity of unburned carbon remaining in the sample, corresponded to 15.69 % for WFA8 and 15.52 % for WFA9. These values were within the range of 1-36 % reported by (Berra et al., 2015; Hassan et al., 2019; Omran et al., 2018; Sigvardsen et al., 2021b).

(g) Portlandite consumption of the wood fly ash WFA8

The pozzolanic activity of WFA8 was determined using a modified Chapelle test as described in section 3.2.7. Two and nine replicates were made for blank test (only CaO) and WFA8 + CaO solution, respectively. The average portlandite consumption was 352 $Ca(OH)_2$ mg/g of WFA8.

(h) pH measurements

According to Behnood et al. (2016), pH is a negative logarithm of the concentrations of active hydrogen ions. It indicates the level of acidity and alkalinity of a given solution. Etiégni et Campbell (1991) stated that the alkalinity of wood ash depends on carbonate, bicarbonate and

hydroxide content. It was also indicated that carbonates and bicarbonates are more abundant at temperatures below 500 °C, while oxides become more common at temperatures greater than 1000 °C. Given that the mineral raw materials were produced at different temperatures, it was interesting to compare their pH. Ten samples including OPC, NHL and eight biomass ashes, were considered and the obtained results are given in Table 3-5.

Table 3-5. pH of mineral raw materials.

Sample	Average pH
OPC	12.6 ± 0.1
NHL	12.7 ± 0.0
WFA1	12.9 ± 0.1
WFA2	12.8 ± 0.1
WFA3	12.6 ± 0.2
WBA	11.4 ± 0.1
WSA	12.7 ± 0.0
WFA7	10.9 ± 0.1
WFA8	12.8 ± 0.0
WFA9	12.8 ± 0.0

It is apparent that most of the biomass ashes had comparable pH to that of OPC and NHL. The lowest pH was obtained from WFA7, while WFA1 was the most alkaline. Globally, the pH of the biomass ashes varies from 10.9 to 12.9, which is in good agreement with the findings reported in the literature. Indeed, wood biomass ashes are highly alkaline with a pH varying between 9 and 13.5 (Carević et al., 2020; Dahl et al., 2010; Elinwa and Ejeh, 2004; Etiégni and Campbell, 1991; Mivière, 2008; Siddique, 2012; Sigvardsen et al., 2021b).

The high pH values obtained from some biomass ashes batches such as WFA1, WFA2, WFA8 and WFA9 can be ascribed to the presence of highly alkaline compounds such as potassium hydroxide (KOH) and sodium hydroxide (NaOH) (Gori et al., 2011).

(i) Morphological and microstructural characteristics of biomass ashes

The morphology and microstructure of the biomass ashes were examined thanks to a JEOL JSM-IT100 scanning electron microscopy (SEM), as described in section 3.2.12. From Figure 3-7, it is evident that all biomass ash samples have mostly irregular, spherical and fibrous shapes. The irregular shape of WFA3 and WBA particles is mainly due to grinding. Moreover, despite the grinding, these two wood ashes still had a higher fraction of coarse particles than the other biomass ashes. Apart from that, a number of unburned wood chips were noticed among the wood fly ash samples, including WFA1, WFA2, WFA8, and WFA9.

Magnifications: ×100 ⟶ ×500

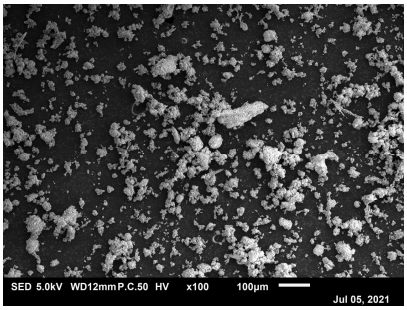

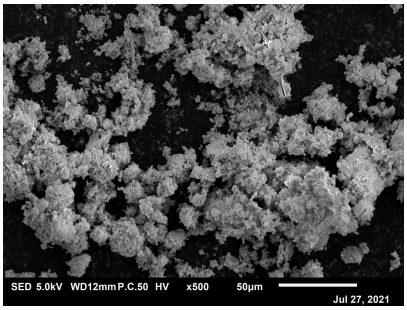

WFA1

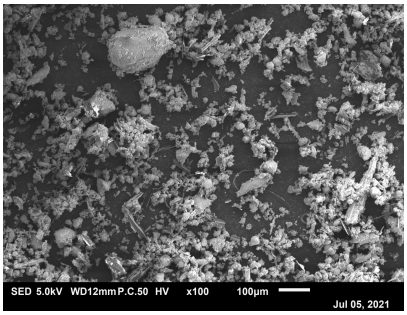

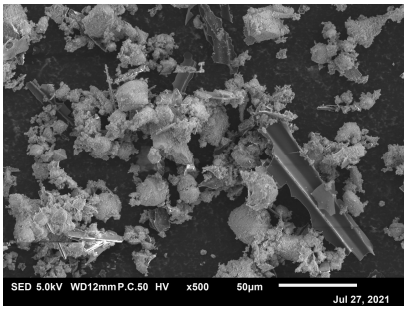

WFA2

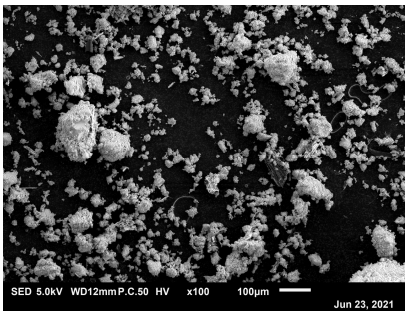

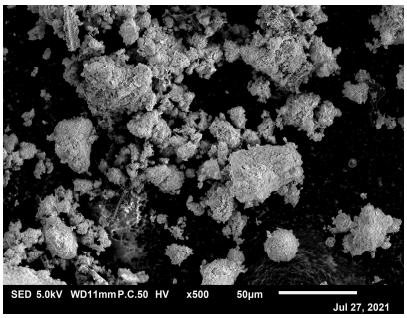

WFA3

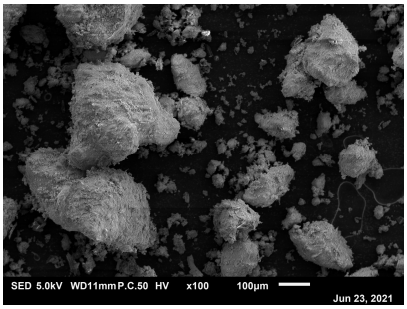

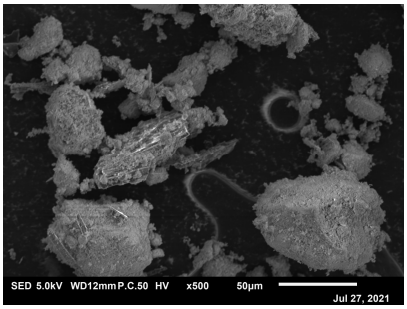

WBA

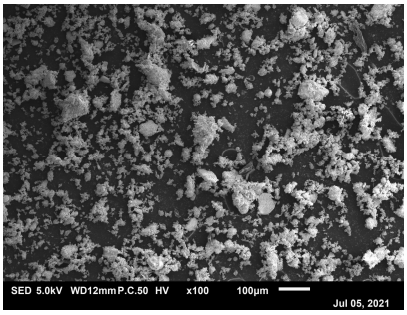

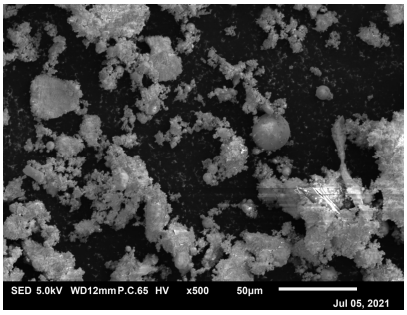

WSA

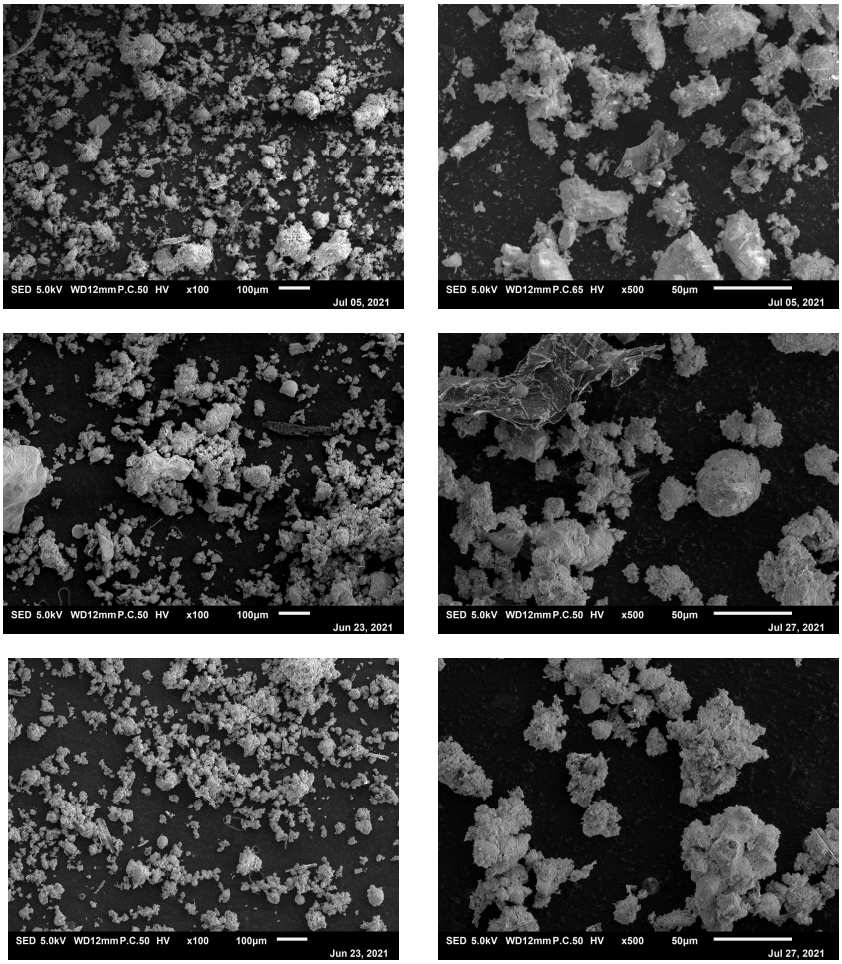

Figure 3-7. SEM micrographs of different biomass ashes studied. The scanning conditions are given below each micrograph.

(j) Microstructural characteristics

The thermogravimetric analysis (TGA) allowed to study the microstructural composition of the mineral raw materials used in this research. This analysis was performed according to the method explained in section 3.2.13. As shown on Figure 3-8 (a, b), the reaction products were identified based on the temperature ranges in which they decomposed.

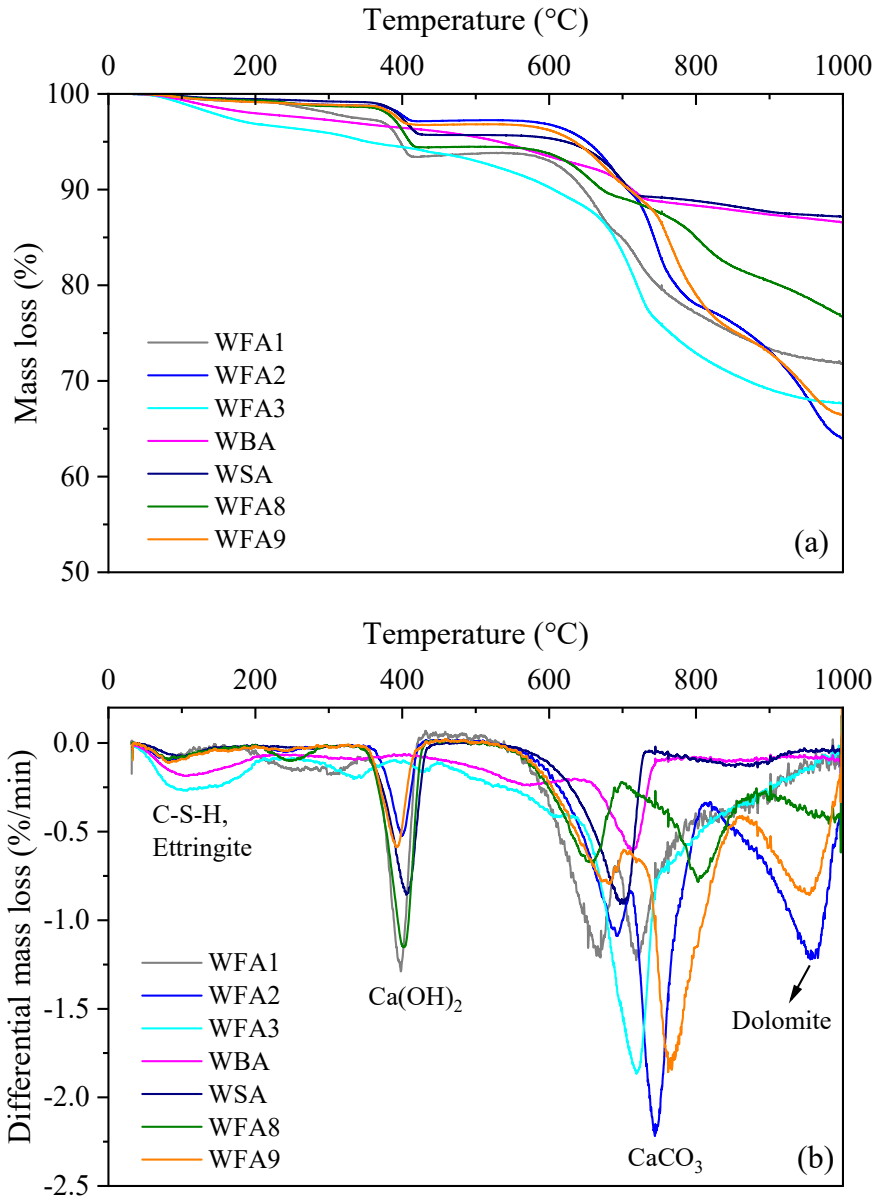

Figure 3-8. TGA curves of some biomass ashes.

Four main endotherms were observed in the samples. The mass loss occurring at 25-200 °C was attributed to evaporation of free water, and decomposition of C-S-H and ettringite. This peak was more pronounced in WFA3 and WBA. The second peak was observed at 350-450 °C and was due decomposition of portlandite. This endotherm was present in all analysed samples, excluding WFA3 and WBA. It is important to note that the most $Ca(OH)_2$ mass loss was observed in WFA1 and WFA8. The large and deep endotherm at 500-800 °C indicated the decomposition of $CaCO_3$. It was detected in all samples but the highest intensities were seen on WFA2, WFA3 and WFA9. Finally, the endotherm at 850-1000 °C can be explained by the decomposition of dolomite (Földvári, 2011; Samtani et al., 2002).

(k) Mineralogical composition

The crystalline components in biomass ashes, NHL, and OPC were identified with X-ray diffraction analysis (XRD) as described in section 3.2.14. From Figure 3-9, it can be seen that the intensity of the peaks of the identified components varies with respect to the analysed material. In general, the crystalline compounds found in OPC and NHL were also detected in some lots of biomass ash but with different contents. On the other hand, the components such as arcanite, dolomite, sylvite, larnite or belite, diopside, etc. were only observed in biomass ash.

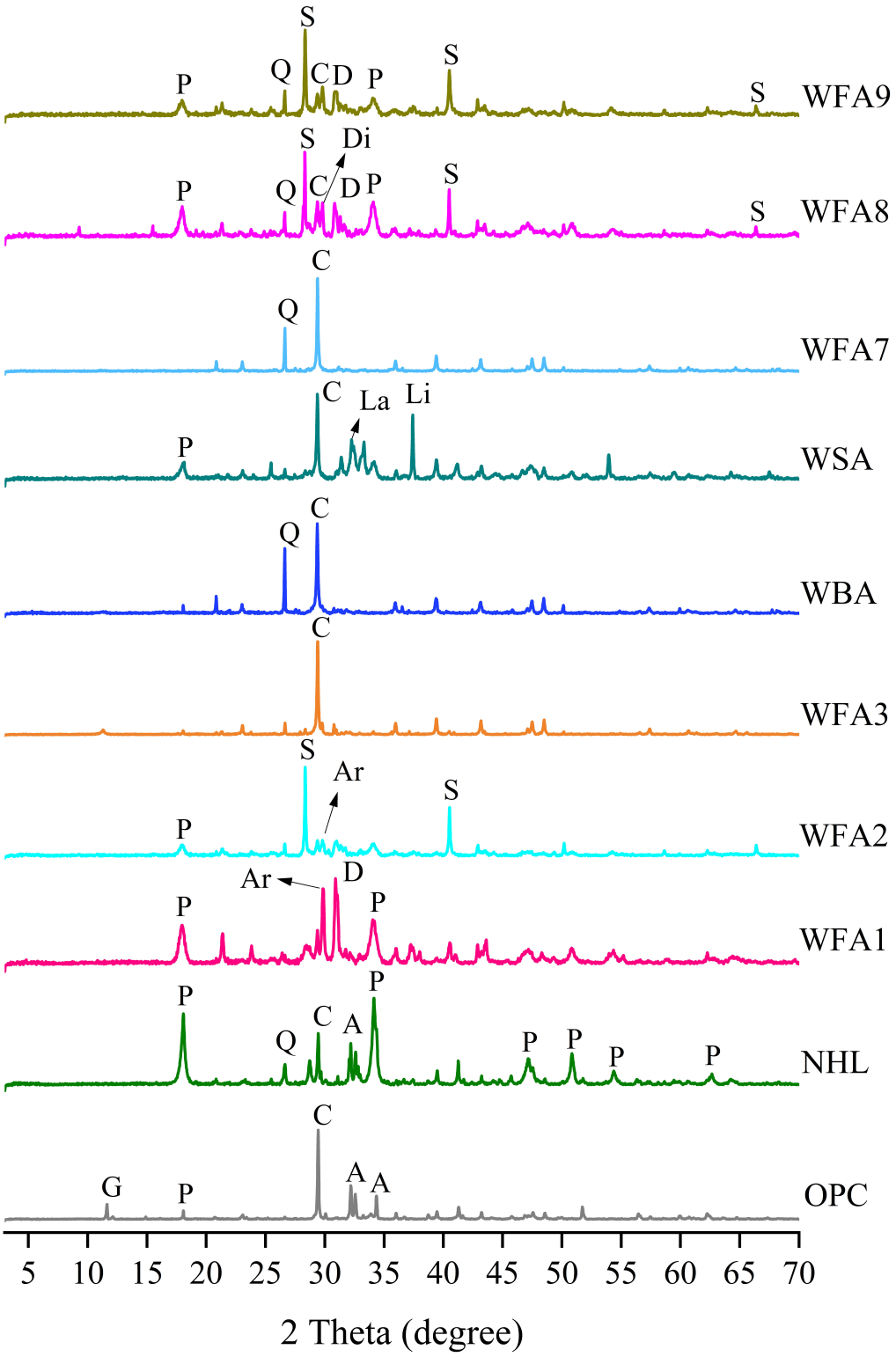

Figure 3-9. XRD patterns of the mineral raw materials: OPC, NHL and eight biomass ashes. Note : G Gypsum; P Portlandite; C Calcite; A Alite; Q Quartz; Ar Arcanite; D Dolomite; S Sylvite; La Larnite; Li Lime; Di Diopside.

Furthermore, all crystalline compounds that occurred in the analysed samples are listed in Table 3-6. It is obvious that the mineralogical composition of the raw mineral materials varies from one to another. The wood fly ashes received in the dry state tend to have a similar crystalline composition. Apart from calcite and quartz which were present in all analysed samples, the potassium-containing compounds such as arcanite, sylvite and syngenite were only found in the wood fly ashes, particularly WFA1, WFA2, WFA3, WFA8 and WFA9.

Major contents of arcanite were seen in WFA1, WFA2 and WFA3, whereas syngenite was dominant in WFA2 and WFA8. Sylvite which is a highly water-soluble compound was most abundant in WFA2, WFA8 and WFA9 but minimally prevalent in WFA1 and WFA3. Major concentrations of dolomite were observed in these aforementioned fly ashes, excluding WFA3. Other than that, it should be noted that WFA3 was the only sample which contained variscite.

Table 3-6. Crystalline compounds in OPC and NHL compared with all biomass ashes used in this study.

Compound	OPC	NHL	WFA1	WFA2	WFA3	WBA	WSA	WFA7	WFA8	WFA9
Albite $NaAlSi_3O_8$			++	++	++	++	++	++	++	++
Alite Ca_3SiO_5	++	++	++			++		++	++	++
Alunite $KAl_3(SO_4)_2(OH)_6$		++		++						
Anhydrite $CaSO_4$							++			++
Antigorite-T $Mg_3(Si_2O_5)OH_4$	++									
Arcanite K_2SO_4			++	++	++					
Calcite $CaCO_3$	++	++	++	++	++	++	++	++	++	++
Diopside $MgCaSi_2O_6$									++	
Dolomite $CaMg(CO_3)_2$			++	++			+		++	++
Ettringite $Ca_6Al_2(SO_4)_3(OH)_{12}\cdot 26H_2O$									+	
Gehlenite $Ca_2Al(AlSi)O_7$							++			
Goethite FeO(OH)							+			+
Gypsum $CaSO_4\cdot H_2O$	++									
Hematite Fe_2O_3							+			
Larnite or Belite Ca_2SiO_4							++			
Lime CaO		+	+	+			++			
Microcline $KAlSi_3O_8$		++	++	++			++			
Orthoclase $KAlSi_3O_8$						++			++	
Periclase MgO			+	+					+	++
Portlandite $Ca(OH)_2$	+	++	++	+	+	++	+		++	++
Quartz SiO_2	Trace	++	+	+	+	++	+	++	+	++
Sylvite KCl			+	++	+				++	++
Syngenite $K_2Ca(SO_4)_2\cdot H_2O$				++					++	
Variscite $AlPO_4\cdot 2H_2O$					++					

Note: ++: major compounds and +: minor compounds.

Apparently, albite was broadly available in all biomass ashes. In addition, all samples contained portlandite was present in all samples, apart from WFA7. The major levels of portlandite were specifically detected in NHL, WFA1, WBA, WFA8 and WFA9. Furthermore, it was noticed that quartz was present in all evaluated powders. In fact, the highest quantities of quartz were spotted in NHL, WBA, WFA7 and WFA9.

Comparing OPC to NHL, it is clear that both materials typically consist of similar crystalline phases. Nevertheless, there were certain phases that were observed in OPC that were not seen in NHL and vice versa. For example, OPC contains antigorite-T and gypsum while these compounds are not present in NHL. Apart from that, major amounts of alunite and microcline

were observed in NHL while these compounds were not seen in OPC. it was also noticed that the level of quartz in NHL was relatively greater than that in OPC.

It should be pointed out that the mineralogical composition of WSA more complex than that of wood ashes, OPC or NHL. In fact, it contained a large number of phases than other samples and was the only sample to contain major levels of gehlenite and larnite. At the same time, it was also rich in lime and microcline.

3.3.2 Sunflower pith and bark

(a) Particle size distribution

The particle size distribution (PSD) of sunflower pith and bark was measured with two methods: image processing and sieve analysis, as previously stated in section 3.2.1. The 2D image analysis method allowed the determination of the PSD of the sunflower particles based on the dimensions of analysed particles. The protocol employed in this research is described as follows:

- A number of particles were randomly sampled from different locations in the container;
- Use of a Keyence camera to acquire images;
- The adjustment of brightness of the acquired images was realized by selecting "Threshold" (black & white);
- After the adjustment of brightness, the images were converted to 8-bit type;
- Then, ImageJ software was used to count sunflower particles and calculate their morphological characteristics including length, width and area. "Threshold" (black & white) was selected to adjust the pictures, whereas the minimum particle area was set at 0.08 mm^2 to eliminate fibres and dust;
- The obtained PSD results were treated and were presented in form of a line graph and histogram.

The particle size distribution of sunflower pith (SP) and bark (SB) used in this study is shown in Figure 3-10. The major and minor axes refer to the length and width of the particles, correspondingly. The length of SB was greater than SP. Whereas, the width of SB was smaller than SP. Indeed, the results indicate that the length of SP and SB was in the range of 0.3-18.3 mm and 0.4-26.3 mm, respectively. The width varied from 0.1 to 14.7 mm for SP and from 0.1 to 6.8 mm for SB.

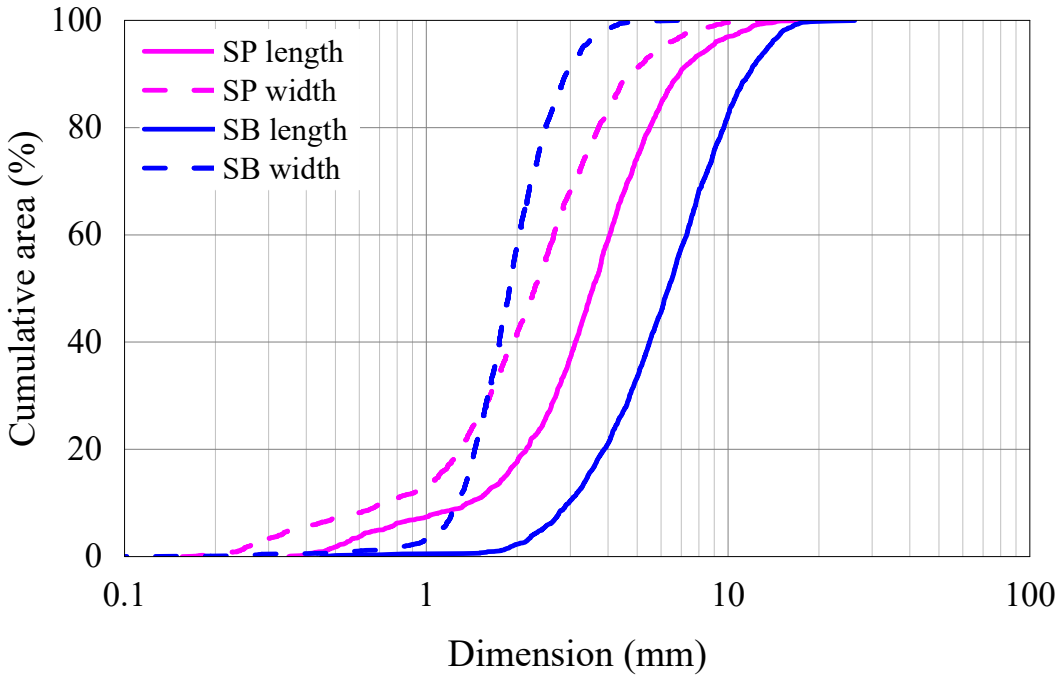

Figure 3-10. Cumulative particle size distribution of sunflower pith and bark by image processing method.

Moreover, the average lengths and widths of the sunflower particles were also calculated and the results are presented in Figure 3-11. As is shown, the average length and width of SP were equal to 4.0 and 2.6 mm, respectively. Meanwhile, for SB, the average length, and width were 6.9 and 2.0 mm, correspondingly.

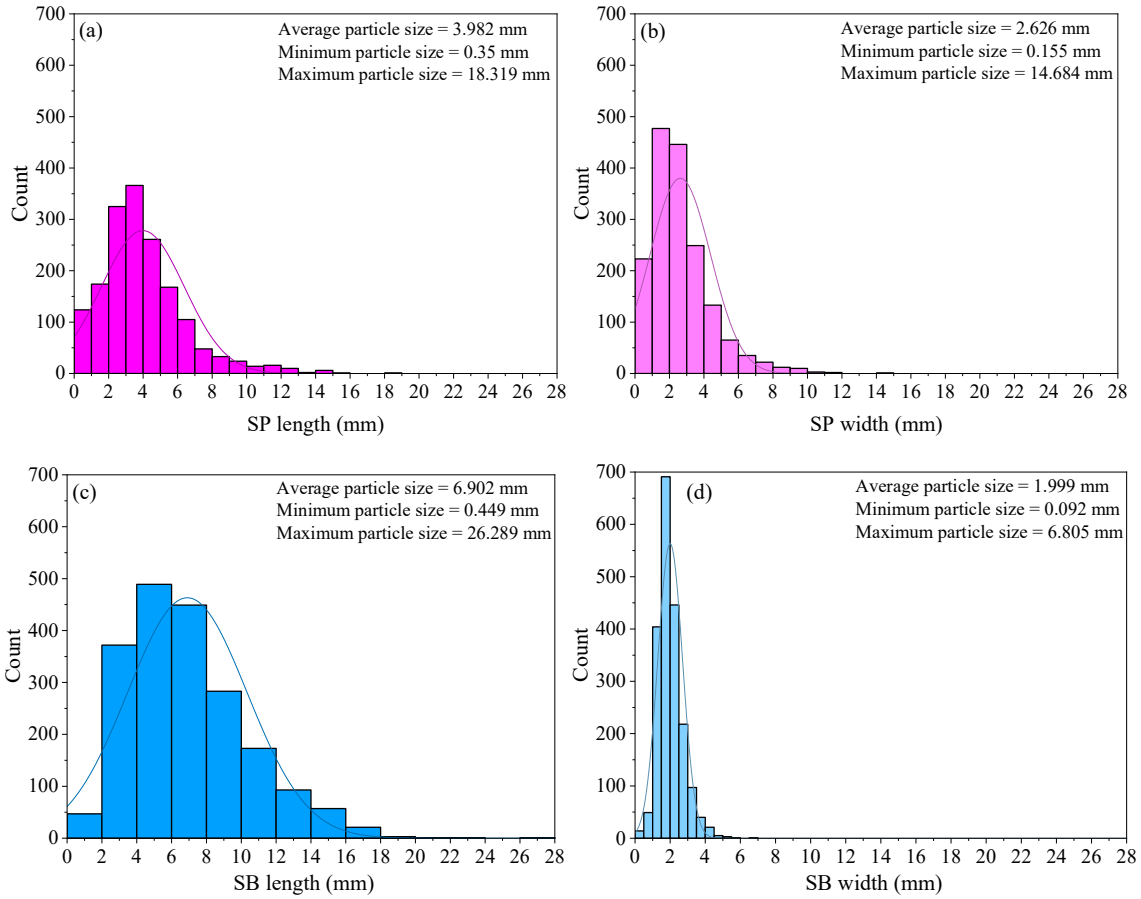

Figure 3-11. Average lengths and widths of (a, b) sunflower pith and (c, d) bark particles.

Furthermore, in contrast to the image processing method, sieve analysis enabled the representation of PSD of sunflower particles relying on the mass of the sample fraction retained on each sieve. The mechanical sieving was carried out on dry SP and SB samples of mass in the range of 30-33.2 g and 200-200.4 g, respectively. Note that the evaluated sunflower particles were previously dried in oven at 60 °C until a constant mass. The apertures of sieves used varied from 10 to 0.25 mm. All the samples were measured in triplicate and the differential particle size distribution results are given in Figure 3-12.

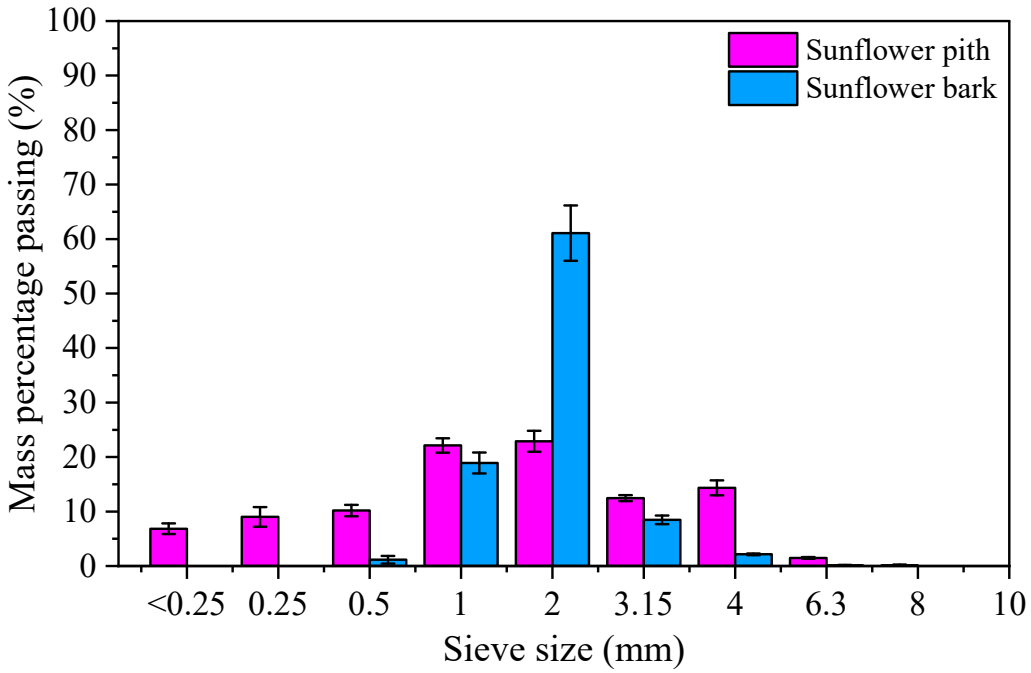

Figure 3-12. Differential particle size distribution of sunflower pith and bark by mechanical sieve analysis.

The sunflower pith particles were dispersed on all series of sieves employed in this experiment. On the contrary, the sunflower bark particles were only observed on the sieves with mesh sizes between 0.5 and 4 mm. It should be mentioned that the sunflower pith retained on the 1 mm and 2 mm sieves represented almost 50 % of the total mass of tested sample. Whilst, the sunflower bark accounting for more than 60 % of the total mass of analysed sample, were held on the 2 mm sieve.

The sunflower pith particles were finer and contained higher dust content than the sunflower bark. The term "dust "refers to all plant particles passing through a 0.25 mm sieve (Amziane and Collet, 2017). According to this definition, the sunflower pith particles had a dust content of approximately 7.8 %, while no dust was found in sunflower bark particles.

(b) Bulk density

The bulk density (ρ) of sunflower bark and pith was determined according to RILEM Technical Committee 236 protocol described in section 3.2.2. The results show that the sunflower pith (SP) evaluated in this study had an average bulk density of 20.63 ± 0.16 kg/m^3 while the bulk densities found in the previous publications vary from 15 to 37 kg/m^3, as shown in Figure 3-13 (a). It should be mentioned that the density measurements were performed on SP samples with a RH of 2.6 %.

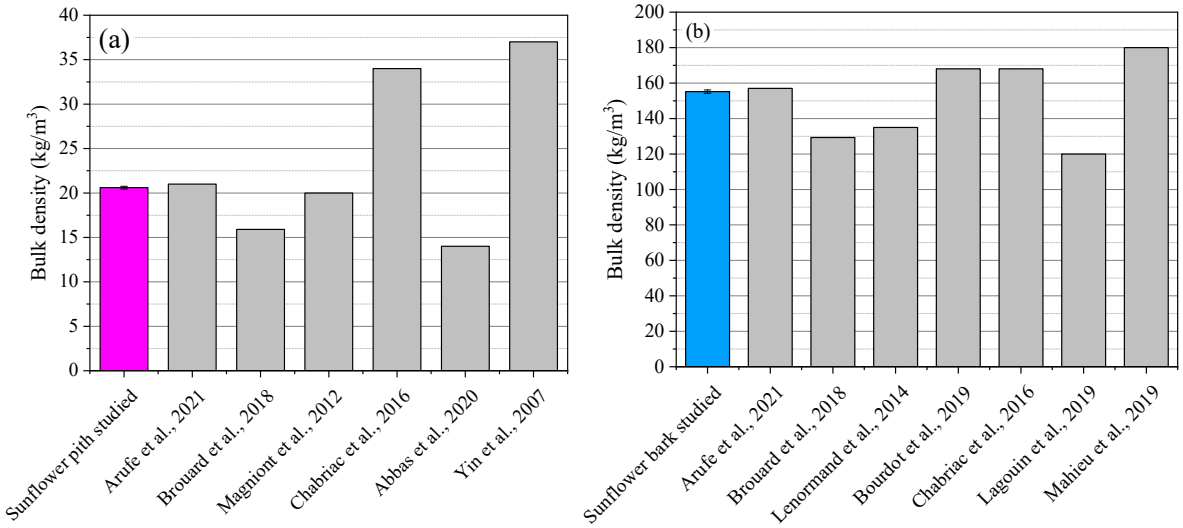

Figure 3-13. Bulk density of sunflower particles: (a) pith and (b) bark.

Similarly, the average bulk density of sunflower bark (SB) valorized in this research study was compared to the data stated in the previous studies. As seen in Figure 3-13 (b), the average bulk density of SB is equal to 155.18 ± 0.95 kg/m^3, which is within the range of 120-180 kg/m^3 reported in the literature. It should be noted that the average relative humidity (RH) of SB prior to testing was 6.4 %.

The literature clearly demonstrates that the bulk density of either SP or SB varies from one study to another. This variability can be explained by numerous factors, including porosity of particles and inter-particular porosity, relative humidity (Amziane and Collet, 2017), measurement methods (Glé et al., 2021), compactness (Amziane and Arnaud, 2013), moisture content, batch of origin, etc.

(c) Skeletal density

The skeletal density of sunflower particles was obtained thanks to a gas pycnometer under an argon atmosphere, as presented in section 3.2.3. The obtained results demonstrate that milling sunflower particles enabled access to more porosity, therefore leading to a significant increment of skeletal density. As given in Table 3-7, the average skeletal density increased from 732 ± 20 to 1029 ± 10 kg/m^3 for sunflower pith (SP) and from 1170 ± 20 to 1542 ± 10 kg/m^3 for sunflower bark (SB).

Table 3-7. Skeletal density and porosity rate of sunflower particles.

Sunflower particles	Average skeletal density (kg/m^3)		θ_{open} (%)	θ_{closed} (%)
	Unground	Ground		
SP	732 ± 20	1029 ± 10	97.1	28.8
SB	1170 ± 20	1542 ± 10	86.2	24.1

A number of studies have reported that the skeletal density of unground sunflower pith, sunflower bark, and hemp shiv varies from 754-3400, 960-1395, and 769-1454 kg/m^3, correspondingly (Abbas, 2021; Arufe et al., 2021; Chabriac et al., 2016; Glé et al., 2021).

Furthermore, knowing the bulk and skeletal densities allowed the determination of open and closed porosity rates of sunflower pith and bark. The calculations were made according to Equation 3-1 and Equation 3-2 presented in section 3.2.4. The findings reveal that sunflower pith exhibits higher open porosity (θ_{open}) and closed porosity (θ_{closed}) than sunflower bark.

(d) Microstructure of the sunflower pith and bark

The observations of the microstructure of sunflower particles were performed with a JEOL JSM-IT100 scanning electron microscopy. Note that the scanning conditions were given in section 3.2.12. As shown in Figure 3-14 (a), sunflower pith consists of parenchymal cells that form a honeycomb or alveolar structure. Besides, Figure 3-14 (b) shows that sunflower bark also comprises parenchymal cells as well as spiral tracheid that make up a vascular structure.

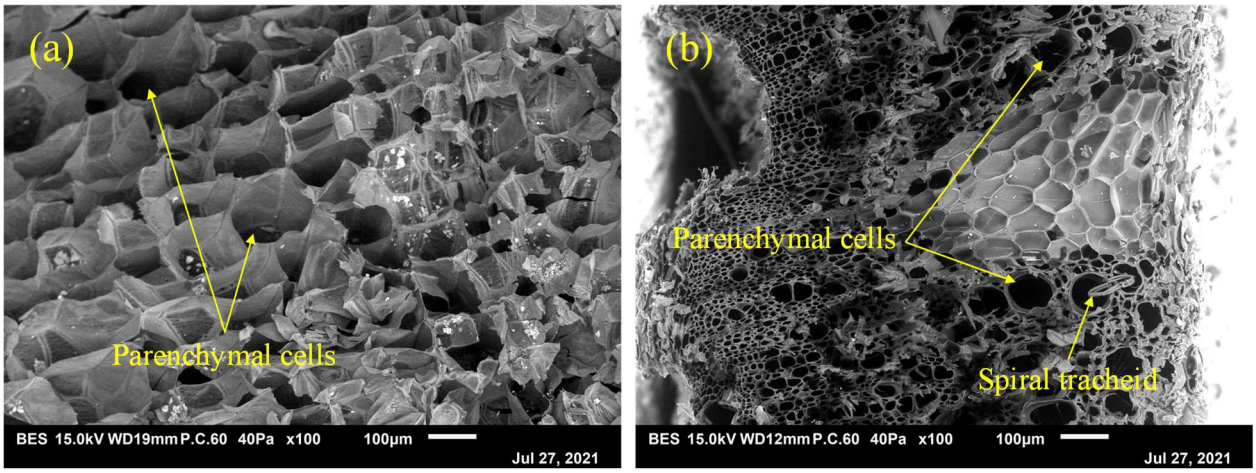

Figure 3-14. Cross sections of sunflower pith (a) and bark (b).

The SEM images proved the high porous structure of sunflower particles. Comparing the cross sections of the sunflower pith (SP) and bark (SB), it is evident that SP comprises large pores with almost identical diameters, while SB is composed of small and large pores. The structure

of sunflower pith contains more voids, which explains the difference in density between these two particles derived from the same plant.

(e) Water absorption capacity

Generally, the absorption of water by plant particles occurs in two phases. The first phase, corresponding to surface absorption, is characterised by the prompt growth of the mass of a given particle due to the large amount of water absorbed by its surface. The second phase referring to the slow water absorption into the plant particle shows the dispersion of the absorbed water into the structure of the particle in 48 h (Mazhoud et al., 2017).

The water absorption capacity of sunflower aggregates was determined according to RILEM TC 236 recommendations as provided in section 3.2.9. The measurements were performed on three different samples of SP and SB of mass 10 and 50 g, respectively. The results indicate that at 5 min, the water absorption of SP and SB was 1305 % and 155 %, correspondingly. Afterwards, at 120 h, SP and SB showed a water absorption of 2017 % and 291 %, respectively, as shown in Figure 3-15.

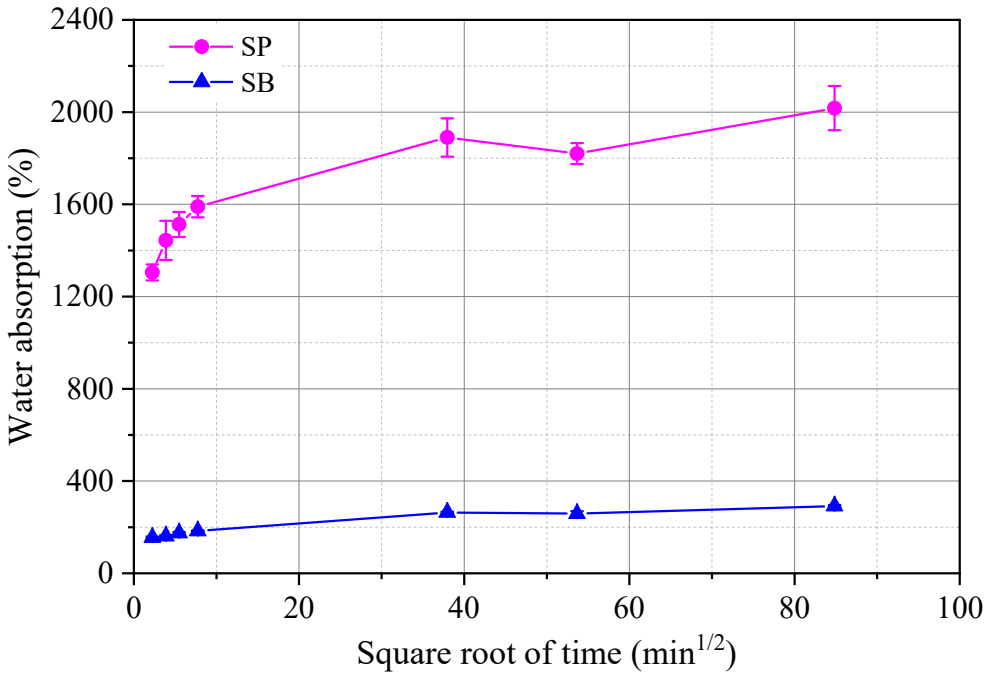

Figure 3-15. Water absorption capacity of sunflower pith and bark.

This high-water absorption rate observed on SP and SB is due to their porous structure which allows them to act as a sponge when soaked in water. As shown in Figure 3-15, the water absorption capacity of SP is much greater than that of SB. Indeed, SP can absorb up to 20 times its weight while SB absorbs about 3 times its weight. It is important to note that the water quantified includes many types of water that occur in the plant particles, like water that is

chemically bound to the sunflower particles and water that is trapped by capillaries in the pores of the sunflower particles.

The water absorption results obtained in this study are coherent with the literature. For example, Magniont et al. (2012) declared that sunflower pith can hold more than nine times its initial weight (917 wt.%), whereas hemp shiv can only retain three times its dry weight (300 wt.%). Moreover, Brouard et al. (2018) measured the water absorption rate of sunflower pith (SP) and bark (SB), and rape straw (RS) under different temperature (T) conditions. At T = 20 °C, the water uptake rate of SP was remarkably higher than that of SB and RS. In fact, after 60 min of immersion, SP absorbed more than 2000 % of its weight, whereas for SB and RS, the water absorption rate was around 300 % and 500 %, respectively.

Furthermore, Lagouin et al. (2019) has also evaluated the sensitivity of the sunflower and maize barks to water. The results showed that sunflower bark (SB) had slightly higher water absorption capacity than maize bark (MB). After 1 min of soaking, SB held 146 % of its mass while MB retained approximately 96 % of its mass.

(f) Water sorption-desorption isotherms

The water sorption isotherms were determined with a dynamic vapour sorption (DVS) method as described in section 3.2.10. At a constant temperature of 23 °C, the moisture content of the samples was observed at a relative humidity of 0, 35, 50, 55, 75 and 85 %. Given the form of adsorption curves obtained from SP and SB, they could belong to Type II sigmoidal isotherms conforming to the IUPAC (International Union of Pure and Applied Chemistry) classification (Sing et al., 1984). It should be mentioned that this type of sigmoidal isotherm was previously chosen by (Collet et al., 2013; Laborel-Préneron et al., 2018b). The findings of this study revealed that the adsorption capacity of SP is significantly higher compared to SB. As a matter of fact, at RH of 86 %, the mass of SP increased by nearly 35 % while SB achieved a mass gain of roughly 25 %, as shown in Figure 3-16.

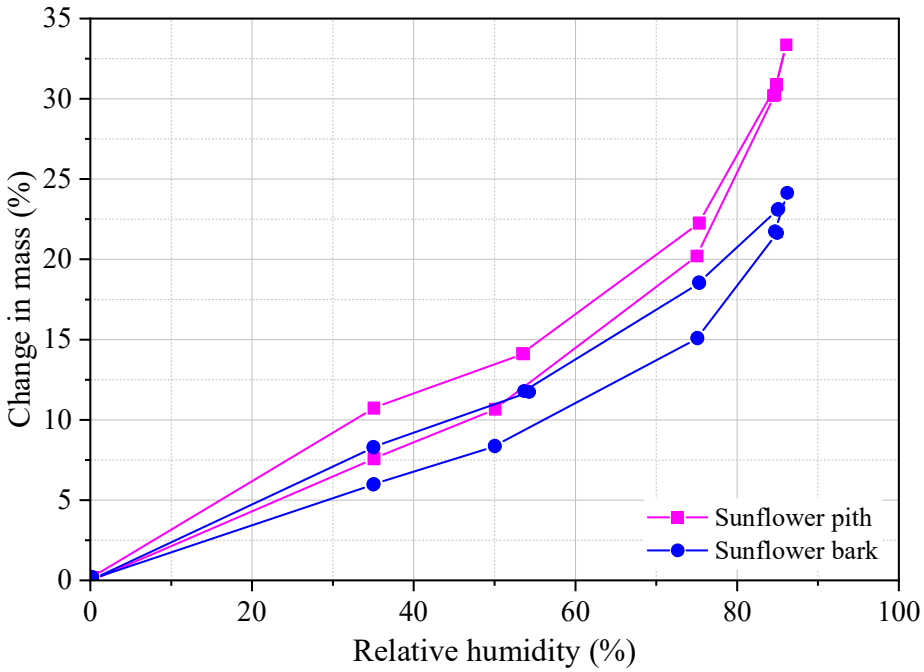

Figure 3-16. Water vapour sorption isotherms of sunflower pith and bark.

(g) Thermal conductivity

The thermal conductivity (λ) of sunflower pith (SP) and bark (SB) was measured with a Heat Flow Meter HFM 446 small/lambda following the protocol described in section 3.2.11. The thermal conductivity of SP was equal to 0.039 ± 0.001 W/m.K and 0.058 ± 0.000 W/m.K for SB. This proves that both sunflower particles have excellent thermal performance. The results obtained in this study are consistent with those found in the literature, as given in Table 3-8. It is clear that the thermal conductivity of plant particles increases with bulk density.

Table 3-8. Comparison of the thermal conductivity of different plant particles.

Reference	Sunflower pith	
	Thermal conductivity λ (W/m.K)	Bulk density ρ (kg/m^3)
Present study	0.039 ± 0.001	20.63 ± 0.16
(Brouard et al., 2018)	0.036	15.6
(Magniont, 2010)	0.051	20
(Abbas et al., 2020)	0.050 ± 0.001	14 ± 4
(Vandenbossche et al., 2012)	0.035	22
	0.042	18
Reference	Sunflower bark	
	λ (W/m.K)	ρ (kg/m^3)
Present study	0.058 ± 0.000	155.18 ± 0.95
(Brouard et al., 2018)	0.053	129.3
(Lenormand et al., 2014)	0.070 ± 0.003	135 ± 3
Reference	Hemp shiv	
	λ (W/m.K)	ρ (kg/m^3)
(Abbas et al., 2020)	0.070 ± 0.006	100 ± 5
(Laborel-Préneron et al., 2018b)	0.051 ± 0.002	153 ± 2
(Lenormand et al., 2014)	0.064 ± 0.008	106 ± 7
(Magniont, 2010)	0.054	134.8
	0.054	164.5

As can be seen, the thermal conductivity and bulk density of sunflower pith range from 0.036-0.051 W/m.K and 14-22 kg/m^3, respectively. On the other hand, the thermal conductivity and bulk density of sunflower bark are reported to be in the range of 0.053-0.07 W/m.K and 129-155 kg/m^3, correspondingly. The thermal performance and density of sunflower bark are close to hemp shiv. As the matter of fact, hemp shiv exhibits a thermal conductivity varying from 0.054 to 0.070 W/m.K while its bulk density is within a range of 100-164 kg/m^3. Furthermore, it is important to underline that the sunflower pith observed relatively lower thermal conductivity and bulk density than sunflower bark and hemp shiv.

(h) Chemical composition of sunflower particles

The proportion of the main chemical components including cellulose, hemicellulose, lignin, ash and soluble compounds in sunflower particles chemical composition were determined in accordance to Van Soest and Wine method as described in section 3.2.6. The sunflower pith (SP) and bark (SB) consist of similar chemical components but in very different proportions. As can be seen in Figure 3-17, the SP is mainly composed by cellulose (37.92 ± 2.62 %),

soluble compounds (37.77 ± 0.41 %) and hemicelluloses (6.38 ± 2.01 %). On the other hand, the major constituents of the SB were cellulose (51.24 ± 0.61 %), hemicelluloses (25.48 ± 1.00 %) and lignin (14.20 ± 0.22 %). The ash content of SP (15.00 ± 0.01 %) was about three times higher than in SB (5.23 ± 0.02 %).

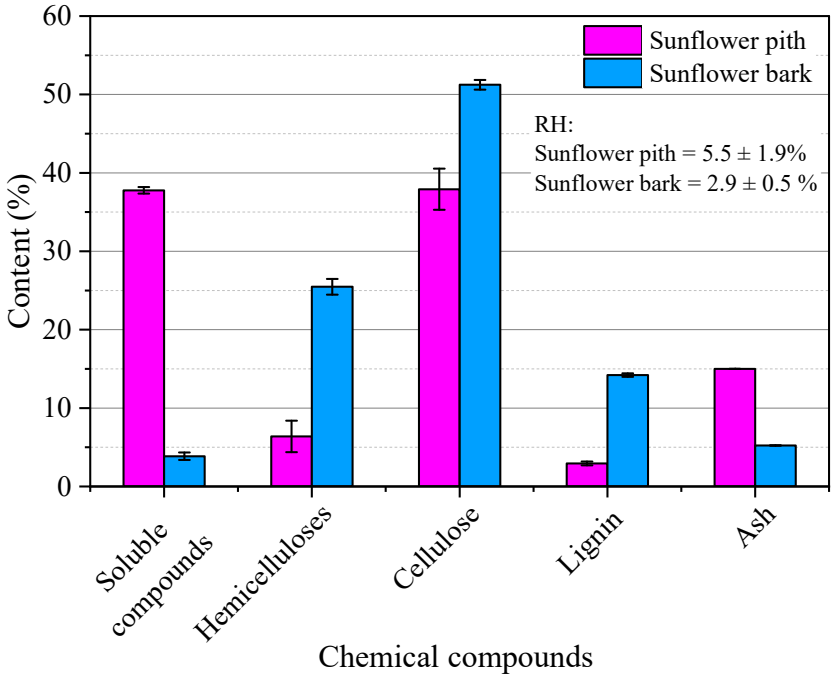

Figure 3-17. Chemical composition of sunflower particles.

Table 3-9 compares the chemical composition results obtained in the present study with those reported in previous works considering not only sunflower pith and bark, but also hemp and flax shives. The sunflower pith has higher soluble compounds and ash contents than sunflower bark, hemp, and flax shiv. On the other hand, the proportions of hemicelluloses and lignin in sunflower pith tend to be significantly lower compared to these other three lignocellulosic plant particles noted earlier.

Table 3-9. Chemical composition of several lignocellulosic plant particles.

	Soluble (%)	Hemicelluloses (%)	Cellulose (%)	Lignin (%)	Ash (%)	Reference
SP studied	37.77 ± 0.41	6.38 ± 2.01	37.92 ± 2.62	2.94 ± 0.23	15.00 ± 0.01	
SB studied	3.86 ± 0.48	25.48 ± 1.00	51.24 ± 0.61	14.20 ± 0.22	5.23 ± 0.02	
Sunflower pith	50.2	5	23	22		(Chabriac et al., 2016)
	38.6 ± 1.1	5.0 ± 1.9	23.3 ± 6.8	21.4 ± 6.4	11.7 ± 0.3	(Arufe et al., 2021)
		4-7	45	3-7	17	(Vandenbossche et al., 2012)
Sunflower bark	8	16	28	46		(Chabriac et al., 2016)
	10.6 ± 0.4	16.8 ± 0.1	46.1 ± 0.2	18.6 ± 0.2	4.9 ± 0.1	(Sabathier et al., 2017)
	6.0 ± 2.2	18.1 ± 2.8	30.3 ± 6.2	41.7 ±8.5	3.8 ± 0.5	(Arufe et al., 2021)
Hemp shiv	17.2 ± 1.1	21.6 ± 1.8	49.0 ± 2.8	8.1 ± 0.6	4.1 ± 1.6	(Arufe et al., 2021)
	17.75 ± 0.51	21.42 ± 0.71	49.97 ± 0.81	9.52 ± 0.11	0.67 ± 0.02	(Viel et al., 2018)
	8.1 - 9.5	16.8 - 18.6	59.4 - 60.8	10.4 - 12.03	2.0 - 2.5	(Glé et al., 2021)
Flax shiv	9.1 ± 1.9	17.6 ± 2.4	43.5 ± 4.7	27.1 ± 4.5	2.7 ± 0.9	(Arufe et al., 2021)
	5,2	19,5	43	32,3		(Mahieu et al., 2019)
	7.56 ± 0.66	24.41 ± 0.64	44.63 ± 0.64	20.98 ± 0.21	1.48 ± 0.16	(Viel et al., 2018)

Furthermore, apart from Van Soest and Wine method, TGA has been used to confirm the presence of hemicelluloses, cellulose and lignin in sunflower particles. These chemical components were quantified in reliance on the temperature range in which their thermal decomposition occurred. Note that TGA was performed as stated in section 3.2.13. The mass loss (TG) and differential mass loss (DTG) curves of the sunflower pith and bark are shown in Figure 3-18 (a) and (b), respectively.

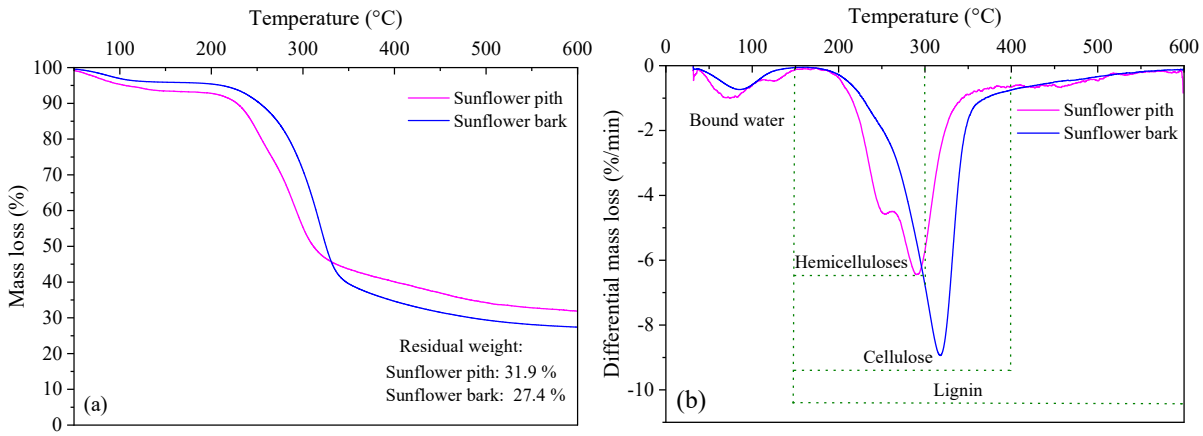

Figure 3-18. TG (a) and DTG (b) curves of the sunflower particles.

The residual mass of the sunflower pith and bark was 31.9 % at 598.9 °C and 27.4 % at 599 °C, respectively. The interpretation of endothermic peaks indicating the degradation of hemicelluloses, cellulose and lignin comprised in sunflower particles, was done according to the data reported in (Antonio-Cisneros and Elizalde-Gonzalez, 2010; Jiang et al., 2019; Mohan et al., 2006; Singh et al., 2009; Stefanidis et al., 2014). The mass loss that appeared between 25 and 150 °C was assigned to evaporation of bound water. The degradation of the sunflower pith and bark started at around 150 °C. The thermal decomposition of hemicelluloses, cellulose and lignin arose at temperature ranges of 150-300 °C, 150-400 °C and 150-600 °C, correspondingly.

(i) pH measurements of the sunflower particles

The acidity or alkalinity of the sunflower particles was measured following the method presented in section 3.2.8. It was vital to know the pH of the raw materials in order to highlight their influence on the alkalinity of the sunflower-based mortars. The obtained results show that the pH of SP and SB is nearly neutral (pH ≈ 7). Indeed, the loose and ground SP exhibited a pH of 7.05 ± 0.01 and 6.92 ± 0.01, respectively. On the other hand, a pH of 7.15 ± 0.02 and 6.92 ± 0.03 was obtained from the loose and ground SB, correspondingly. It is worth mentioning that grinding the sunflower particles resulted in a slight decrease in pH.

Furthermore, the aforementioned findings are in line with the literature. For example, Aggarwal and Singh (1990) have declared that plant fibres extractives are typically acidic in character and this may eventually have a negative effect on the hydration process of cement.

3.4 Conclusion

In this chapter, raw materials, experimental methods and the main properties of the raw materials were presented. At first, the description of the feedstocks, both mineral and bio-based, was made. The mineral materials include eight biomass ashes (six wood fly ashes, one wood bottom ash and one wastepaper sludge ash) and two hydraulic binders, namely natural hydraulic lime and ordinary Portland cement. The bio-based aggregates are sunflower particles, including pith and bark. It is worth noting that the above raw materials are locally supplied and available. Secondly, the experimental methods employed for the characterization of the raw materials were provided and described. Following this, the physical, chemical, microstructural and hygrothermal properties of all collected materials were investigated. However, it should be mentioned that some features were not assessed for WFA1, WFA2, WSA and WFA7 due to their insufficient quantity.

The obtained findings revealed significant differences in the properties of biomass ashes. Regarding the physical characteristics, it is evident that wood fly ashes (WFA1, WFA2, WFA8 and WFA9) received in a dry state comprised finer particles than WFA3, WBA and WFA7 received in a wet state. The bulk density of four considered wood ashes was lower than that of OPC. Also, when compared to NHL, the bulk density of WFA3, WFA8 and WFA9 was lower, while that of WBA was greater.

Other than that, the chemical properties of biomass ashes varied from one ash to another. Nevertheless, the results indicate that all analysed powders are rich in CaO. The SiO_2 content in certain biomass ashes was comparable to that in OPC and NHL. Moreover, it is noteworthy that wood fly ashes contained higher amounts of K_2O and SO_3 compared to other samples. The variability of the chemical composition of biomass ashes can be attributed to feedstock origin, combustion temperatures and technology as well as storage conditions. Apart from that, the pH measurements showed that biomass ashes were highly alkaline (pH = 10.9-12.9). Their pH was comparable to OPC and NHL.

Concerning the microstructure composition, TGA revealed the presence of reaction products such as C-S-H, ettringite, portlandite and carbonates (calcite, dolomite, etc.) in all examined ashes. XRD confirmed the TGA results and identified other crystalline phases (for example: anhydrite, arcanite, sylvite, syngenite, periclase, etc.) in the biomass ashes. Calcite was abundantly available in all analysed powders, whereas albite was only observed in biomass ashes. Furthermore, it was found that the ashes received in a wet state appeared to contain fewer crystalline compounds than ashes received in a dry state.

Regarding sunflower particles, the physical characterization showed that the morphology of the pith and bark was different. Indeed, SP particles tend to be spherical (circular) whereas SB particles were parallelepipedal (rectangular) in shape. In terms of density, the bulk and skeletal densities of SP are relatively lower than SB. For instance, the average bulk density of SP was 20.63 ± 0.16 kg/m^3 while for SB, it was equal to 155.18 ± 0.95 kg/m^3. As for hygrothermal performance, the water absorption capacity of SP was significantly higher than that of SB. Whilst, the thermal conductivity of SB (0.058 ± 0.000) W/m.K appeared to be greater than SP (0.039 ± 0.001) W/m.K. Nevertheless, both particles remain very efficient in terms of thermal insulation performance. These remarkable differences in physical and hygrothermal properties of both sunflower particles, can be explained by the highly porous structure of SP particles.

In terms of the chemical composition, both sunflower particles consist of identical chemical compounds but in different proportions. To illustrate, the level of soluble compounds was nearly 37.8 % in SP, while it was 3.9 % in SB. In addition, the ash content in SP and SB was estimated at 15 % and 5.2 %, respectively. Apart from that, it is also clear that SB was richer in hemicelluloses, cellulose and lignin compared to SP. Indeed, cellulose represented 51.2 % in SB and 37.9 % in SP, whereas hemicelluloses accounted for up to 6.4 % and 25.5 % in SP and SB, correspondingly. Lastly, the fraction of lignin was approximately 2.9 % in SP and 14.2 % in SB. Other than that, it is noteworthy that the pH of both sunflower particles was almost identical and was close to 7.

Chapter 4: Characterization of the binding matrices elaborated with wood ashes

This chapter presents the characterization results of thirty different wood ash pastes developed as potential binding matrices for the sunflower pith mortars and prefabricated sunflower bark building elements. Three wood fly ash (WFA3, WFA8, WFA9) and one wood bottom ash (WBA) are used as the main components of the mixtures, representing 80, 90 and 100 % by mass. In addition, natural hydraulic lime (NHL3.5) and ordinary Portland cement (OPC32.5N) are also incorporated as mineral additives at a ratio of 5, 10 and 20 % (by mass of wood ash).

After preparing the wood ash pastes, the samples will be stored in the laboratory at ambient temperature and humidity conditions. The setting, mechanical, morphological and microstructural properties of the wood ash pastes will be investigated through a series of experimental analyses at different curing ages. After that, the findings will be presented and discussed before drawing the main conclusions.

4.1 Water optimisation for wood ash pastes

As mentioned in the previous chapter, several batches of biomass ashes were collected. However, owing to insufficient quantities of WFA1, WFA2, WSA and WFA7, only the following four wood ashes: WFA3, WBA, WFA8 and WFA9, are considered in this chapter.

The determination of water-to-wood ash (W/A) ratios was crucial because the quantity of mixing water affects the strength development of the materials. Besides that, due to the high variability of wood ashes in water demand, it is essential to evaluate their behaviour before their application in pastes, mortars, concretes, prefabricated building elements, etc.

It is worth noting that, at the time of preliminary strength tests, the ashes that were available included WFA1, WFA2, WFA3, WBA, WSA and WFA7. However, despite the availability of WFA3 and WBA, we could not perform the mechanical tests on them because their samples were fragile. It was difficult to hold or move these samples without breaking them. At 28 days, the obtained compressive strength results showed that WFA1 and WFA2 pastes exhibited better strength development than other ashes. Hence, more quantities of these two ashes were supplied and the newly received wood fly ashes were designated WFA8 and WFA9, and replaced WFA1 and WFA2, respectively.

Numerous wood ash pastes were prepared using W/A ratios ranging from 0.40 to 0.70. In order to monitor the mechanical performance of the wood ash pastes over time, the compressive strength was measured at 3, 7, 14 and 28 days. The optimum water-to-wood ash ratios were selected based on the 28-day compressive strength (R_c) of the wood ash paste samples and the texture of their fresh pastes. The evaluated samples had small dimensions 10×10×60 mm^3 to limit the amount of material used. Figure 4-1 presents the R_c results obtained from WFA1, WFA2, WSA and WFA7 pastes.

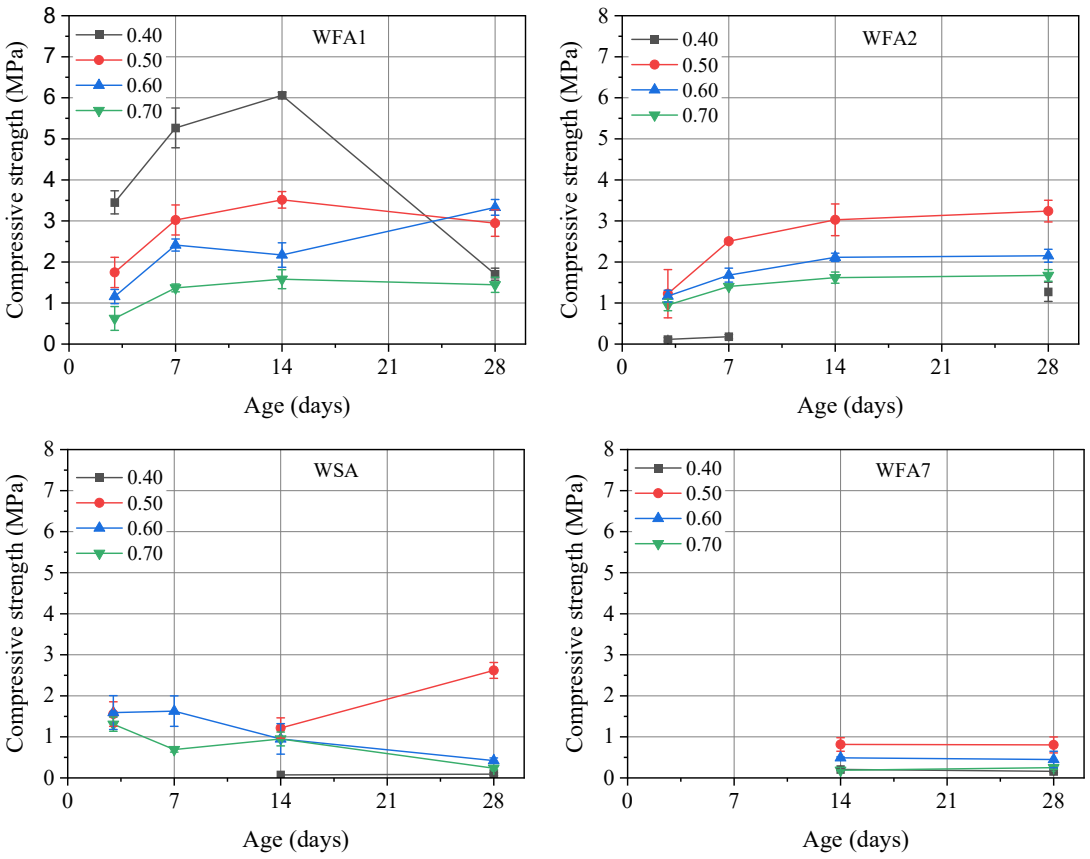

Figure 4-1.Compressive strength results of WFA1, WFA2, WSA and WFA7 pastes.

On the other hand, considering the large amount of WFA3 and WBA available, the interest to study the effect of the treatment they underwent (neutralisation by water) and that of the particle size on the mechanical properties, it was decided to continue the assessment of these two batches. The objective was to see if mixing them with lime or cement could improve the mechanical properties.

WFA8 and WFA9 are not seen in Figure 4-1 because we received them after the completion of preliminary mechanical tests. Thus, their water demand and that of WFA3 and WBA were estimated based on the texture of their fresh pastes, as shown in Table 4-1.

Table 4-1. Water-to-ash ratios and comments on the texture of fresh pastes.

	Remarks on the texture of fresh pastes			
W/A ratio	WFA3	WBA	WFA8	WFA9
0.40	Ashes are in excess compared to water; it is impossible to formulate the samples.		Cohesive, very sticky mixture with a low workability	
0.50	Ashes in excess compared to water, difficult to formulate the samples		Cohesive and very sticky mixture with a good workability	
0.60	Ashes in excess compared to water, a mixture with low workability	Ashes in excessive quantity compared to water, difficult to formulate the samples	Cohesive and very sticky mixture with a high flowability	
0.70	Good workability, easy to formulate the samples	Good workability, easy to prepare the samples	Cohesive and very sticky mixture with a high flowability	
Particle size (µm)	1-1000*	1-1000*	0.1-1000	

*Where *: particle size after grinding.*

The fresh WFA8 and WFA9 pastes obtained using a W/A ratio of 0.40 were stiff, non-flowable and had a significant amount of unhydrated ash. For WFA3 and WBA pastes, the W/A ratios of 0.40, 0.50 and 0.60 were insufficient as the pastes were powdery and friable. The W/A of 0.70 was adequate for WFA3 and WBA while too high for the other biomass ashes studied. The texture of WFA8 and WFA9 fresh pastes was very sticky and cohesive, in contrast to WFA3 and WBA pastes, which had a non-sticky and non-cohesive texture.

The W/A ratios that provided the homogenous pastes with good workability and flowability were 0.50 for WFA8 and WFA9 and 0.70 for WFA3 and WBA. It is worth noting that these selected W/A ratios are within the range of 0.48-1.50 suggested by (Illikainen et al., 2014; Ohenoja et al., 2016).

4.2 Composition of wood ash pastes

Three batches of wood fly ash and one wood bottom ash were used as the main constituents of the binding matrices. Moreover, natural hydraulic lime and ordinary Portland cement were added as mineral additives to improve the mechanical properties of the pastes. In general, two binary systems were proposed:

i. Wood ash + Natural hydraulic lime (NHL);
ii. Wood ash + Ordinary Portland cement (OPC).

The wood ash accounted for 80, 90, 95 and 100 %, while the amount of NHL and OPC was 5, 10 and 20 % by mass of wood ash, as shown in Table 4-2, Table 4-3 and Table 4-4.

Table 4-2. Composition of the control pastes.

Mix notation	Paste composition	W/NHL and W/OPC ratios	W/A ratio
NHL100	100 % NHL	0.5	
OPC100	100 % OPC	0.35	
WFA3-100	100 % WFA3		0.7
WBA-100	100 % WBA		0.7
WFA8-100	100 % WFA8		0.5
WFA9-100	100 % WFA9		0.5

Where A (wood ash); W (water).

Table 4-3. Composition of the wood ash pastes incorporated with natural hydraulic lime.

	Mix notation	Paste composition	W/A ratio
Pastes with natural hydraulic lime	WFA3-NHL5	95 % WFA3 + 5 % NHL	0.7
	WBA-NHL5	95 % WBA + 5 % NHL	0.7
	WFA8-NHL5	95 % WFA8 + 5 % NHL	0.5
	WFA9-NHL5	95 % WFA9 + 5 % NHL	0.5
	WFA3-NHL10	90 % WFA3 + 10 % NHL	0.7
	WBA-NHL10	90 % WBA + 10 % NHL	0.7
	WFA8-NHL10	90 % WFA8 + 10 % NHL	0.5
	WFA9-NHL10	90 % WFA9 + 10 % NHL	0.5
	WFA3-NHL20	80 % WFA3 + 20 % NHL	0.7
	WBA-NHL20	80 % WBA + 20 % NHL	0.7
	WFA8-NHL20	80 % WFA8 + 20 % NHL	0.5
	WFA9-NHL20	80 % WFA9 + 20 % NHL	0.5

Table 4-4. Composition of wood ash pastes blended with ordinary Portland cement.

	Mix notation	Paste composition	W/A ratio
Pastes with ordinary Portland cement	WFA3-OPC5	95 % WFA3 + 5 % OPC	0.7
	WBA-OPC5	95 % WBA + 5 % OPC	0.7
	WFA8-OPC5	95 % WFA8 + 5 % OPC	0.5
	WFA9-OPC5	95 % WFA9 + 5 % OPC	0.5
	WFA3-OPC10	90 % WFA3 + 10 % OPC	0.7
	WBA-OPC10	90 % WBA + 10 % OPC	0.7
	WFA8-OPC10	90 % WFA8 + 10 % OPC	0.5
	WFA9-OPC10	90 % WFA9 + 10 % OPC	0.5
	WFA3-OPC20	80 % WFA3 + 20 % OPC	0.7
	WBA-OPC20	80 % WBA + 20 % OPC	0.7
	WFA8-OPC20	80 % WFA8 + 20 % OPC	0.5
	WFA9-OPC20	80 % WFA9 + 20 % OPC	0.5

According to Table 4-2, Table 4-3 and Table 4-4, the water demand for WFA3 and WBA is significantly higher than for WFA8 and WFA9. This is due to higher porosity, loss in the ignition (LOI) and irregular particle shape of WFA3 and WBA (Ohenoja et al., 2016; Wang et al., 2008). The water demand of the pastes was highly dependent on the type of wood ash used.

4.3 Preparation of wood ash pastes

An automatic standard mortar mixer (Controlab) pre-programmed according to NF EN 196-1 (Afnor, 2016), was used to mix the materials. The dry materials were first weighed with a digital scale (accuracy: ± 0.01 g), then placed in the mixing bowl and mixed with tap water. The water-to-ash ratio (W/A) was 0.5 for the pastes containing WFA8 and WFA9 and 0.7 for the pastes made of WFA3 and WBA. The water-to-cement and water-to-lime ratios adapted in the preparation of the reference pastes composed of 100 % OPC, and 100 % NHL were 0.35 and 0.5, respectively. The mixing sequence is shown in Table 4-5.

Table 4-5. Mixing sequence.

Step	Speed (rpm)	Time (s)
Weighing of dry materials (wood ash, OPC, NHL)	-	-
Introduction of the dry materials	-	-
Introduction of the water	-	
Mixing at a low speed	140	60
Mixing at a high speed	285	30
Short break - scraping the bowl	-	30
Long break	-	60
Mixing at a high speed	285	60
Cumulative mixing time (breaks included)	-	240

Note: rpm (round per minute); s (second).

The mixtures were compacted using the Proctor normal energy test. This method has been previously used by (Hussain et al., 2022; Seifi et al., 2019). The compaction was applied to improve the density and strength of the wood ash pastes. The Proctor compaction procedure is described as follows:

- The height of fall (h) was fixed at 178.8 mm;
- A wooden plate of length and width identical to the sample was placed on top of the fresh mixture to facilitate the compaction;
- The fresh mixture was filled up to 2/3 of the mould, and then, this layer was compacted by striking seven times per lap. In other words, 42 strokes and six laps were made to complete the compaction of the first layer;
- After the completion of the first layer compaction, we added on top of it a mould increase, and then, we re-introduced the fresh mixture in the mould to form the second layer;
- The compaction of the second layer was done similarly to the previous layer. This means that a total of 84 strokes were applied for each sample.

The Proctor compaction energy used was 600.3 kN.m/m^3 (Seifi et al., 2019), and it was computed according to Equation 4-1:

$$E_P = \frac{N_S \times N_L \times M \times g \times h}{V} \qquad \text{Equation 4-1}$$

where E_P: Proctor compaction energy per volume; N_S: number of strokes (42 for samples intended for use in mechanical tests or 185 for samples to be used in thermal conductivity tests); N_L: number of

layers (2); M: mass of the moving device (1.043 kg); g: standard gravity acceleration (9.81 m/s^2); h: height of fall (0.1788m); V: volume of the mould (0.000256 for samples intended for use in mechanical tests or 0.001125m^3 for samples to be used in thermal conductivity tests).

Furthermore, the steel moulds of size 40×40×160 mm^3, a feeding hopper and two wood pieces were also used to prepare the wood ash pastes, as shown in Figure 4-2. Also, oil was applied to the moulds to facilitate the demoulding of the samples and protect them from corrosion.

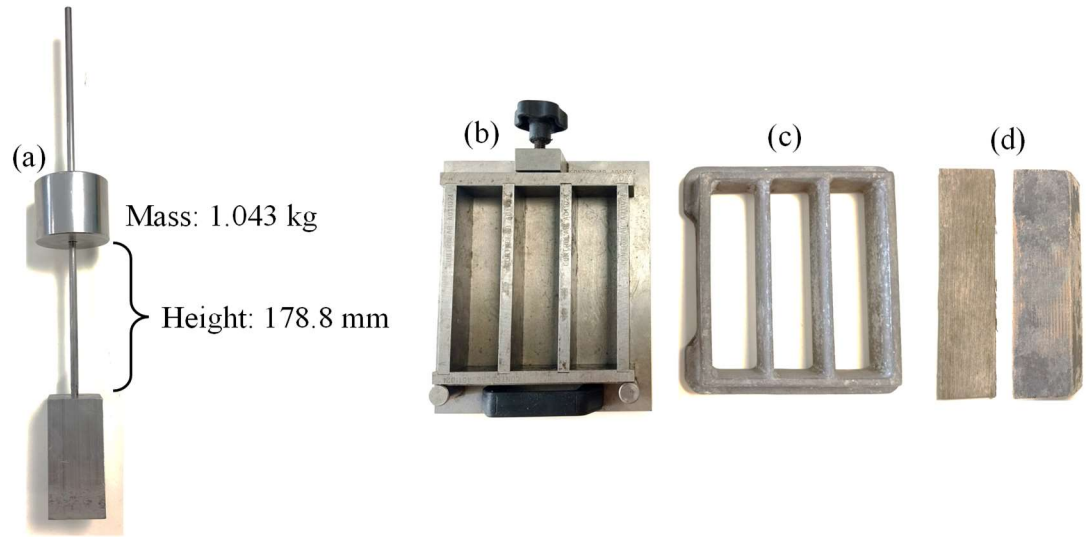

Figure 4-2. Tools used in the preparation of the samples. (a) falling mass (b) mould (c) feeding hopper (d) wood pieces.

After moulding, the samples were placed in the laboratory, and after 24 h, they were demoulded and dried at ambient temperature and relative humidity conditions until the required curing age.

4.4 Experimental methods

4.4.1 Initial and final setting time

The main objective of this experiment was to evaluate the ability of wood ash to harden in contact with water. Owing to the prolonged setting and time constraints, only WFA8 was assessed. The measurements have been performed on the WFA8 pastes blended with natural hydraulic lime (NHL) and ordinary Portland cement (OPC) using manual Vicat apparatus. The NHL or OPC content was 5, 10 and 20 % by mass of WFA8.

The samples were prepared following the mixing sequence described in Table 4-5. After mixing, the fresh pastes were poured into three plastic truncated cone-shaped moulds (height 40 mm, diameter 60 mm at the top and 70 mm at the bottom) and placed on glass plates. The samples' initial and final setting time was determined according to (NF EN 196-3, 2017). The initial setting time was obtained when the needle penetration depth was 35 mm. The final

setting time was reached when the needle could not pierce the paste to greater than 0.5 mm or when the needle penetrated the paste and made a light impression on the surface. At the same time, circular attachment has not done so.

4.4.2 Mechanical properties

The mechanical properties of the wood ash pastes were assessed with a hydraulic press machine (Shimadzu, model AGS-X) at a loading rate of 0.5 mm/min. The three-point flexural strength test was carried out on the prismatic samples of dimensions 40×40×160 mm^3. The half prisms obtained from the flexural strength test were cut with a Bosch metal saw into cubic pieces of sizes 40×40×40 mm^3. The obtained cubes were then used to measure the compressive strength. Both strength parameters were determined at 7, 14 and 28 days. For each formulation, three samples were tested in the flexural strength test, while three or four samples were considered in the compressive strength test. Figure 4-3 and Figure 4-4 show typical examples of samples under flexural and compressive strength tests.

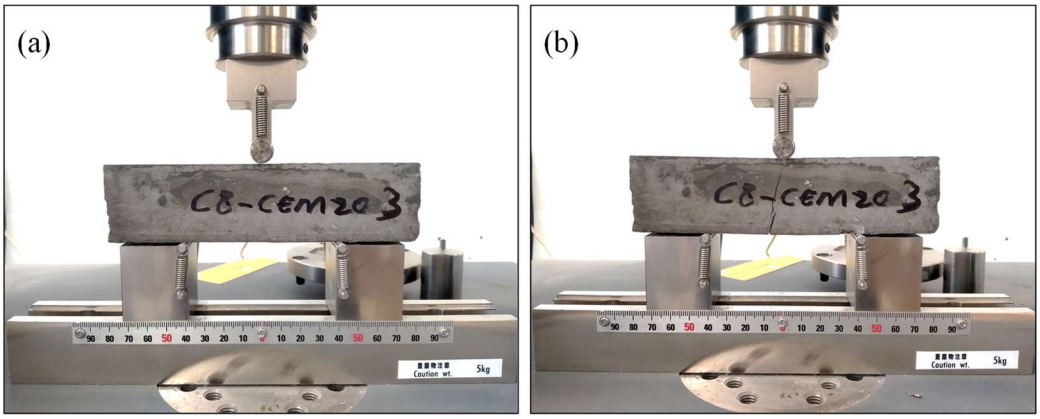

Figure 4-3. A typical WFA8-OPC20 sample under flexural strength test: (a) at the beginning and (b) at the end of the test.

The flexural strength (R_f) was calculated according to Equation 4-2.

$$R_f = \frac{1.5 \times F_{fmax} \times l}{b \times h^2} \qquad \text{Equation 4-2}$$

where F_{fmax}: maximum load applied to the prismatic sample at rupture (N); l: the distance between the supports (mm); b: width of the sample (mm); h: height of the sample (mm).

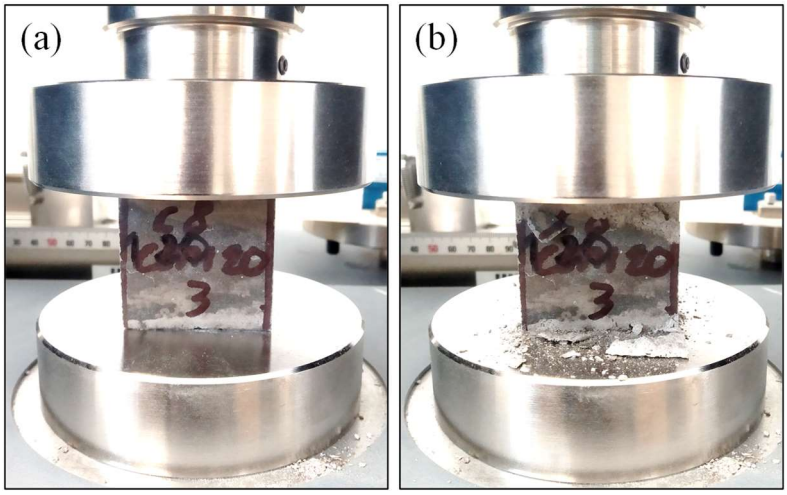

Figure 4-4. A typical WFA8-OPC20 sample under compressive strength test: (a) at the beginning (b) at the end of the test.

Whilst, the compressive strength (R_c) was computed based on Equation 4-3.

$$R_c = \frac{F_{cmax}}{A} \qquad \text{Equation 4-3}$$

where F_{cmax}: maximum load applied on the sample at rupture (N); A: the area of the contact surface of the sample (mm^2). So, Rc is expressed in MPa.

Before each test, the mass and dimensions of the samples were measured using a digital scale (accuracy: ± 0.01 g) and a digital caliper, respectively. These data were then used to calculate the wood ash pastes' bulk density, flexural strength and compressive strength.

4.4.3 Morphological characteristics

A JEOL JSM-IT100 scanning electron microscopy (SEM) was used to study the morphology of the wood ash pastes at 28 days. The analysis was carried out on ground samples, and the observations were made in a high-vacuum (HV) model using a secondary electron detector (SED) with an energy of 5kV and a distance (WD) of 12 mm.

4.4.4 Thermogravimetric analysis

A NETZCH-TG 209 F1 was employed to evaluate the evolution of the wood ash paste hydration products. The thermogravimetric analysis (TGA) was performed on ground samples at 7 and 28 days at a heating rate of 10 °C/minute under an argon atmosphere in a dynamic heating interval ranging from 25 to 1000 °C. One measurement was made for each sample.

4.4.5 Mineralogical characteristics

The crystalline compounds in some wood ash pastes were identified by a Bruker D8 Advance x-ray diffractometer (XRD) at 28 days. This equipment had a 2 Theta (θ) configuration, used

a copper anode Cu Kα radiation generator (λ = 1.540 Å) and was equipped with a LynxEye OD detector. The double diffraction angle (2θ) ranged from 3 to 70 with a step size of 0.015° and an acquisition speed of 0.5 seconds per step. The scanning graphs were treated using DIFFRAC.EVA software.

The samples' preparation was done according to RILEM TC-238 SCM recommendation on hydration stoppage by solvent exchange (Snellings et al., 2018). A wood ash paste was preliminary ground into a powder with a maximum particle diameter of less than 50 µm. Then, a powdered paste sample with a mass of about 100 g was soaked into isopropanol and stirred for 15-30 minutes.

Subsequently, the suspension was carefully filtered with a Büchner filter. In addition, about 20 mL of isopropanol (1×) and 20 mL of diethyl ether (2×) were used to rinse the residue from the glass beaker. The treated wood ash paste sample was dried for 8 min ± 30 sec in a Memmert-ventilated oven at 40 ± 5 °C. After drying, the wood ash paste samples were stored in two desiccators containing silica gel and soda lime to prevent carbonation until the time of analysis.

4.5 Results and discussion

4.5.1 Wood ash pastes containing natural hydraulic lime

(a) Initial and final setting times

The setting of WFA8 pastes containing 5, 10 and 20 % natural hydraulic lime (NHL) by mass of WFA8 was studied. It can be observed from Figure 4-5 and Table 4-6 shows that the WFA8 pastes have longer setting time than the reference NHL100. The addition of 5-20 % NHL content significantly reduced the setting time of the pastes.

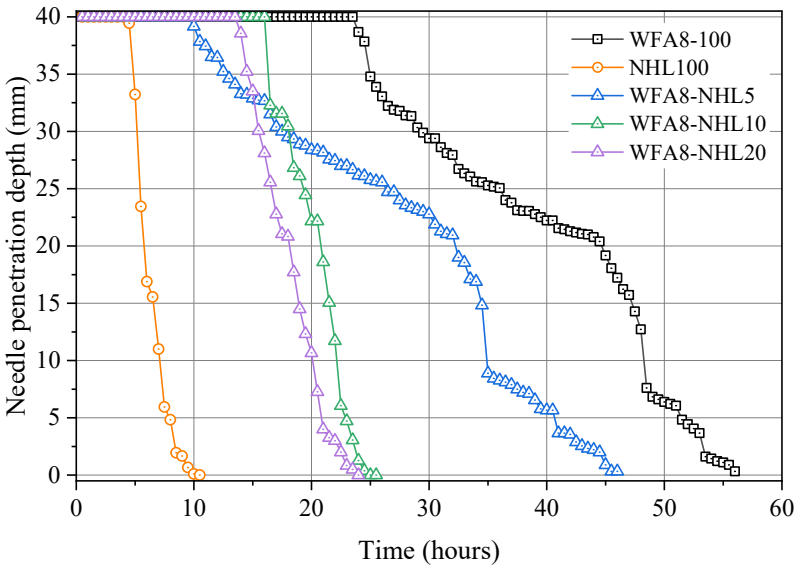

Figure 4-5. Setting time of WFA8 pastes containing natural hydraulic lime.

Table 4-6. Initial and final setting time data.

Mix notation	Initial setting time (hours)	Final setting time (hours)
NHL100	4.5	10
WFA8-100	25	56
WFA8-NHL5	12.5	46
WFA8-NHL10	16.5	25
WFA8-NHL20	14.5	24

The initial setting time was reduced from 25 hours for WFA8-100 to 12.5, 16.5 and 12.5 hours for WFA8 pastes containing 5, 10 and 20 % NHL, respectively. Similarly, the final setting time declined from 56 hours for WFA8-100 to 46, 25 and 24 hours for the WFA8 pastes comprising 5, 10 and 20 % NHL, simultaneously.

(b) Flexural strength

The flexural strength (R_f) results from the pastes made of wood ashes and natural hydraulic lime at 7, 14 and 28 days are presented in Figure 4-6 (a, b, c, d) and Table 4-7. As can be seen, wood ash pastes show lower flexural strength than NHL100. Significantly changes in R_f have been observed between 7 and 14 days. In this period, some mixtures show a rapid growth in R_f, while for other pastes, such as WFA3-NHL20, WBA-NHL (5, 10, 20) and WFA9-NHL10, it dropped slightly. No substantial variations in R_f have been noticed from 14 to 28 days.

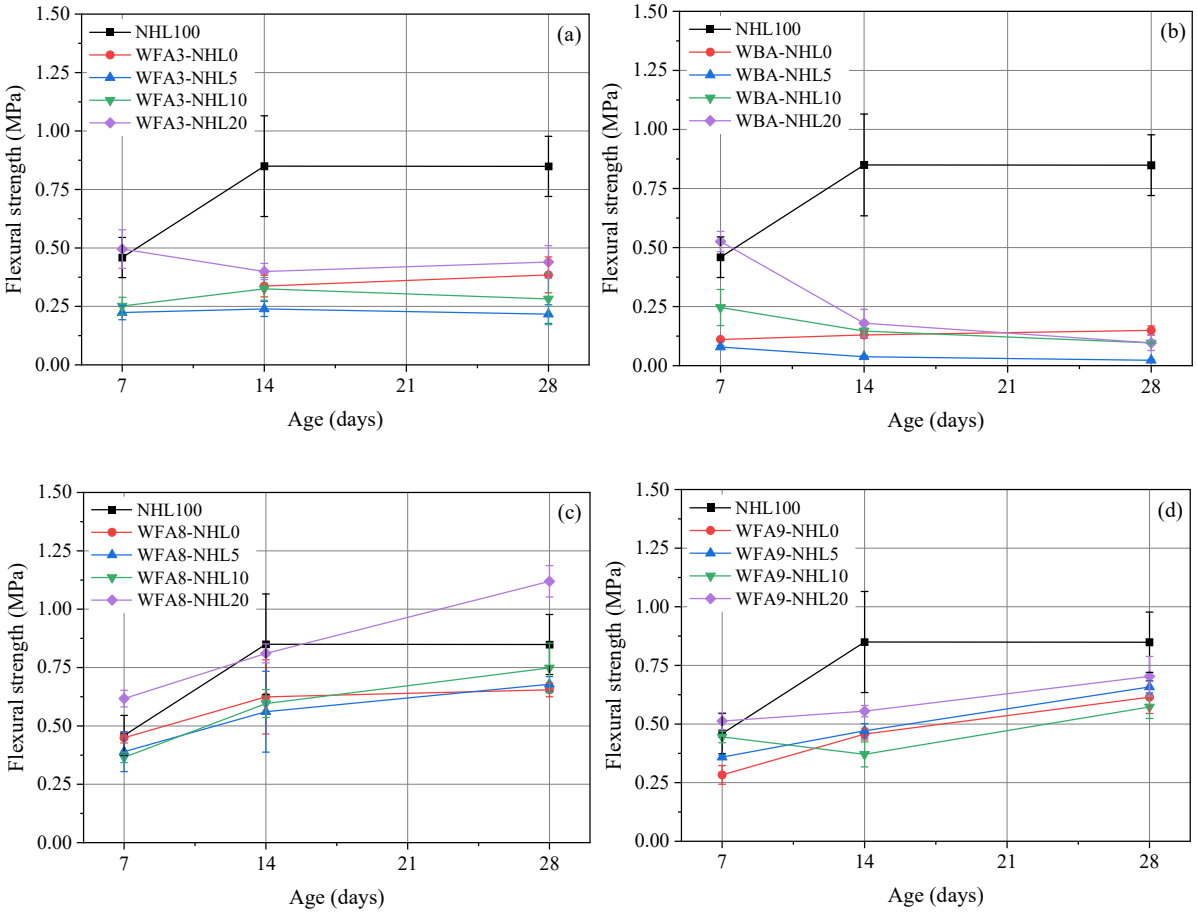

Figure 4-6. Flexural strength of wood ash pastes containing different percentages of NHL at 7, 14 and 28 days: (a) WFA3; (b) WBA; (c) WFA8; (d) WFA9.

The trend in flexural strength for WFA8 and WFA9 pastes increased gradually with time, while for WFA3 pastes, it seemed to remain somewhat stable. Regarding the WBA pastes, the flexural strength increased with the increase in NHL percentages. However, their trend in R_f appeared to decrease slightly with time.

Table 4-7. Flexural strength data of all wood ash-NHL pastes.

Mix notation	Flexural strength (MPa)		
	7 days	14 days	28 days
NHL100	0.46 ± 0.09	0.85 ± 0.22	0.85 ± 0.13
WFA3-NHL0		0.34 ± 0.05	0.38 ± 0.08
WFA3-NHL5	0.22 ± 0.03	0.24 ± 0.03	0.22 ± 0.04
WFA3-NHL10	0.25 ± 0.04	0.32 ± 0.05	0.28 ± 0.11
WFA3-NHL20	0.50 ± 0.08	0.40 ± 0.03	0.44 ± 0.07
WBA-NHL0	0.11 ± 0.00	0.13 ± 0.01	0.15 ± 0.02
WBA-NHL5	0.08 ± 0.01	0.04 ± 0.00	0.02 ± 0.00
WBA-NHL10	0.25 ± 0.08	0.15 ± 0.01	0.10 ± 0.00
WBA-NHL20	0.53 ± 0.04	0.18 ± 0.06	0.10 ± 0.03
WFA8-NHL0	0.45 ± 0.02	0.62 ± 0.16	0.65 ± 0.03
WFA8-NHL5	0.39 ± 0.09	0.56 ± 0.17	0.68 ± 0.03
WFA8-NHL10	0.37 ± 0.02	0.60 ± 0.06	0.75 ± 0.11
WFA8-NHL20	0.62 ± 0.04	0.81 ± 0.04	1.12 ± 0.07
WFA9-NHL0	0.28 ± 0.04	0.46 ± 0.03	0.61 ± 0.07
WFA9-NHL5	0.36 ± 0.01	0.47 ± 0.03	0.66 ± 0.03
WFA9-NHL10	0.45 ± 0.02	0.37 ± 0.05	0.57 ± 0.05
WFA9-NHL20	0.51 ± 0.04	0.55 ± 0.02	0.70 ± 0.08

Overall, the addition of NHL positively affected the flexural strength of the wood ash pastes. 5 and 10 % NHL content showed minor and moderate effects on the R_f values of the wood ash pastes. On the contrary, a more pronounced impact has been noted on the pastes containing 20 % NHL. At 28 days, the average flexural strength of wood ash pastes was in the range of:

- 0.38 MPa (WFA3-NHL0) and 0.44 MPa (WFA3-NHL20) for WFA3-NHL pastes;
- 0.02 MPa (WBA-NHL5) and 0.15 MPa (WBA-NHL0) for WBA-NHL pastes;
- 0.65 MPa (WFA8-NHL0) and 1.12 MPa (WFA8-NHL20) for WFA8-NHL pastes;
- 0.57 MPa (WFA9-NHL10) and 0.70 MPa (WFA9-NHL20) for WFA9-NHL pastes.

(c) Compressive strength

The compressive strength (R_c) results of the wood ash-NHL pastes are provided in Figure 4-7 (a, b, c, d) and Table 4-8. Globally, the wood ash pastes had considerably lower compressive strength than NHL100, except WFA3-NHL20. The average 28-day compressive strength of wood ash pastes ranged between:

- 0.92 MPa (WFA3-NHL0) and 2.59 MPa (WFA3-NHL20) for WFA3-NHL pastes;
- 0.05 MPa (WBA-NHL5) and 0.24 MPa (WBA-NHL0) for WBA-NHL pastes;
- 0.77 MPa (WFA8-NHL0) and 1.82 MPa (WFA8-NHL20) for WFA8-NHL pastes;
- 0.72 MPa (WFA9-NHL0) and 0.96 MPa (WFA9-NHL20) for WFA9-NHL pastes.

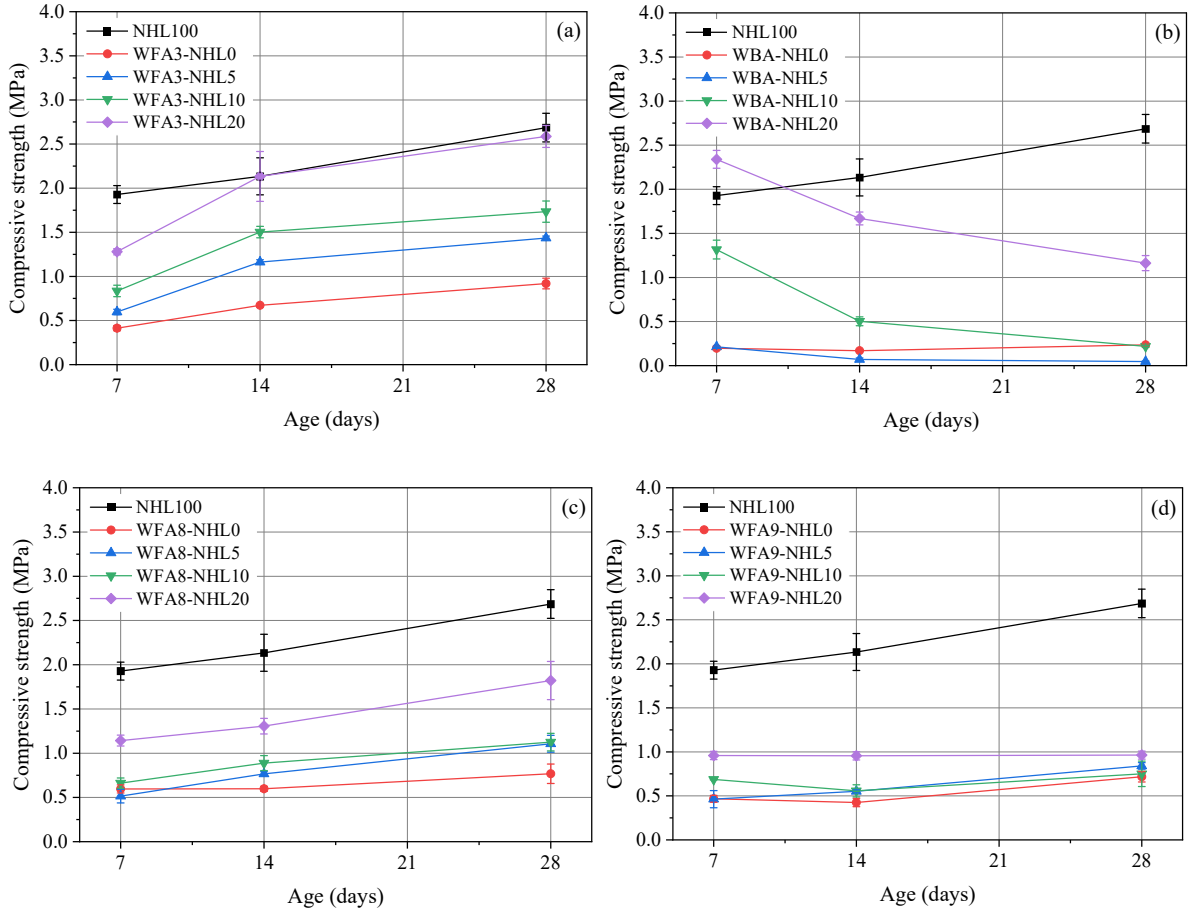

Figure 4-7. Compressive strength of wood ash pastes containing different percentages of NHL at 7, 14 and 28 days: (a) WFA3; (b) WBA; (c) WFA8; (d) WFA9.

The presence of NHL in the wood ash pastes favourably influenced their compressive strengths, except for WBA-based pastes. The compressive strength of WFA3, WFA8, and WFA9 pastes increased with increasing NHL content and curing time, except for WFA9-NHL20, which remained relatively unchanged over time.

On the contrary, WBA-NHL10 and WBA-NHL20 pastes exhibited a reduction in R_c as the curing time increased. This behaviour was also seen in the flexural strength of these pastes and can be explained by the fact that WFA3 and WBA had already reacted during their first contact with water. When these two batches of wood ashes were used for paste preparation, it was the second time they had been hydrated.

Apart from that, it is also speculated that the slow evaporation of mixing water may have left cavities within the pastes that progressively increased and weakened the pastes as the curing time increased.

Table 4-8. Compressive strength data of all wood ash-NHL pastes.

Mix notation	Compressive strength (MPa)		
	7 days	14 days	28 days
NHL100	1.93 ± 0.10	2.13 ± 0.21	2.69 ± 0.16
WFA3-NHL0	0.41 ± 0.03	0.67 ± 0.02	0.92 ± 0.06
WFA3-NHL5	0.60 ± 0.03	1.16 ± 0.03	1.43 ± 0.02
WFA3-NHL10	0.83 ± 0.06	1.50 ± 0.06	1.73 ± 0.12
WFA3-NHL20	1.28 ± 0.03	2.13 ± 0.28	2.59 ± 0.12
WBA4-NHL0	0.20 ± 0.02	0.17 ± 0.01	0.24 ± 0.01
WBA4-NHL5	0.21 ± 0.01	0.07 ± 0.02	0.05 ± 0.01
WBA4-NHL10	1.32 ± 0.11	0.50 ± 0.05	0.22 ± 0.01
WBA4-NHL20	2.34 ± 0.10	1.67 ± 0.07	1.16 ± 0.09
WFA8-NHL0	0.60 ± 0.05	0.60 ± 0.03	0.77 ± 0.11
WFA8-NHL5	0.51 ± 0.08	0.77 ± 0.02	1.11 ± 0.10
WFA8-NHL10	0.66 ± 0.06	0.89 ± 0.02	1.13 ± 0.10
WFA8-NHL20	1.14 ± 0.06	1.31 ± 0.09	1.82 ± 0.22
WFA9-NHL0	0.47 ± 0.04	0.42 ± 0.05	0.72 ± 0.06
WFA9-NHL5	0.46 ± 0.10	0.55 ± 0.02	0.84 ± 0.04
WFA9-NHL10	0.69 ± 0.01	0.56 ± 0.07	0.75 ± 0.14
WFA9-NHL20	0.96 ± 0.05	0.96 ± 0.05	0.96 ± 0.05

In general, the increment in compressive strength of wood ash-NHL pastes is due to NHL hydration and pozzolanic reactions of wood ashes. On the contrary, the lower R_c observed on WFA3 and WBA pastes can be attributed to the weak reactivity of these ashes because it was the second time they were hydrated. It should also be noted that the physical properties of WFA3 and WBA, such as coarse particles, high porosity and irregular particle shape, may have contributed to their poor mechanical performance.

Furthermore, the compressive strength improvement coefficient (Ci_{Rc}) was calculated based on Equation 4-4 and the obtained results are presented in Figure 4-8.

$$Ci_{Rc} = \frac{Rc_{7,14,28}}{Rc_7} \qquad \text{Equation 4-4}$$

where Ci_{Rc}: coefficient of improvement of compressive strength; $Rc_{7,14,28}$: the compressive strength of the wood ash pastes at 7, 14 and 28 days; Rc_7: the compressive strength at 7 days.

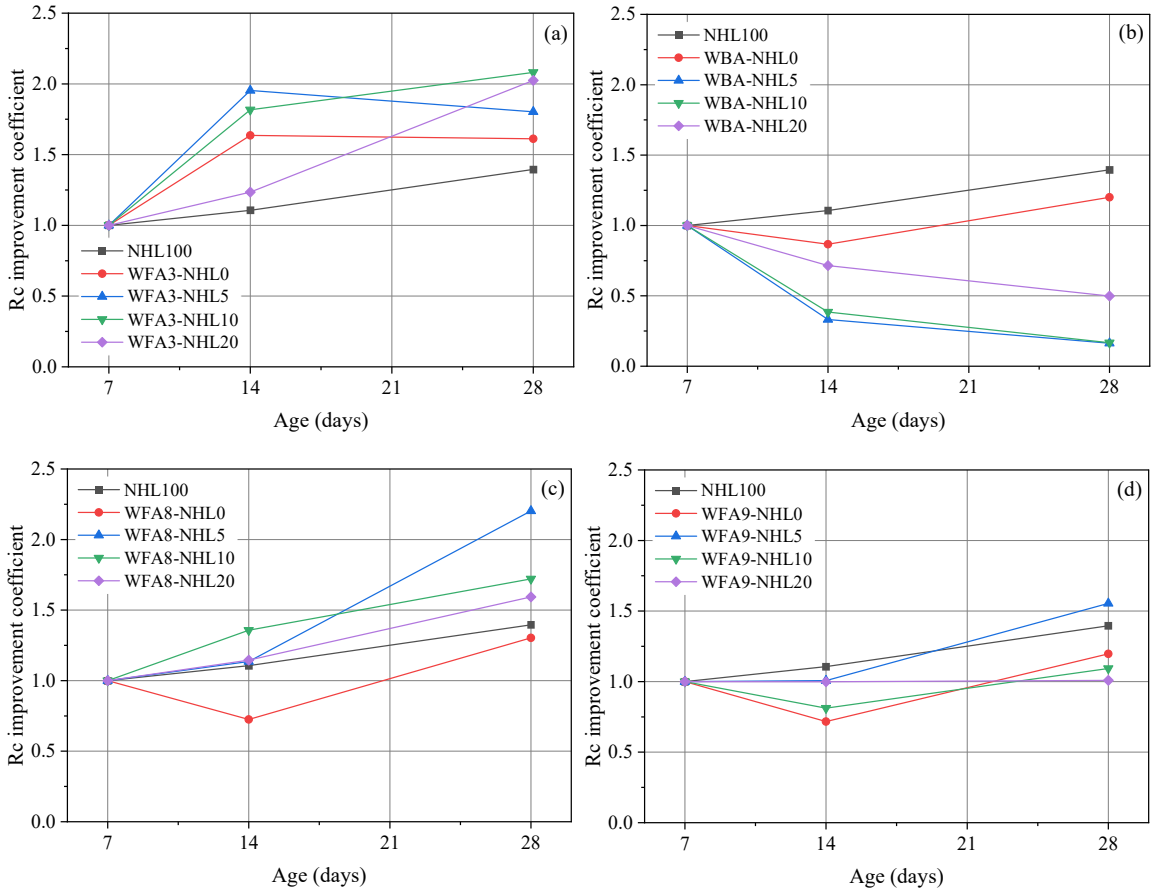

Figure 4-8. Compressive strength improvement coefficient of wood ash-NHL pastes as a function of time: (a) WFA3; (b) WBA; (c) WFA8; (d) WFA9.

According to Figure 4-8:

- All WFA3 pastes show a remarkable improvement in compressive strength. From 7 to 14 days, the compressive strength increases rapidly and remains more or less stable between 14 and 28 days;
- The presence of the NHL did not improve the compressive strength of the WBA pastes. The trend in R_c declined with increasing curing time, except for WBA-NHL5, which increased slightly from 14 to 28 days.
- For WFA8-NHL and WFA9-NHL pastes, more critical improvements in R_c were observed on 5 % NHL. It is also evident that the compressive strength trend increases between 14 and 28 days.

(d) Correlation between compressive strength and bulk density of wood ash-natural hydraulic lime pastes

The relationship between compressive strength (R_c) and bulk density (ρ) of the wood ash-NHL pastes at 7, 14 and 28 days was evaluated. As shown in Figure 4-9 (a, b, c, d), the compressive strength of the samples increases with increasing bulk density and curing time. Nevertheless,

for some pastes, especially WFA3-NHL, WBA-NHL and WFA9-NHL, bulk density lowered slightly as the curing time was extended.

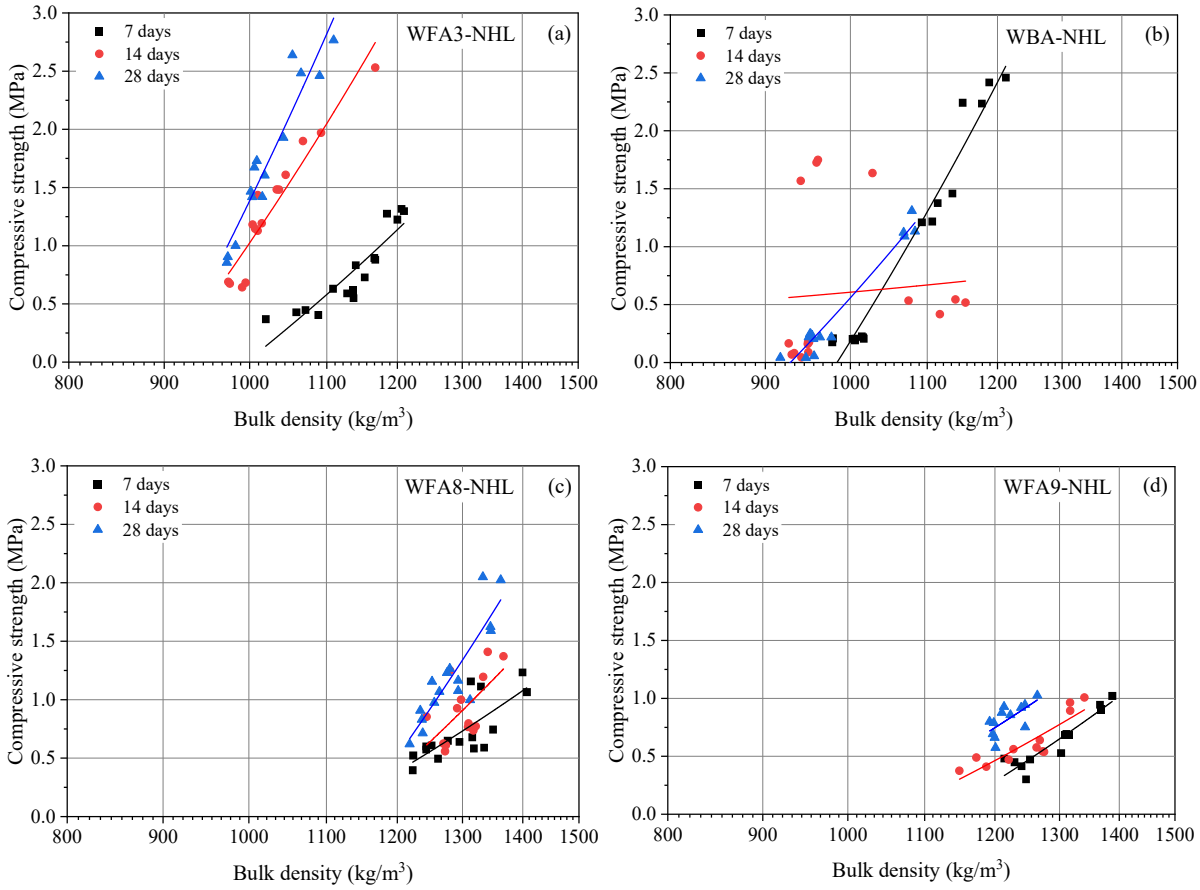

Figure 4-9. Correlation between compressive strength and bulk density of wood ash-NHL pastes at different curing ages: (a) WFA3; (b) WBA; (c) WFA8; (d) WFA9.

The bulk densities and compressive strengths of the wood ash-NHL pastes were respectively within the range of:

- 972-1210 kg/m^3 and 0.37-2.77 MPa for WFA3-NHL pastes (Figure 4-9 (a));
- 917-1212 kg/m^3 and 0.04-2.46 MPa for WBA-NHL pastes (Figure 4-9 (b));
- 1218-1407 kg/m^3 and 0.40-2.05 MPa for WFA8-NHL pastes (Figure 4-9 (c));
- 1148-1388 kg/m^3 and 0.30-1.03 MPa for WFA9-NHL pastes (Figure 4-9 (d)).

(e) Mass variations

The changes in the mass of the wood ash-NHL samples during the curing time were also monitored. The data presented here are from the wood ash pastes selected for the 28-day mechanical tests. As can be seen in Figure 4-10 (a, b, c, d), the mass data were recorded at 7, 14 and 28 days.

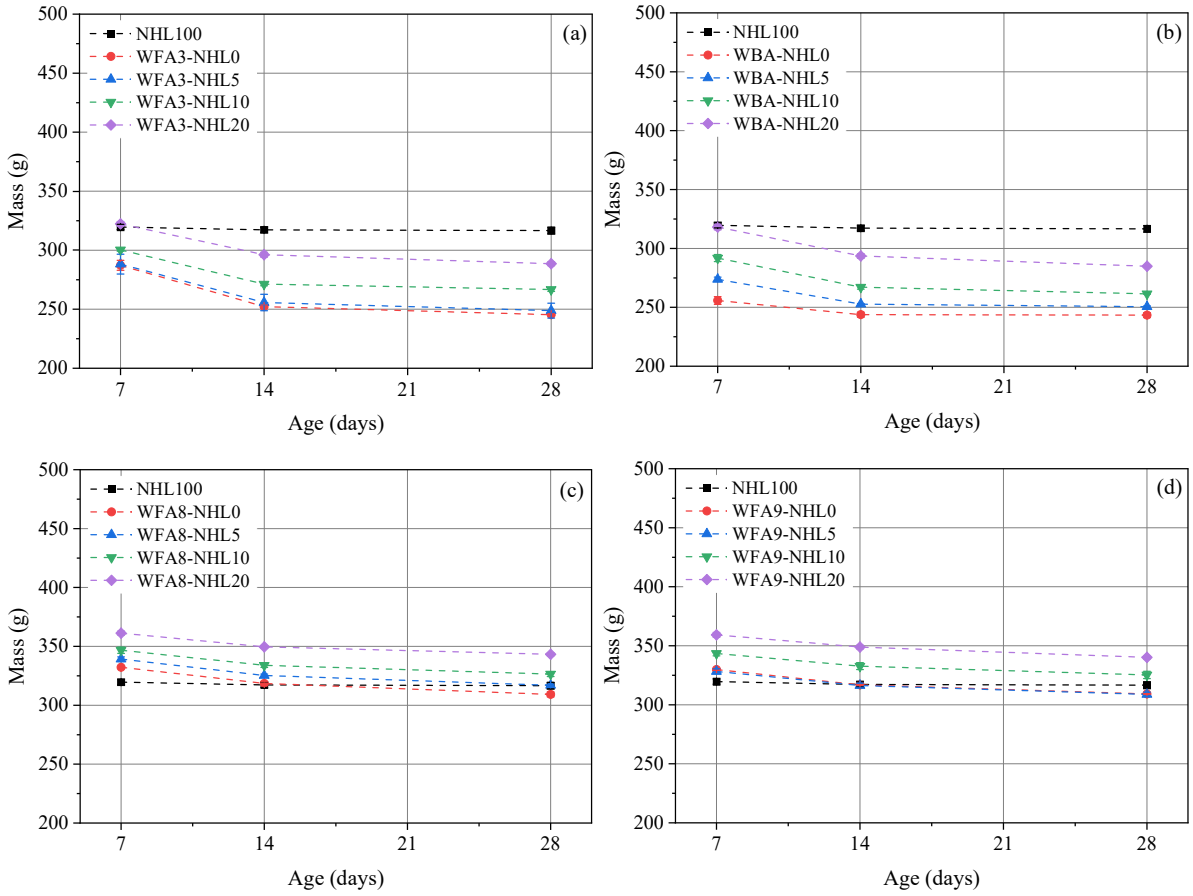

Figure 4-10. Mass evolution of wood ash-NHL pastes from 7 to 28 days: (a) WFA3; (b) WBA; (c) WFA8; (d) WFA9.

From the above graphs, the mass of wood ash-NHL pastes decreased gradually with the increase in curing time. In contrast, the trend in mass for NHL100 stayed stable as the curing age increased. Besides, it is worth noting that the incorporation of NHL raised the mass of the wood ash pastes. The average mass of wood ash-NHL pastes fluctuated from:

- 245 to 322 g for WFA3-NHL pastes (Figure 4-10 (a));
- 243 to 318 g for WBA-NHL pastes (Figure 4-10 (b));
- 309 to 361 g for WFA8-NHL pastes (Figure 4-10 (c));
- 309 to 359 g for WFA9-NHL pastes (Figure 4-10 (d)).

(f) Thermogravimetric analysis

The TGA curves obtained from the wood ash-NHL pastes at 7 and 28 days are presented and discussed in this section. It should be pointed out that the findings of this study were interpreted based on the literature surveyed, as summarised in Table 4-9.

Table 4-9. Typical mineral phases in various cement-based materials identified by the TGA method.

Compound	Degradation temperature range (°C)	Type of reaction	Experimental settings	Reference
C-S-H, AFt phases	50-140	Endothermic	Temperature range of 25-1000°C; heating rate of 20°C/min; nitrogen atmosphere.	(Zhu et al., 2020)
Friedel's salt	250-400			
Portlandite	400-500			
Calcite	500-700			
C-S-H, AFt	50-200	Endothermic	Temperature range of 35-975 °C; heating of 10°C/min; nitrogen atmosphere at a rate flow of 20 mL/min.	(Puerta-Falla et al., 2015)
Mc, Hc	180-300			
Hydrogrossular phases (Hy)	315-360			
Portlandite	400-500			
Calcite	600-800			
C-S-H	At an inflation point of 160	Endothermic	Temperature up to 1000 °C; The heating rate of 10 °C/min; nitrogen atmosphere.	(Frías Rojas, 2006)
Hydrogarnet	230-330 (at an inflation point of 292)			
Calcium carbonate	635-733			
Ettringite (AFt), C-S-H or CAH	100	Endothermic	From room temperature to 990 °C; heating rate of 3 °C/min; inert nitrogen atmosphere.	(Ohenoja et al., 2020)
Brucite	350			
Portlandite	450			
Calcite	500-850			
C-S-H	25-200	Endothermic	Mass of the sample: 7 mg; temperature range of 25-850 °C; heating rate 10 °C/min; air atmosphere at a rate flow of 100 mL/min.	(Gomes et al., 2005)
Portlandite	400-500			
Carbonate phases	500-850			
Portlandite	350-450	Endothermic	Temperature range of 20-1000 °C; heating rate of 10°C/min; nitrogen atmosphere.	(Cizer et al., 2012)
Calcite	650-850			

Note: calcium silicate hydrates (C-S-H); aluminate ferrite tri-sulphate (AFt) phases; aluminate ferrite mono-sulphate (AFm) phases; calcium-aluminate hydrate (CAH); calcium hydroxide ($Ca(OH)_2$) or portlandite (CH); calcium carbonate or calcite ($CaCO_3$); hydrogarnet (C_3AH_6); brucite ($Mg(OH)_2$.

In this case study, the main endothermic reactions were observed in the subsequent temperature ranges:

- 25-100 °C: Evaporation of the free water;
- 50-200 °C: Dehydration of calcium silicate hydrates (C-S-H), ettringite;

- 200-300 °C: Decomposition of alumina ferrite mono-sulphate (AFM) phases, (calcium monocarboaluminate phase (Mc), calcium hemicarboaluminate phase (Hc), or calcium aluminate phase (Hx));
- 300-400°C: Dehydration of hydrogrossular (Hy) or hydrogarnet (H);
- 400-500 °C: Dehydroxylation of calcium hydroxide ($Ca(OH)_2$) or portlandite;
- 500-600 °C: Structural modification of unreacted quartz (SiO_2);
- 500-800 °C: Decarbonation of calcium carbonate or calcite ($CaCO_3$);
- 900-1000 °C: Decomposition of dolomite ($CaMg(CO_3)_2$).

It can be seen from Figure 4-11 (a, b) and Figure 4-12 (a, b) that all WFA3-NHL pastes show similar mass loss (TG) and differential mass loss (DTG) curves, except NHL100. The peaks from 400-500 °C were only present in NHL100 and WFA3-NHL20. The mass losses occurring at 600-800 °C were the most predominant among WFA3-NHL pastes.

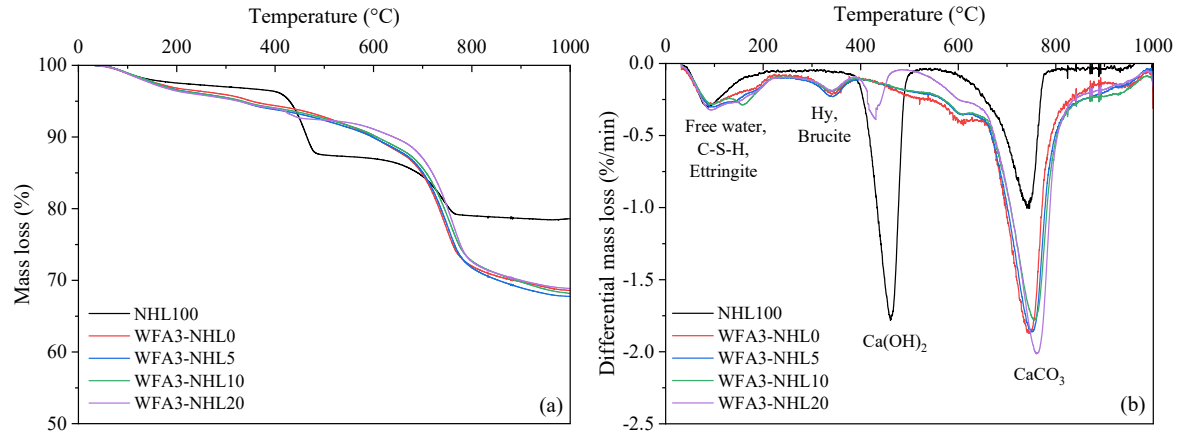

Figure 4-11. TGA curves of WFA3-NHL pastes at 7 days.

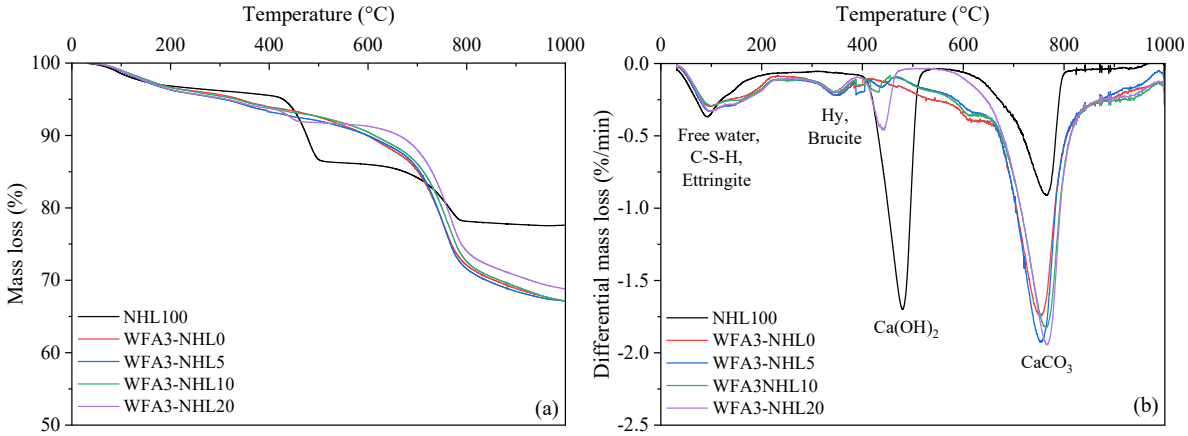

Figure 4-12. TGA curves of WFA3-NHL pastes at 28 days.

The TG and DTG curves of WBA-NHL pastes at 7 and 28 days are given in Figure 4-13 (a, b) and Figure 4-14 (a, b), respectively. No mass loss associated with $Ca(OH)_2$ was noticed on the WBA-NHL pastes, apart from WBA-NHL20 at 28 days. The endotherms appearing from 500 to 600 °C are probably due to the inversion of unreacted silica (SiO_2). The peaks observed between 500 and 800 °C correspond to the decarbonisation of $CaCO_3$. The intensities of the $CaCO_3$ peaks increase lightly with NHL content but diminish marginally with the curing age.

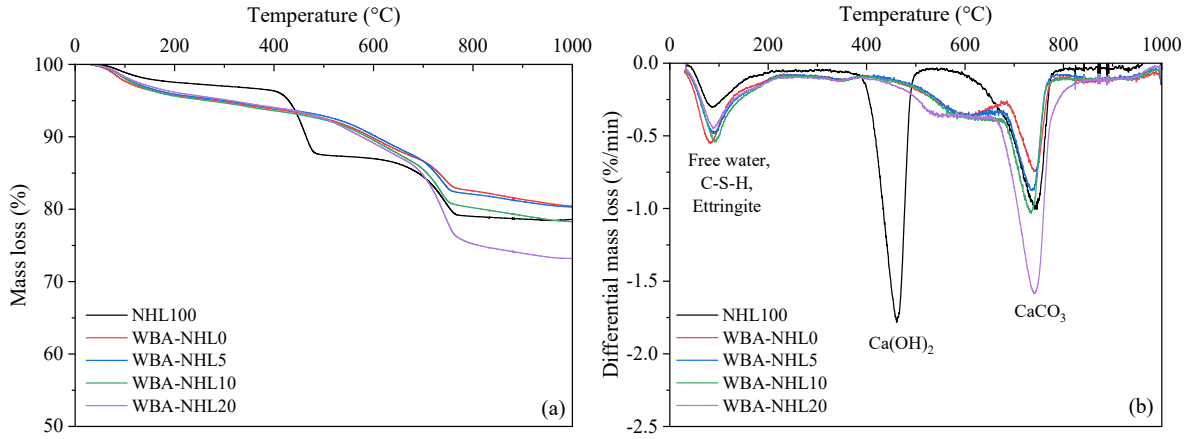

Figure 4-13. TGA curves of WBA-NHL pastes at 7 days.

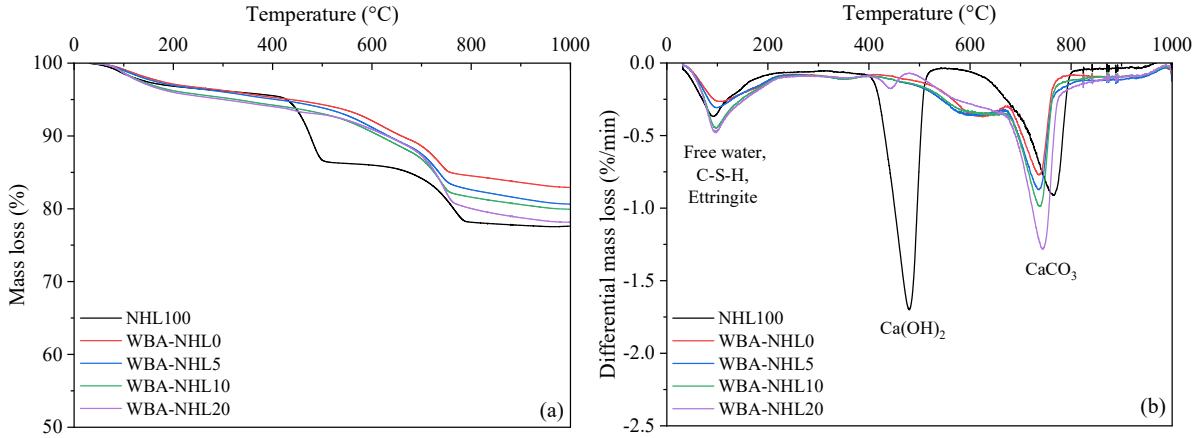

Figure 4-14. TGA curves of the WBA-NHL pastes at 28 days.

As reflected in Figure 4-15 (a, b) and Figure 4-16 (a, b), the minor mass losses found from 200 to 400 °C can be explained by the dehydroxylation of AFm phases, hydrogarnet or brucite. The endotherms at 400-500 °C were considerably deeper and sharper than those of WBA-NHL and WFA3-NHL pastes. The broad endotherm occurring from 500-900 °C, consists of two close mass losses, that can be ascribed to the decomposition of calcite and other carbonate varieties, such as vaterite, aragonite, dolomite, magnesite, etc. (Földvári, 2011; Ohenoja et al., 2020; Stepkowska et al., 2003).

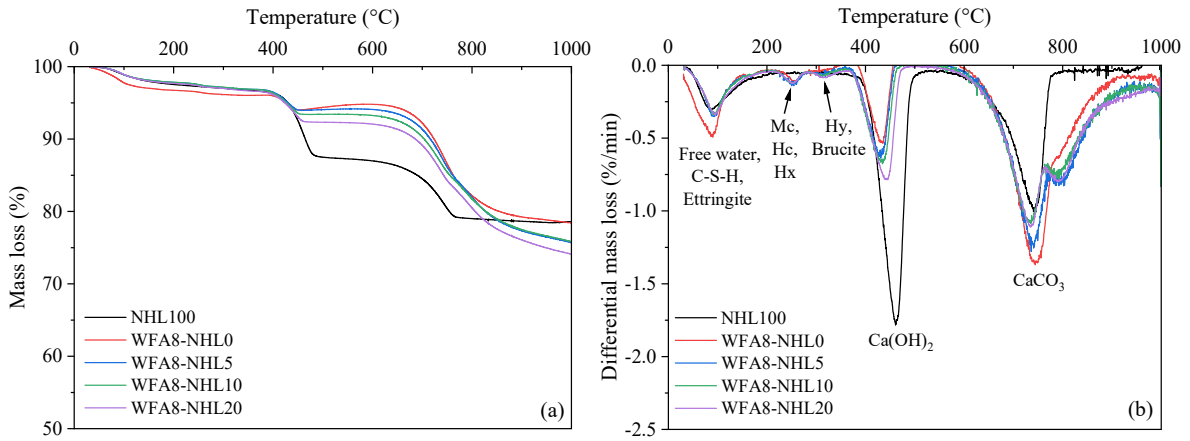

Figure 4-15. TGA curves of WFA8-NHL pastes at 7 days.

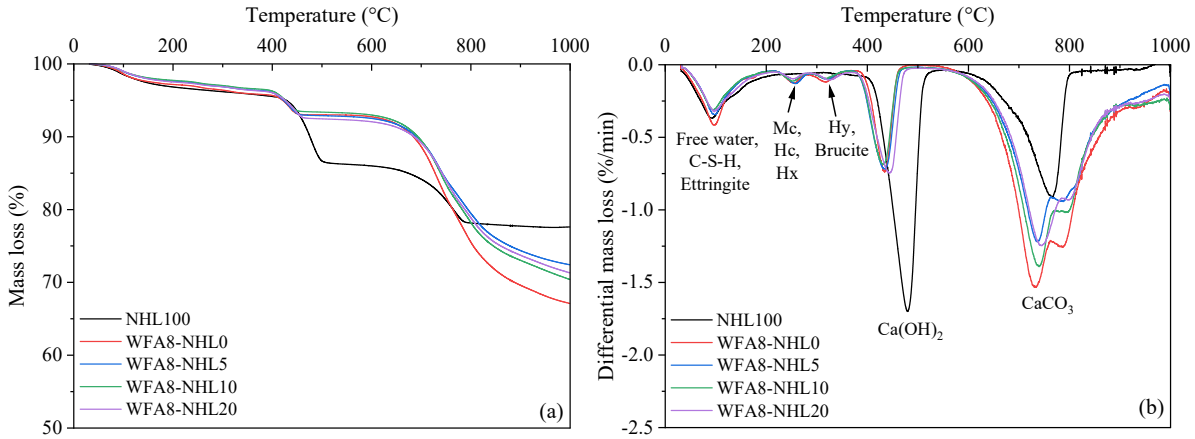

Figure 4-16. TGA curves of WFA8-NHL pastes at 28 days.

As seen in Figure 4-17 (a, b) and Figure 4-18 (a, b), the TG and DTG of WFA9-NHL pastes are similar to those of WFA8-NHL. Concerning the endotherms at (400-500 °C), the mass losses exhibited by WFA8-NHL were higher than those observed on WFA9-NHL pastes. Besides that, the calcite peaks of WFA8-NHL tended to be wider, whereas for WFA9-NHL they were somewhat deeper and sharper. The WFA9-NHL pastes showed mass losses at around 850-1000 °C and were attributed to the dolomite decomposition (Földvári, 2011; Samtani et al., 2002).

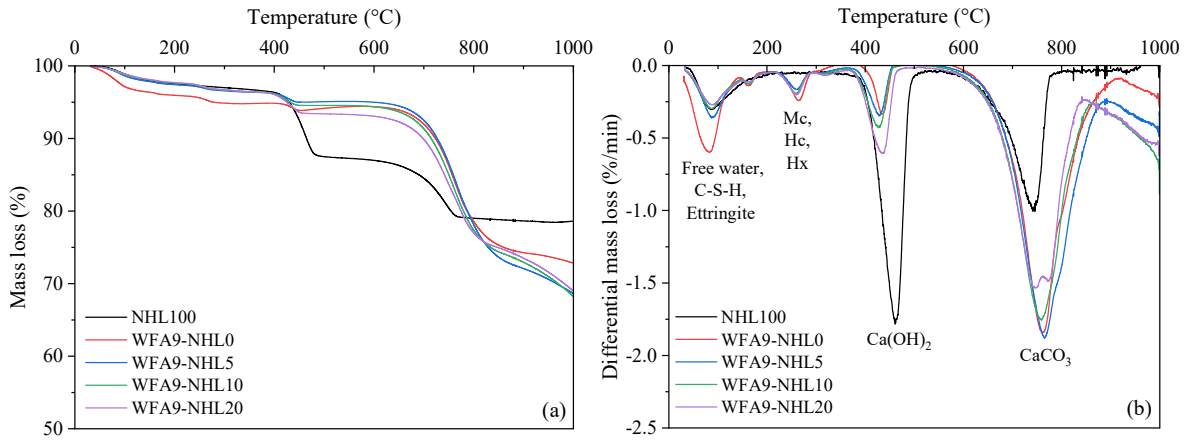

Figure 4-17. TGA curves of WFA9-NHL pastes at 7 days.

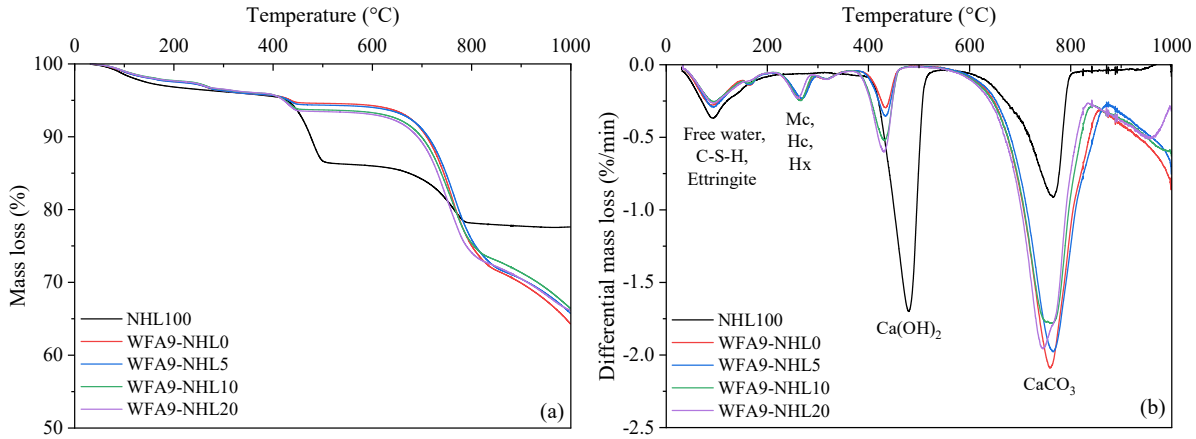

Figure 4-18. TGA curves of WFA9-NHL pastes at 28 days.

4.5.2 Wood ash pastes blended with ordinary Portland cement

(a) Initial and final setting time

The setting time of the wood fly ash WFA8 pastes containing 5, 10 and 20 % ordinary Portland cement (OPC) by mass of WFA8 was determined. As is evident in Figure 4-19 and Table 4-10, the addition of OPC substantially improved the setting of the wood ash pastes.

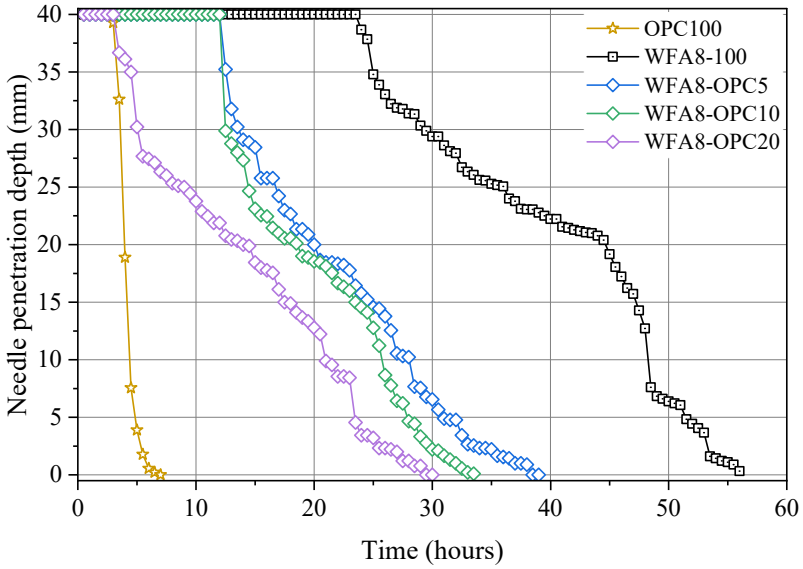

Figure 4-19. Setting time of WFA8 pastes containing ordinary Portland cement.

Table 4-10. Initial and final setting time data.

Mix notation	Initial setting time (hours)	Final setting time (hours)
OPC100	3.5	7
WFA8-100	25	56
WFA8-OPC5	12.5	38.5
WFA8-OPC10	12.5	33.5
WFA8-OPC20	4.5	30

Indeed, the initial setting time decreased from 25 hours for WFA8-100 to 12.5 for WFA8-OPC (5, 10) and 4.5 hours for WFA8-OPC20. The final setting time has also lessened from 56 hours for WFA8-100 to 38.5, 33.5 and 30 hours for WFA8 pastes containing 5, 10 and 20 % OPC, respectively.

The lack of solidification and delayed setting among wood ash systems have been previously reported in the literature. Steenari and Lindqvit (1997) declared that the presence of high content of unburnt matter prevents the wood ashes from solidifying after the addition of water.

Kula et al. (2001) and Wang et al. (2008) have observed longer setting times among the cement mixes blended with wood fly ash, coal fly ash and bottom ash. The authors ascribed the retardation effect to the chemical and physical characteristics of the ashes, particularly fineness and free lime (CaO) content in the cement mixes. Furthermore, Berra et al. (2015) also evaluated the setting of the cement pastes in which cement was replaced by 15-30 % content of wood fly ash. The results revealed higher setting times in the pastes containing wood fly ash

than in the control paste. The authors have attributed this behaviour to high sulphate and heavy metals contents of the wood fly ashes.

(b) Flexural strength

The flexural strength (R_f) results of the wood ash-OPC pastes are provided in Figure 4-20 (a, b, c, d) and Table 4-11. As is obvious, the flexural strength of WFA8-OPC and WFA9-OPC pastes increases with the increase in OPC content and curing time. Besides, the above mixtures also exhibited a significant growth in R_f between 14 and 28 days. In contrast, the flexural strength of the WFA3-OPC pastes remained fairly stable as the curing time increased, while for WBA pastes, it appeared to decrease marginally.

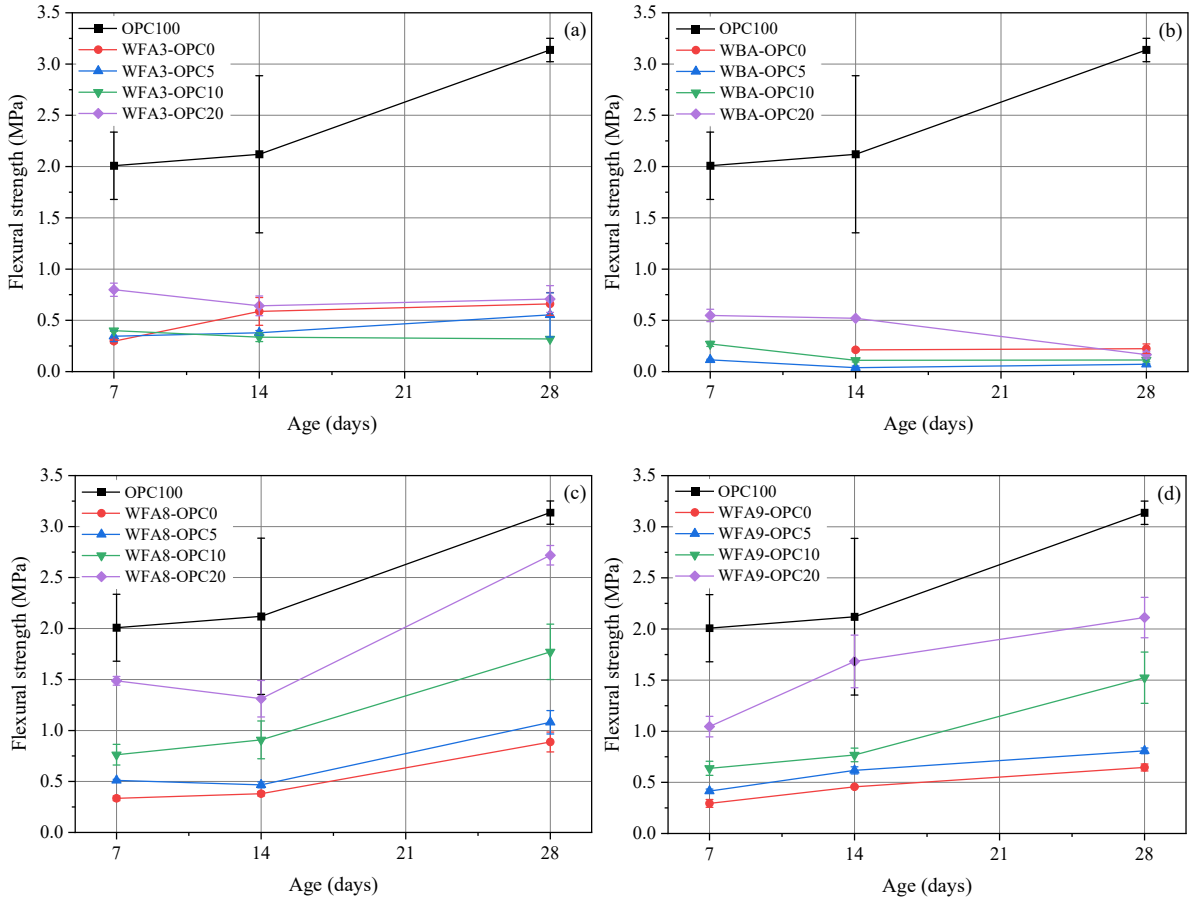

Figure 4-20. Flexural strength of wood ash pastes containing different percentages of OPC at 7, 14 and 28 days: (a) WFA3; (b) WBA; (c) WFA8; (d) WFA9.

Table 4-11. Flexural strength data for all wood ash-OPC pastes.

Mix notation	Flexural strength (MPa)		
	7 days	14 days	28 days
OPC100	2.01 ± 0.33	2.12 ± 0.77	3.14 ± 0.11
WFA3-OPC0	0.30 ± 0.02	0.59 ± 0.14	0.66 ± 0.11
WFA3-OPC5	0.34 ± 0.05	0.38 ± 0.02	0.55 ± 0.21
WFA3-OPC10	0.40 ± 0.01	0.34 ± 0.04	0.32 ± 0.00
WFA3-OPC20	0.80 ± 0.06	0.64 ± 0.10	0.71 ± 0.13
WBA-OPC0	n.t.	0.21 ± 0.01	0.22 ± 0.05
WBA-OPC5	0.11 ± 0.01	0.04 ± 0.02	0.07 ± 0.01
WBA-OPC10	0.27 ± 0.02	0.11 ± 0.02	0.11 ± 0.02
WBA-OPC20	0.55 ± 0.06	0.52 ± 0.00	0.17 ± 0.03
WFA8-OPC0	0.33 ± 0.02	0.38 ± 0.02	0.89 ± 0.10
WFA8-OPC5	0.51 ± 0.01	0.47 ± 0.03	1.08 ± 0.11
WFA8-OPC10	0.76 ± 0.10	0.91 ± 0.19	1.77 ± 0.27
WFA8-OPC20	1.49 ± 0.04	1.31 ± 0.18	2.72 ± 0.10
WFA9-OPC0	0.29 ± 0.04	0.46 ± 0.01	0.65 ± 0.03
WFA9-OPC5	0.41 ± 0.02	0.62 ± 0.03	0.81 ± 0.03
WFA9-OPC10	0.64 ± 0.07	0.77 ± 0.07	1.52 ± 0.25
WFA9-OPC20	1.05 ± 0.10	1.68 ± 0.26	2.11 ± 0.20

Note: n.t.: not tested.

At 28 days, the average flexural strength of the wood ash pastes varied between:

- 0.32 MPa (WFA3-OPC10) and 0.71 MPa (WFA3-OPC20) for WFA3-OPC pastes;
- 0.07 MPa (WBA-OPC5) and 0.22 MPa (WBA-OPC0) for WBA-OPC pastes;
- 0.89 MPa (WFA8-OPC0) and 2.72 MPa (WFA8-OPC20) for WFA8-OPC pastes;
- 0.65 MPa (WFA9-OPC0) and 2.11 MPa (WFA9-OPC20) for WFA9-OPC pastes.

Overall, the lowest and highest flexural strength values were obtained from the WBA-OPC and WFA8-OPC pastes, respectively.

(c) Compressive strength

The compressive strength (R_c) results obtained from the wood ash-OPC pastes are presented in Figure 4-21 (a, b, c, d) and Table 4-12. It should be noted that the standard 28-day compressive strength of the OPC used in this study is 32.5 MPa; however, due to the limited capacity of the hydraulic press sensor, the test was interrupted and stopped when the stress reached 29 MPa.

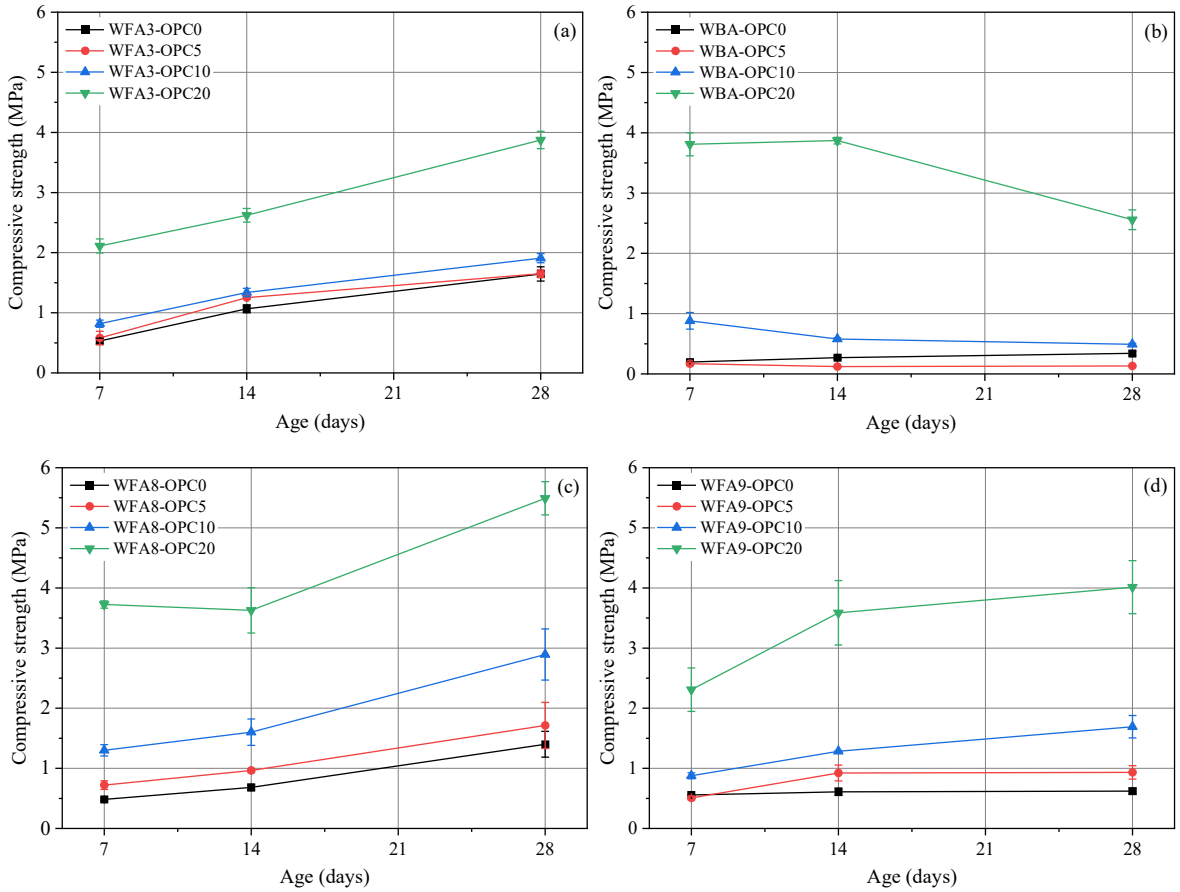

Figure 4-21. Compressive strength of wood ash pastes containing different percentages of OPC at 7, 14 and 28 days: (a) WFA3; (b) WBA; (c) WFA8; (d) WFA9.

Table 4-12. Compressive strength data for all wood ash-OPC pastes.

Mix notation	Compressive strength (MPa)		
	7 days	14 days	28 days
OPC100	28.03 ± 0.64	28.68 ± 0.86	29.00 ± 0.32
WFA3-OPC0	0.53 ± 0.05	1.07 ± 0.07	1.65 ± 0.12
WFA3-OPC5	0.58 ± 0.11	1.25 ± 0.02	1.65 ± 0.06
WFA3-OPC10	0.82 ± 0.06	1.34 ± 0.07	1.91 ± 0.08
WFA3-OPC20	2.11 ± 0.12	2.62 ± 0.11	3.87 ± 0.14
WBA-OPC0	0.20 ± 0.00	0.27 ± 0.03	0.34 ± 0.03
WBA-OPC5	0.17 ± 0.02	0.12 ± 0.01	0.13 ± 0.01
WBA-OPC10	0.88 ± 0.14	0.58 ± 0.02	0.49 ± 0.02
WBA-OPC20	3.81 ± 0.19	3.87 ± 0.05	2.56 ± 0.16
WFA8-OPC0	0.48 ± 0.02	0.68 ± 0.04	1.40 ± 0.21
WFA8-OPC5	0.72 ± 0.07	0.96 ± 0.03	1.71 ± 0.38
WFA8-OPC10	1.30 ± 0.09	1.60 ± 0.22	2.89 ± 0.43
WFA8-OPC20	3.72 ± 0.06	3.63 ± 0.38	5.49 ± 0.28
WFA9-OPC0	0.56 ± 0.00	0.61 ± 0.06	0.62 ± 0.05
WFA9-OPC5	0.51 ± 0.03	0.92 ± 0.13	0.93 ± 0.11
WFA9-OPC10	0.88 ± 0.05	1.28 ± 0.01	1.69 ± 0.11
WFA9-OPC20	2.31 ± 0.36	3.59 ± 0.54	4.01 ± 0.44

From the aforementioned findings, it is clear that the compressive strength of the WFA3-OPC, WFA8-OPC and WFA9-OPC pastes increases with the increase in OPC content and curing age. Nevertheless, for the WBA-OPC pastes, the compressive strength appears to increase with increasing OPC proportion and it drops when the curing time is increased. The presence of OPC remarkably contributed to the compressive strength development of the wood ash pastes. At 28 days, the average compressive strength of the wood ash-OPC pastes ranged between:

- 1.65 MPa (WFA3-OPC (0,5)) and 3.87 MPa (WFA3-OPC20) for WFA3-OPC pastes;
- 0.13 MPa (WBA-OPC5) and 2.56 MPa (WBA-OPC20) for WBA-OPC pastes;
- 1.40 MPa (WFA8-OPC0) and 5.49 MPa (WFA8-OPC20) for WFA8-OPC pastes;
- 0.62 MPa (WFA9-OPC0) and 4.01 MPa (WFA9-OPC20) for WFA9-OPC pastes.

The highest compressive strength was obtained from the wood ash containing 20 % OPC. This is due to the participation of OPC in the formation of hydration products, such as C-S-H, $Ca(OH)_2$, etc., responsible for the strength development.

In contrast, the least R_c values were found among the WBA-OPC pastes, particularly WBA-OPC5. The reduction in R_c and R_f observed on the WBA-OPC pastes is attributed to similar causes as those mentioned earlier in section 4.5.1(c).

Overall, the compressive strength results obtained in this study are comparable with those found in the literature, as shown in Table 2-4. Besides, the reduction in compressive strength observed with increasing wood ash content has also been reported in (Fořt et al., 2021; Lessard et al., 2017a).

Furthermore, the compressive strength improvement coefficient (Ci_{Rc}) of the wood ash-OPC pastes was calculated, as in section 4.5.1(c) and the results are plotted in Figure 4-22 (a, b, c, d).

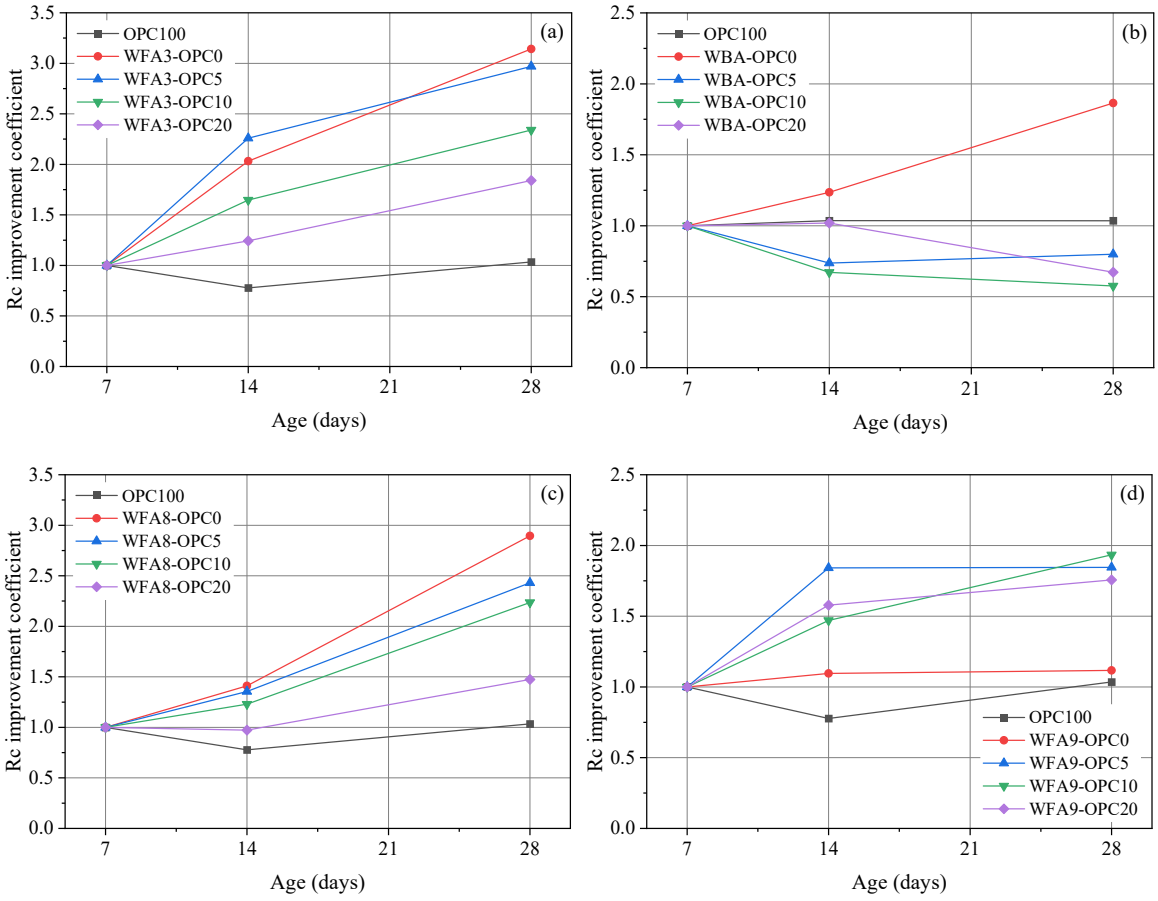

Figure 4-22. Compressive strength improvement coefficient of wood ash-OPC pastes as function of time: (a) WFA3; (b) WBA; (c) WFA8; (d) WFA9.

From above graphs, it is apparent that:

- The compressive strength of the WFA3-OPC pastes significantly improved at all ages. The improvement coefficient decreases with the increase in OPC content.
- No compressive strength improvement was noted among WBA-OPC pastes, except for WBA-OPC0. The improvement coefficient reduces with increasing curing time.

- For the WFA8-OPC pastes, their compressive strength substantially increased between 14 and 28 days. The improvement coefficient decreases with increasing OPC proportion.
- Concerning WFA9-OPC pastes, their compressive strength rose sharply from 7 to 14 days and remained more or less persistent until 28 days. The improvement coefficient of WFA9 paste without OPC content was significantly lower than those of the WFA9 containing OPC.

From this, it can be concluded that the compressive strength of the wood ash-OPC pastes depended on the type of wood ash, amount of OPC and curing time.

(d) Relationship between compressive strength and bulk density

The correlation between compressive strength (R_c) and bulk density (ρ) of the wood ash pastes at 7, 14 and 28 days was examined, and the results are shown in Figure 4-23 (a, b, c, d). It can be observed that the compressive strength increases with the rise in bulk density and curing time. Apart from that, the bulk density diminishes as the curing time increases.

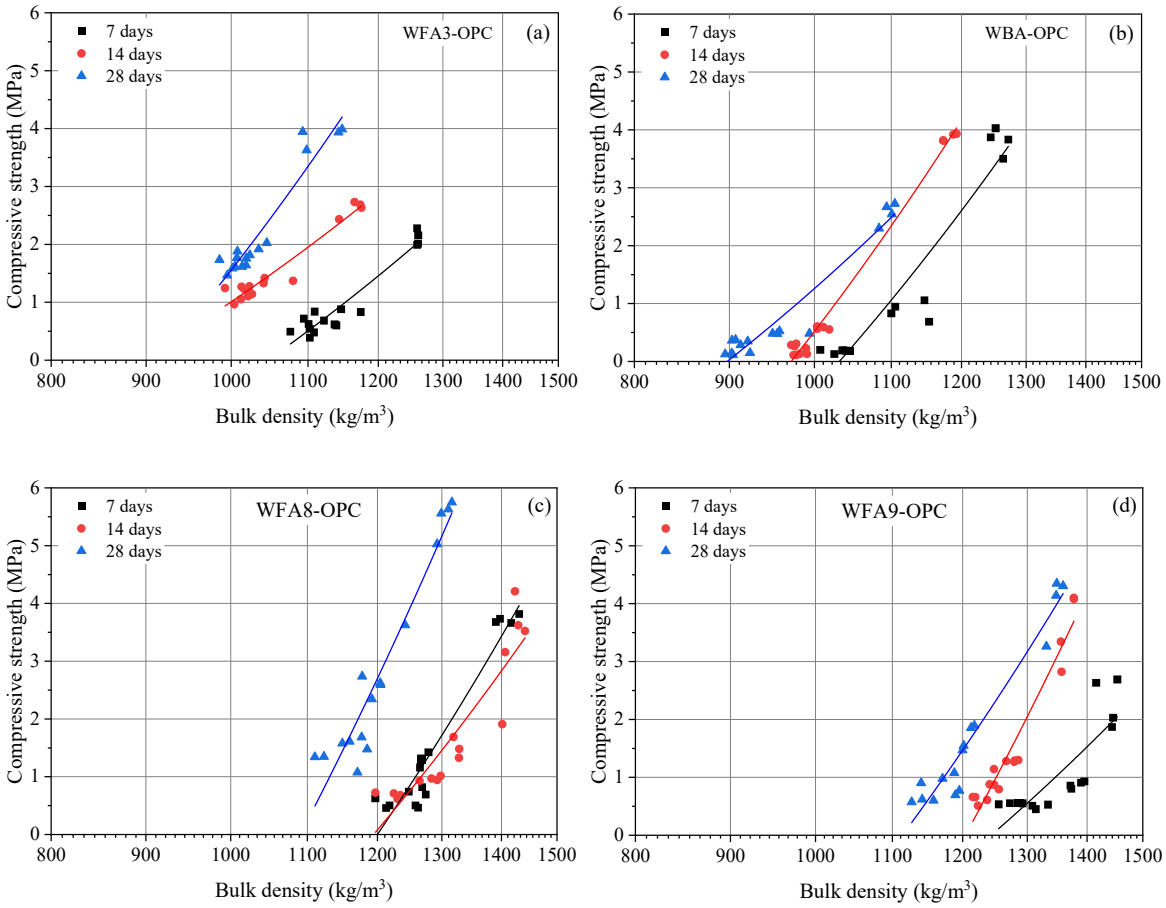

Figure 4-23. Correlation between wood ash-OPC pastes' compressive strength and bulk density at different curing ages: (a) WFA3; (b) WBA; (c) WFA8; (d) WFA9.

Generally, the bulk densities and compressive strengths of the evaluated wood ash pastes varied respectively from:

- 986-1261 kg/m^3 and 0.39-3.99 MPa for WFA3-OPC pastes (Figure 4-23 (a));
- 895-1272 kg/m^3 and 0.11-4.03 MPa for WBA-OPC pastes (Figure 4-23 (b));
- 1110-1442 kg/m^3 and 0.46-5.75 MPa for WFA8-OPC pastes (Figure 4-23 (c));
- 1126-1453 kg/m^3 and 0.45-4.35 MPa for WFA9-OPC pastes (Figure 4-23 (d)).

(e) Mass evolution

The mass fluctuations of the wood ash pastes during the curing time were closely observed. As mentioned earlier, the data provided in this section were taken from the wood ash pastes chosen for the 28-day mechanical tests. As can be seen in Figure 4-24 (a, b, c, d), the mass was registered at 7, 14 and 28 days.

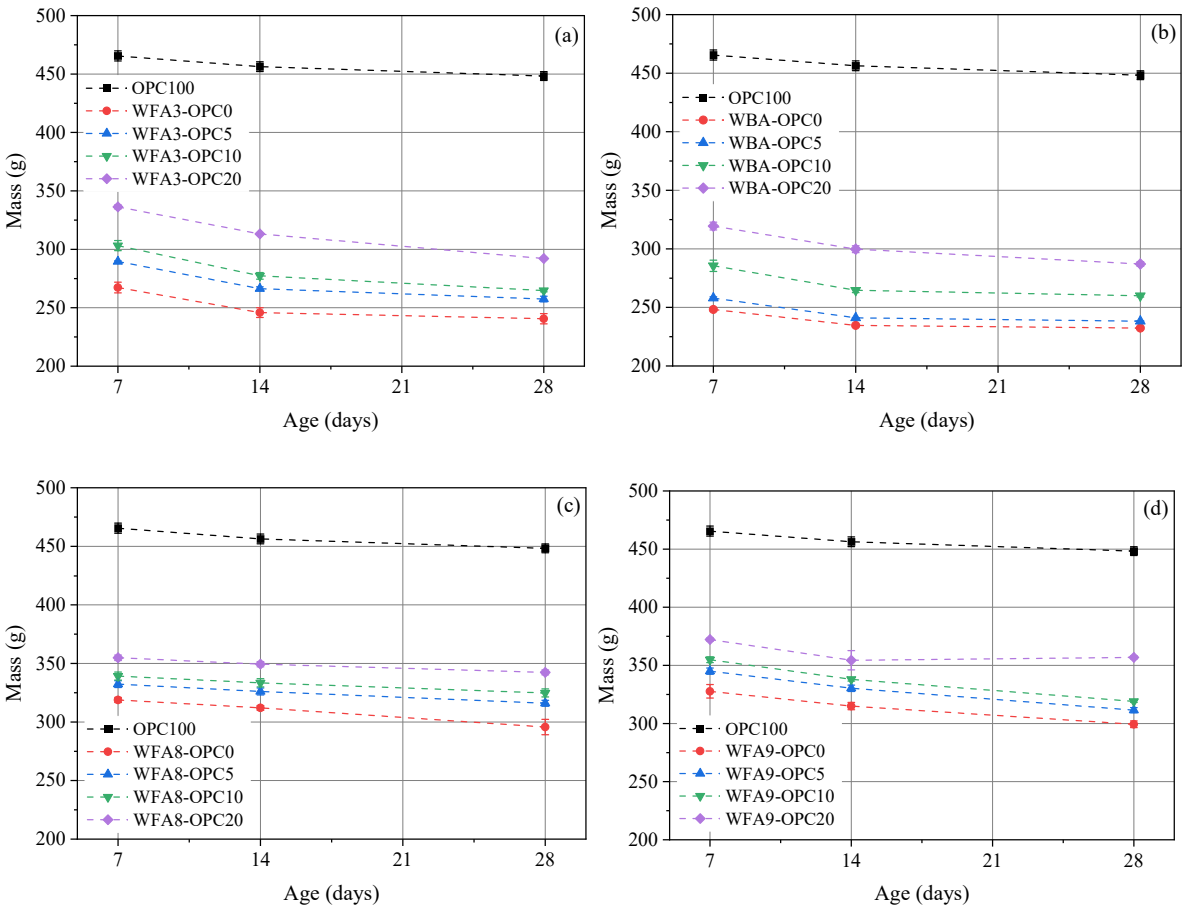

Note that the standard deviations are not clearly visible because they were relatively small.

Figure 4-24. Mass evolution of wood ash-OPC pastes from 7 to 28 days: (a) WFA3; (b) WBA; (c) WFA8; (d) WFA9.

According to Figure 4-24, the reference paste OPC100 shows significantly higher mass than the wood ash pastes. The trend in mass for all the samples slightly declines as the OPC content decreases. In addition, it is also noted that the mass of the pastes reduced marginally with increasing curing age.

Overall, the average mass of the wood ash pastes ranged from:

- 241 to 336 g for WFA3-OPC pastes (Figure 4-24 (a));
- 232 to 319 g for WBA-OPC pastes (Figure 4-24 (b));
- 296 to 355 g for WFA8-OPC pastes (Figure 4-24 (c));
- 299 to 372 g for WFA9-NHL pastes (Figure 4-24 (d)).

The incorporation of OPC increased the mass of the wood ash pastes. Also, as noted previously on the wood ash-NHL pastes, the WFA8-OPC and WFA9-OPC pastes observed higher mass than WFA3-OPC and WBA-OPC pastes.

(f) Scanning electron microscopy

The morphology and microstructure of the binding matrices were observed using scanning electron microscopy (SEM) at 28 days. The SEM micrographs of hydrated wood ash-OPC pastes are presented in Figure 4-25. As evident, two micrographs with magnifications of ×500 and ×2500 were selected for each sample. The major crystalline phases found in the analysed samples and their morphologies are listed in Table 4-13.

Table 4-13. Main phases visible on SEM micrographs of wood ash-OPC pastes at 28 days.

Phase	Morphology
Ettringite $Ca_6Al_2(SO_4)_3(OH)_{12}\cdot 26H_2O$	Needle-shaped particles
Calcium silicate hydrates C-S-H	Gel
Portlandite $Ca(OH)_2$	Lamellar or plate-shaped particles
Calcite $CaCO_3$	Rhombohedral crystal structure

From the SEM micrographs in Figure 4-25, it is evident that the microstructure of the OPC100 paste is denser than the wood ash pastes. In addition, some unburned wood particles (primarily black in colour) were observed in all wood ash mixtures. Comparing the wood ash-contained mixtures indicates that WFA3 and WBA pastes exhibited higher porosity and less packed microstructure than the WFA8 and WFA9 mixtures.

In terms of reaction products, the crystalline phases such as C-S-H, ettringite and CH were observed on the OPC100, WFA8 and WFA9 pastes. Other than that, calcite was also dominant in WFA8 and WFA9 mixtures. Finally, for the WFA3 and WBA pastes, only C-S-H was identified.

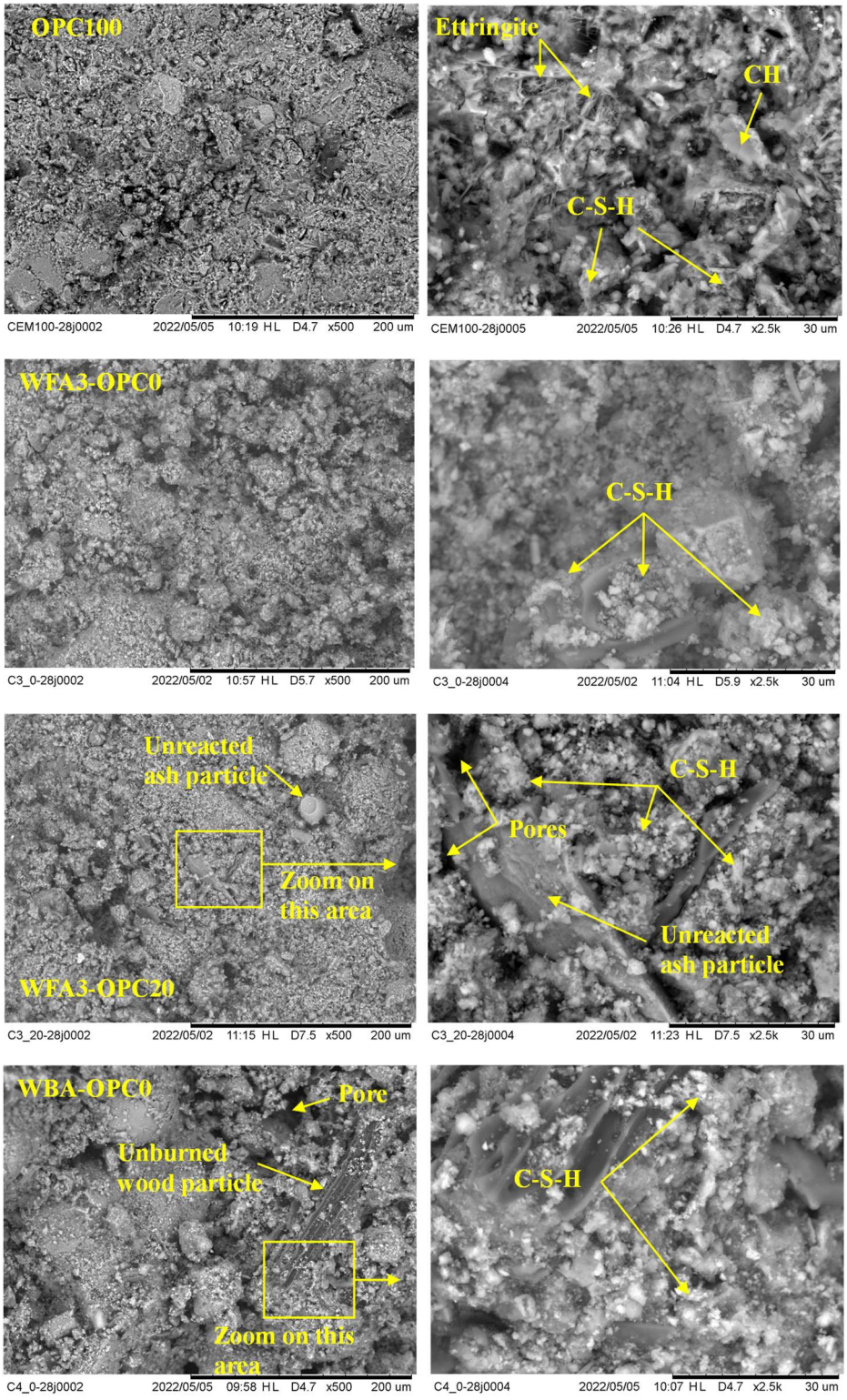

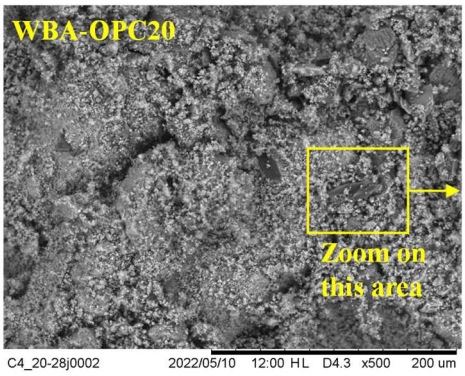
WBA-OPC20
Zoom on
this area
C4_20-28j0002 2022/05/10 12:00 HL D4.3 x500 200 um

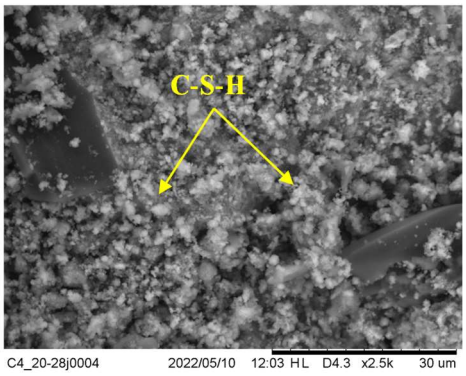
C-S-H
C4_20-28j0004 2022/05/10 12:03 HL D4.3 x2.5k 30 um

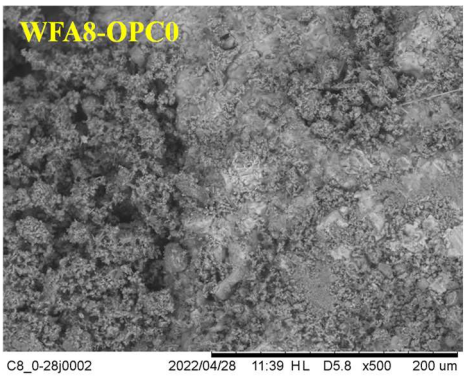
WFA8-OPC0
C8_0-28j0002 2022/04/28 11:39 HL D5.8 x500 200 um

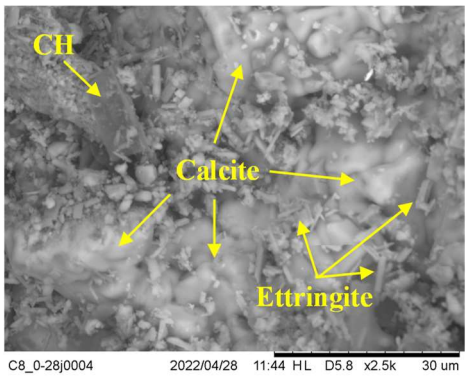
CH
Calcite
Ettringite
C8_0-28j0004 2022/04/28 11:44 HL D5.8 x2.5k 30 um

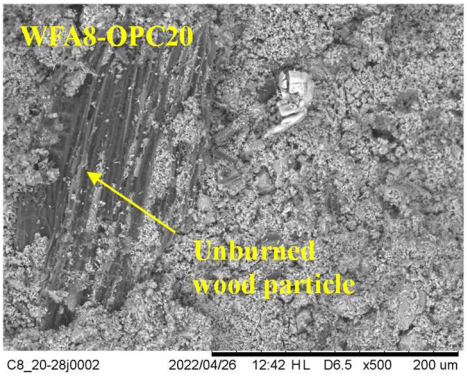
WFA8-OPC20
Unburned
wood particle
C8_20-28j0002 2022/04/26 12:42 HL D6.5 x500 200 um

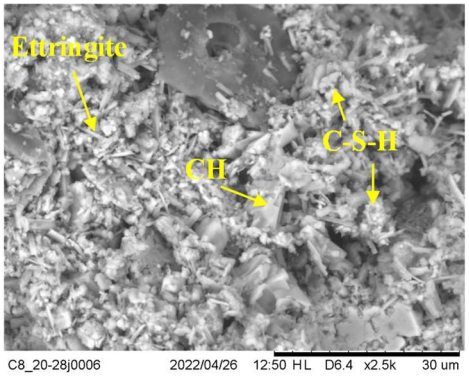
Ettringite
C-S-H
CH
C8_20-28j0006 2022/04/26 12:50 HL D6.4 x2.5k 30 um

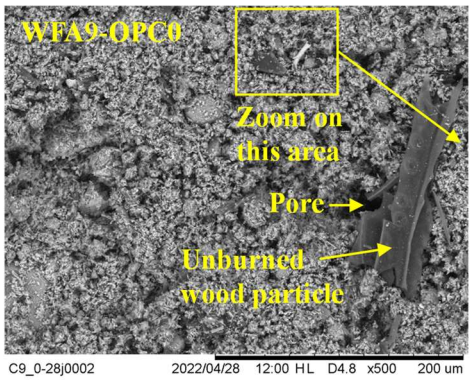
WFA9-OPC0
Zoom on
this area
Pore
Unburned
wood particle
C9_0-28j0002 2022/04/28 12:00 HL D4.8 x500 200 um

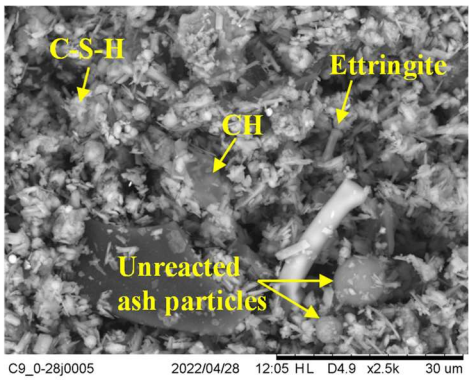
C-S-H
Ettringite
CH
Unreacted
ash particles
C9_0-28j0005 2022/04/28 12:05 HL D4.9 x2.5k 30 um

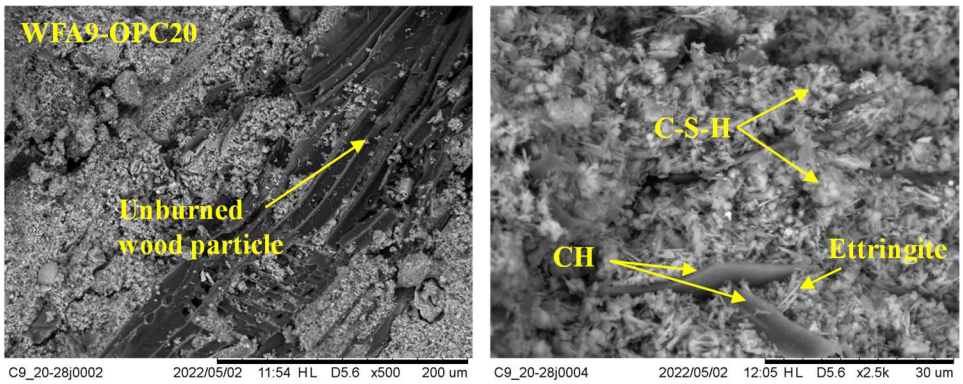

Figure 4-25. SEM micrographs of wood ash-OPC pastes at 28 days.

(g) Thermogravimetric analysis

The TG and DTG curves of WFA3-OPC pastes are given in Figure 4-26 (a, b) and Figure 4-27 (a, b). As can be seen, all WFA3-OPC samples display identical mass losses, except WFA3-OPC0 (at 7 days). The latter showed a significant mass loss at 100 °C due to its high-water content. Other than that, no AFm phases were disclosed, but minor mass losses due to the decomposition of the hydrogrossular phase or brucite were noticed on all WFA3-OPC pastes. Over time, the intensities of the $Ca(OH)_2$ peaks have increased somewhat, while those of $CaCO_3$ diminished insignificantly.

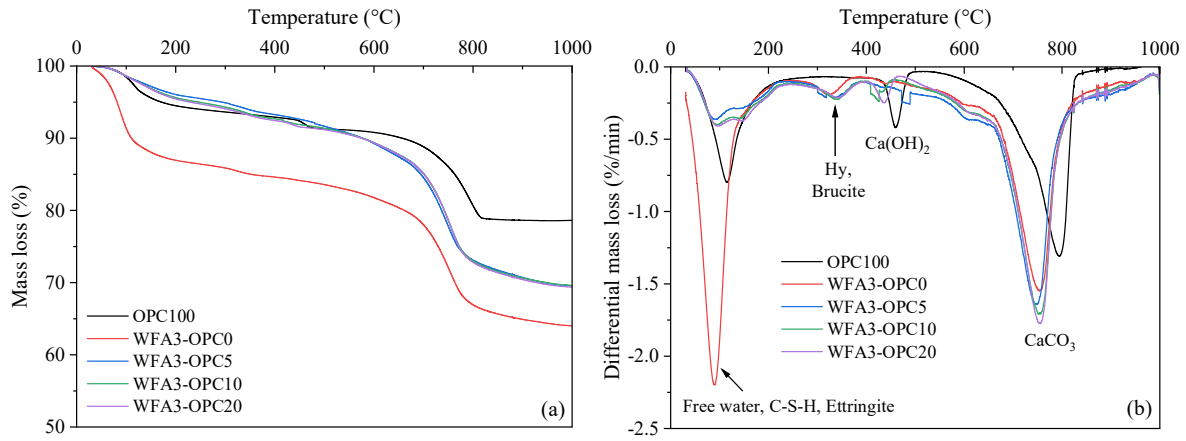

Figure 4-26. TGA curves of WFA3-OPC pastes at 7 days.

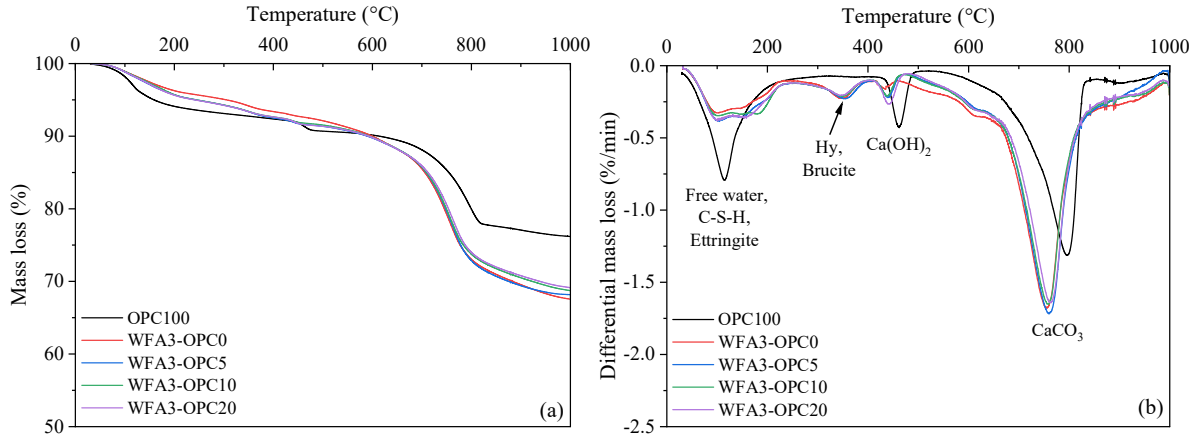

Figure 4-27. TGA curves of WFA3-OPC pastes at 28 days.

As illustrated in Figure 4-28 (a, b) and Figure 4-29 (a, b), no peaks at 400-500 °C were observed among the WBA-OPC pastes. This shows the absence of $Ca(OH)_2$ in these particular pastes. On the other hand, two major endotherms (50-200 °C) and (500-800 °C) were identified, and they tend to increase with OPC content. At 28 days, the mass losses due to the drying of free water and dehydration of C-S-H and ettringite for the WBA-OPC20 became more pronounced compared to the other samples. Besides that, the mass losses at 500-600 °C were attributed to the increased reactivity of quartz before its structural transition from trigonal (α) to hexagonal (β). This chemical reaction typically occurs from 550 to 573 °C (Balek et al., 1995; Földvári, 2011; Klimesch and Ray, 1997).

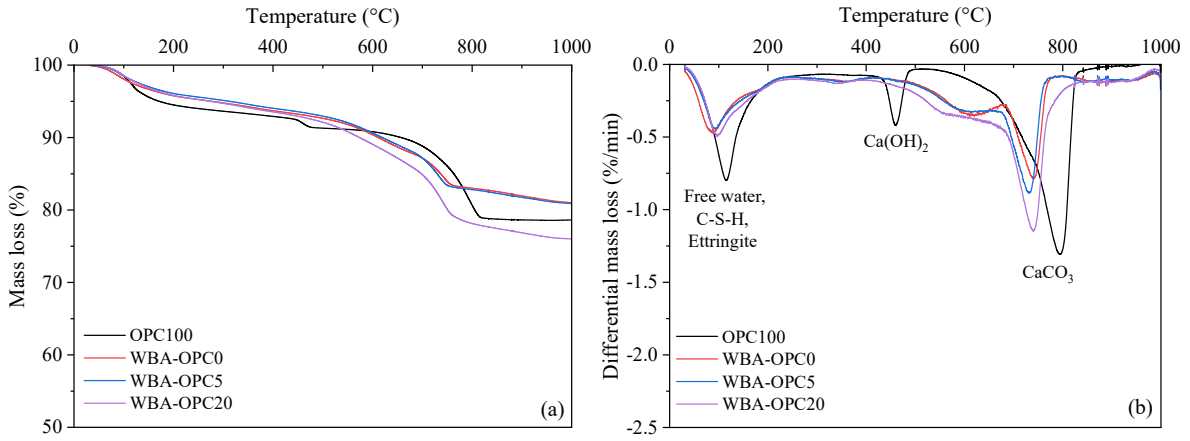

Figure 4-28. TGA curves of WBA-OPC pastes at 7 days.

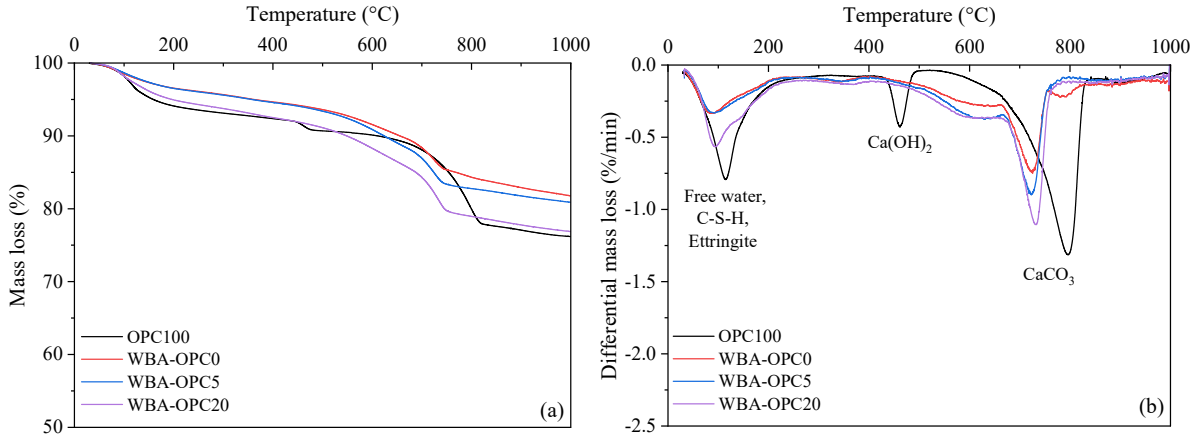

Figure 4-29. TGA curves of WBA-OPC pastes at 28 days.

As shown in Figure 4-30 (a, b) and Figure 4-31 (a, b), all WFA8-OPC pastes exhibited comparable TG and DTG curves. However, the intensities of their endotherms slightly differed. It is noted that the mass losses, due to $Ca(OH)_2$ decomposition, marginally reduced over time, while those of $CaCO_3$ declined slightly. The wide peaks at 600-900 °C represent two close mass losses, which are due to the thermal decomposition of $CaCO_3$ and other carbonates.

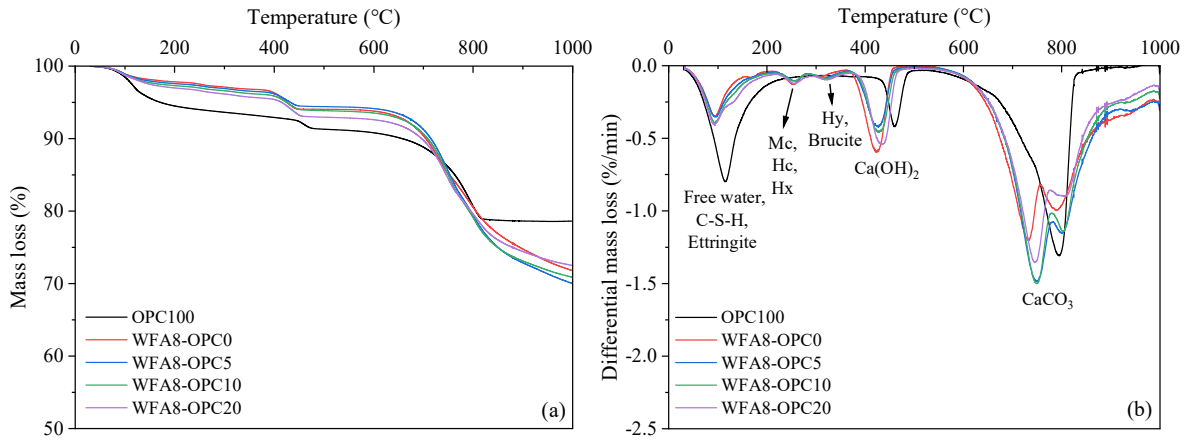

Figure 4-30. TGA curves of WFA8-OPC pastes at 7 days.

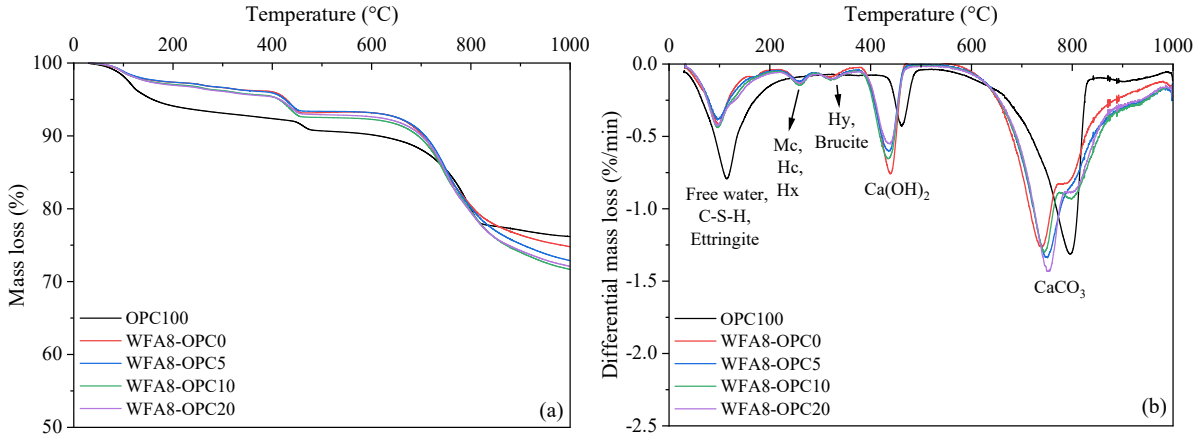

Figure 4-31. TGA curves of WFA8-OPC pastes at 28 days.

Finally, the TG and DTG curves of WFA9-OPC pastes are presented in Figure 4-32 (a, b) and Figure 4-33 (a, b). It occurs that all WFA9-OPC pastes show close thermal stability regardless of their different OPC contents. The intensities of peaks at (25-200 °C), (200-300 °C) and (400-500 °C) remained more or less stable with time, while those from 600 to 900 °C increased slightly. The endotherms at (880-1000 °C), indicating the dolomite decomposition, were observed on WFA9-OPC5 at 7 days and all WFA9-OPC samples at 28 days.

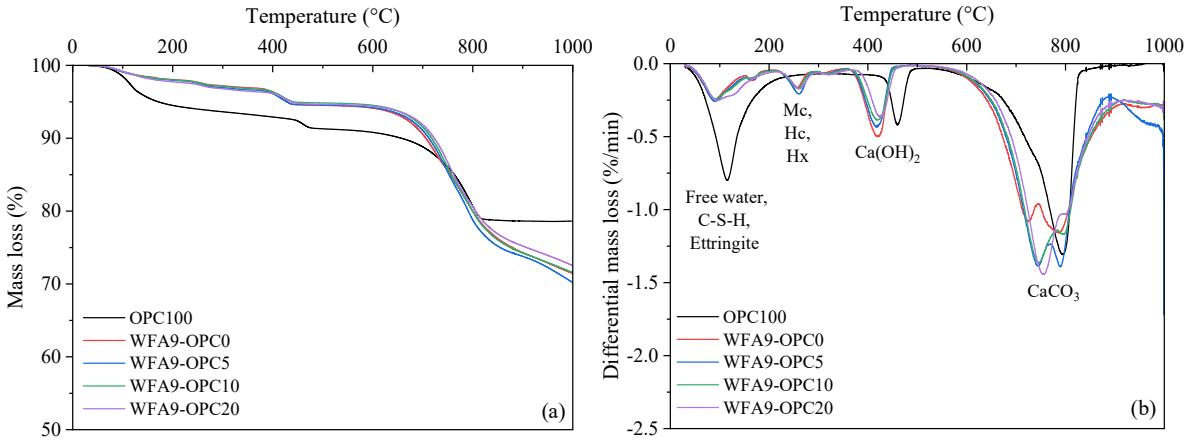

Figure 4-32. TGA curves of WFA9-OPC pastes at 7 days.

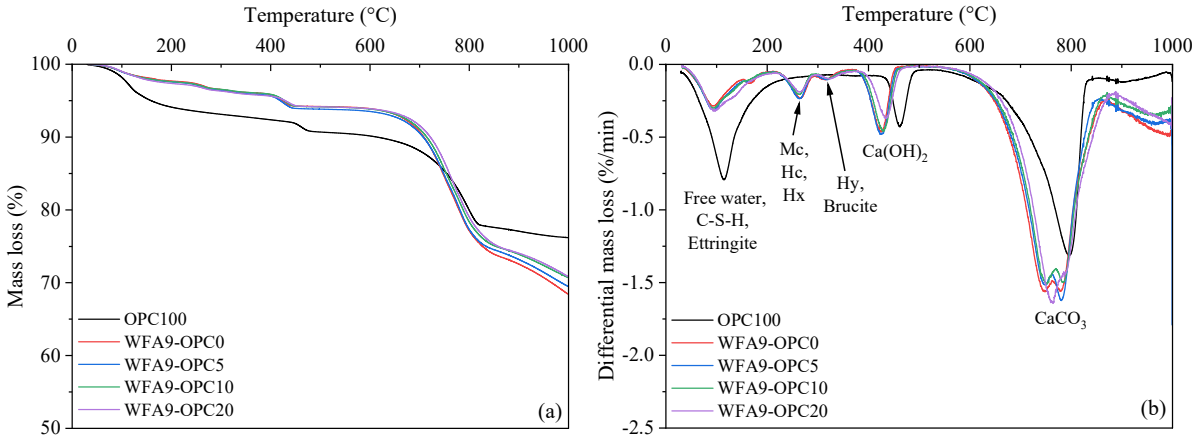

Figure 4-33. TGA curves of WFA9-OPC pastes at 28 days.

It is important to mention that the above-presented TGA results are analogous to the previous findings. Nevertheless, although, in this study, the mass loss at 50-200 °C is ascribed to the decomposition of C-S-H and ettringite, it has been reported that calcium aluminate hydrate (CAH) also occurs in this temperature range (Ohenoja et al., 2020; Wang et al., 2019b). In addition, the endothermic peak at 200-300 °C, attributed to the decomposition of three alumina ferrite mono (AFm) phases such as Mc, Hc and Hx, could also include other AFm phases, such as monosulfoaluminate, Friedel's salt, hydroxy-AFm, strätlingite, etc.(Baquerizo et al., 2015; Frías Rojas, 2006; Puerta-Falla et al., 2015; Zhu et al., 2020). Furthermore, while the endotherm (300-400 °C) was attributed to the dehydroxylation of Hy and H, Ohenoja et al. (2020) detected brucite ($Mg(OH)_2$) in a similar temperature area, specifically at 350 °C.

(h) X-ray diffraction

The mineralogical composition of the wood ash-OPC pastes was examined by X-ray diffraction (XRD) after 28 days of curing. The XRD complemented TGA results and also enabled to identify more crystalline phases in the wood ash-OPC pastes. Due to limited accessibility to the XRD, a few samples, including WBA-OPC0, WBA-OPC20, WFA8-OPC0, WFA8-OPC20 and OPC100, were analysed. The obtained results are shown Figure 4-34 and Figure 4-35 and Table 4-14.

The XRD patterns in Figure 4-34 reveal that calcite ($CaCO_3$) and quartz (SiO_2) were the main components of WBA-OPC0 and WBA-OPC20. However, no traces of neither C-S-H nor ettringite were detected by XRD in these pastes. The estimates demonstrated that the amount of SiO_2 in WBA-OPC0 was considerably higher than that in WBA-OPC20. Also, WBA-OPC0 had a lower quantity of $CaCO_3$ than WBA-OPC20. Hence, the presence of OPC promoted the carbonation of WBA pastes.

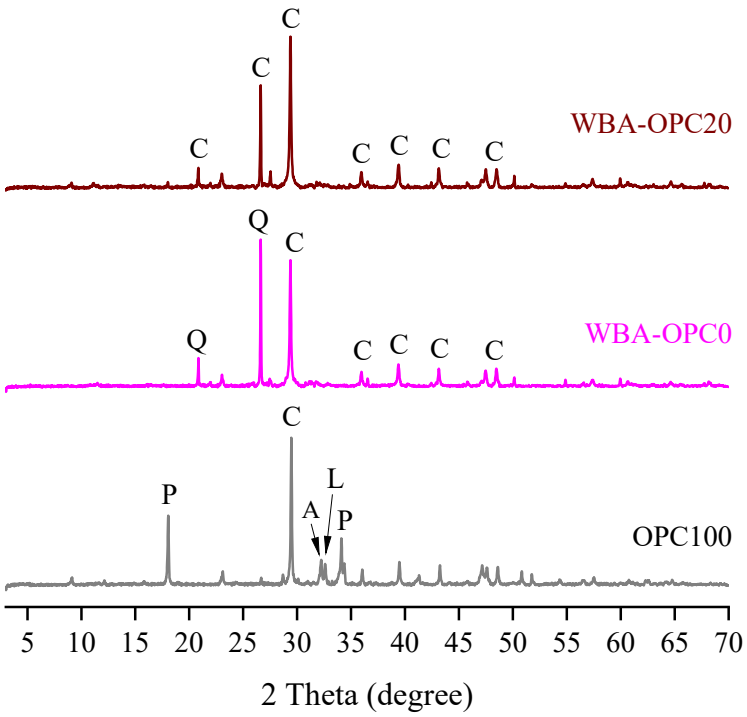

Figure 4-34. XRD patterns of WBA-OPC0, WBA-OPC20 and OPC100 pastes at 28 days. Note: P (Portlandite); C (Calcite); A (Alite); L (Larnite); Q (Quartz).

Furthermore, the XRD patterns of WFA8-OPC0 and WFA8-OPC20, shown in Figure 4-35, revealed that these pastes contained many crystalline phases compared to OPC100. The hydration of WFA8-OPC0 paste led to the transformation of some phases, such as diopside,

orthoclase, etc. and the formation of new compounds, including arcanite, serandite and harmotome.

Besides that, the addition of 20% OPC content in WFA8 paste contributed to the alunite formation and to a significant increase in alite, albite and calcite proportions. It is also worth noting that the amount of portlandite and quartz increased slightly.

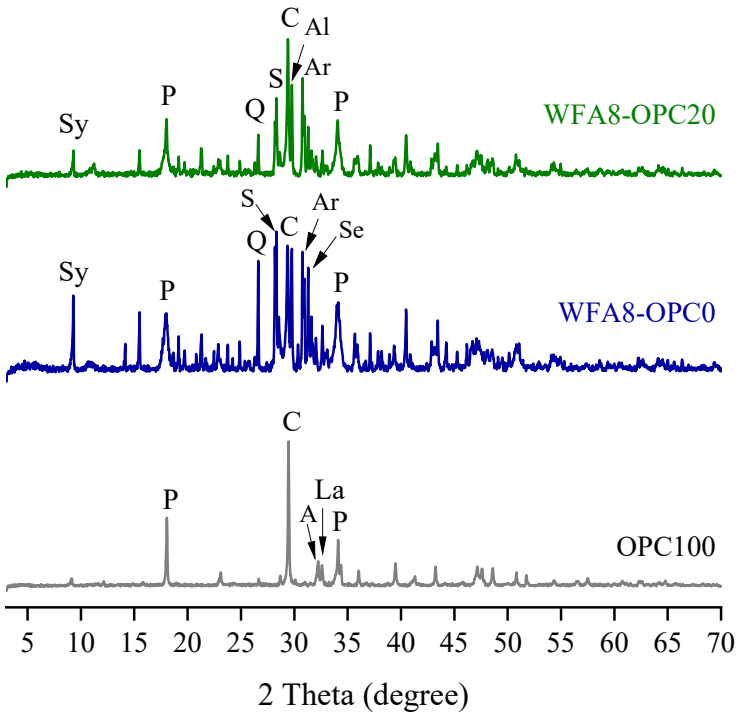

Figure 4-35. XRD patterns of WFA8-OPC0, WFA8-OPC20 and OPC100 pastes at 28 days. Note: P (Portlandite); C (Calcite); A (Alite); La (Larnite); Sy (Syngenite); Q (Quartz); S (Sylvite); Ar (Arcanite); Se (Serandite); Al (Alunite).

All crystalline compounds identified in the wood ash pastes analysed are listed in Table 4-14.

The major phases found include:

- Calcite, alite, belite, portlandite and ettringite for OPC100;
- Calcite, quartz and orthoclase for WBA-OPC0 and WBA-OPC20;
- Syngenite, arcanite, serandite, alite, calcite, albite and harmotome for WFA8-OPC0 and WFA8-OPC20. In addition, alunite appeared in WFA8-OPC20 following the incorporation of OPC.

Table 4-14. Crystalline compounds identified in some of the binding matrices developed in this study at 28 days.

Crystalline compound	OPC100	WBA-OPC0	WBA-OPC20	WFA8-OPC0	WFA8-OPC20
Albite $NaAlSi_3O_8$		++		++	++
Alite Ca_3SiO_5	++			++	++
Alunite $KAl_3(SO_4)_2(OH)_6$					++
Antigorite $Mg_3(Si_2O_5)OH_4$	+				
Arcanite K_2SO_4				++	++
Baryte $BaSO_4$		+	+	+	+
Calcite $CaCO_3$	++	++	++	++	++
Dolomite $CaMg(CO_3)_2$		+	+		
Ettringite $Ca_6Al_2(SO_4)_3(OH)_{12}\cdot 26H_2O$	++			+	+
Gypsum $CaSO_4\cdot 2H_2O$		+	+		
Halite NaCl		Trace	Trace		
Harmotome $Ba_2(Si_{12}Al_4)O_{32}\cdot 12H_2O$				++	++
Larnite or Belite Ca_2SiO_4	++				
Lepodocrocite FeO(OH)				Trace	
Orthoclase $KAlSi_3O_8$		++	++		
Periclase MgO				+	+
Portlandite $Ca(OH)_2$	++			+	+
Quartz SiO_2	+	++	++	+	+
Serandite $Na(MnCa)_2Si_3O_8(OH)$				++	++
Sylvite KCl				+	+
Syngenite $K_2Ca(SO_4)_2\cdot H_2O$				++	++

Note: ++ shows major compounds and + represents minor compounds.

In summary, XRD detected many crystalline phases in the evaluated wood ash-OPC pastes. As noted, WFA8-OPC (0, 20) pastes had more compounds than OPC100 and WBA-OPC (0, 20) pastes. The addition of OPC to WFA8 paste resulted in the alunite formation, while for WBA paste, no changes were observed. This is one of the raisons why WBA-OPC pastes presented low flexural and compressive strength. In terms of the presence of ettringite, portlandite and calcite contents, the XRD results agree with those of TGA.

4.6 Conclusion

In this chapter, thirty different wood ash pastes were designed and prepared. Four batches of wood ashes, including three fly ashes (WFA3, WFA8 and WFA9) and one bottom ash (WBA) were used as the main components of the pastes. In addition, natural hydraulic lime (NHL) and ordinary Portland cement (OPC) were incorporated as mineral additives to improve the strength. At desired curing ages, the setting, mechanical and microstructural properties of the resulted wood ash pastes were investigated.

Regarding setting, the wood fly ash WFA8 presents longer initial and final setting time. However, the addition of 5, 10 and 20 % NHL or OPC contents accelerated significantly the setting of the wood ash pastes. For NHL-contained pastes, the initial and final setting time decreased from 25 to 12.5 hours and 56 to 24 hours, respectively. In the case of OPC-contained pastes, the initial setting time reduced from 25 to 4.5 hours while the final setting time declined from 56 to 30 hours.

Moreover, the mechanical tests showed that the wood ash pastes containing NHL exhibited lower flexural and compressive strengths than those blended with OPC. Overall, for the NHL-contained pastes, the flexural strength and compressive strength varied from 0.02 to 1.12 MPa and 0.05 to 2.59 MPa, simultaneously. Concerning OPC-contained pastes, the flexural strength comprised between 0.04 and 2.72 MPa, while the compressive strength was in the range of 0.12 and 5.49 MPa. These findings are comparable to those of building materials with similar wood ash contents.

It was noted that the flexural and compressive strength of wood ash highly depended on the type of wood ash, NHL or OPC content, bulk density, mass and curing time. The influence of NHL on the mechanical performance of the wood ash pastes was less pronounced compared to OPC. The trend in strength development among the wood ashes received in a wet state was different from that of the wood fly ashes received in a dry state. For example, the flexural and compressive of the WBA pastes declined as the curing time increased, whereas for WFA8 and WFA9 pastes, the 28-day flexural and compressive strengths were superior to those at 7 days. In general, the use of 5 and 10 % NHL or OPC moderately improved the mechanical performance of the wood ash pastes. Considering only NHL-contained pastes, the highest R_f and R_c values were obtained from the WFA3, WFA8 and WFA9 pastes containing 20 % NHL. On the other hand, among the OPC-contained pastes, the excellent flexural and compressive strengths were found on WFA8 and WFA9 pastes containing 20 % OPC.

Furthermore, in terms of the microstructure, the major phases identified by scanning electron microscopy (SEM) and thermogravimetric analysis (TGA) were ettringite, calcium silica hydrates (C-S-H), portlandite and calcite. A more profound investigation made using x-ray diffraction (XRD) on some wood ash-OPC pastes revealed the formation of alunite following the addition of OPC in WFA8-OPC20 at 28 days. In contrast, no impact of OPC was noted in WBA-OPC20 at a similar curing age.

Ultimately, this chapter has proven that WFA8 and WFA9 have better mechanical properties than WFA3 and WBA. Due to time constraints, it would not be possible to use both WFA8 and WFA9 in the following phases of this study. Therefore, only two WFA8 pastes containing 10 and 20 % OPC are selected and will be used as binding matrices for sunflower pith mortars and prefabricated sunflower bark building elements that we intend to develop in Chapters 5 and 6, respectively.

Chapter 5: Valorization of sunflower pith in mortar for implementing by projection process

In this chapter, six different sunflower pith mortars will be produced using two low-carbon binders developed from wood fly ash and ordinary Portland cement. The wood fly ash represents 80-90 % while the cement accounts for 10-20 % of the formulation of the binder. In this experimental program, the sunflower pith particles are added into the mixtures as aggregates in a proportion ranging from 5, 10 and 15 % by mass of binder.

The mechanical, microstructural, thermal, hygroscopic properties of the produced mixtures will be examined at different curing ages (7, 14, 28, 56, 90 days). Afterwards, the obtained results will be presented and discussed, before drawing the main conclusions.

5.1 Mix proportion

Six distinct sunflower pith (SP) mortars for implementation by projection (or spraying) were prepared based on two wood ash-based binders and sunflower pith particles. The binding matrices were composed of 80 % and 90 % of wood fly ash (WFA8) contents mixed with ordinary Portland cement (OPC) at levels ranging from 10 to 20 % by mass of WFA8. The resulted formulations are M1: 80 % WFA8 + 20 % OPC and M8: 90 % WFA8 + 10 % OPC. The control paste (M0) made of 100 % wood fly ash was also prepared.

In this experimental phase, the sunflower pith particles (SP) were used as aggregates of the mixtures and their contents were 5, 10 and 15 % by mass of the binder. The objective is to study the effect of plant particles on the performance of binders with high wood fly ash content. The notation and composition of all SP formulations are presented in Table 5-1. Besides, Table 5-2, Figure 5-1 and Figure 5-2 demonstrate the mass and volume accounted for by raw material, including mixing water, in sunflower bark mortar formulations.

Table 5-1. Composition of the sunflower pith mortars (by mass).

Mix notation	Binder composition	Aggregates	W/A ratio	W/B ratio
M0	100 % WFA8		0.50	
M1	80 % WFA8 + 20 % OPC		0.50	
M2	80 % WFA8 + 20 % OPC	5 % SP		1.10
M3	80 % WFA8 + 20 % OPC	10 % SP		1.60
M4	80 % WFA8 + 20 % OPC	15 % SP		2.20
M8	90 % WFA8 +10 % OPC		0.50	
M9	90 % WFA8 + 10 % OPC	5 % SP		1.10
M10	90 % WFA8 + 10 % OPC	10 % SP		1.60
M11	90 %WFA8 + 10 % OPC	15 % SP		2.20

Table 5-2. Mix proportion of the sunflower pith mortars (by volume).

Mix notation	WFA8 (%)	OPC (%)	SP (%)	Water (%)
M0	84.2	0.0	0.0	15.8
M1	79.4	5.7	0.0	14.9
M2	36.8	2.6	41.7	18.9
M3	24.5	1.8	55.5	18.3
M4	18.2	1.3	61.8	18.7
M8	82.0	2.6	0.0	15.3
M9	40.0	1.3	40.4	18.3
M10	26.9	0.9	54.3	17.9
M11	20.1	0.6	60.9	18.4

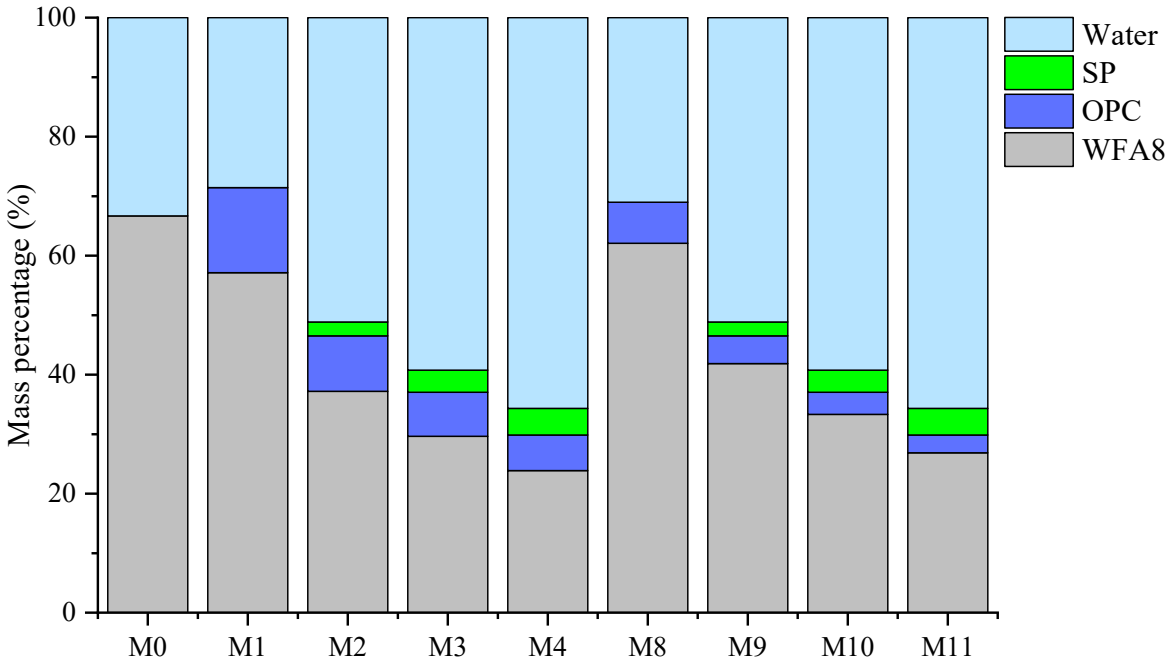

Figure 5-1. Mass composition of the sunflower pith mortars.

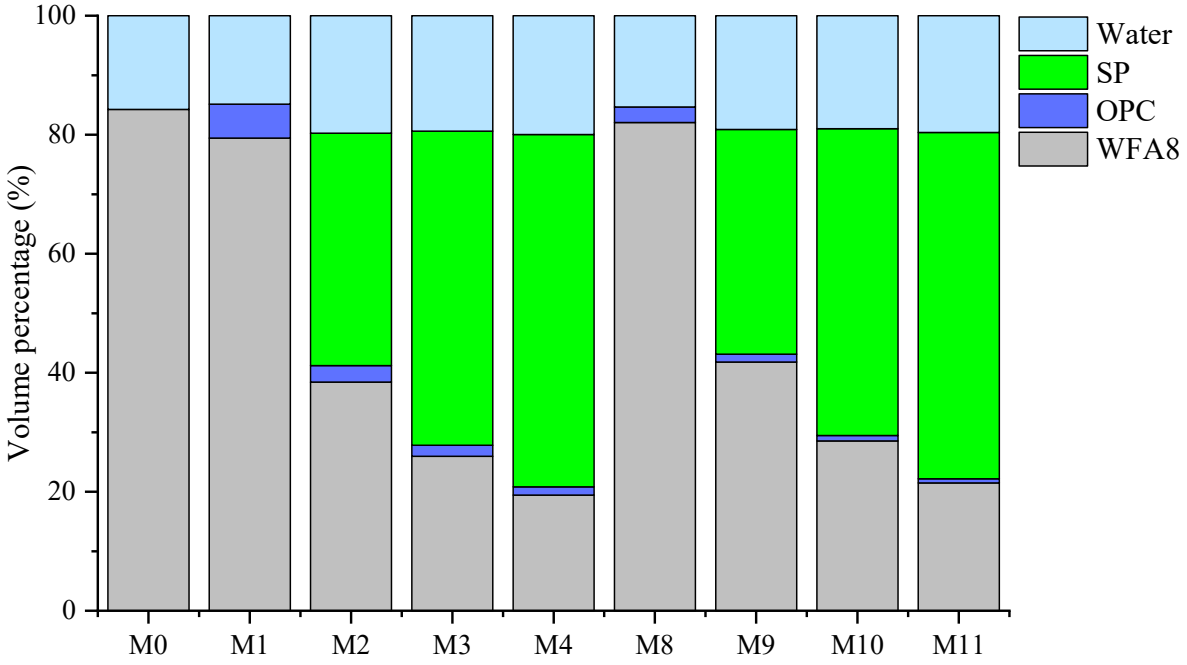

Figure 5-2. Illustration of volume occupied by each constituent of sunflower pith mortars.

As can be seen on Figure 5-1 and Figure 5-2, sunflower pith particles present a low mass but they occupy a large volume.

5.2 Preparation of sunflower pith mortars

The sunflower pith mortars were prepared using an automatic standard mortar mixer (Controlab) according to NF EN 196-1 (Afnor, 2016). The dry materials, namely WFA8, OPC and SP were weighed using an electronic balance (accuracy: ± 0.01 g), placed in a stainless mixing bowl and mixed with tap water. The mixing duration is 4 minutes including the breaks. The detailed sequence of mixing is shown in Table 5-3.

Table 5-3. Mixing sequence.

Step	Speed (rpm)	Time (s)
Introduction of the dry materials. First, WFA8, followed by OPC and lastly SP.	-	-
Addition of the water	-	
Mixing at a low speed	140	60
Mixing at a high speed	285	30
Short break - scraping the bowl	-	30
Long break	-	60
Mixing at a high speed	285	60
Cumulative mixing time (breaks included)	-	240

Note: rpm: round per minute.

It is important to note that the quantity of water added to the mixtures was estimated taking into account the water demand for the binding matrix and the water absorption capacity of sunflower pith. Since the SP mortars to be produced are intended to be manufactured by spraying process, the mixtures should have a good flowability and cohesiveness. Therefore, to determine the appropriate water-to-binder (W/B) ratio, a pre-test was performed on SP mortars by adjusting the amount of mixing water until a desired mix texture was achieved.

The fresh sunflower pith mortars intended for mechanical testing were poured into steel moulds of dimensions: 40×40×160 mm^3. Whilst, the fresh mortar mixtures for thermal conductivity measurement were cast into plastic moulds with dimensions: 150×150×50 mm^3.

Due to the morphology of sunflower pith, the Proctor compaction was not applied on the mortars. However, a light compaction (three strokes) was performed with a piece of wood to eliminate voids within the fresh SP mortar sample.

The sunflower pith mortars were demoulded 48 h after casting. Although, the samples were sufficiently cured, they still contained a high-water content and were weak. Thus, the demoulding was done very carefully.

After mixing, the fresh sunflower pith mortar mixtures were poured and kept in the moulds until the required demoulding time. The SP mortar samples were demoulded after 48 h and stored in the laboratory at ambient temperature (T = 23.6 °C) and relative humidity (RH = 48 %) conditions until the desired testing age. The T and RH conditions have been monitored during the drying process. As shown in Figure 5-3, the temperature and relative humidity in the laboratory fluctuated as they were dependent on the actual weather conditions. Note that the temperature and relative humidity data collection was done as follows:

- Two devices for measuring the temperature and relative humidity were used;
- The surveys were taken on weekdays, excluding weekends and holidays;
- The readings were recorded three times per day (morning, noon, evening);
- At each time of the survey, two values were recorded for each parameter.

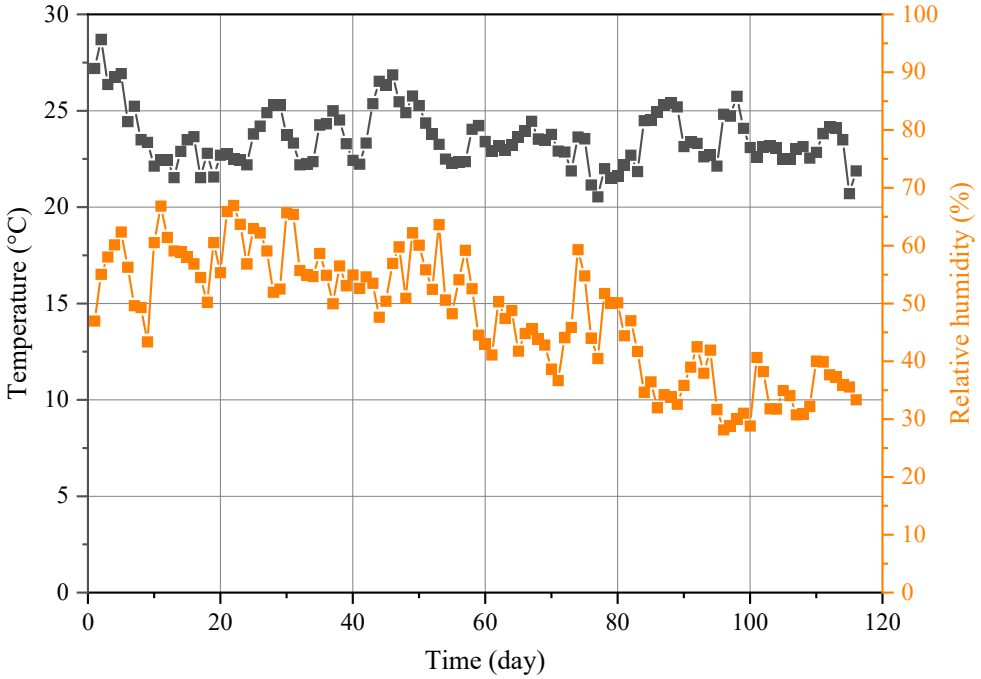

Figure 5-3. Data of temperature and relative humidity collected during the curing time.

According to Figure 5-3, the average temperature was 23.6 ºC, while the minimum and maximum temperatures varied between 20.5 to 28.7 ºC. The average relative humidity was equal to 48 %, whereas the minimum and maximum RH ranged from 28.2 to 67.0 %.

5.3 Experimental methods

5.3.1 Mechanical properties

The flexural and compressive strengths were determined using a hydraulic press machine (Shimadzu, model AGS-X), at a loading rate of 2 mm/min. The three-point flexion test was carried out on the prismatic SP-based mortar samples of dimensions 40×40×160 mm^3. The half prisms remained after the flexural strength test were cut with a Bosch metal saw into cubic samples of dimensions 40×40×40 mm^3. The obtained cubes were used to determine the compressive strength. Both flexural and compressive strengths were examined at five different curing ages, namely 3, 7, 14, 28, 56 and 90 days. The measurements were made in triplicate for flexural strength, while for compressive strength, four samples were considered.

Furthermore, the elastic modulus (E) indicating the stiffness of sunflower bark mortars was calculated as the slope of the linear part of the strain-stress curve obtained from the compressive strength test results. This method has been previously used in (Elfordy et al., 2008; Zmamou, 2015).

5.3.2 Microstructural properties

A Hitachi Tabletop Microscope TM3000 was used to observe the microstructure of SP mortars. The analysis was performed on ground mortar samples in analytical mode with an energy of 5 kV and a distance (WD) of 12 mm. The observations were made after 28 days of curing.

5.3.3 Thermogravimetric analysis

The thermogravimetric measurements on sunflower pith mortar samples were conducted using a NETZCH-TG 209 F1 instrument at 28 days, following a similar experimental setup as in section 4.4.4 of Chapter 4. The TGA allowed the detection of products from the hydration and carbonation reactions. The hydration of the samples was stopped by solvent exchange method using isopropanol. Besides, the amounts of portlandite and calcite were also calculated by means of tangent method.

5.3.4 Formation of hydration products

A Bruker D8 Advance x-ray diffractometer (XRD) was employed to investigate the mineralogical composition of the SP mortars. This analysis allowed to identify the crystalline compounds in the SP mortar samples after 28 days of curing. As previously mentioned in Chapter 3, the XRD had 2 Theta (θ) configuration using copper anode Cu Kα radiation generator (λ = 1.540 Å) and was equipped with LynxEye OD detector. The double diffraction

angle (2θ) ranged from 3 to 70 with step size of 0.015° and acquisition speed of 0.5 seconds per step. The scanning graphs were treated using DIFFRAC.EVA software.

The pre-treatment of the sunflower pith mortar samples was made according to RILEM TC-238 SCM recommendation on hydration stoppage by solvent exchange (Snellings et al., 2018), as previously described in section 4.4.5 of Chapter 4.

5.3.5 Thermal conductivity

The thermal conductivity of SP mortars was measured using an instrument and settings similar to those in section 3.2.11 of Chapter 3. Nevertheless, it is noteworthy that there were slight modifications in terms of sample preparation and conditioning. Prior to testing, the mass and dimensions of each sample were taken. The latter was placed in a mould made of expanded polystyrene with open top and bottom sides, and then covered on both sides with two plastic rubber sheets. The measurements were performed on sunflower pith mortars cured in the laboratory and ambient temperature and relative humidity conditions at 28, 56, 90 and 120 days of age.

5.3.6 Hygroscopic properties

The water adsorption and desorption isotherms of SP mortar samples were determined using a ProUmid Dynamic Vapour Sorption (DVS) under similar experimental settings as in section 3.2.10. The analysis was performed on the SP mortar pieces with a mass between 1.3 and 2.6 g placed in aluminium cups. Note that the mass of the control samples (without sunflower particles) varied from 2.1 to 2.7 g.

5.3.7 Wetting and drying cycles

The behaviour of SP mortars under fluctuating temperature and humidity conditions was assessed through a series of wetting and drying cycles from the 8^{th} to 28^{th} day of curing. The experimental setup is shown in Figure 5-4. One wetting and drying cycle corresponded to 24h of immersion in a water bath and 24h of drying in a ventilated oven at 50 °C. To illustrate the impact of wetting and drying cycles on the samples over time, the mass of each sample was recorded before wetting and drying. In addition, the flexural and compressive strengths of the latter were determined at the age of 28 days. Eventually, the obtained results were compared to those of the samples cured in laboratory at ambient temperature and relative humidity conditions.

Figure 5-4. Sunflower pith mortar samples during the wetting and drying cycles experiment.

5.4 Results and discussion

5.4.1 Mechanical properties

(a) Behaviour of sunflower pith-based mortars under flexural and compressive strengths tests

The incorporation of sunflower pith (SP) modified the mechanical behaviour of the lightweight mortars. Figure 5-5 (a) and (b) shows typical behaviours of the control pastes and some SP mortar samples under the flexural strength test at 28 days. It is apparent that the samples without SP content had higher resistance to flexion stress and were quite brittle compared to the SP mortars. In addition, no deformations were noticed on the control pastes before failure; conversely, moderate deformations were visible on the SP mortar samples.

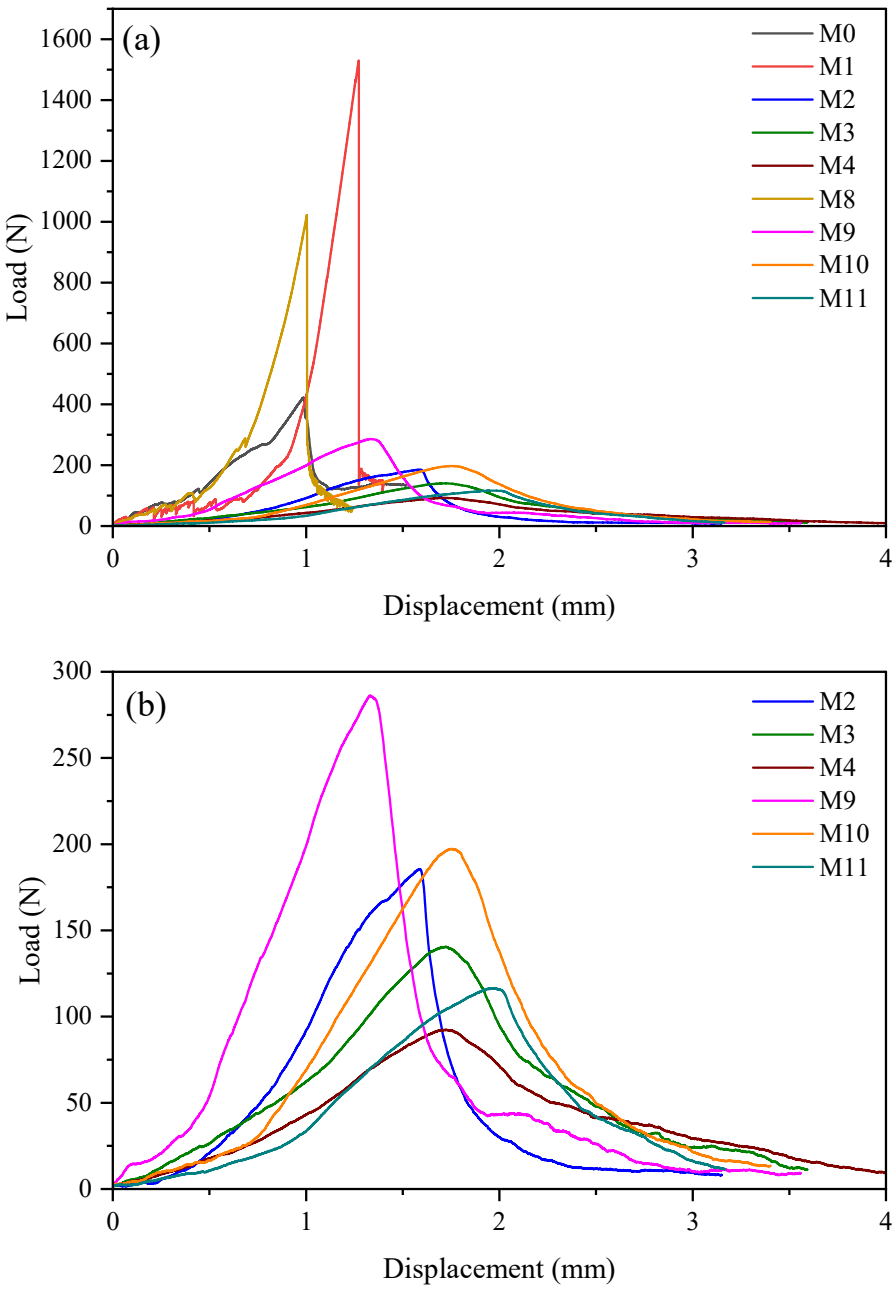

Figure 5-5. Typical examples showing the behaviour of sunflower pith mortars under flexural strength test at 28 days.

When the maximum load (Fmax) was achieved, the crack appeared of the SP mortar sample and the latter continued to deform until it was no longer able to resist the load. The crack was typically a straight line, extending from the bottom to top and through the middle of the prismatic sample. At Fmax, SP particles did not hold together two parts of the sample separated by the crack; therefore, the sample was easily failed.

Furthermore, the load-displacement curves given in Figure 5-6 (a, b), demonstrate the difference between the behaviour of the wood ash-based binders (M1-1, M8-2) and SP mortars, during the compressive strength test at 28 days of curing.

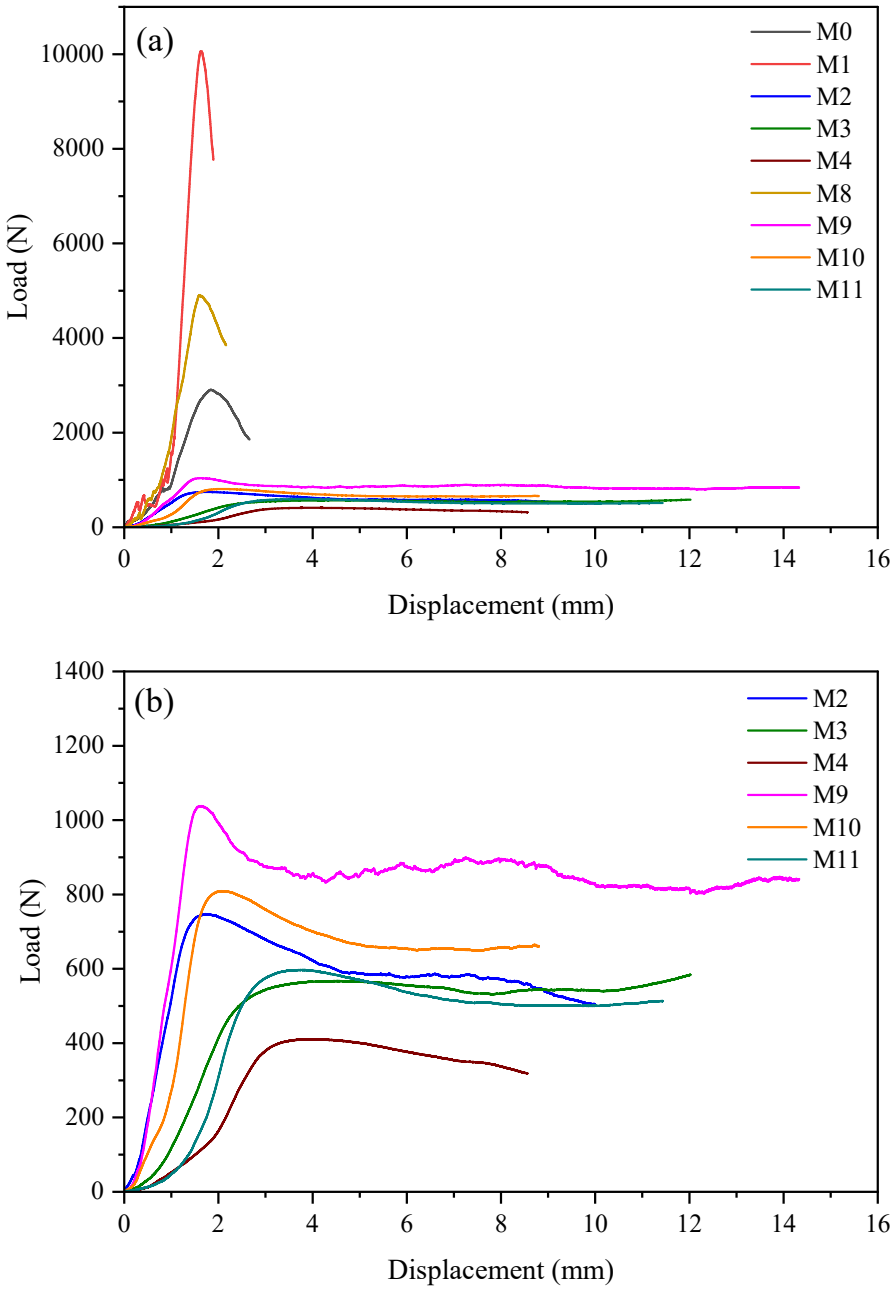

Figure 5-6. Typical examples illustrating the behaviour of sunflower pith mortars under compressive strength test at 28 days.

At first, it is important to mention that the addition of SP led to a significant reduction in compressive strength. Secondly, unlike the wood ash binders, once the ultimate stress was reached, the SP mortar samples did not break. Instead, the stress slightly reduced and then remained constant (or formed a plateau) while the strain continued to increase. At this point,

the deformations of the SP mortar samples were quite obvious as their height decreased with increasing test duration and their cross-sectional area was enlarged, as shown in Figure 5-7.

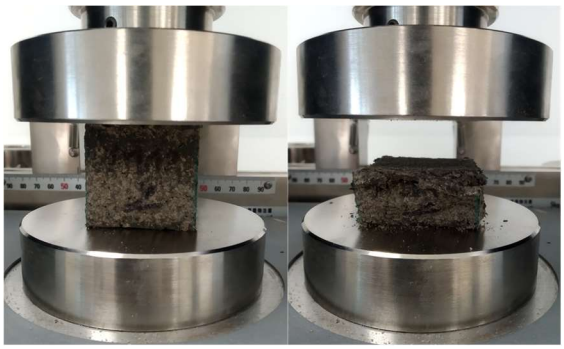

Figure 5-7. M11-2 sample before and after the compressive strength test at 28 days.

In comparison with the wood ash-based binders, the sunflower pith mortars typically exhibited a ductile behaviour and substantially low flexural and compressive strengths at 28 days. Cérézo (2005) has noticed identical behaviour in the hemp concretes that the author studied. The stress-strain curves of different hemp concretes revealed that the concrete mixture with high concentration of the binder presented an easily identifiable stress peak compared to the concrete that was rich in plant particles. Considering a noticeable plateau at the maximum stress, the author concluded that the concrete with high hemp shiv contents presented a stronger ductile behaviour than other hemp concretes under cyclic compression after 1 year of curing (Cérézo, 2005).

Furthermore, Arnaud and Gourlay (2012) also observed a long ductility plateau on the stress-strain curves of hemp concretes with lower binder contents. The authors have attributed this behaviour to the dominant quantity of hemp particles that prevented the binder matrix from acting as a major influence on the mechanical performance of the concrete.

Other than that, in some instances, the stress-strain curves of bio-based concretes may present an increase in stress instead of the formation of a plateau. Elfordy et al. (2008) have declared that in most cases, the deformation of compressed hemp concrete sample does not cause the fracture. Rather, it leads to a continuous increase in stress as a result of irreversible compaction of the porous material.

(b) Flexural strength

The flexural strengths of the SP-based mortars at 7, 14, 28, 56 and 90 days of curing are presented in Figure 5-8 (a, b) and Table 5-4. The binding matrices (M1 and M8) present higher flexural strength than the mortar mixtures containing SP particles. It should also be noted that

the binder with a high concentration of OPC showed the best R_f at all ages. For the first binder M1, R_f ranged from 1.49 MPa at 7 days to 2.77 MPa at 90 days. Regarding the second binder M8, R_f improved from 0.76 MPa at 7 days to 1.94 MPa at 90 days. The remarkable increase in flexural strength between 7 and 28 days can be mainly attributed to the hydration reactions of OPC present in the mix proportion. Moreover, the increase in R_f from 28 to 90 days can be explained by the pozzolanic activity of the wood fly ash WFA8.

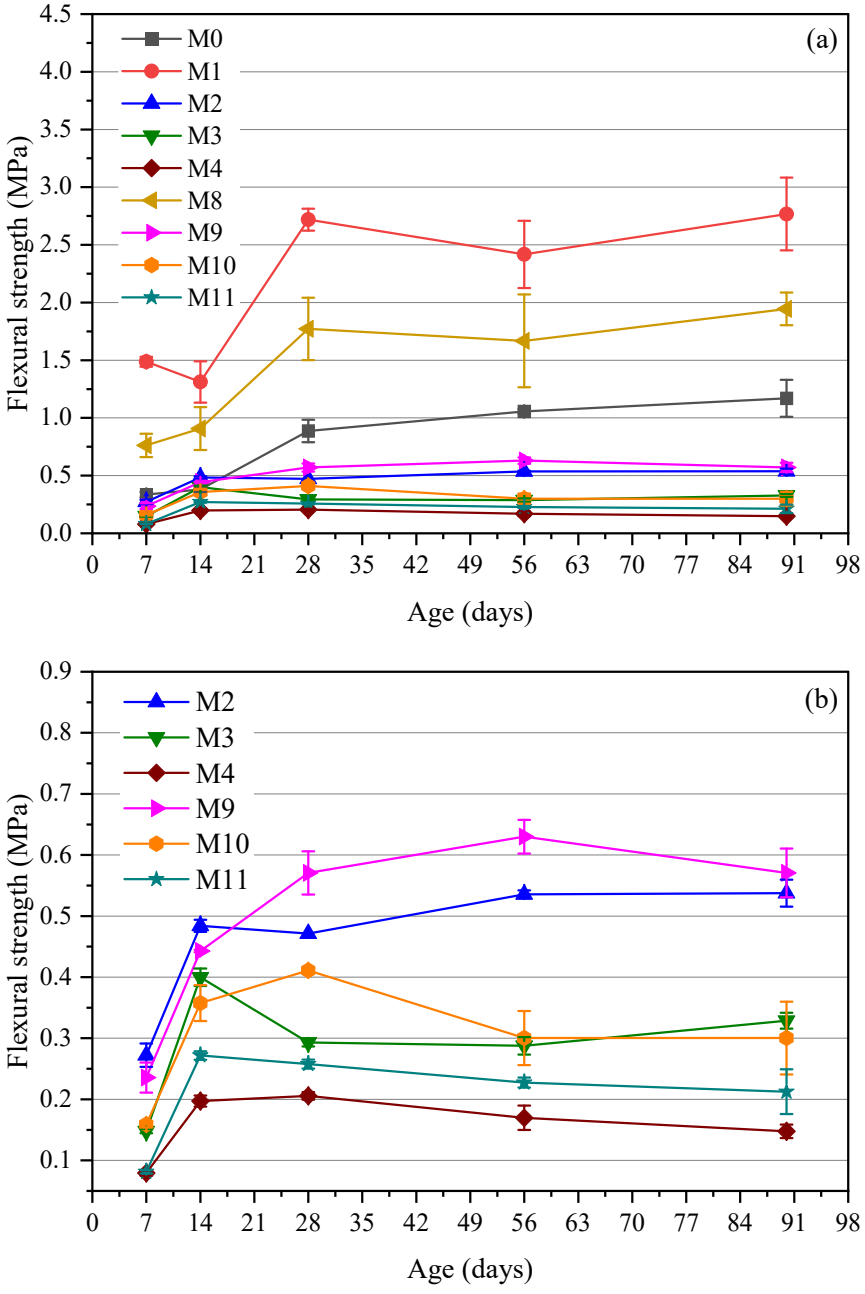

Figure 5-8. Flexural strength of sunflower pith mortars at different curing ages. (a) all mixtures (b) only mixtures containing sunflower pith.

Concerning the sunflower pith mortars, the R_f is comprised in the range of 0.08-0.27 MPa at 7 days and 0.15-0.57 MPa at 90 days. This shows that the flexural strength increased with

increasing curing time. In addition, it should be pointed out that the R_f of sunflower pith mortars has remarkably improved between 7 and 14 days. Overall, slight R_f fluctuations were noticed on the tested samples from 28 to 90 days.

Table 5-4. Flexural strength data of all sunflower pith mortars from 7 to 90 days.

Mix notation	Flexural strength (MPa)				
	7 days	14 days	28 days	56 days	90 days
M0	0.33 ± 0.02	0.38 ± 0.02	0.89 ± 0.10	1.06 ± 0.02	1.17 ± 0.16
M1	1.49 ± 0.04	1.31 ± 0.18	2.72 ± 0.10	2.42 ± 0.29	2.77 ± 0.32
M2	0.27 ± 0.02	0.48 ± 0.01	0.47 ± 0.00	0.54 ± 0.01	0.54 ± 0.02
M3	0.15 ± 0.00	0.40 ± 0.01	0.29 ± 0.01	0.29 ± 0.01	0.33 ± 0.01
M4	0.08 ± 0.00	0.20 ± 0.01	0.21 ± 0.01	0.17 ± 0.02	0.15 ± 0.01
M8	0.76 ± 0.10	0.91 ± 0.19	1.77 ± 0.27	1.67 ± 0.40	1.94 ± 0.14
M9	0.24 ± 0.02	0.44 ± 0.00	0.57 ± 0.04	0.63 ± 0.03	0.57 ± 0.04
M10	0.16 ± 0.00	0.36 ± 0.03	0.41 ± 0.00	0.30 ± 0.04	0.30 ± 0.06
M11	0.08 ± 0.00	0.27 ± 0.01	0.26 ± 0.01	0.23 ± 0.01	0.21 ± 0.04

The above results fall in line with previously reported by other authors. The flexural strength of hempcrete blocks with densities between 522 and 581 kg/m^3, was found to be between 0.75 and 1.20 MPa, respectively (Elfordy et al., 2008). Similarly, Walker et al. (2014) have also studied the mechanical properties of hemp-lime concrete at two curing ages, and the findings revealed a flexural strength of 0.06-0.12 MPa at 3 months and 0.1-0.2 MPa at 1 year.

(c) Compressive strength

The compressive strength (R_c) results of sunflower pith mortars at the age varying from 7 to 90 days are given in Figure 5-9 (a, b) and Table 5-5. It is apparent that the compressive strength increases not only with increasing curing time but also, with the concentration of the binder. In fact, the samples without SP content presented greater R_c than those containing SP particles. The compressive strength of the mixtures decreased as the amount of SP increased. At 7 days, the compressive strengths of the binding matrices M1 and M8 was equal to 3.72 and 1.30 MPa, respectively. At the same time, SP mortars presented the R_c ranging between 0.11 to 0.29 MPa.

It should be noted that, a pronounced growth in compressive strength was noticed between 7 and 28 days for the binders while for SP mortars, it was observed in the time frame from 7 to 14 days. From 28 days, the R_c trend gradually increased for binding matrices. On the other hand, for SP mortars, it remained fairly stable with minor variations. At 90 days, the compressive strengths of M1 and M8 reached 7.04 and 4.05 MPa, respectively. Simultaneously, SP mortars showed the compressive strengths comprising between 0.23 and 0.59 MPa.

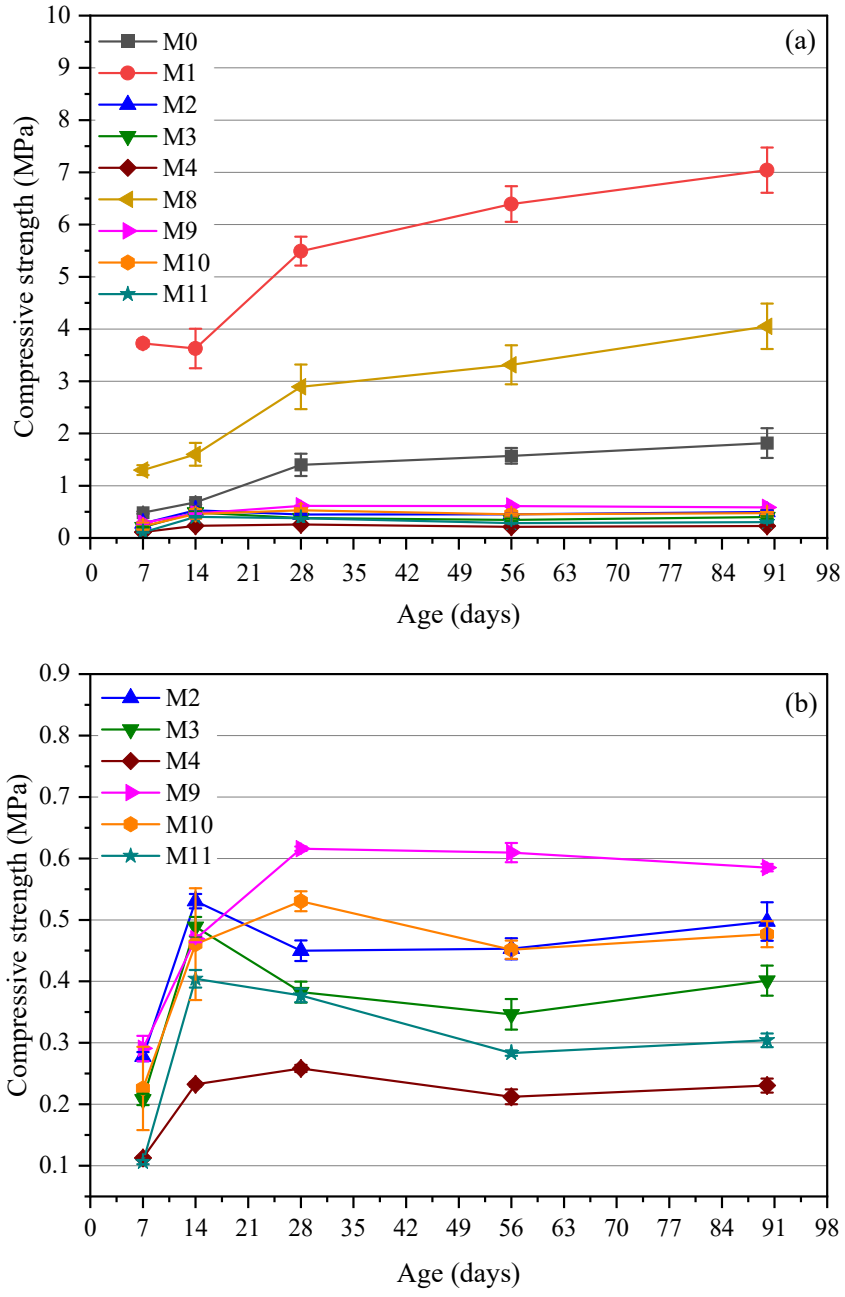

Figure 5-9. Compressive strength of sunflower pith mortars at different curing ages. (a) all mixtures (b) only mixtures containing sunflower pith.

In addition to the graphs, the compressive strength results of the investigated samples have been summarised in Table 5-5.

Table 5-5. Compressive strength of the sunflower mortars at different curing ages.

Mix notation	Compressive strength (MPa)				
	7 days	14 days	28 days	56 days	90 days
M0	0.48 ± 0.02	0.68 ± 0.04	1.40 ± 0.21	1.57 ± 0.15	1.82 ± 0.28
M1	3.72 ± 0.06	3.63 ± 0.38	5.49 ± 0.28	6.39 ± 0.34	7.04 ± 0.43
M2	0.28 ± 0.01	0.53 ± 0.01	0.45 ± 0.02	0.45 ± 0.02	0.50 ± 0.03
M3	0.21 ± 0.01	0.49 ± 0.02	0.38 ± 0.02	0.35 ± 0.02	0.40 ± 0.02
M4	0.11 ± 0.00	0.23 ± 0.00	0.26 ± 0.01	0.21 ± 0.01	0.23 ± 0.01
M8	1.30 ± 0.09	1.60 ± 0.22	2.89 ± 0.43	3.32 ± 0.37	4.05 ± 0.44
M9	0.29 ± 0.02	0.47 ± 0.01	0.62 ± 0.00	0.61 ± 0.02	0.59 ± 0.01
M10	0.23 ± 0.07	0.46 ± 0.09	0.53 ± 0.02	0.45 ± 0.01	0.48 ± 0.02
M11	0.11 ± 0.00	0.40 ± 0.01	0.38 ± 0.01	0.28 ± 0.00	0.30 ± 0.01

The low compressive strength of the sunflower pith-based mortars was ascribed to:

- High proportion of sunflower pith particles in the mixture. As previously demonstrated in Figure 5-2, sunflower pith represented a significant volume fraction of the mortar mixtures.
- Physical properties of SP that are not favourable for strength development. For example, in Chapter 3, it was found that the bulk density of SP is around 20.6 kg/m^3, which is considerably lower compared to other bio-based aggregates (sunflower bark, hemp shiv, etc.). Other than that, it was noticed that SP is characterised by a high porosity. The rate of open and closed porosities is equal to 97.1 % and 28.8 %, respectively.
- The water competition between SP and the binding matrix which could have played a role in the lower mechanical performance of the mortars. In fact, it is assumed that due to the greater water absorption capacity of SP, a large quantity of the mixing water was absorbed by its pores, hence leaving a limited amount of water for hydration and pozzolanic reactions of the binding matrix (wood ash and OPC). A similar behaviour has been noticed on lime-hemp concrete. Arizzi et al. (2015) claimed that hemp particles absorb the majority of the water from the matrix and thus induce the superficial deposition and poor adhesion of the lime to hemp particles.
- The chemical composition of SP which could have interfered with the bonding and interactions between the aggregates and the binding matrix. Barbieri et al. (2020) attributed the lower compressive strength of wheat husk concrete to weaker particle-binder interface. Furthermore, as summarised earlier in Table 2-8 of Chapter 2, many studies have shown that the setting and strength development problems in bio-based concretes are due to numerous chemical compounds, such as monosaccharides, polysaccharides phenolic

compounds in lignocellulosic plant particles, degradation products due to mortar conditions, etc.

Furthermore, the alkalinity of the bio-based materials can also affect the strength development. Therefore, a comparison between the pH of the four binding matrices (OPC100, M0, M1, M8) and four sunflower pith mortar formulations (M2, M4, M9, M11) was made and the results are given in Figure 5-10.

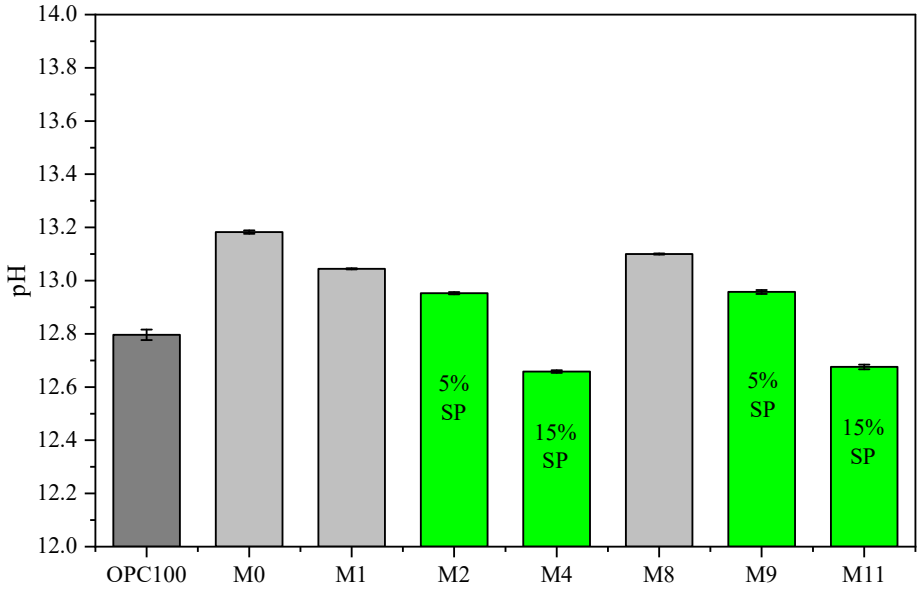

Figure 5-10. pH of some hardened mineral binding matrices and SP-based mortars.

It is apparent that the pH of M2, M4, M9 and M11 decreases with increasing sunflower pith content. On the other hand, considering the binding matrices, the presence of wood fly ash (WFA8) clearly increased the pH of the pastes. The pH has increased from 12.80 for the paste composed of 100 % cement (OPC100) to 13.18 for M0 (paste made of 100 % WFA8). The pH of the pastes containing WFA8 is higher than that sunflower pith mortars. This drop in pH can be attributed not only to the dissolution of water-soluble compounds from sunflower pith but also, its initial lower pH (6.9-7.0).

Comparing with the mechanical performance results shown in Figure 5-8 and Figure 5-9, it is clear that the flexural and compressive strengths of M2, M4, M9 and M11 decrease with the decrease in pH. In contrast, for the binding matrices, the increase in pH led to reduction in the above strength parameters. As previously presented in Chapter 4, the 28-day flexural (R_f) and compressive (R_c) strengths for OPC100 are 3.14 and 32.5 MPa, respectively while for M0, R_f and R_c equal to 0.89 and 1.51 MPa, simultaneously.

In brief, as can be seen in Table 2-7 of Chapter 2, the compressive strength of the sunflower pith mortars presented above are in the same range as those found in the literature.

(d) Relationship between compressive strength and flexural strength at 28 days

Based on the experimental data provided in sections 5.4.1 (b) and 5.4.1 (c), it is speculated that the formulations with high compressive strength also have elevated flexural strength. To approve this assumption, a relationship between compressive strength and flexural strength of sunflower pith mortars was established from the results obtained at 28 days, as shown in Figure 5-11.

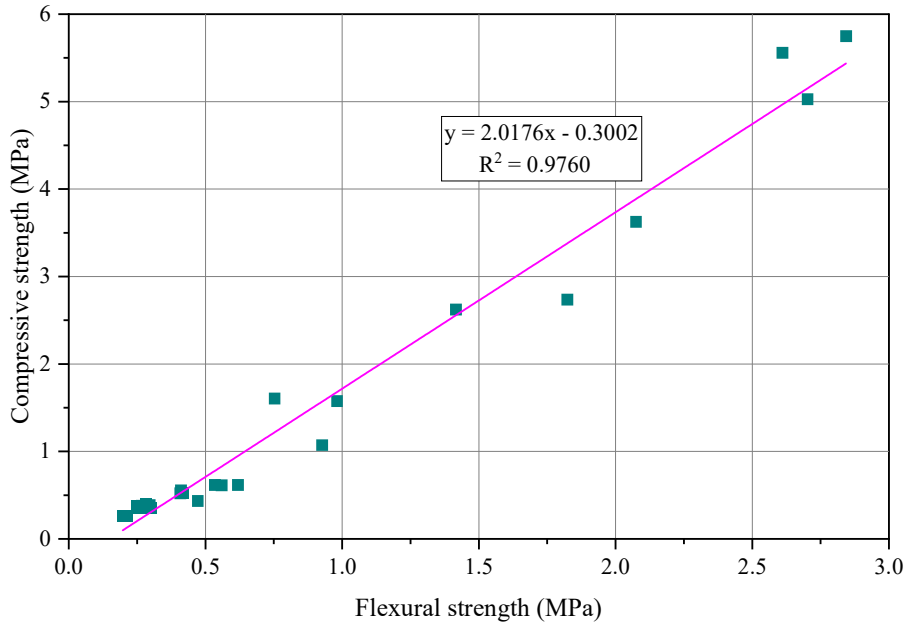

Figure 5-11. Relationship between compressive strength and flexural strength of all formulations at 28 days.

The regression line's equation is y = 2.0176x – 0.3002 with an R^2 of 0.9760. This shows that the compressive strengths are two times higher than the flexural strengths for the evaluated sunflower pith mortars. In addition, since R^2 value is close to 1, there is a linear correlation between these two strength parameters.

(e) Correlation between compressive strength and bulk density of all formulations studied.

The compressive strength of a given bio-based or cement-based material depends on its density. Generally, materials with higher compressive strength also have a higher bulk density. To examine whether this is applicable to the sunflower pith mortars developed in this study, the correlation between compressive strength and bulk density at 7, 14, 28, 56, 90 days was done, as illustrated in Figure 5-12.

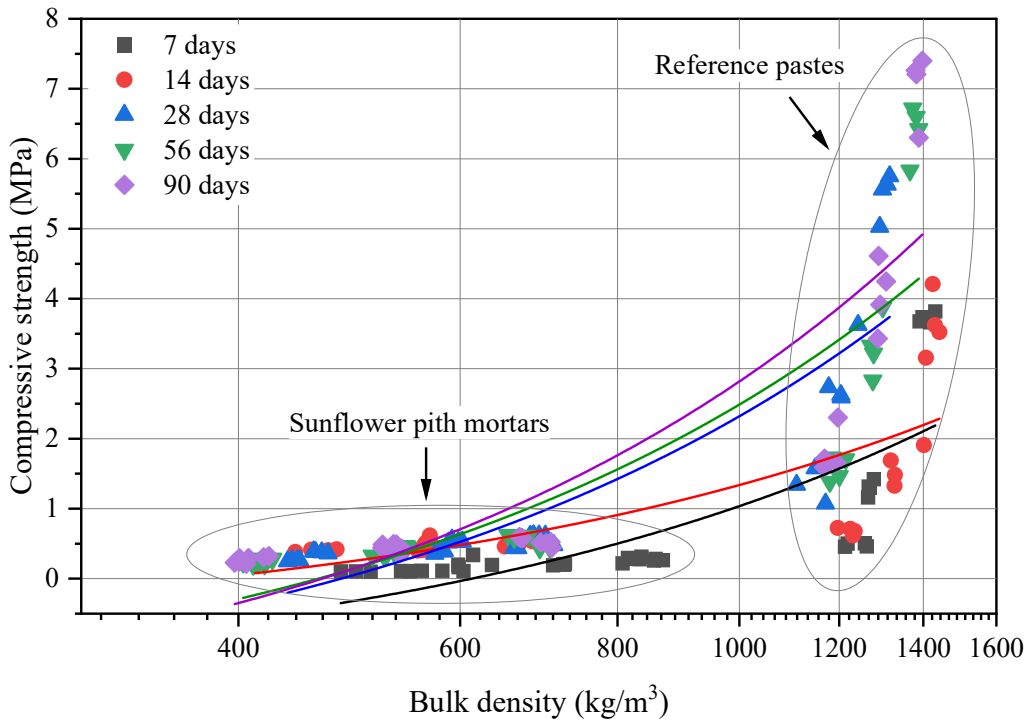

Figure 5-12. Correlation between compressive strength and bulk density of all formulations studied.

The compressive strength (R_c) of sunflower pith mortars increases with the increasing bulk density (ρ) and curing age. Comparing with the reference pastes (M0, M1, M8), the sunflower pith mortars are lighter and exhibit significantly lower compressive strength. The average bulk density of SP mortars ranges between 402 and 846 kg/m^3 while for the reference pastes, it varies from 1147 to 1425 kg/m^3. Furthermore, the average compressive strength ranges from 0.11 to 0.62 MPa for SP mortars and from 0.48 to 7.04 MPa for reference pastes.

(f) Elastic modulus

The elastic modulus (E) data of the sunflower pith mortars are presented in Figure 5-13 and Table 5-6. As mentioned earlier, the calculations were made based on the compressive strength results obtained at 7, 14, 28, 56 and 90 days. From Figure 5-13 (a, b), it is evident that the elastic modulus of the reference pastes M1 and M8 increases with the increasing curing time. Similarly, for M0, but when the maximum E value was reached at 56 days, it declined. On the other hand, the elastic modulus of SP mortars has fluctuated but, overall, no significant changes have been noticed.

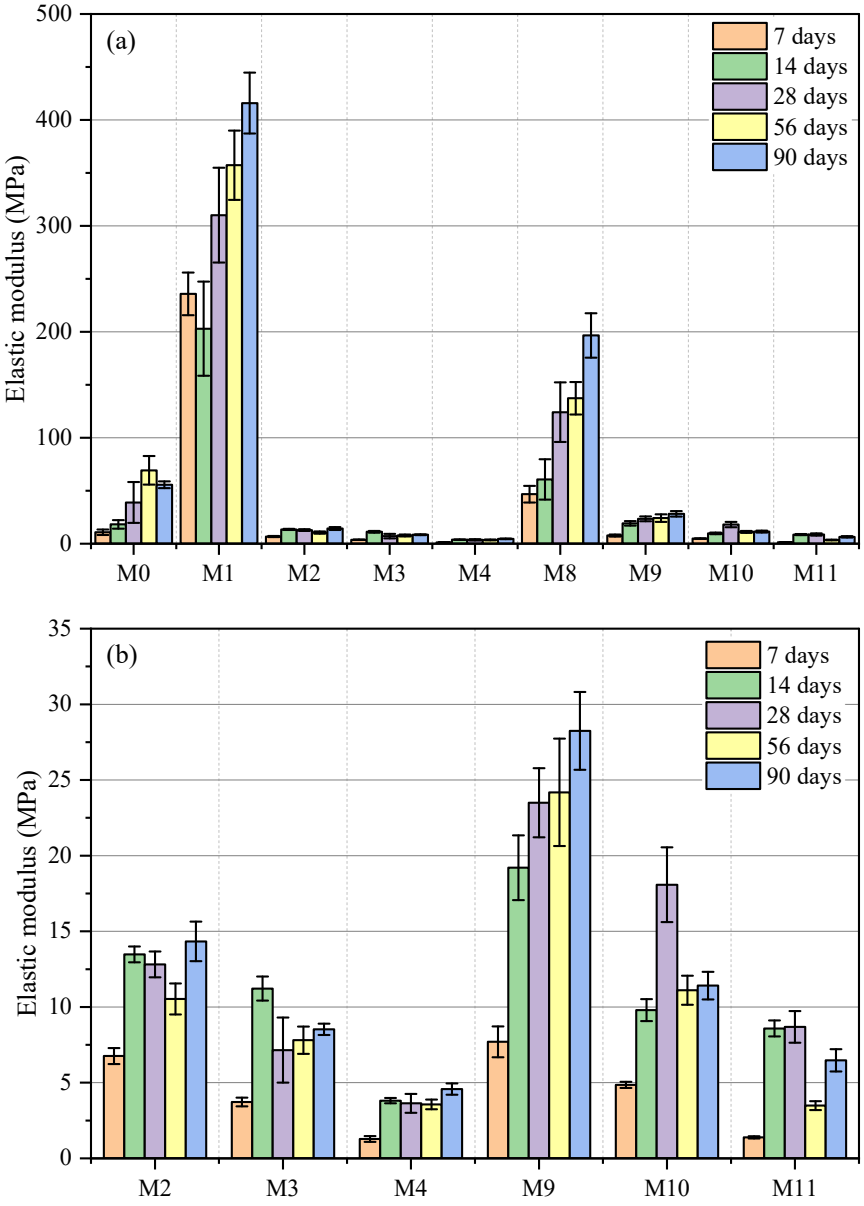

Figure 5-13. Elastic modulus of sunflower pith mortars at different curing ages. (a) all formulations (b) only sunflower pith mortars.

The reference pastes (M0, M1, M8) show considerably higher E values than the sunflower pith mortars at all curing ages. This substantial difference between elastic modulus of the reference pastes and SP mortars is attributed to the sunflower pith particles. As shown in Figure 5-13 (b), the elastic modulus of the mixtures decreases as the sunflower pith content increases.

Besides, the binding matrices had also influenced the stiffness of the mixtures. In fact, the SP mortars prepared using the binding matrix M1 (80 % WFA8 + 20 % OPC) indicate greater elastic modulus values than the SP mortars made of M8 (90 % WFA8 + 10 % OPC). This is evidence that the addition of high wood fly ash content decreases the elastic modulus of the mixtures. In general, at 90 days, the average elastic modulus of the sunflower pith mortars

varied between 4.58 and 28.24 MPa, whereas for the reference pastes, it ranged from 55.65 to 415.93 MPa.

Table 5-6. Elastic modulus data for all formulations from 7 to 90 days.

Mix notation	Elastic modulus (MPa)				
	7 days	14 days	28 days	56 days	90 days
M0	10.77 ± 2.61	18.23 ± 4.01	38.91 ± 19.27	69.27 ± 13.54	55.65 ± 3.25
M1	235.83 ± 20.06	202.94 ± 44.42	310.14 ± 44.77	357.25 ± 32.69	415.93 ± 28.72
M2	6.76 ± 0.53	13.48 ± 0.52	12.82 ± 0.85	10.53 ± 1.03	14.33 ± 1.31
M3	3.73 ± 0.29	11.22 ± 0.79	7.15 ± 2.15	7.81 ± 0.90	8.52 ± 0.37
M4	1.28 ± 0.19	3.81 ± 0.18	3.64 ± 0.63	3.57 ± 0.32	4.58 ± 0.37
M8	46.74 ± 7.90	60.67 ± 19.01	124.15 ± 28.17	137.29 ± 15.34	196.63 ± 20.95
M9	7.70 ± 1.02	19.20 ± 2.14	23.50 ± 2.28	24.18 ± 3.55	28.24 ± 2.57
M10	4.86 ± 0.21	9.80 ± 0.73	18.08 ± 2.47	11.11 ± 0.96	11.42 ± 0.91
M11	1.39 ± 0.08	8.58 ± 0.53	8.69 ± 1.05	3.49 ± 0.29	6.48 ± 0.74

5.4.2 Morphological and microstructural properties

In addition to the mechanical tests, further investigations were conducted on the sunflower pith mortars to highlight the changes in their microstructure over time. The microstructure of the samples was observed using the scanning electron microscopy (SEM) at 28 days. The thermogravimetric analysis (TGA) and X-ray diffraction (XRD) were performed to identify the reaction products and crystalline phases in the SP-based mortars after 28 days of curing.

(a) Scanning electron microscopy

The SEM micrographs of the sunflower pith and the binding matrix interface for M2, M4, M9 and M11 at 28 days are presented in Figure 5-14. As a reminder, M2 and M4 were made of a binding matrix comprising 80 % WFA8 + 20 % OPC, whereas the sunflower pith particles represented 5 % and 15 %, respectively. Concerning M9 and M11, the binding matrix used was composed of 90 % WFA8 + 10 % OPC. As for the first two formulations mentioned above, the sunflower pith particles accounted for 5 % for M9 and 15 % for M11. Two magnifications applied to the mortars were ×500 and ×2500.

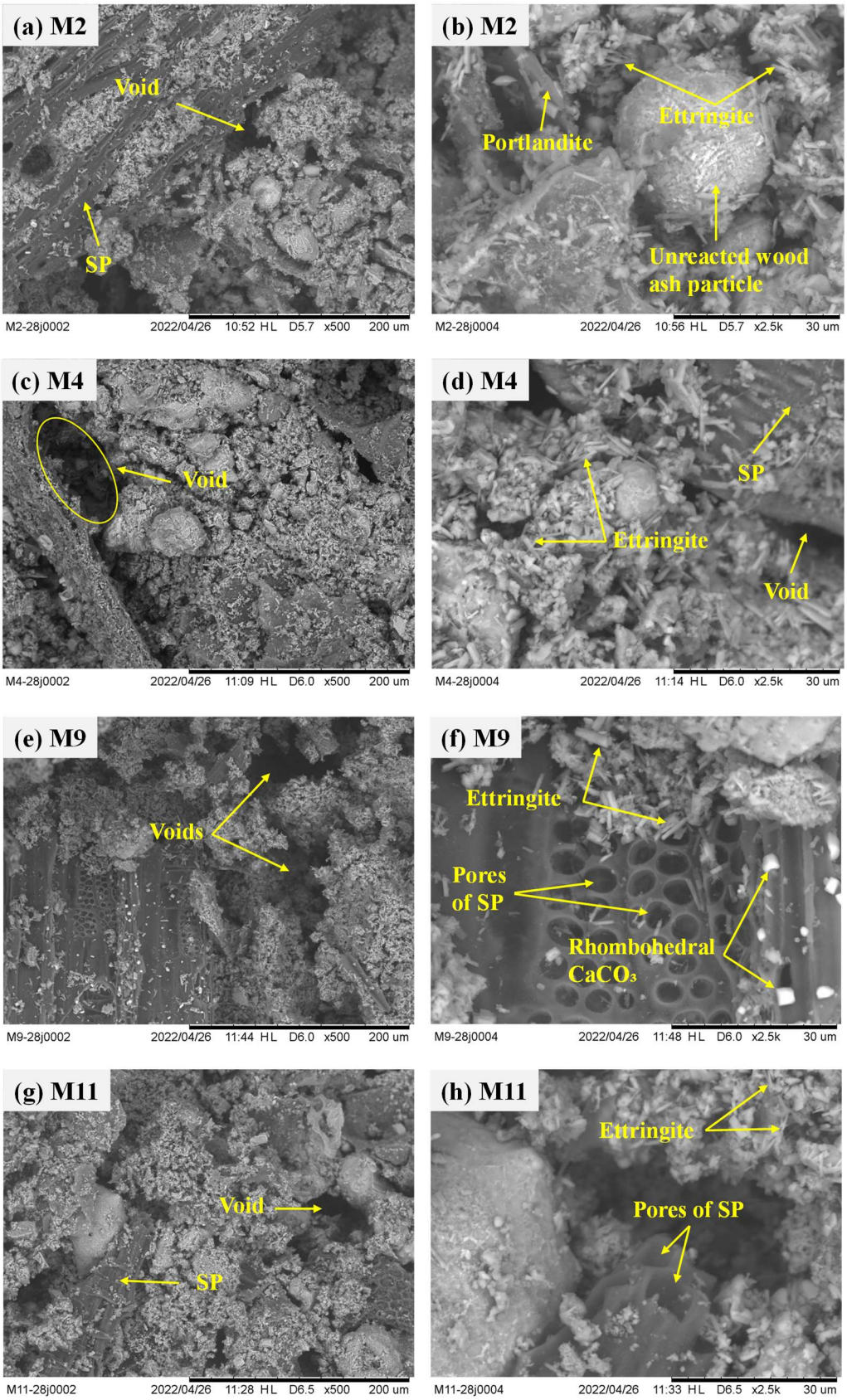

Figure 5-14. SEM micrographs of the binding matrix and sunflower pith interface: M2, M4, M9 and M11 at 28 days. The scanning conditions are shown at the bottom of each micrograph.

As shown in Figure 5-14, the microstructure of the sunflower pith mortars is less dense and contains a large number of voids. Besides that, the pores in the sunflower pith cell wall are also still visible in the mortars after 28 days of curing. This clearly shows that the compounds formed during the binding matrix hydration, did not completely fill all the cavities within the mortars.

Furthermore, it was also noticed that the microstructure of all the evaluated mortars appeared to be rich in calcium. Moreover, all sunflower pith mortars contained ettringite, whereas portlandite was only seen in M2.

(b) Thermogravimetric analysis

Thermogravimetric analysis (TGA) was used to detect the hydration products comprising the microstructure of SP-based mortars after 28 days of curing. The TGA curves obtained from the analysed samples are presented in Figure 5-15 (a, b). Note that the analysis was performed on powder mortar samples in duplicate. From Figure 5-15 (a), the samples degraded gradually with rising temperature. The significant mass losses were observed at high temperatures (above 600 °C). It should be mentioned that in general, the residual mass of each sample accounted for more than 50 %.

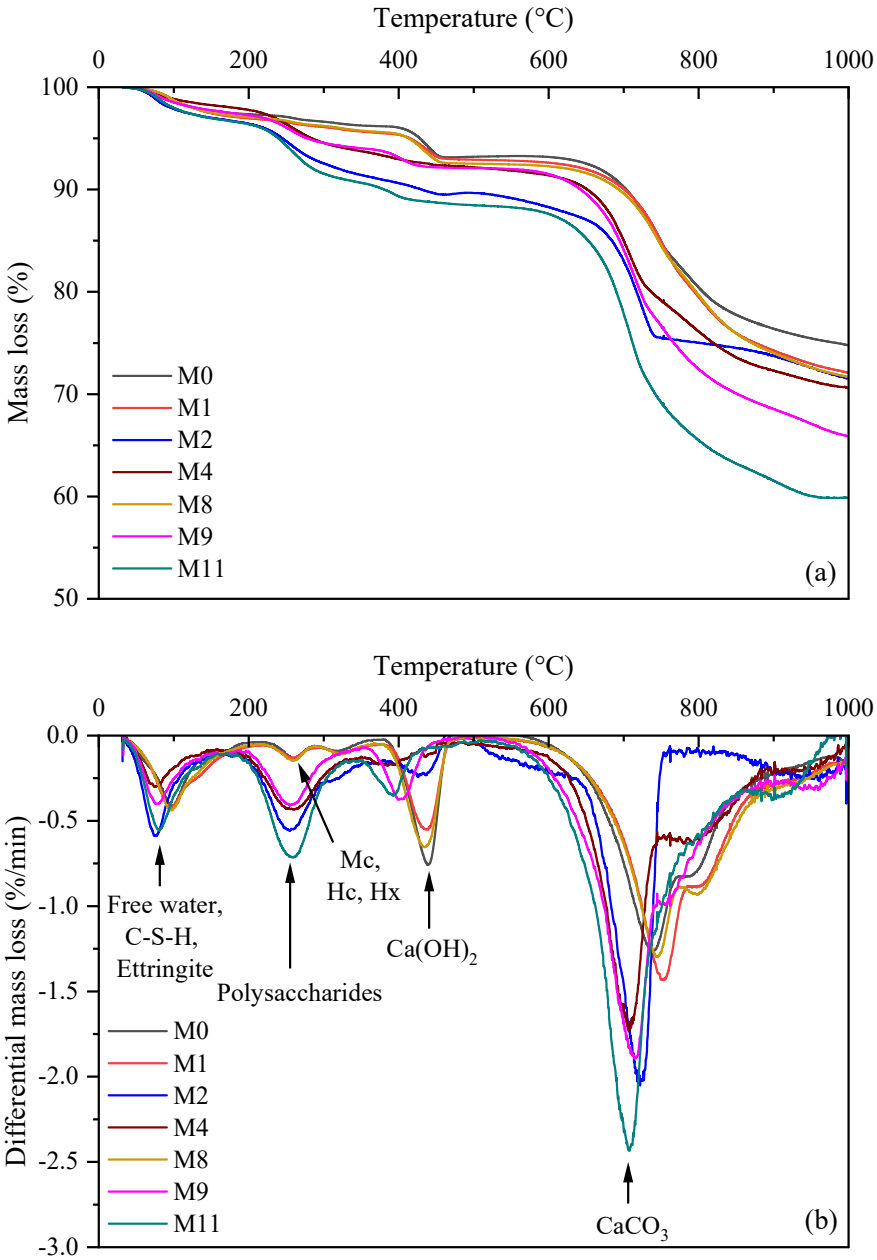

Figure 5-15. TGA curves of the sunflower pith mortars at 28 days.

Furthermore, as shown in Figure 5-15 (b), the peaks at 25-200 °C indicate the evaporation of free water, C-S-H and ettringite. At this temperature range, the mass losses for M2 and M11 are greater than for the other samples. In addition, due to high water content in SP-based mortars, the peaks maximum points occurred at lower temperatures (70-80 °C) and the peak heights are higher than those of the reference pastes.

Afterwards, the endotherms from 200 to 300 °C are caused by the degradation of polysaccharides in SP-based mortars (Nozahic, 2012). Nevertheless, given the presence of monocarboaluminate (Mc), hemicarbonaluminate (Hc) and calcium aluminate phase (Hx) in

the binding matrices, these compounds could also be found in sunflower pith mortars. Note that it is complicated to determine the mass loss percentage associated with each compound because they all occur in a similar temperature range. However, it has been noticed that the mass losses in sunflower pith mortars are more pronounced compared to M1 and M8.

Other than that, the peaks (at 400-500 °C) indicating $Ca(OH)_2$ dehydration, are greater for the binding matrices compared to SP-based mortars. This demonstrates that M1 and M8 exhibited higher water loss from portlandite compared to that of sunflower pith mortars. The $Ca(OH)_2$ decomposition reaction is shown in Equation 5-1.

$$Ca(OH)_{2(s)} \rightarrow CaO_{(s)} + H_2O_{(g)} \qquad \text{Equation 5-1}$$

The amount of $Ca(OH)_2$ was estimated from the water loss (LH_2O) taking place at 400-500 °C according to Equation 5-2.

$$Ca(OH)_2\ (\%) = LH_2O\ (\%) \times \frac{M_W(Ca(OH)_2)}{M_W(H_2O)} \qquad \text{Equation 5-2}$$

where $M_W(Ca(OH)_2)$ and $M_W(H_2O)$ are molecular weights of calcium hydroxide (74 g/mol) and water (18 g/mol), respectively. Note that the molecular weight of $Ca(OH)_2$ divided by that of H_2O refers to initial calcium hydroxide content in a system (Lopez Fernandez, 2009).

It should be noted that the absence of endotherms reflecting the decomposition of cellulose and lignin on Figure 5-15, may be explained by the presence of a mineral binding matrix of which the hydration products could have caused the deterioration of these two compounds during the curing process.

Lastly, the characteristic $CaCO_3$ peaks appeared overall at temperatures between 600 and 900 °C. It is evident that the sunflower pith-based mortars, namely M2, M4, M9 and M11 observed deeper and sharper endotherms. In contrast, the binding matrices M1 and M8 exhibited shorter and broader peaks. The calcite ($CaCO_3$) decomposition reaction is given in Equation 5-3.

$$CaCO_{3(s)} \rightarrow CaO_{(s)} + CO_{2(g)} \qquad \text{Equation 5-3}$$

The $CaCO_3$ amount was computed based on the carbon dioxide loss (LCO_2) that occurred from 600 to 900 °C using Equation 5-4.

$$CaCO_3\ (\%) = LCO_2(\%) \times \frac{M_W\ (CaCO_3)}{M_W(CO_2)} \qquad \text{Equation 5-4}$$

where $M_W(CaCO_3)$ and $M_W(CO_2)$ are the molecular weights of calcite and carbon dioxide, respectively.

The equations cited above have been previously employed by many researchers, such as (Chang and Chen, 2006; Diquélou et al., 2015; Govin et al., 2006). In this study, the mass losses on the TG curves were calculated using the tangential method (Villagrán-Zaccardi et al., 2017), with the NETZSCH Proteus software. In Figure 5-16, the formulation M2-1 is chosen as an example to illustrate a treated TG curve.

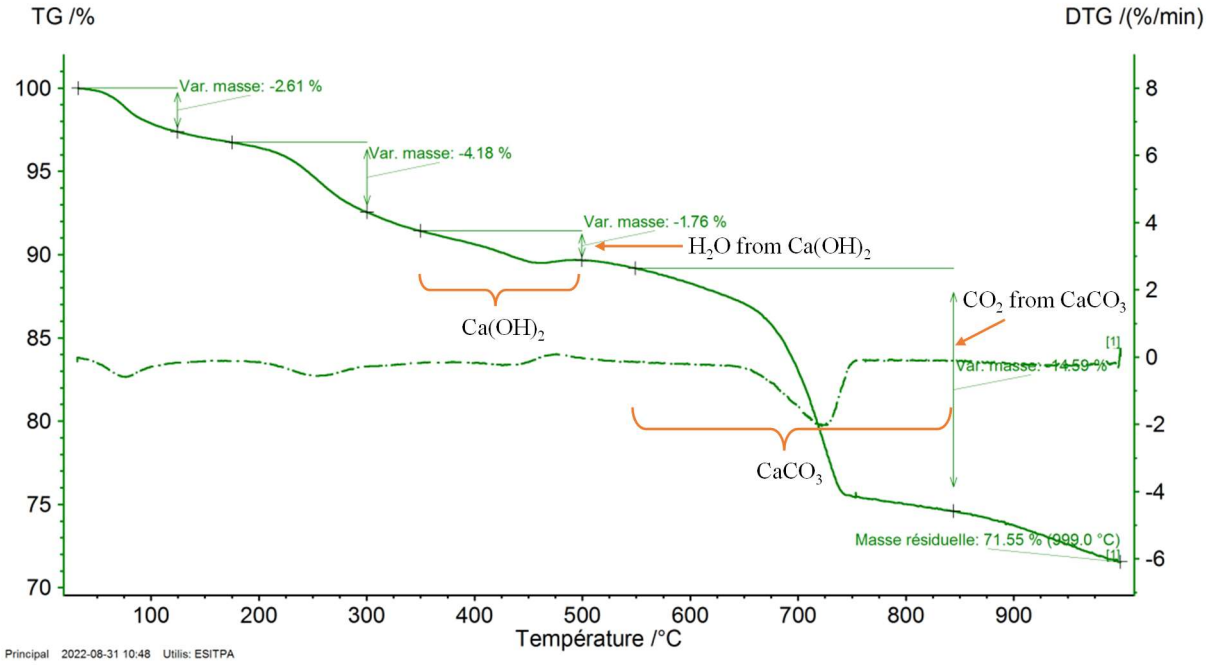

Figure 5-16. Example of a TG curve treated using NETZSCH Proteus software.

The portlandite and calcite contents obtained in the sunflower pith-based mortars are presented in Figure 5-17. As it is obvious, the reference pastes M1 and M8 are richer in $Ca(OH)_2$ than the SP-based mortars. The M8 contains more calcium hydroxide than M1 and the SP mortar samples. The amount of $Ca(OH)_2$ is stable in M2, M4, M9 and M11 regardless their compositions.

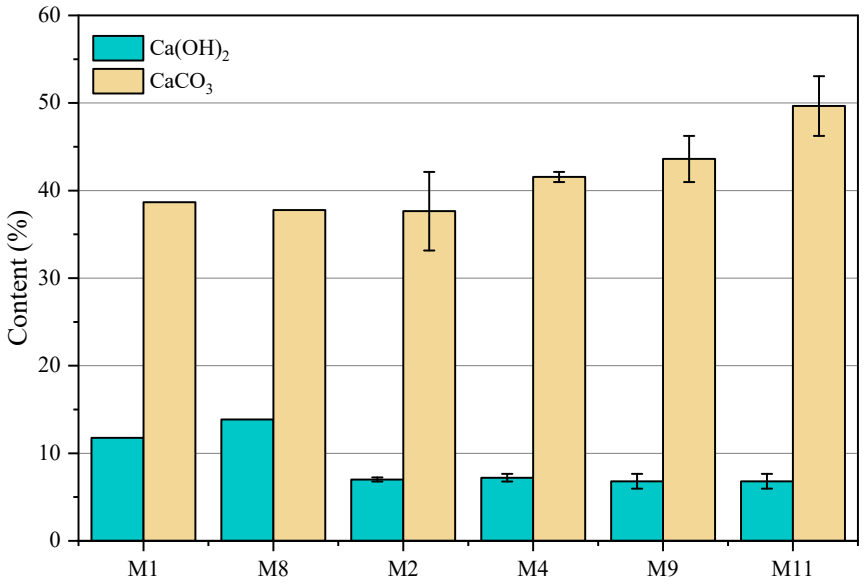

Figure 5-17. Estimated contents of $Ca(OH)_2$ and $CaCO_3$ in the sunflower pith mortars at 28 days. Note that M1 and M8 were selected for comparison purpose.

On the other hand, all analysed samples show significant amounts of calcium carbonate. The correlation between $CaCO_3$ and mixture components shows that it increases with increasing proportions of wood fly ash and sunflower pith particles in the mixtures.

In summary, the TGA results reveal the presence of the hydration products such as C-S-H, ettringite, portlandite in the sunflower pith-based mortars after 28 days of curing. It is also pointed out that the carbonation is more extensive in sunflower pith mortars compared to the reference pastes. The portlandite content tend to remain fairly constant while the amount of calcite appears to increase with the increase in wood fly ash and sunflower pith particles.

(c) Mineralogical composition

Further characterization of the sunflower pith-based mortars microstructure was conducted with X-ray diffraction (XRD) as described in section 4.4.5 of Chapter 4. Evaluating the XRD patterns given in Figure 5-18, it appears that M2, M4, M9 and M11 have an identical mineralogical composition. As shown in Table 3-1, the crystalline compounds found in the samples include syngenite, alite, albite, calcite, dolomite, sylvite, ettringite, portlandite, quartz, periclase and goethite.

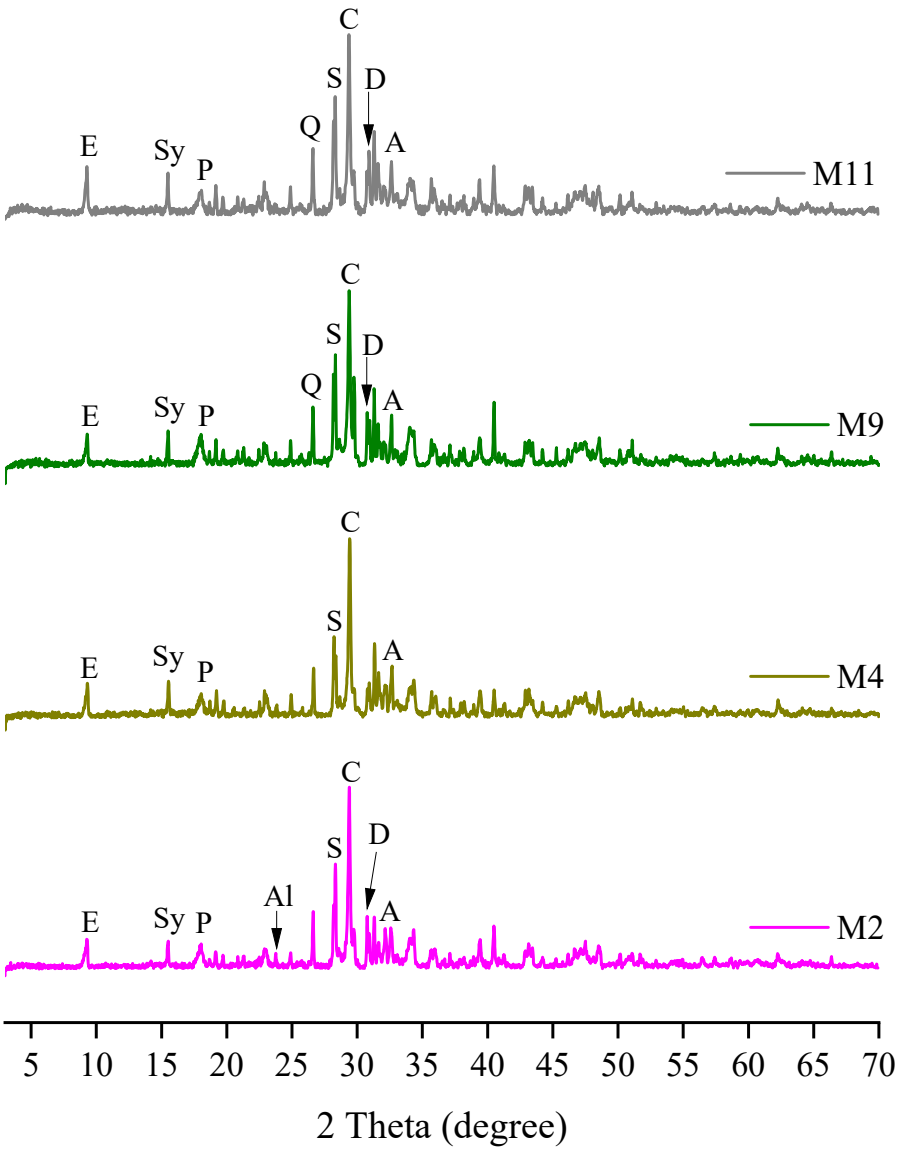

Figure 5-18. XRD patterns of the SP-based mortars: M2, M4, M9 and M11 after 28 days of curing. Note: E Ettringite; Sy Syngenite; P Portlandite; Al Albite; S Sylvite; C Calcite; D Dolomite; A Alite; Q Quartz.

More specifically, the major crystalline phases in M2, M4, M9 and M11 are albite, alite, calcite, and syngenite. In addition, dolomite was also extensively present in all SP-based mortars, except M4, and sylvite was only detected in M2. It is apparent that the compounds previously observed on the wood fly ash (WFA8) and ordinary Portland cement (OPC) at substantial levels, are still present in the developed mortars after 28 days of curing. This is evidence of the essential contribution of the binding matrix to the mineralogical composition of the sunflower pith-based mortars.

Table 5-7. All crystalline phases detected in M2, M4, M9 and M11 at 28 days.

Compound	M2	M4	M9	M11
Albite $NaAlSi_3O_8$	++	++	++	++
Alite Ca_3SiO_5	++	++	++	++
Calcite $CaCO_3$	++	++	++	++
Dolomite $CaMg(CO_3)_2$	++	+	++	++
Ettringite $Ca_6Al_2(SO_4)_3(OH)_{12}\cdot 26H_2O$	+	+	+	+
Goethite $FeHO_2$	+	Trace	+	+
Periclase MgO	+	+	+	+
Portlandite $Ca(OH)_2$	+	+	+	+
Quartz SiO_2	+	+	+	+
Sylvite KCl	++	+	+	+
Syngenite $K_2Ca(SO_4)_2\cdot H_2O$	++	++	++	++

Note: ++: major compounds and +: minor compounds.

5.4.3 Thermal and hygroscopic properties

(a) Thermal conductivity

The thermal conductivity (λ) of the sunflower pith-based mortars has been measured at 28, 56, 90 and 120 days. To optimise the number of samples and the duration of the thermal conductivity measurements, it was chosen to study the reference paste with a low cement and high wood fly ash (M8) contents, as well as the mortars with the highest (15 % SP) and lowest (5 % SP) amount of plant particles, which are M9 and M11. The obtained results are presented in Figure 5-19 and Figure 5-20.

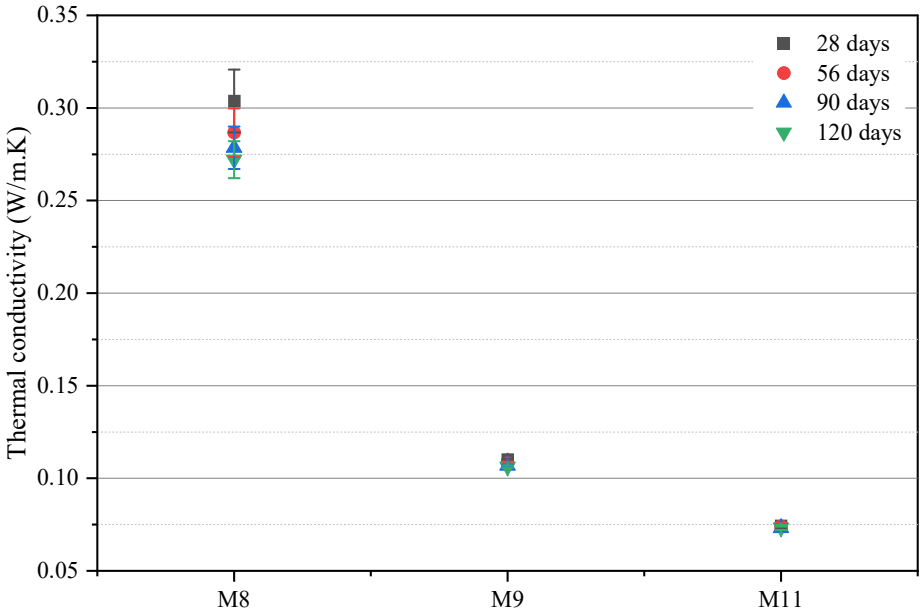

Figure 5-19. Thermal conductivity as function of formulations and curing time.

From Figure 5-19, it is apparent that the addition of sunflower pith considerably reduced the thermal conductivity of the mixtures. As time progressed, the λ values for M9 and M11 did not change significantly, whereas, for M8, noticeable variations were noted.

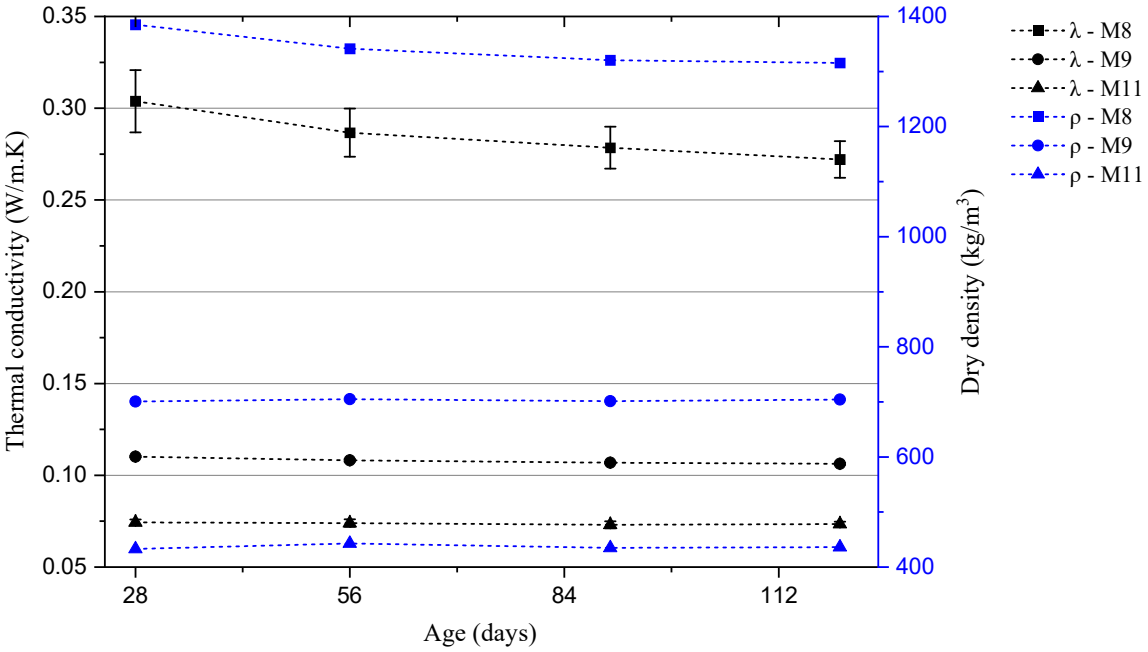

Figure 5-20. Relationship between thermal conductivity and dry density over time.

Referring to Figure 5-20, firstly, the thermal conductivity (λ) and dry density (ρ) of the sunflower pith-based mortars diminished slightly over time. Secondly, the reference formulation M8 shows greater λ and ρ than M9 and M11 at all ages. As a matter of fact, the average thermal conductivity of M9 ranged from 0.1063 to 0.1102 W/m.K and for M11, between 0.0734 to 0.0744 W/m.K whereas for M8, it was in the range of 0.2721 W/m.K and 0.3038 W/m.K. On the other hand, the dry densities of M9, M11 and M8 are respectively 701-704 kg/m^3, 433-443 kg/m^3 and 1316-1385 kg/m^3. Finally, the thermal conductivity of the samples depends strongly on their dry densities. In other words, the lower the density, the lower the thermal conductivity, and vice versa.

Furthermore, as shown in Figure 5-21, there is a linear correlation between the thermal conductivity and the compressive strength of the analysed formulations. Indeed, λ increases with the increase in R_c at 28, 56 and 90 days.

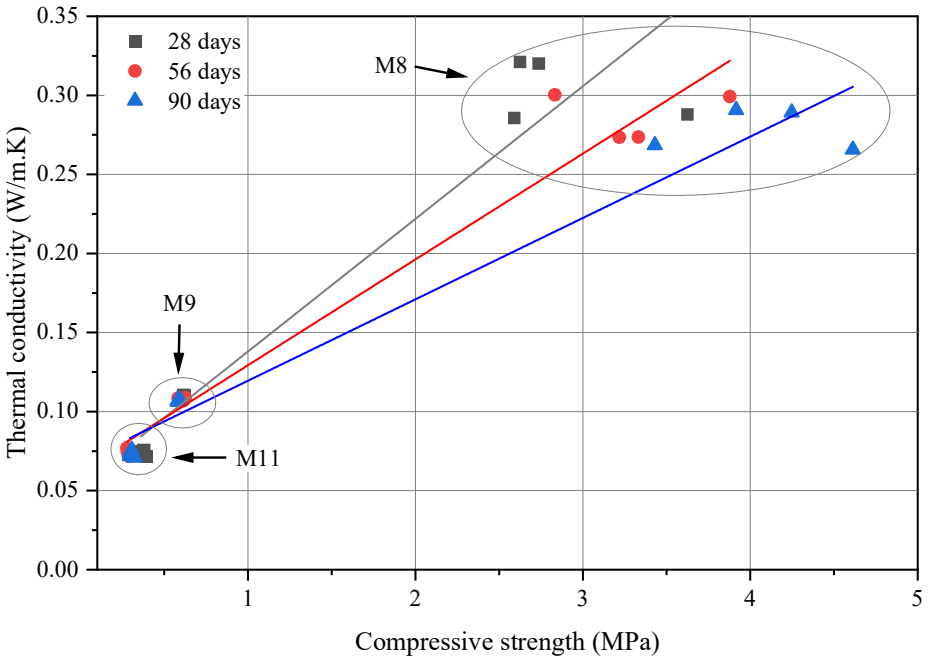

Figure 5-21. Thermal conductivity as function of compressive strength.

In summary, the thermal conductivity of the samples generally improves with time. The λ values of M9 and M11 remained more or less stable in comparison with M8. Besides, it was also revealed that M9 and M11 better thermal conductivity and lower dry densities than M8. Hence, the sunflower pith played a key role in improving the thermal insulation efficiency of the lightweight bio-based mortars elaborated in this experimental phase. The findings of the present work are close with those reported in the literature, as listed in Table 2-9 of Chapter 2.

(b) Moisture sorption isotherms

An excellent insulating bio-based insulation material should not only have a good thermal conductivity, but should also be able to effectively store and transfer moisture. In this regard, the evolution of the capacity of SP-based mortars to store and release moisture at a constant temperature of 23 °C and variable relative humidity (from 0 to 92 %, and vice versa), was examined using a dynamic vapour sorption (DVS) instrument and the results are provided in Figure 5-22 (a, b).

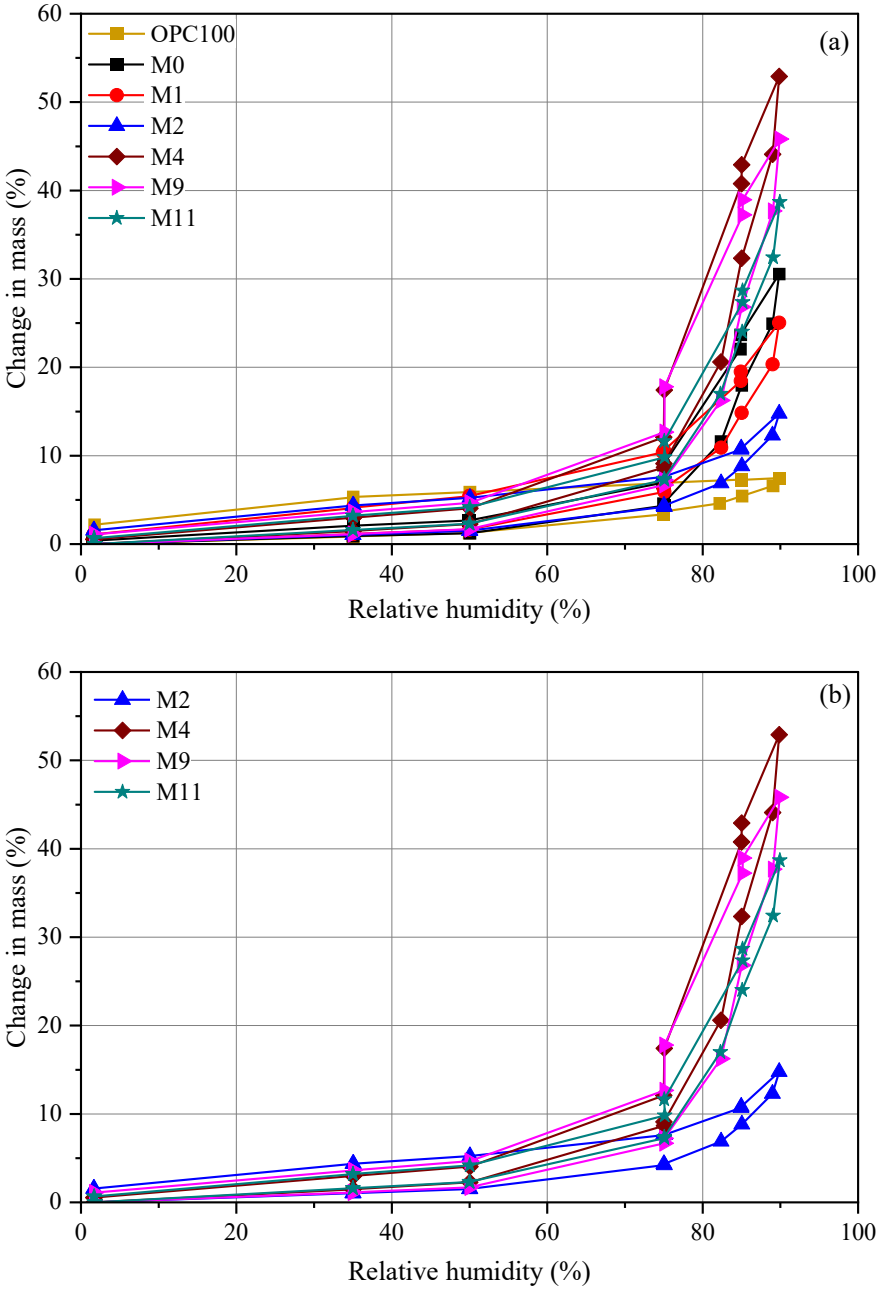

Figure 5-22. Adsorption and desorption of sunflower pith-based mortars and pastes made of wood fly ash and ordinary Portland cement at 23 °C. (a) all formulations and (b) only sunflower pith mortars.

The adsorption isotherm curves of the evaluated samples increase with increasing relative humidity (RH). Conversely, the desorption isotherm patterns declined as RH reduced. Apart from that, moisture content was also dependent on the amount of sunflower pith (SP) added. The reference pastes (without SP content) showed a lower moisture sorption ability than sunflower pith-based mortars. Also, it was noticed that the mass change became more significant as the amount of wood fly ash (WFA8) increased. This shift of the moisture content can be ascribed to an increment of porosity in the samples.

Overall, the moisture content rose steadily, but when RH exceeded 75 %, it increased sharply. M0, M1 and OPC100 reached the ultimate moisture content at an RH of 90 % and the latter varied between 7.5 and 30 %. For sunflower pith-based mortars, the lower mass change observed on M2 is due to the high concentration of cement (20 % by mass) in the binding matrix. On the contrary, the presence of sunflower pith contributed positively to the moisture storage and transfer capacity of the mortars. At 90 % RH, the moisture content of the SP-based mortars was 53 % for M4, 45 % for M9, 39 % for M11 and 15 % for M2.

5.4.4 Wetting and drying cycles

The behaviour of sunflower pith mortars under altering temperature and humidity conditions has been examined through the wetting and drying (W/D) cycles experiment. The samples have been subjected to six cycles of W/D. Due to the internal rules of the laboratory, the experiment was designed so that the weekend would arrive when the samples are being dried in the oven. Consequently, three cycles were longer than others. The 28-day mechanical properties of the SP mortars exposed to W/D cycles are compared to those of the SP mortars cured under laboratory ambient temperature and humidity conditions. The obtained flexural strength (R_f) and compressive strength (R_c) results are shown Figure 5-23 and Figure 5-24, respectively.

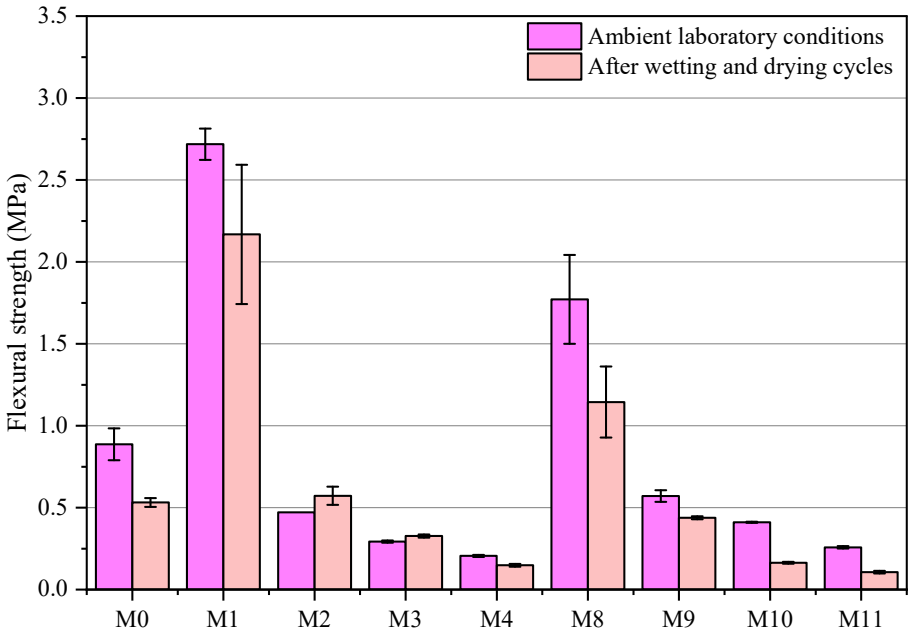

Figure 5-23. Flexural strength of the sunflower pith mortars after wetting and drying cycles.

From Figure 5-23, the samples subjected to the wetting and drying cycles were influenced in two different ways. The sunflower pith mortars, such as M2 and M3 showed a modest improvement in flexural strength, while it declined significantly for M4, M9, M10 and M11.

In addition, a more severe negative impact of the wetting and drying cycles was observed on the reference pastes M0, M1 and M8.

Besides, under both curing conditions, the flexural strength decreases as the amount of sunflower pith particles increases. At 28 days, the lowest and highest reduction in flexural strength of the SP mortars was found on the formulations M9 (23.20 %) and M10 (60.28 %), respectively. On the other hand, the increase in R_f noticed on M2 and M3 was about 21.48 % and 11.68 %, respectively. In the case of M0, M1 and M8, the latter decreased by 40.06 %, 20.26 % and 35.39 %, simultaneously.

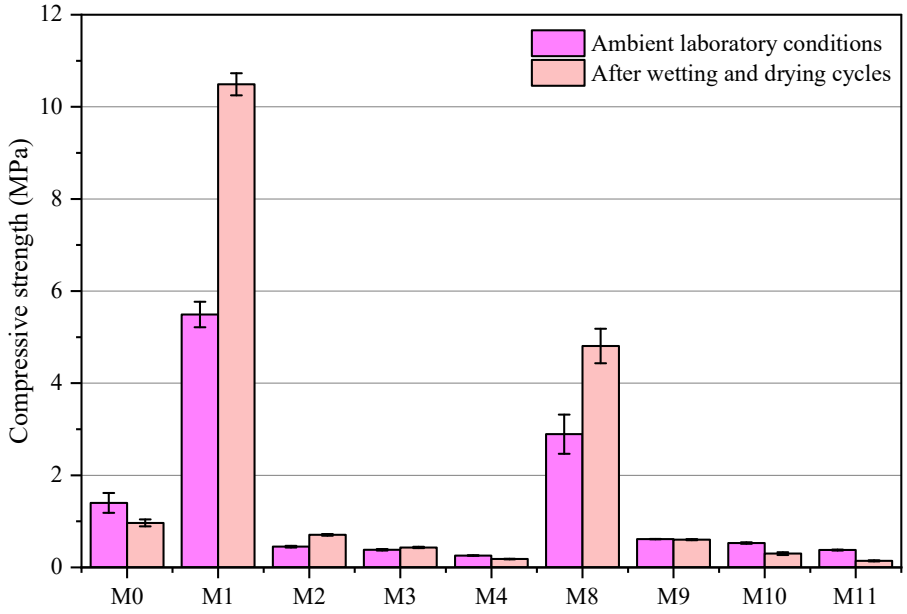

Figure 5-24. Compressive strength of sunflower pith mortars after wetting and drying cycles.

According to Figure 5-24, the compressive strength (R_c) of the sunflower pith mortars is significantly lower than that of M1 and M8. It is evident that the wetting and drying cycles positively contributed to the compressive strength of reference pastes (M1 and M8) and some SP mortars. Indeed, the latter has become twice higher for M1 (an increase of 91.02 %) while for M8 it increased by 57.10 %. Furthermore, the formulation M2 and M3 also presented an increase in compressive strength of 57.10 % and 13.30 %, respectively. On the contrary, for M0, M4, M9, M10 and M11, it tended to decline with a reduction of 30.97, 29.63, 2.19, 43.46 and 62.07 %, simultaneously.

Comparing with the literature, a 46-81 % drop in compressive strength of three hemp concretes after 10 cycles of drying and wetting was reported by Sonebi et al. (2015). The authors attributed this to the softening of hemp concrete, weakening interface area between hemp shiv

and binder, and increase in porosity (Sonebi et al., 2015). Besides, Sassoni et al. (2015) also demonstrated that accelerated ageing had a negative impact on the strength of hemp-based panels, with a decrease in compressive strength of 31-75 %.

Similarly, Sheridan et al. (2020b) also noted a significant decrease in compressive strength of hemp and rapeseed concrete after 20 immersion weathering cycles. However, the authors found that hemp and rapeseed concrete containing polyacrylic acid as a viscosity modifying agent (VMA) indicated higher compressive strength than those without VMA.

Another study by Benmahiddine et al. (2020) concluded that exposing hemp concrete to successive immersion and drying cycles resulted in reduction of compressive strength by 51 %, increase in total porosity of 2.64 %, increase in water vapour permeability of 38.24 % and lowered the thermal conductivity by 6.63 %.

Based on the above studies, the reduction in compressive strength observed in the sunflower pith mortars examined in this study is explained by the significant mass loss, increased porosity, weakened interface between the sunflower pith and the binding matrix, high permeability that may promote carbonation and deterioration of the samples.

On the other hand, the improvement in compressive strength of some mixtures, namely M1, M2, M3 and M8 can be attributed to extra hydration that occurred when they were brought back into contact with water. The immersion appears to have allowed the cement and wood fly ash to reach full hydration, resulting in the formation of additional hydration products.

The mass fluctuations of the sunflower pith-based mortars compared to the reference pastes are shown in Figure 5-25. As can be observed, M1 and M8 showed relatively smaller mass variations with respect to the SP-based mortars. The increase in change in mass correlated strongly with the amount of sunflower pith. In fact, the samples with higher sunflower pith content exhibited drastic mass changes during wetting and drying cycles.

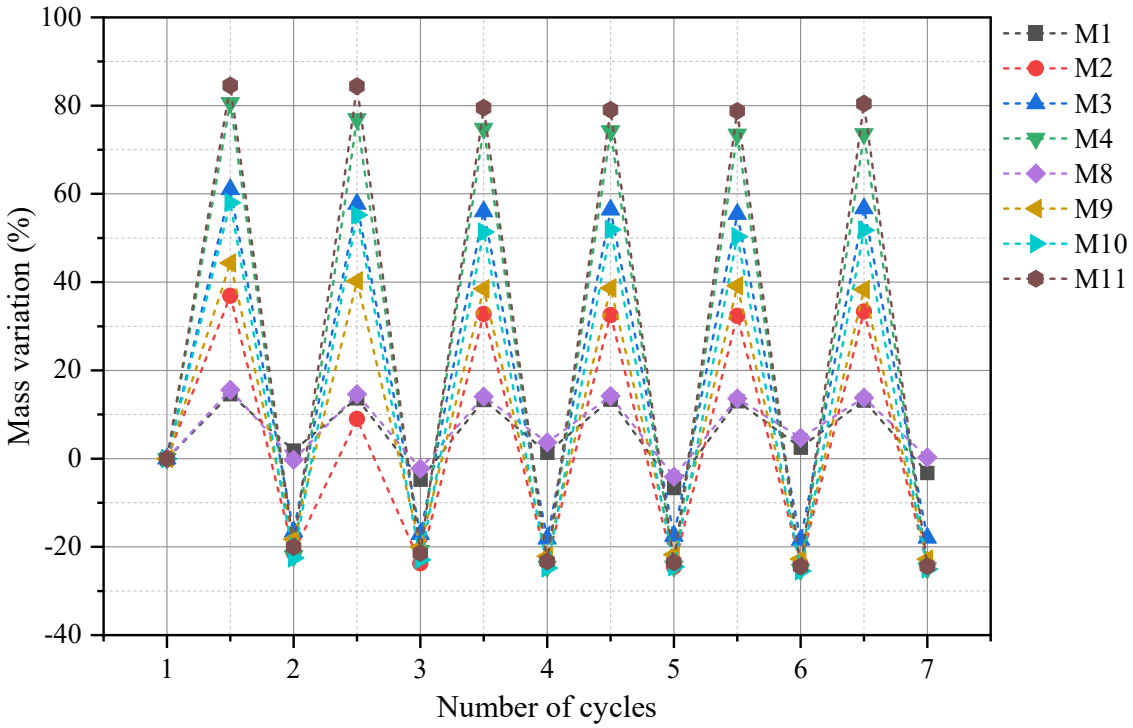

Figure 5-25. Variation of mass of the sunflower pith mortars during the wetting and drying cycles.

Following accelerated ageing, the mass loss recorded for the sunflower pith mortars was in the range of 17.93-25.06 % while for the reference pastes, it was 3.26 % for M1 and 0.26 % for M8. Lastly, it is noteworthy that, the recordings taken after each immersion have also proved the high-water absorption capacity of sunflower pith mortars. As is evident, the mass gain varied from 8.98 to 84.56 % for sunflower pith mortars. Regarding the reference pastes, it was in the range of 13.03-14.59 % for M1 and 13.61-15.58 % for M8.

5.5 Conclusion

In this chapter, six different sunflower pith mortar formulations have been prepared using two low-carbon binding matrices consisting of 80-90 % wood fly ash and 10-20 % ordinary Portland cement. The amount of sunflower pith ranged from 5 to 15 % (by mass of binder). At the desired curing ages, the mechanical, microstructural, thermal, hygroscopic properties and durability of the sunflower pith mortars were investigated.

With respect to mechanical properties, the results presented in this chapter were comparable to those of other bio-based building materials reported in the literature. The addition of sunflower pith changed the mechanical behaviour of the SP mortars. Indeed, the stiffness and brittleness of sunflower pith mortars were reduced while becoming flexible. The sunflower pith mortars presented a flexural strength varying from 0.08-0.27 MPa at 7 days and from 0.15-0.57 MPa

at 90 days. In addition, their compressive strength ranged from 0.11-0.29 MPa at 7 days and from 0.23-0.59 MPa at 90 days. The sunflower pith mortars, namely M2, M3, M9 and M10 exceeded the threshold value of the compressive strength >0.3 MPa at 60 and 90 days recommended for hemp mortars (SEBTP - Société d'édition du bâtiment et des travaux publics, 2012). The rapid growth observed in flexural and compressive strengths between 7 and 28 days of curing is ascribed to cement hydration. The gradual increase in compressive strength seen on the reference pastes, from 28 to 90 days, is attributed to the pozzolanic activity of wood fly ash.

SEM micrographs revealed that the sunflower pith mortars had a less dense, porous microstructure with a weak interface between sunflower pith and wood ash binder. The hydration products such as C-S-H, ettringite, $Ca(OH)_2$ were visible on the SEM micrographs of the samples but, were not as abundant as those usually observed on conventional cementitious materials. The TGA results confirmed the presence of hydration products in the SP mortars. In addition, the samples were also found to have larger and deeper peaks indicating calcite decomposition. The estimation of the amounts of portlandite and calcite ($CaCO_3$) in the samples indicated that $CaCO_3$ was more predominant than $Ca(OH)_2$ in the sunflower pith mortars. It was noted that calcite correlated strongly with the wood fly ash and sunflower pith contents in the mortars. XRD supported the TGA results and identified other crystalline phases present in the sunflower pith mortars.

The thermal conductivity of sunflower pith mortars was low and depended on sunflower pith content, dry density of the sample and curing age. In general, the thermal conductivity ranged between 0.073 and 0.110 W/m.K and the dry density between 435 and 705 kg/m^3. DVS illustrated that sunflower pith mortars exhibit a high-water absorption capacity. At 90 % RH, the moisture content for all SP mortars ranged from 15 to 53 %.

The wetting and drying cycles reduced the flexural and compressive strengths of all sunflower pith mortars, except M2 and M3. This could be due to the high proportion of cement and low amount of sunflower pith in the mix proportion of these two mixtures above. Overall, the flexural and compressive strengths of the sunflower pith mortars subjected to W/D cycles decreased with the increase in sunflower pith content in the mortars.

In summary, the above results prove that sunflower pith and wood fly ash can be used in the production of alternative bio-based insulation materials for buildings, with mechanical and hygrothermal performances equivalent to those of other currently available bio-based materials.

Chapter 6: Sunflower bark in prefabricated building elements

In this chapter, six different sunflower bark mixtures will be designed and prepared using two binding matrices similar to those used previously in Chapter 5 with sunflower pith. In this experimental program, the aggregates are sunflower bark particles and they are added up to 20, 25 and 30 % by mass of the binder.

As was done for the sunflower pith mortars, the mechanical, microstructural, thermal and hygroscopic properties of the produced sunflower bark mixtures will be investigated through a series of experimental analyses at the desired curing ages. Then, the results will be presented and discussed before establishing main conclusions.

6.1 Mix proportion

Six different sunflower bark (SB) mixtures for lightweight prefabricated blocks are prepared using two wood ash-based binders and sunflower bark particles. The binding matrices used in the formulation of the SB mortars were the same as those utilised earlier in the sunflower pith mortars. These binders comprise 80-90 % of wood fly ash (WFA8) and 10-20 % of ordinary Portland cement (OPC) contents (M1, M8). The reference pastes made of 100 % wood fly ash (M0) are also studied. The aggregates are sunflower bark particles (SB), representing 20, 25 and 30% of the binder mass. The notation and components of the designed mixtures are shown in Table 6-1. In addition, Table 6-2, Figure 6-1 and Figure 6-2 were made to illustrate the mass and volume represented by each raw material, including water, in the sunflower bark mixtures.

Table 6-1. Composition of the sunflower bark mixtures (by mass).

Mix notation	Binder composition	Aggregates	W/A ratio	W/B ratio
M0	100 % WFA8		0.50	
M1	80 % WFA8 + 20 % OPC		0.50	
M5	80 % WFA8 + 20 % OPC	20 % SB		0.90
M6	80 % WFA8 + 20 % OPC	25 % SB		0.95
M7	80 % WFA8 + 20 % OPC	30 % SB		1
M8	90 % WFA8 +10 % OPC		0.50	
M12	90 %WFA8 + 10 % OPC	20 % SB		0.90
M13	90 % WFA8 + 10 % OPC	25 % SB		0.95
M14	90 % WFA8 + 10 % OPC	30 % SB		1

Table 6-2. Mix proportion of sunflower bark mixtures by volume.

Mix notation	WFA8 (%)	OPC (%)	SB (%)	Water (%)
M0	84.2	0.0	0.0	15.8
M1	79.4	5.7	0.0	14.9
M5	47.7	3.4	28.8	20.1
M6	44.1	3.2	33.2	19.6
M7	40.9	2.9	37.0	19.1
M8	82.0	2.6	0.0	15.3
M12	51.5	1.6	27.6	19.3
M13	47.7	1.5	31.9	18.8
M14	44.4	1.4	35.7	18.5

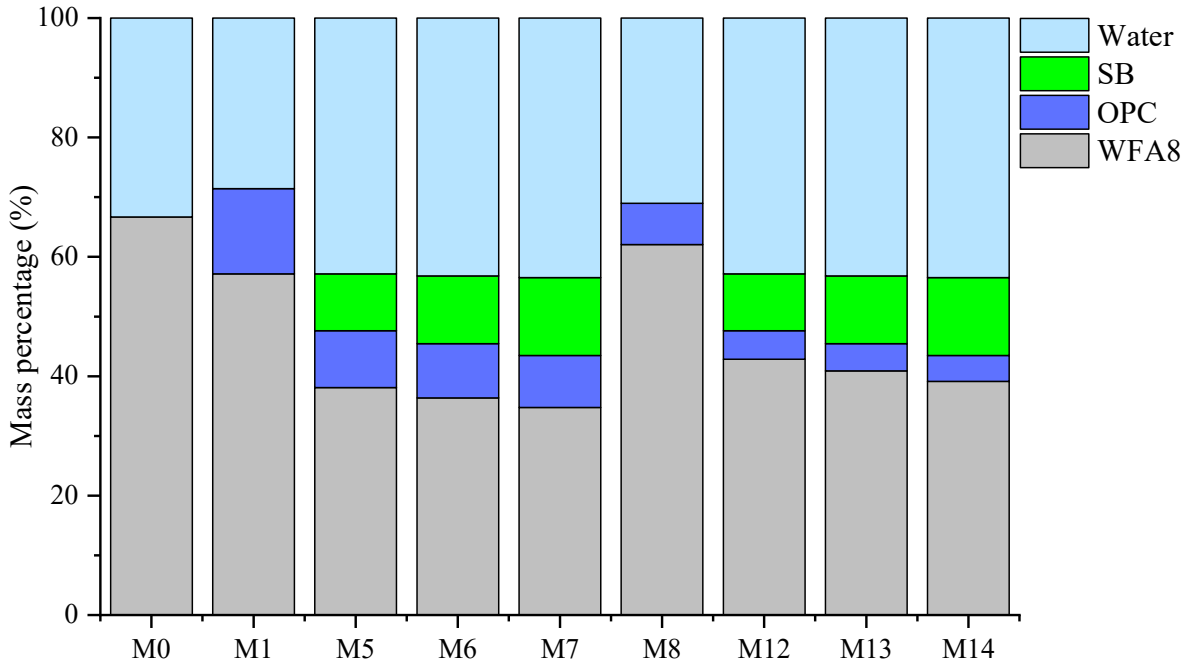

Figure 6-1. Illustration of mass ratios of sunflower bark mixtures.

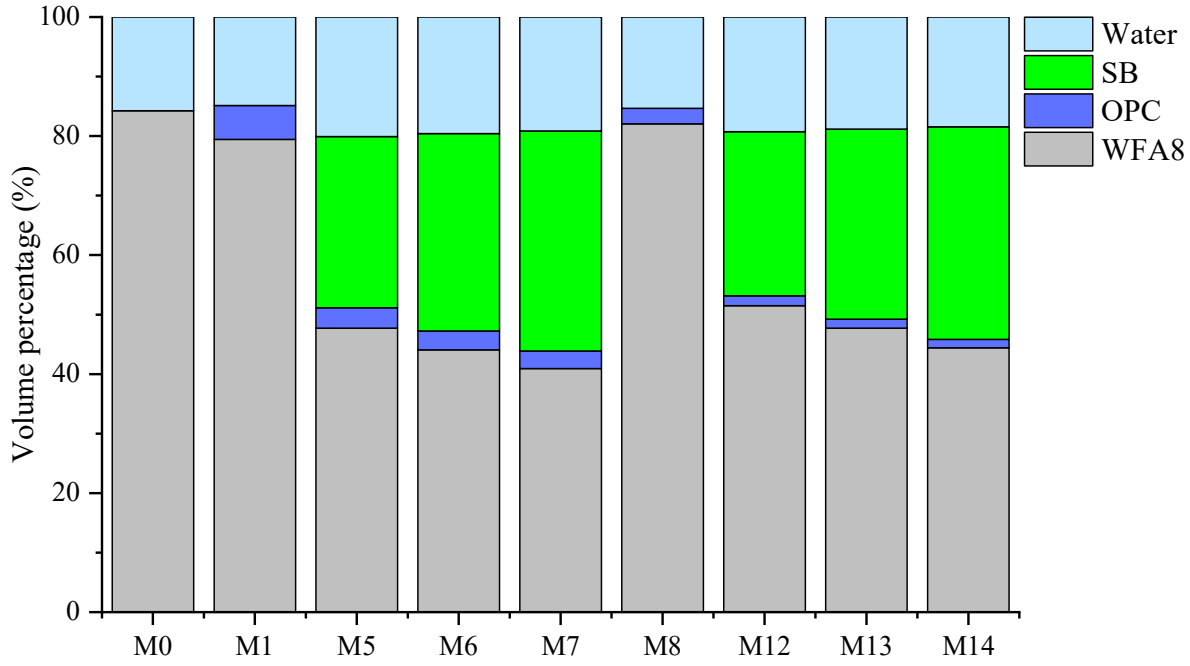

Figure 6-2.Illustration of volume occupied by the constituents of sunflower bark mixtures.

6.2 Preparation of sunflower bark mixtures

The sunflower bark mixtures were elaborated, as in section 5.2 of Chapter 5 but, with a few modifications in some procedures. Concerning the mixing sequence, no changes were made except that sunflower bark was added in place of sunflower pith (SP) (see Table 6-1). The water-to-binder ratio (W/B) was estimated similarly to SP mortars.

The compaction method employed in the preparation of SB mixtures was a Proctor normal energy with an energy of 600.3 kN.m/m^3 for those designed for mechanical testing and 601.7 kN.m/m^3 for thermal conductivity determination. The compaction of the sunflower bark mixtures was performed in a manner analogous to that of the binding matrices. More detailed information on the compaction procedures has been previously provided in section 4.3 of Chapter 4.

The sunflower bark mixture samples were removed from the moulds 24 h after pouring. Since they were already hardened, the demoulding was easy and time efficient. The SB mixture samples were cured with SP mortars samples in the laboratory at ambient temperature and relative humidity conditions until the required curing age. The curing conditions were identical to those for sunflower pith mortars presented in section 5.2 of Chapter 5.

6.3 Characterization methods

The mechanical properties (R_f and R_c) of sunflower bark mixtures were measured at 7, 14, 28, 56 and 90 days. The procedure followed in this experiment is provided in section 5.3.1. In addition, the microstructure of the bio-based mixtures was observed using scanning electron microscopy (SEM), as in section 5.3.2 at 28 days. Thermogravimetric analysis was also conducted on the SB mixtures, as explained in section 5.3.3 at 28 days. Besides, the mineralogical composition of the SB mixtures was examined by x-ray diffraction (XRD), as described in section 5.3.4 at 28 days.

The sunflower bark mixtures' thermal conductivity (λ) was measured, as in section 5.3.5 at 28, 56, 90 and 120 days. Afterwards, their moisture sorption (adsorption and desorption) isotherms were determined with dynamic vapour sorption (DVS), as described in section 5.3.6. The measurements were carried out on small pieces of SB mixtures with a mass between 2.1 and 2.9 g. Finally, the performance of the sunflower bark mixtures exposed to the wetting and drying cycles was evaluated according to the procedure in section 5.3.7.

6.4 Results and discussion

6.4.1 Mechanical properties

(a) Behaviour of sunflower bark mixtures under flexural and compressive strengths tests

The influence of sunflower bark on the behaviour of the wood ash binding matrices during the flexural strength test was evaluated. The comparison of the load-displacement curves of the tested formulations at 28 days is shown in Figure 6-3 (a, b). Note that one sample is randomly

selected for each formulation. Figure 6-3 (a) presents the curves of all evaluated samples. On the other hand, Figure 6-3 (b) illustrates only sunflower bark mixtures because there is a huge difference between the maximum load for mixtures with and without plant particles. As can be seen, the incorporation of sunflower bark (SB) significantly reduced the flexural strength and brittleness of the mixtures. After reaching the maximum load (F_{max}), the formulations without SB content broke and failed. On the contrary, the strength of the mixtures containing sunflower bark gradually decreased until the rupture occurred.

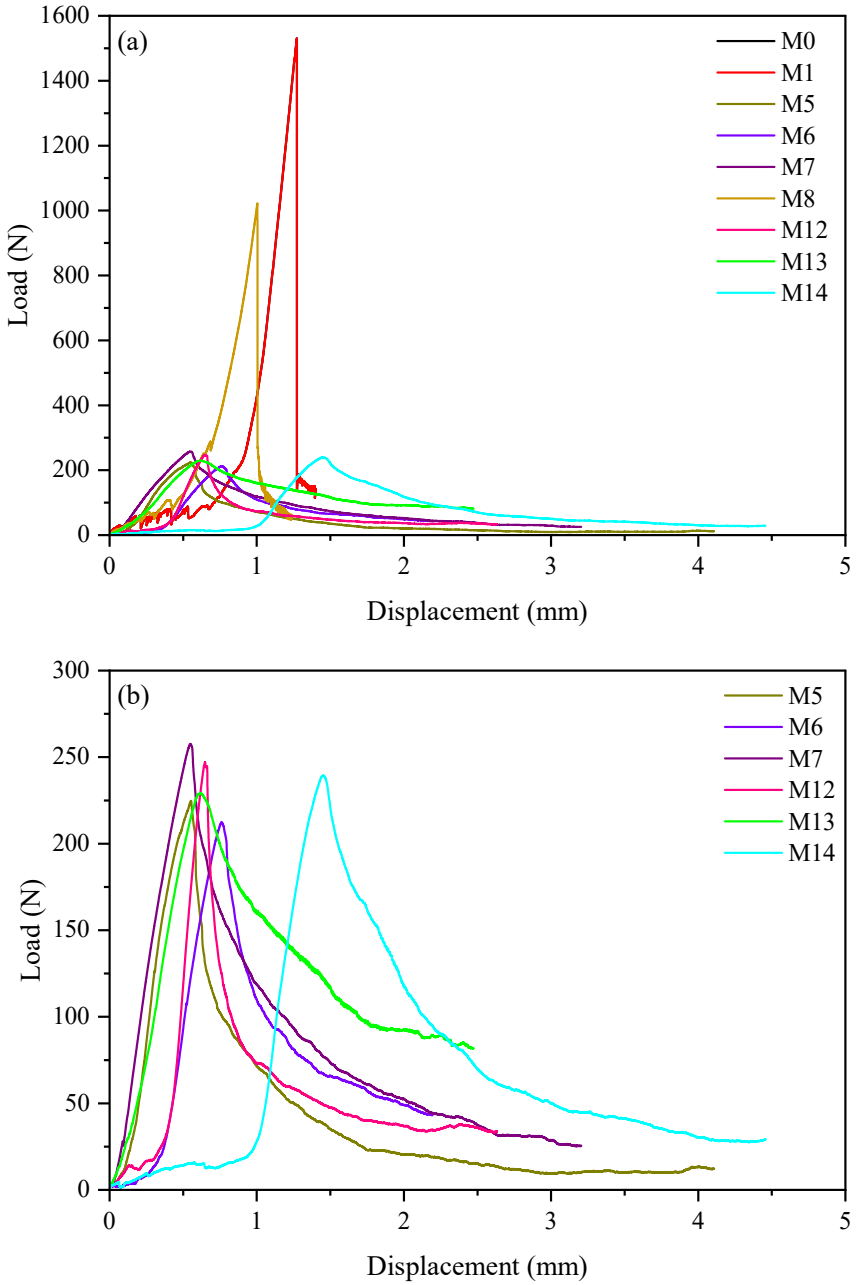

Figure 6-3. Typical load-displacement curves of sunflower bark mixtures under flexural strength test at 28 days. (a) all mixtures and (b) only sunflower bark mixtures.

Concurrently, the cracks also started appearing on the sunflower bark mixtures and expanded similarly as for sunflower pith mortars in section 5.4.1(a).

The influence of sunflower bark particles on the mixtures' behaviour under the compressive strength test was also inspected. According to Figure 6-4 (a, b), the two reference pastes used as binders show relatively higher strength than the formulations incorporating sunflower bark. After attaining the peak stress (σ_{max}), the stress sharply drops for the reference samples, while for the SB mixtures, it has reduced progressively and, at some point, remains somewhat persistent. This behaviour is identical to that observed earlier on sunflower pith mortars.

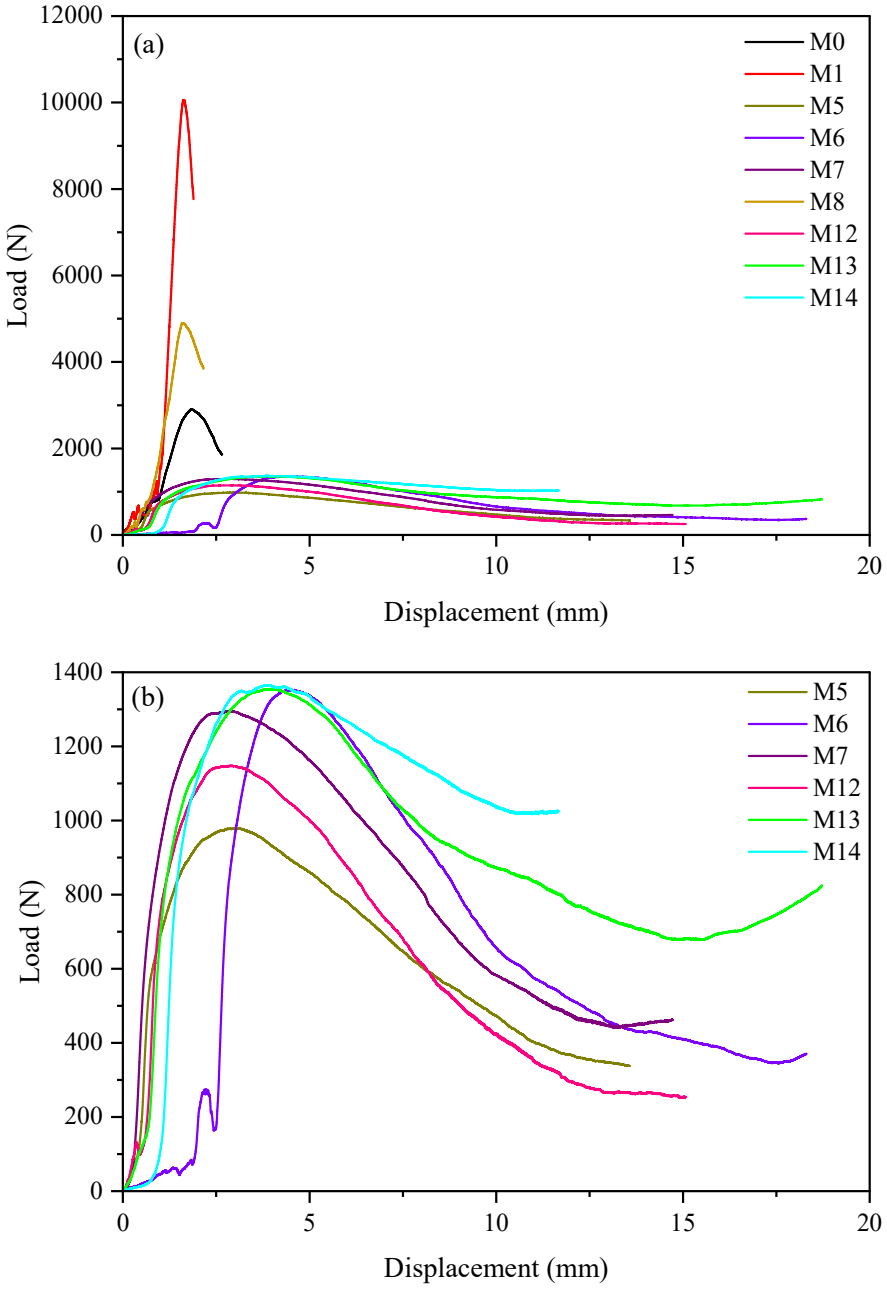

Figure 6-4. Typical load-displacement curves of sunflower bark mixtures under compressive strength test at 28 days. (a) all mixtures and (b) only sunflower bark mixtures.

(b) Flexural strength

The flexural strength (R_f) of sunflower bark mixtures results obtained at different curing ages (7, 14, 28, 56 and 90 days) are presented in Figure 6-5 (a, b) and Table 6-3. The sunflower bark mixtures exhibit relatively lower R_f than reference pastes (M1 and M8) at all ages. For instance, at 7 days, the flexural strength of sunflower bark mixtures ranged from 0.39 to 0.45 MPa, while for M1 and M8, it corresponded to 1.49 MPa and 0.76 MPa, simultaneously.

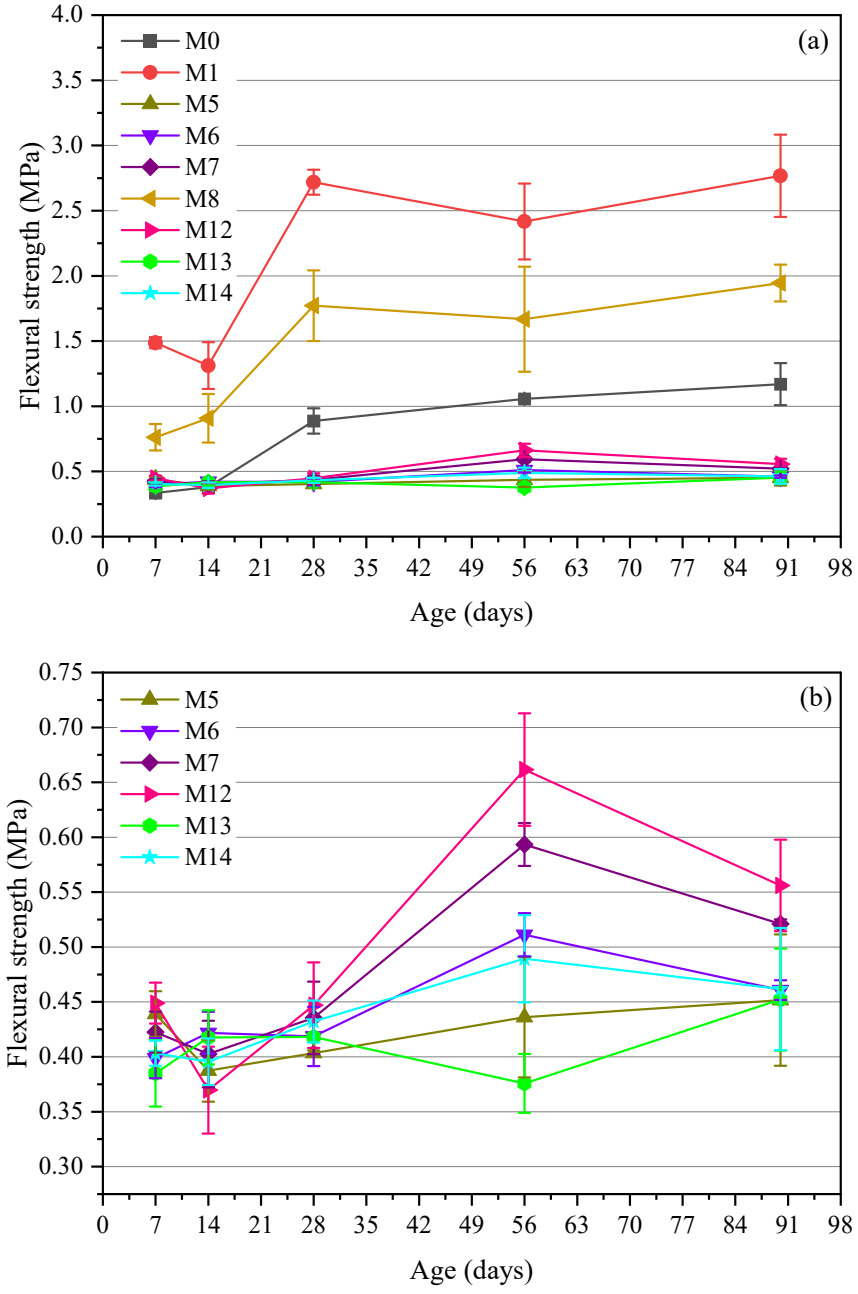

Figure 6-5. Flexural strength of sunflower bark mixtures at different curing ages. (a) all mixtures and (b) only sunflower bark mixtures.

The flexural strength of the samples generally increased with time, but there were also quite a few fluctuations. The first substantial increase that occurred between 14 and 28 days on M1

and M8 can be ascribed to the cement hydration. In addition, the second sharp growth observed on certain SB mixtures from 28 to 56 days can be attributed to the pozzolanic activity of the wood fly ash (WFA8). On the other hand, it is also interesting to note that from 56 to 90 days, the trend in R_f seems to rise slightly for M5, M13, M1 and M8, while it marginally decreases for the other mixtures. Finally, the sunflower bark mortars achieved flexural strengths varying from 0.45 to 0.56 MPa at 90 days. At the same age, M1 and M8 have attained a flexural strength of 2.77 MPa and 1.94 MPa, respectively.

Table 6-3. Flexural strength data for all formulations from 7 to 90 days.

Mix notation	Flexural strength (MPa)				
	7 days	14 days	28 days	56 days	90 days
M0	0.33 ± 0.02	0.38 ± 0.02	0.89 ± 0.10	1.06 ± 0.02	1.17 ± 0.16
M1	1.49 ± 0.04	1.31 ± 0.18	2.72 ± 0.10	2.42 ± 0.29	2.77 ± 0.32
M5	0.44 ± 0.02	0.39 ± 0.03	0.40 ± 0.00	0.44 ± 0.05	0.45 ± 0.06
M6	0.40 ± 0.02	0.42 ± 0.02	0.42 ± 0.03	0.51 ± 0.02	0.46 ± 0.01
M7	0.42 ± 0.02	0.40 ± 0.03	0.44 ± 0.03	0.59 ± 0.02	0.52 ± 0.00
M8	0.76 ± 0.10	0.91 ± 0.19	1.77 ± 0.27	1.67 ± 0.40	1.94 ± 0.14
M12	0.45 ± 0.02	0.37 ± 0.04	0.45 ± 0.04	0.66 ± 0.05	0.56 ± 0.04
M13	0.39 ± 0.03	0.42 ± 0.02	0.42 ± 0.00	0.38 ± 0.03	0.45 ± 0.05
M14	0.40 ± 0.01	0.40 ± 0.02	0.43 ± 0.02	0.49 ± 0.04	0.46 ± 0.06

Abbott (2014) stated that the flexural strength of a commercial hempcrete from The Limecrete Company Ltd varies from 0.30 to 0.40 MPa. Therefore, the results obtained in this study are acceptable.

(c) Compressive strength

The strength development during the first 28 days of curing is mainly governed by hydration reaction. Then after 28 days, the carbonation of aerial lime and portlandite causes an increase in volume of 12 %, without swelling the paste but with a modification in the size of the pores. This increases the mechanical strength of the carbonated paste (Amziane and Arnaud, 2013; Chabannes et al., 2014; Tronet et al., 2016).

In this case study, the compressive strength (R_c) results obtained from the sunflower bark mortars are provided in Figure 6-6 (a, b) and Table 6-4. The compressive strength of the sunflower bark mixtures varied over time, but no substantial improvement was noted. At 7 days, the SB mortars yielded compressive strengths ranging from 0.47 to 0.65 MPa, while at 90 days, it varied between 0.49 MPa and 0.65 MPa. On the other hand, R_c values of M1 were 3.72 MPa at 7 days and increased to 7.04 MPa at 90 days, while for M8 it increased from 1.30

to 4.05 MPa in the same period. This proves that adding sunflower bark to wood ash-based binding matrices significantly reduced the compressive strength of the mixtures.

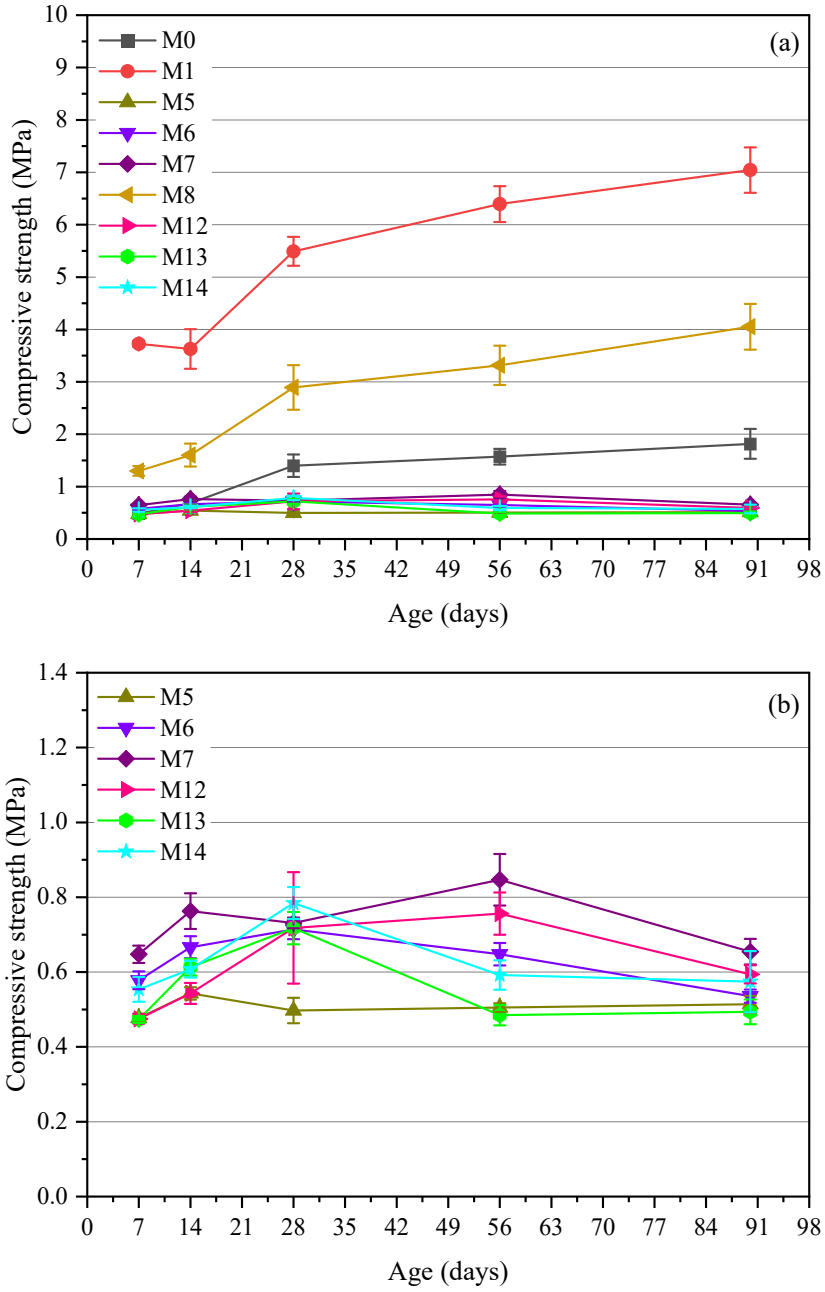

Figure 6-6. Compressive strength of sunflower bark mortars at different curing ages. (a) all mixtures and (b) only sunflower bark mixtures.

The lower R_c in SB mixtures can be ascribed to the physical and chemical characteristics of sunflower bark including a high porosity, a low density, the content of hemicellulose, sugar, starch, tannins, phenols, lignin, pectins, etc. (Sobral, 2004; Walker, 2013).

A large amount of water absorbed by the plant particles is also detrimental to the hydration of the binder (Amziane and Arnaud, 2013), as it facilitates the dissolution of water-soluble

compounds. According to Sobral (2004), these compounds prevent the cementitious system containing plant fibres from achieving their full strength and durability. The leaching of glucose decreases the concentration of Ca^{2+} during the hydration of cement and interrupts the formation of hydration products (Doudart de la Grée et al., 2017; Wu et al., 2021).

Table 6-4. Compressive strength data for all formulations from 7 to 90 days.

Mix notation	Compressive strength (MPa)				
	7 days	14 days	28 days	56 days	90 days
M0	0.48 ± 0.02	0.68 ± 0.04	1.40 ± 0.21	1.57 ± 0.15	1.82 ± 0.28
M1	3.72 ± 0.06	3.63 ± 0.38	5.49 ± 0.28	6.39 ± 0.34	7.04 ± 0.43
M5	0.48 ± 0.01	0.54 ± 0.02	0.50 ± 0.03	0.51 ± 0.01	0.51 ± 0.02
M6	0.58 ± 0.02	0.67 ± 0.03	0.71 ± 0.03	0.65 ± 0.03	0.54 ± 0.02
M7	0.65 ± 0.02	0.76 ± 0.05	0.73 ± 0.01	0.85 ± 0.07	0.65 ± 0.03
M8	1.30 ± 0.09	1.60 ± 0.22	2.89 ± 0.43	3.32 ± 0.37	4.05 ± 0.44
M12	0.47 ± 0.01	0.54 ± 0.03	0.72 ± 0.15	0.76 ± 0.06	0.59 ± 0.02
M13	0.47 ± 0.01	0.61 ± 0.02	0.72 ± 0.04	0.48 ± 0.03	0.49 ± 0.03
M14	0.55 ± 0.03	0.61 ± 0.02	0.78 ± 0.04	0.59 ± 0.04	0.57 ± 0.08

In addition, the low compressive strength of bio-based concretes may also related to a weaker interface of plant particle and mineral binder (Barbieri et al., 2020). The minor reductions in strength observed on some formulations during the curing time can be due to the transformation of hydration products.

The effect of sunflower bark on the pH of the binding matrices was examined and the findings are given in Figure 6-7. It is evident that the SB mixtures present lower pH than the wood fly ash (WFA8) or OPC pastes.

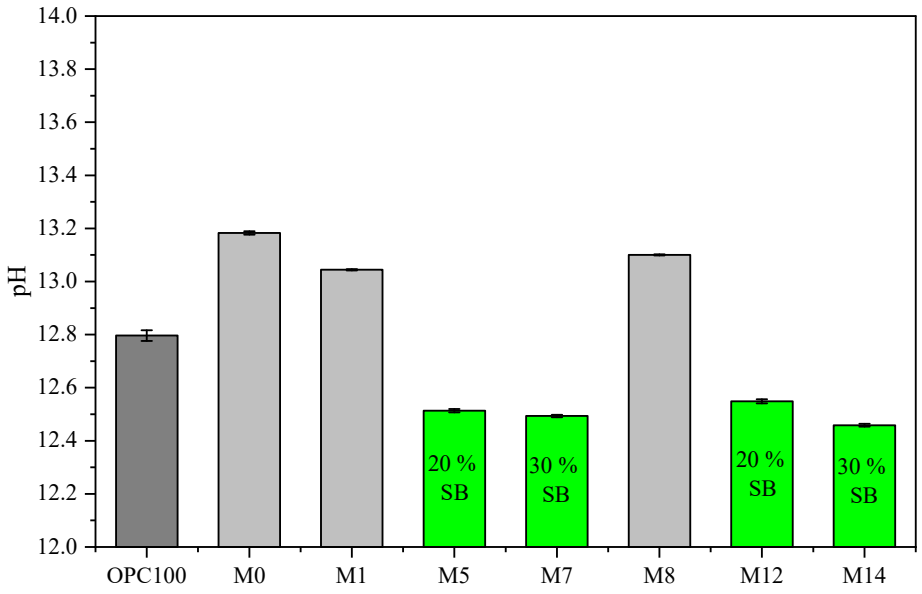

Figure 6-7. pH of the sunflower bark mixtures compared with OPC and WFA8-based pastes.

Sunflower bark mixtures exhibited pH values ranging from 12.46 to 12.55 but they marginally decreased with the increase in sunflower bark content. In the case of the reference pastes, OPC100 shows a pH of 12.79, whereas, for WFA8 pastes (M0, M1 and M8), it varies between 13.04 and 13.18. This proves that pH of the paste increases with an increase in WFA8. The apparent substantial reduction in pH can be assigned to the calcium carbonate content in the SB mixtures (Gori et al., 2011).

(d) Relationship between flexural strength and compressive strength at 28 days.

The relationship between flexural strength and compressive strength of the sunflower bark mixtures at 28 days is illustrated in Figure 6-8.

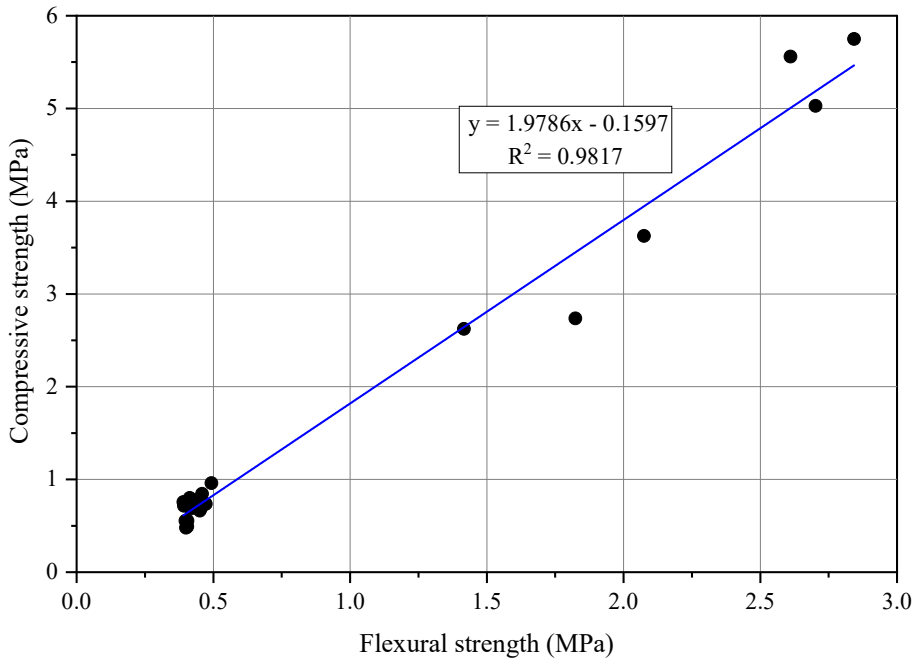

Figure 6-8. Relationship between compressive and flexural strengths of the sunflower bark mixtures at 28 days.

As seen above, the equation for the resulting regression line is y = 1.9786x + 0.1597 with an R^2 of 0.9817. This proves a linear correlation between the flexural strength and compressive strength of the sunflower bark mixtures.

(e) Relationship between compressive strength and bulk density of all mixtures studied.

The correlation between compressive strength and bulk density of the formulations, including sunflower bark mixtures and reference pastes evaluated in this study at different curing time is given in Figure 6-9. As it can be seen the compressive strength tend to increase with increasing bulk density and age.

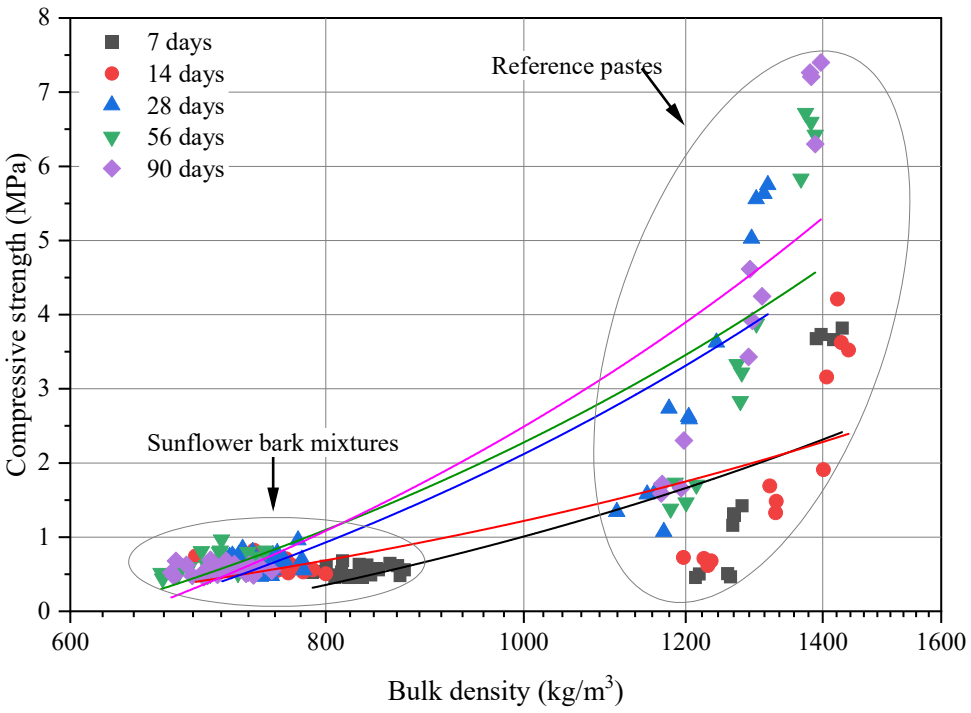

Figure 6-9. Relationship between compressive strength and bulk density of all mixtures studied.

The compressive strengths of the formulations evaluated in this study but their bulk densities appear moderately vary. These findings indicate that incorporating sunflower bark into the wood ash-based binding matrices significantly reduced compressive strength and dry density of the mixtures.

(f) Elastic modulus

The elastic modulus (E) results of the sunflower bark mortars are given in Figure 6-10 (a, b) and Table 6-5. As it can be seen, the reference pastes M1 and M8 display the highest E values and they typically increase with increasing curing time. On the other hand, the elastic modulus of sunflower bark mortars is found to be relatively low and no significant changes have been observed as the curing time increased. This drastic decline in the elastic modulus is due to the presence of sunflower bark particles.

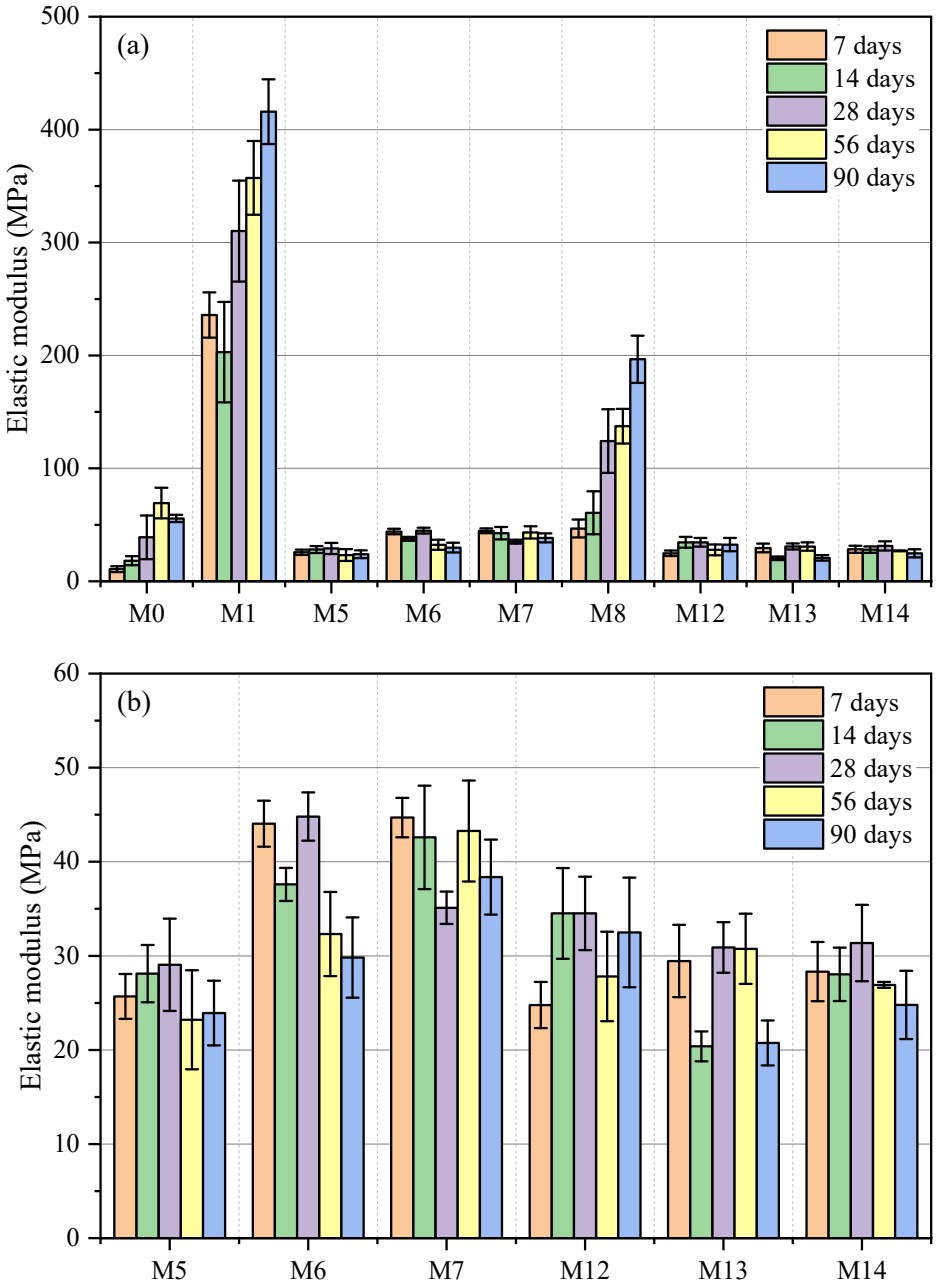

Figure 6-10. Elastic modulus of sunflower bark mixtures at different curing ages. (a) all mixtures and (b) only sunflower bark mixtures.

In addition, it has been noticed that the choice of the binder also had a minor impact on the stiffness of the SB mixtures. Indeed, the formulations M5, M6 and M7, made using M1 (80 % WFA8 + 20 % OPC) show slightly higher elastic modulus values than those of M12, M13 and M14 prepared based on M8 (90 % WFA8 + 10 % OPC). Overall, the average elastic modulus of the sunflower bark mixtures at 90 days ranged from 20.74 to 38.38 MPa. These values are slightly higher than 20 MPa recommended by Association Construire en Chanvre for a hemp mortar intended for rendering (SEBTP - Société d'édition du bâtiment et des travaux publics, 2012).

Table 6-5. Elastic modulus data for all formulations from 7 to 90 days.

Mix notation	Elastic modulus (E) (MPa)				
	7 days	14 days	28 days	56 days	90 days
M0	10.77 ± 2.61	18.23 ± 4.01	38.91 ± 19.27	69.27 ± 13.54	55.65 ± 3.25
M1	235.83 ± 20.06	202.94 ± 44.42	310.14 ± 44.77	357.25 ± 32.69	415.93 ± 28.72
M5	25.69 ± 2.39	28.11 ± 3.05	29.05 ± 4.90	23.21 ± 5.25	23.92 ± 3.44
M6	44.05 ± 2.45	37.59 ± 1.76	44.81 ± 2.57	32.32 ± 4.47	29.82 ± 4.26
M7	44.70 ± 2.10	42.59 ± 5.50	35.11 ± 1.72	43.27 ± 5.37	38.38 ± 3.98
M8	46.74 ± 7.90	60.67 ± 19.01	124.15 ± 28.17	137.29 ± 15.34	196.63 ± 20.95
M12	24.77 ± 2.45	34.51 ± 4.83	34.51 ± 3.89	27.81 ± 4.75	32.49 ± 5.82
M13	29.45 ± 3.85	20.38 ± 1.59	30.89 ± 2.69	30.75 ± 3.73	20.74 ± 2.38
M14	28.33 ± 3.14	28.04 ± 2.84	31.37 ± 4.06	26.91 ± 0.31	24.79 ± 3.63

6.4.2 Morphological and microstructural properties

The changes in the microstructure of sunflower bark mixtures have been evaluated by using three methods, namely scanning electron microscopy (SEM), thermogravimetric analysis (TGA) and x-ray diffraction (XRD) at 28 days. In addition, these experimental analyses also provided more evidence to explain the inferior mechanical performance of SB mixtures.

(a) Scanning electron microscopy

The SEM micrographs of the sunflower bark mixtures at 28 days are presented in Figure 6-11. It should be mentioned that the observations were made on the mixtures with the least and the highest sunflower bark content. This choice was made due to the limited time. As it can be seen, the microstructure of the samples is covered with hydration products and contains many voids. The SB mixtures appear rich in calcium (Ca^{2+}) based compounds. Indeed, the hydration products observed in the analysed samples include CSH gel and portlandite. The SB mixture M12 also contained dolomite. Two magnifications applied to the mixtures were ×500 and ×2500.

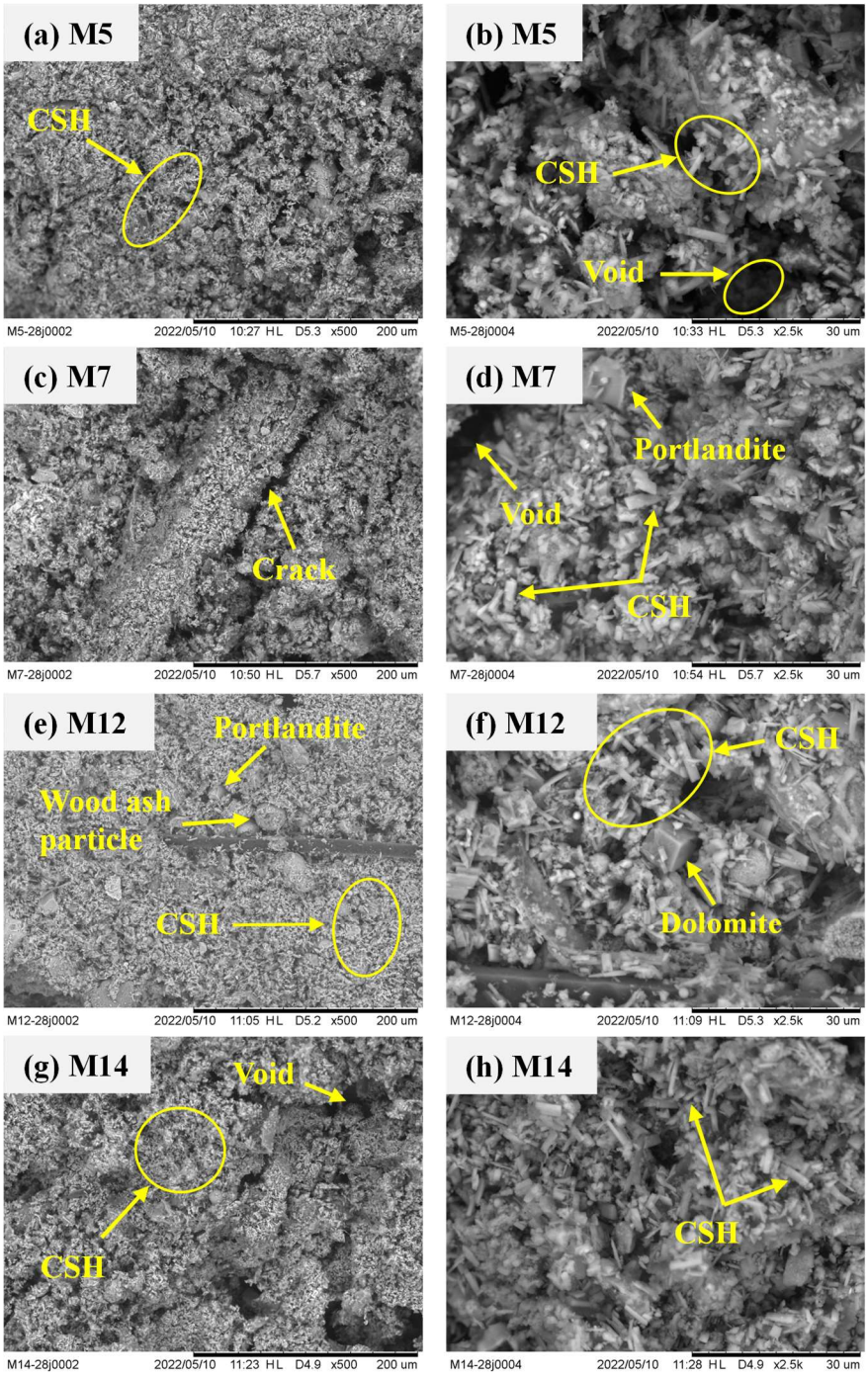

Figure 6-11. SEM micrographs of the sunflower bark mortars at 28 days.

From Figure 6-11 (c), we can observe that the sunflower bark particle crosses the image and is completely covered with the mineral binding matrix.

(b) Thermogravimetric analysis

The TGA curves of the sunflower bark (SB) mixtures at 28 days are presented in Figure 6-12 (a, b). The measurements were made on the powdered SB mixtures in two replicates, as previously done on the sunflower pith mortars. The thermal degradation of the sunflower bark

mixture samples occurs gradually and intensifies with the increase in temperature. The mass losses between 25 and 200 °C represent the evaporation of unbound or free water, C-S-H and ettringite. The SB mixtures had higher mass losses than M1 and M8 pastes, likely due to their high moisture content.

The mass losses from 200 to 350 °C are mainly attributed to the decomposition of polysaccharides (hemicelluloses, cellulose) in the sunflower bark particles. The heights of endothermic peaks in this temperature range appear to depend on the amount of SB. The mixtures containing 20 % SB, namely M5 and M12, observed lower peaks than M7 and M14, which have 30 % SB. In parallel, the reference pastes (M1 and M8) displayed minor peaks that can be assigned to the decomposition of monocarboaluminate (Mc), hemicarbonaluminate (Hc) or calcium aluminate phase (Hx).

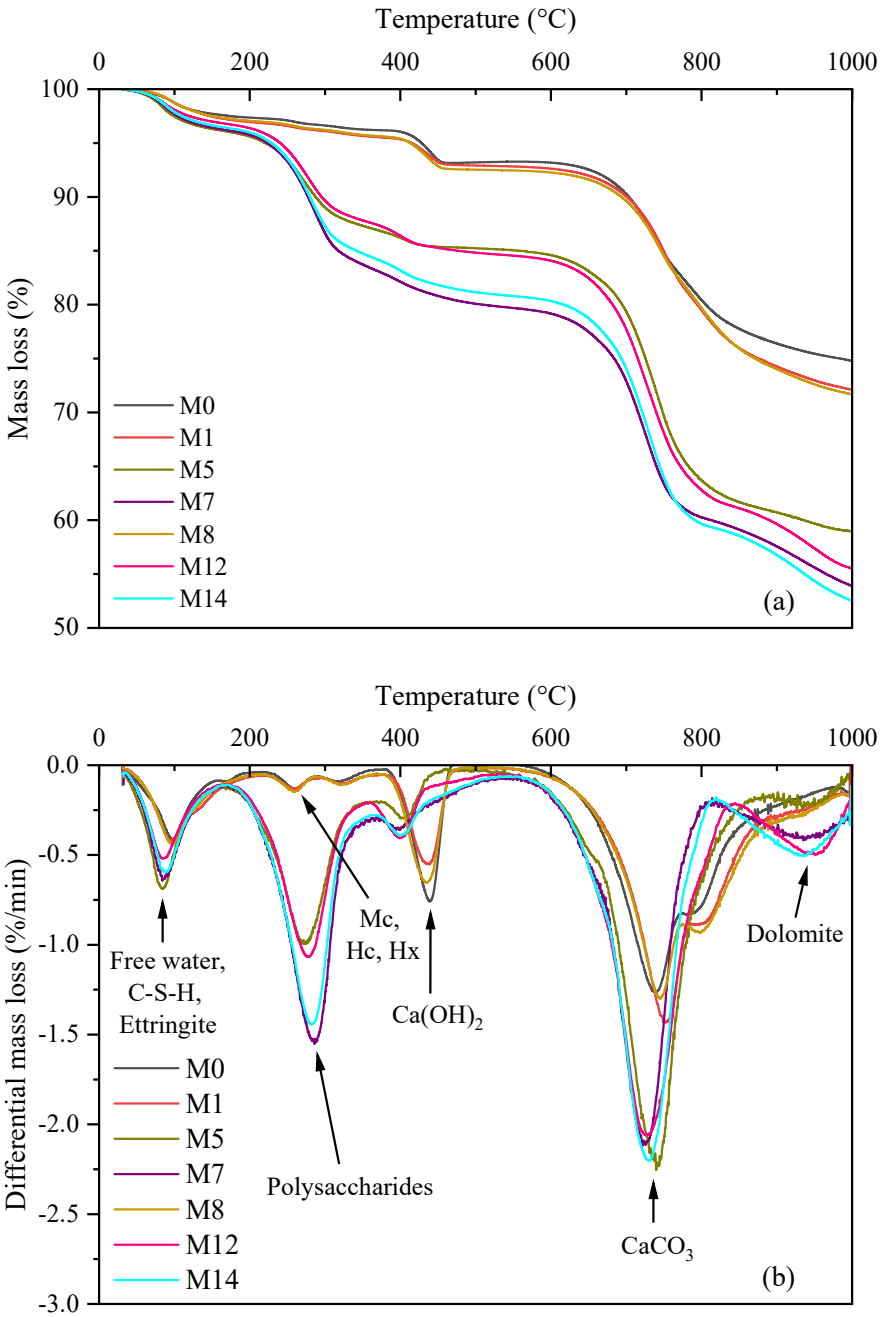

Figure 6-12. TGA curves of sunflower bark mortars at 28 days.

Moreover, the endothermic peaks at 350-500 °C indicate the dehydroxylation of calcium hydroxide ($Ca(OH)_2$). The formulations M1 and M8 present more profound peaks than those of the sunflower bark mixtures. This can be explained by the fact that sunflower bark interfered with the hydration of the binding matrices, thus lessening the quantity of $Ca(OH)_2$ that can be formed.

The broad and deep peaks between 550 and 800 °C correspond to the decomposition of calcite ($CaCO_3$). The sunflower bark mixtures show more pronounced mass losses than those found on M1 and M8. This could be an indicator of severe carbonation taking place in the SB mixtures. Previously, Nozahic (2012) also observed an ample carbonation in the hemp concrete and attributed it to direct portlandite or indirect C-S-H transformations. Lastly, the mass losses at about 800-1000 °C in the sunflower bark mixtures could be due to the decomposition of dolomite (Földvári, 2011; Samtani et al., 2002).

Furthermore, the portlandite and calcite contents in the sunflower bark mixtures were calculated according to the method described in section 5.4.2(b) and the obtained results are plotted in Figure 6-13.

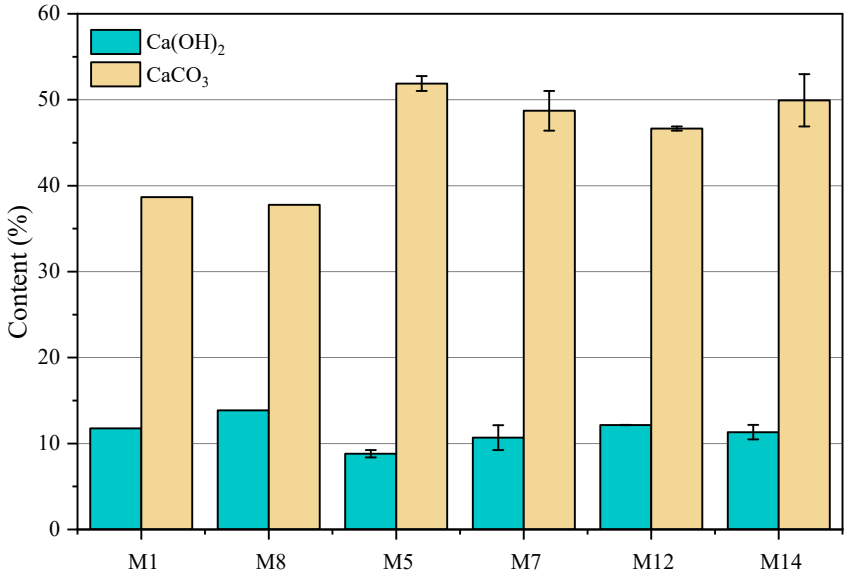

Figure 6-13. Portlandite and calcite contents in the sunflower bark mixtures at 28 days.

As can be seen, there is a large gap between the percentages of portlandite and calcite. The formulations with higher $Ca(OH)_2$ content tend to have lower $CaCO_3$ content and vice versa. It should also be noted that all the mixtures studied appear to have comparable $Ca(OH)_2$ contents. For the sunflower bark mixtures, it ranges from 8.81-12.15 %, while for M1 and M8, it is about 11.77 % and 13.87 %, respectively.

Concerning $CaCO_3$ levels, moderate differences can be seen depending on the composition of the mixture. The sunflower bark mixtures show higher calcium carbonate content compared to the reference pastes. This can be attributed to the presence of sunflower bark that increased the porosity of the mixtures. The $CaCO_3$ content in the SB mixtures ranges from 46.65 to 51.89 %. In the case of the reference samples, it was approximately 38.68 % for M1 and 37.78 % for M8.

In summary, the TGA results confirmed the presence of hydration products, including C-S-H, ettringite and portlandite in the sunflower bark mixtures. In addition, it was also found that the addition of sunflower bark resulted in a minor drop in $Ca(OH)_2$ content while it promoted the formation of $CaCO_3$ in the mixtures.

(c) X-ray diffraction

The crystalline compounds in the sunflower bark (SB) mixtures were identified using X-ray diffraction (XRD) after 28 days of curing. The obtained findings are presented in Figure 6-14 and Table 6-6. The SB mortars indicate a homogenous mineralogical composition. Moreover, the comparison of the XRD patterns of SB mixtures and those of the wood fly ash pastes (M0 and M1) previously shown in Figure 4-35, revealed a minor influence of sunflower bark on the crystalline composition of the binding matrices.

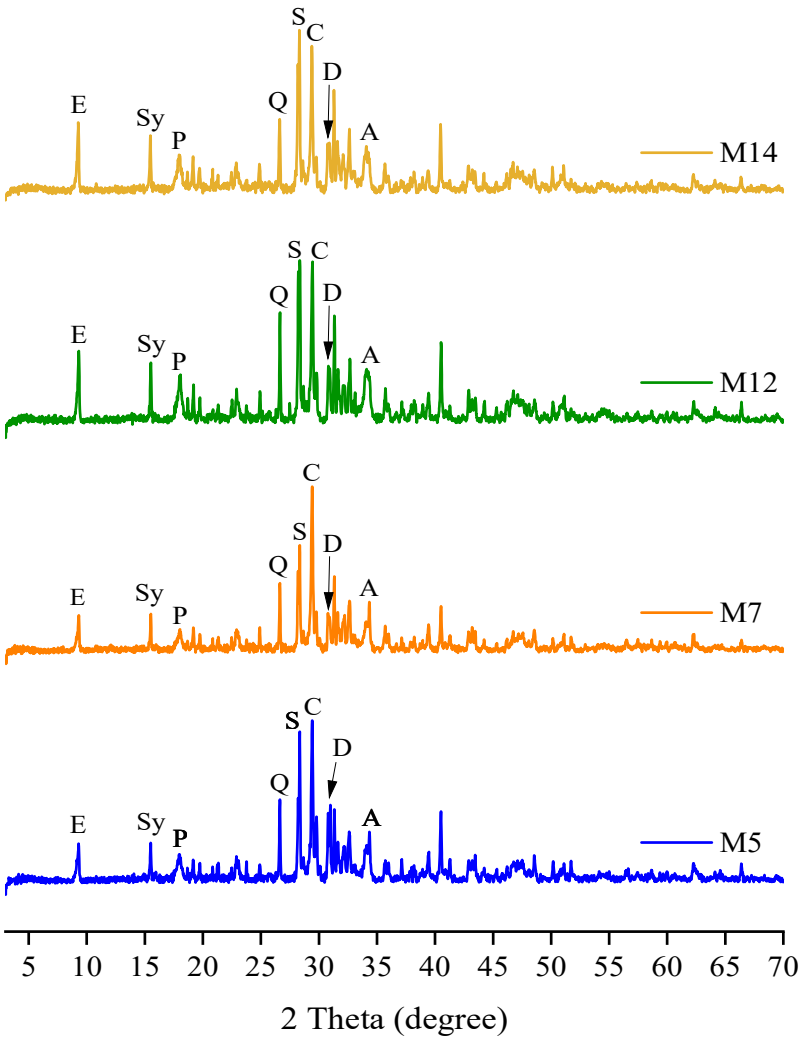

Figure 6-14. XRD patterns of sunflower bark mixtures: M5, M7, M12 and M14 after 28 days of curing. Note: E Ettringite; Sy Syngenite; P Portlandite; Al Albite; S Sylvite; C Calcite; D Dolomite; A Alite; Q Quartz.

The crystalline compounds found in the sunflower bark mixture samples are listed in Table 6-6. As can be seen, significant concentrations of albite, alite, calcite and syngenite have been identified in all samples analysed. Other than that, significant amounts of quartz and sylvite were only observed in M5 and M7. Furthermore, dolomite was also abundant in M5, while substantial ettringite contents were encountered in M14. Finally, it should be noted that portlandite, goethite and periclase are part of the identified phases but in minor proportions.

Table 6-6. Crystalline compounds identified in sunflower bark mixtures at 28 days.

Compound	M5	M7	M12	M14
Albite $NaAlSi_3O_8$	++	++	++	++
Alite Ca_3SiO_5	++	++	++	++
Calcite $CaCO_3$	++	++	++	++
Dolomite $CaMg(CO_3)_2$	++	+	+	+
Ettringite $Ca_6Al_2(SO_4)_3(OH)_{12}\cdot 26H_2O$	+	+	+	++
Goethite $FeHO_2$	+	+	+	+
Periclase MgO	+	+	+	+
Portlandite $Ca(OH)_2$	+	+	+	+
Quartz SiO_2	++	+	++	+
Sylvite KCl	++	+	++	+
Syngenite $K_2Ca(SO_4)_2\cdot H_2O$	++	++	++	++

Note: ++ is: major compounds and +: minor compounds.

6.4.3 Thermal and hygroscopic properties

Bio-based materials are recognised for their excellent thermal and hygroscopic behaviour, as they ensure good thermal comfort in the building and regulate indoor humidity levels. In parallel, they can also contribute to reducing building energy demand, especially heating and cooling. As the sunflower bark mixtures produced in this chapter are intended for use as a non-structural element and insulation material in buildings, it is essential to examine their hygroscopic characteristics.

(a) Thermal conductivity

The evolution of thermal conductivity (λ) and dry density (ρ) of sunflower bark (SB) mixtures over a period between 28 days and 120 days is presented in Figure 6-15 and Figure 6-16. The thermal conductivity measurements were carried out on M8 as a reference paste and two SB mortars, such as M12 and M14.

The thermal conductivity of M8, M12 and M14 was 0.3038, 0.1428 and 0.1316 W/m.K when their dry densities were 1385, 774 and 717 kg/m^3, respectively, at 28 days. Moreover, at 120 days, M8, M12 and M14 had achieved a thermal conductivity of 0.2721, 0.1263 and 0.1270 W/m.K, while the dry densities were 1316, 759 and 720 kg/m^3, simultaneously. This is evidence that the thermal conductivity and dry density of the SB mixtures decrease with the increment in curing time. This change can be attributed to a slow evaporation of unbound water, which leaves air voids within the mixture and thus makes it lighter. Note that the slight

contrasting increase in density for M14 is probably due to moisture input because the measurements were made during the winter season.

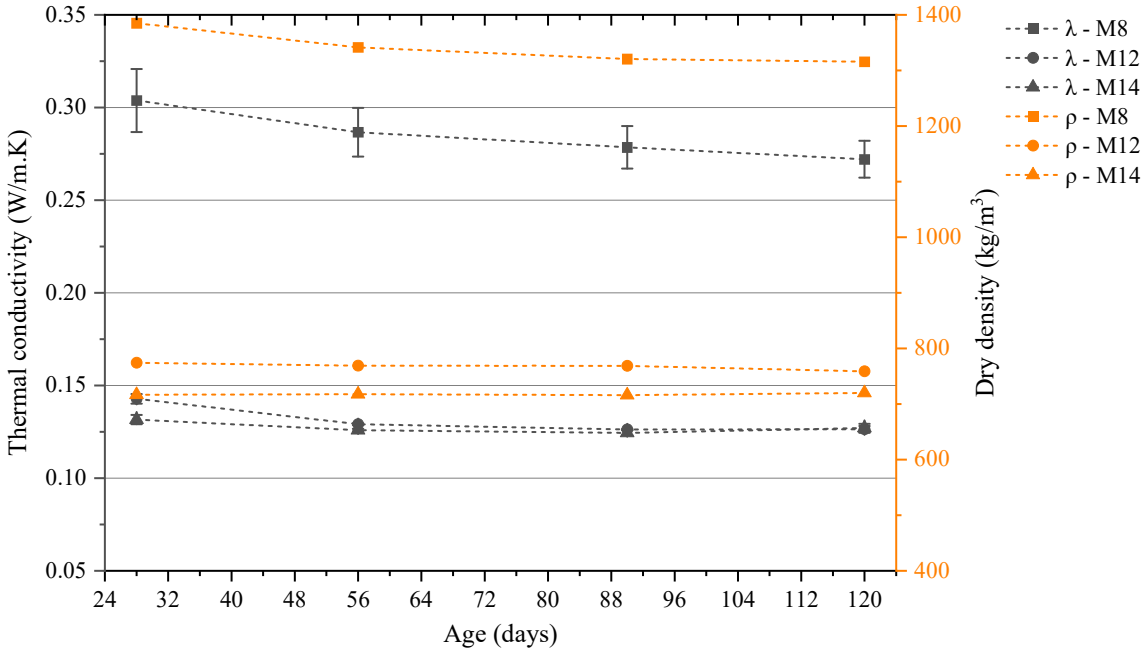

Figure 6-15. Evolution of the thermal conductivity and dry density of sunflower bark mixtures with respect to time.

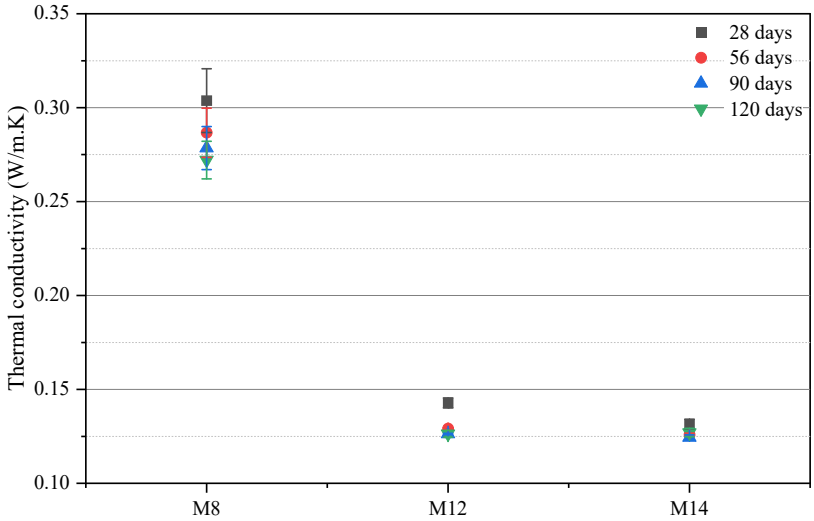

Figure 6-16. Evolution of thermal conductivity as function of formulations and time.

Furthermore, the thermal conductivity also depends on the quantity of plant particles in the mixtures. The addition of sunflower bark significantly lessened the thermal conductivity of the mixtures. Indeed, the latter decreases with the increase in the sunflower bark content.

As shown in Figure 6-17, the thermal conductivity and dry density data obtained from the sunflower (pith and bark) mixtures developed in this study are consistent with those for sunflower and hemp concretes found in the literature.

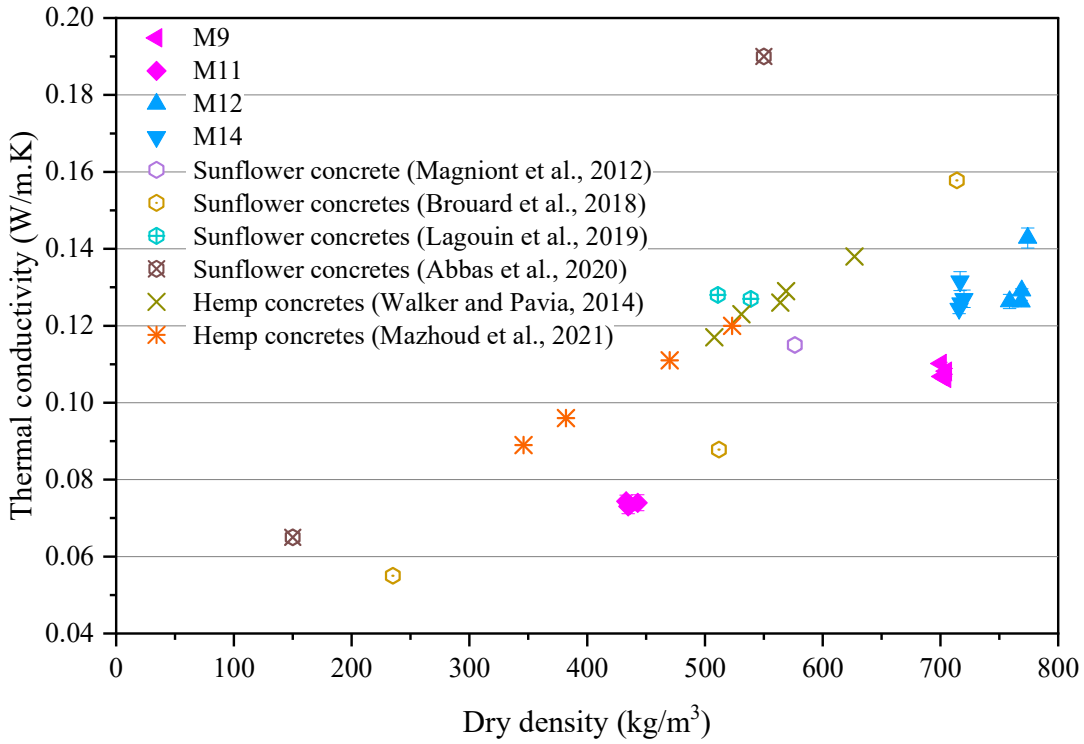

Figure 6-17. Thermal conductivity of different sunflower mortars/concretes as function of dry density.

(b) Hygroscopic properties

The kinetics of moisture sorption isotherms of sunflower bark mortars obtained at a constant temperature of 23 °C and relative humidity (RH) ranging from 0 to 92 %, and vice versa, are presented in Figure 6-18 (a, b). The adsorption isotherm curves increase gradually up to 50 % RH, then, increase sharply until they reach 92 % RH. Conversely, the kinetics of desorption drastically drop between 50-92 % RH and afterwards decrease slowly until attaining 0 % RH.

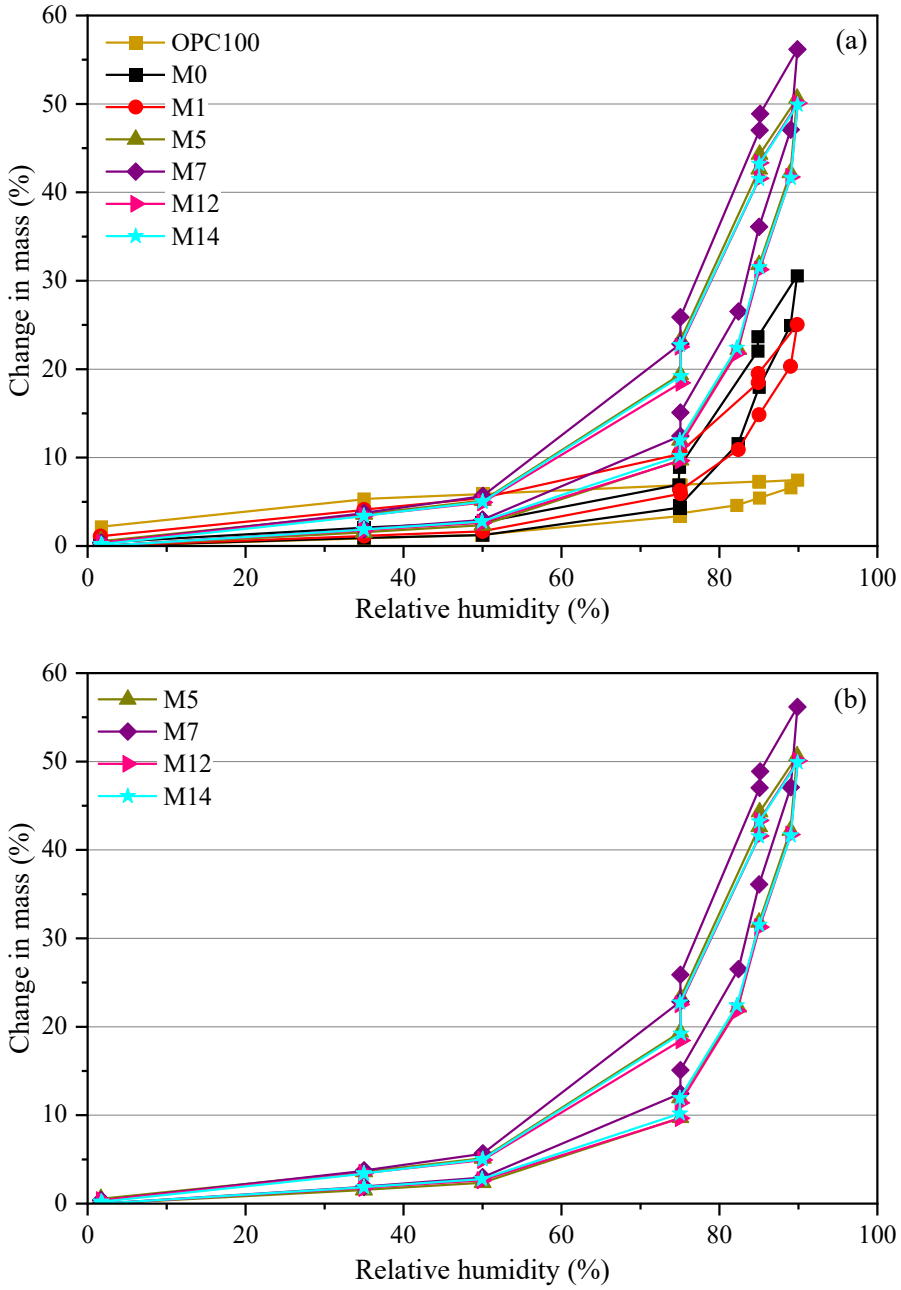

Figure 6-18. Adsorption and desorption isotherms of sunflower bark mixtures at 23 °C. (a) all mixtures and (b) only sunflower bark mixtures.

Moreover, the moisture content appears to depend on the sunflower bark proportion in the mixtures. In fact, sunflower bark mixtures observe higher mass change than the reference pastes (OPC100, M0 and M1). The lower moisture content in OPC100, M0 and M1 can be attributed to their lower porosity and permeability. On the other hand, although the bio-based mortars were produced by adding 20 to 30 % sunflower bark content, no significant difference is noticed in their sorption isotherms. At 90 % RH, formulation M7 showed the highest moisture content (56.18 %), while the mass change for M5, M12 and M14 was about 50 %.

6.4.4 Wetting and drying cycles

The exposure environment is one of the factors affecting the overall properties and durability of bio-based materials. Therefore, it was interesting to evaluate the behaviour of sunflower bark mixtures produced in this study under wetting and drying cycles. During the experiment, mass changes were monitored, and the 28-day flexural and compressive strengths were measured and compared to those of samples cured at ambient laboratory conditions. The mechanical performance results are presented in Figure 6-19 and Figure 6-20, respectively.

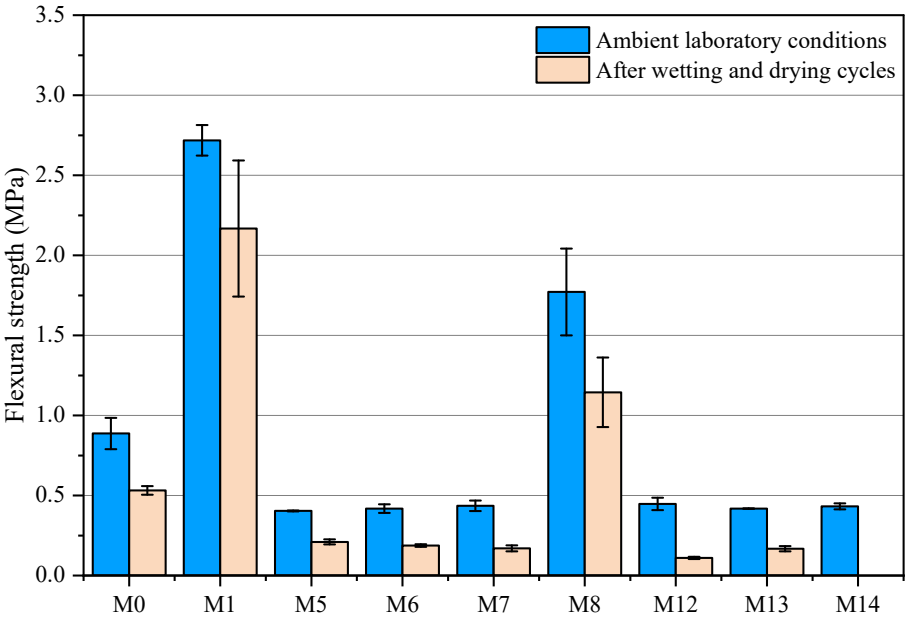

Figure 6-19. Flexural strength of sunflower bark mixtures at 28 days.

From Figure 6-19, the samples exposed to wetting and drying (W/D) cycles show lower flexural strengths (R_f) compared to those cured at ambient laboratory conditions. The flexural strengths of the reference pastes M1 and M8 decreased by 20.26 % and 35.39 %, respectively. Furthermore, the sunflower bark mixtures also observed significant R_f values reductions. The minimum decrease was recorded on M5 (47.96 %), while the maximum was obtained from M12 (75.46 %). Note that M14 was broken after the third W/D cycle.

Moreover, the other SB mixtures, such as M6, M7 and M13, showed a decrease in R_f of 55.30 %, 61.05 % and 60.01 % simultaneously. For SB mixtures (M5, M6 and M7) made of M1 (80 % WFA8 + 20 % OPC) binder, the drops in flexural strength increase with an increase in sunflower bark content. In contrast, the reductions in R_f for SB mixtures (M12, M13) made of M8 (90 % WFA8 + 10 % OPC) binder diminish as sunflower bark content increases.

As shown in Figure 6-20, wetting and drying cycles were quite beneficial for M1 and M8 as their R_c increased by 91.02 % and 66.15 %, respectively. It is assumed that immersion of the pastes in water enabled further hydration of the wood fly ash and cement.

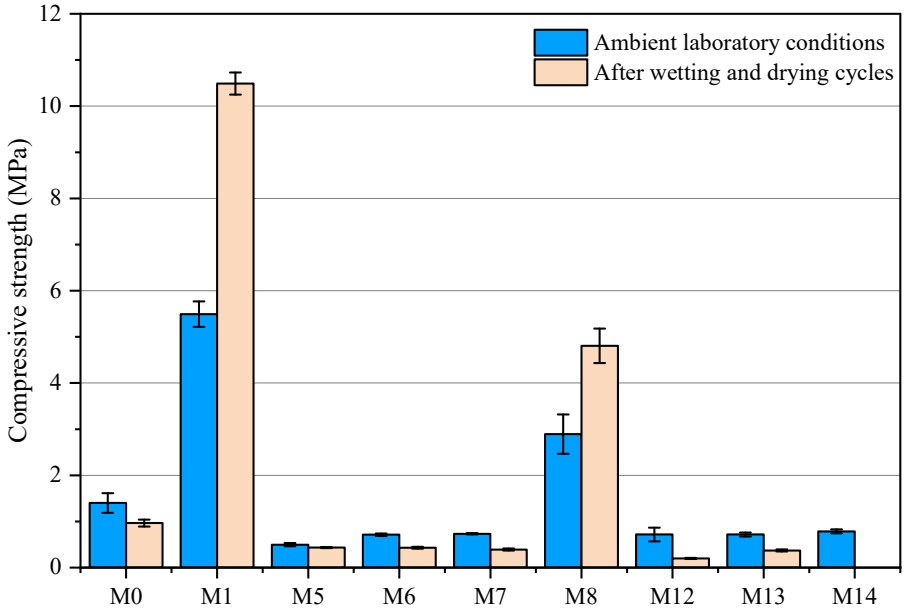

Figure 6-20. Compressive strength of sunflower bark mixtures at 28 days.

On the contrary, W/D cycles have negatively affected the compressive strength of the sunflower bark mixtures. The latter reduced by 12.50 %, 39.80 % and 46.44 % for M5, M6 and M7, respectively. As for M12 and M13, the R_c dropped simultaneously by 72.09 % and 48.26 %. Regarding SB mixtures (M5, M6, M7) made of M1 binder, the reductions in R_c become more critical with increased sunflower bark content. However, the drops in R_c for SB mortars (M12, M13) made of M8 binder appear to diminish with the increment of the sunflower bark content.

Apart from that, the mass changes of sunflower bark mixtures are shown in Figure 6-21. The wetting and drying cycles significantly affected the mass of SB mortars compared to the reference pastes. The mass oscillations for the sunflower bark mixtures were uniform and had close magnitudes. At 28 days, the minor mass loss among SB mixtures was recorded on M7 (15.68 %), while the highest was found on M10 (25.06 %). At a similar age, M1 lost only about 3.26 % of its mass, whereas no mass loss was noticed in M8. The significant decrease in mass found on SB mixtures can be ascribed to the presence of sunflower bark particles, which have increased the porosity and permeability of the mixtures.

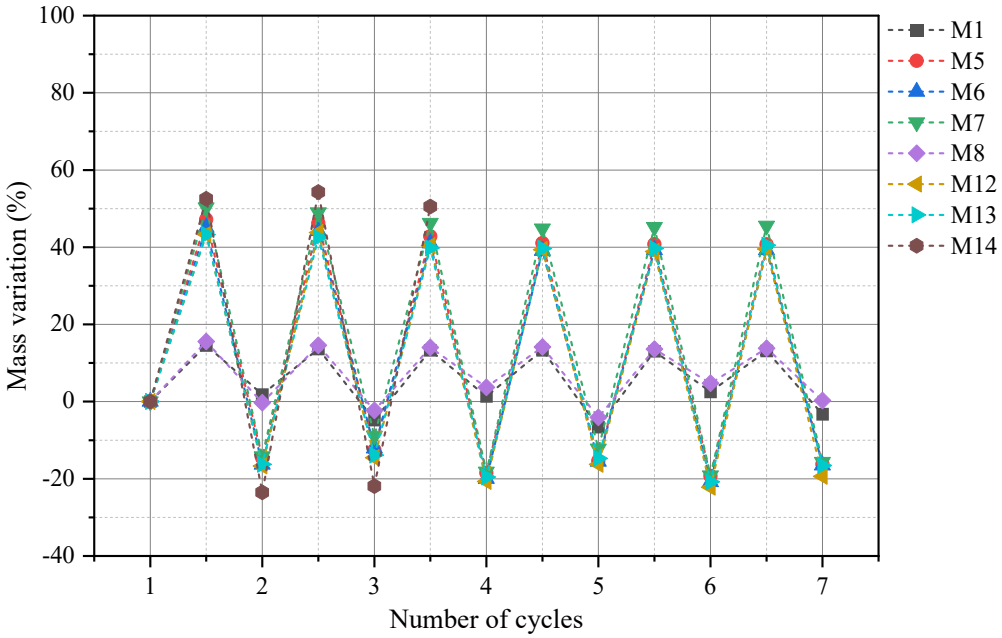

Figure 6-21. Mass variation during the wetting and drying cycles experiment.

Besides that, the sunflower bark mixtures have also experienced remarkable mass gains throughout the wetting and drying cycles. The least mass growth among SB mixtures was noted on M12 (38.89 %), whilst the most mass gain was registered on M14 (54.31 %). For the reference pastes, the mass increase from the beginning until the end of the W/D cycles was in the range of (13.03-14.59) % for M1 and (13.61-15.58) % for M8.

6.5 Conclusion

In this chapter, six distinct sunflower bark mixtures have been designed and prepared using two binding matrices composed of 80-90 % wood fly ash and 10-20 % ordinary Portland cement. The sunflower bark was added at levels between 20 and 30 % by mass of the binder. The mechanical, microstructural, thermal and hygroscopic properties of the resulted sunflower bark mixtures were examined at different curing ages.

The mechanical test results of the sunflower bark mixtures are in the agreement with those of the other bio-based mortars/concretes found in the literature. It is noticed that adding sunflower bark into the mixtures resulted in a significant decrease in the strength properties. The SB mixtures yielded flexural strengths ranging from 0.39-0.45 MPa at 7 days and have increased to reach 0.45-0.56 MPa at 90 days. Simultaneously, the compressive strengths were in the ranges of 0.47-0.65 MPa at 7 days and 0.49-0.65 MPa at 90 days. Despite some oscillations in flexural and compressive strength trends, overall, no significant improvement was observed. The increases in strength are attributed to the hydration of the cement, pozzolanic activity of wood fly ash and carbonation of the mixtures. On the other hand, the declines could be due to chemical transformations of hydration products.

SEM micrographs show that SB mixtures exhibit a weak interface between sunflower bark and binding matrix. The microstructure of SB mixtures presents lots of voids, is less dense and contains hydration products. The TGA results confirmed the presence of ettringite and portlandite in the samples. In addition, they also showed that the mass losses associated with calcium carbonate decomposition were significant in all SB mixtures. The estimates revealed that the $Ca(OH)_2$ content was within the range of 8.81-12.15 %, while $CaCO_3$ represented 46.65-51.89 %. These findings were persistent with XRD analysis, which showed that calcite was one of the primary compounds in the SB mixtures. Minor levels of portlandite and ettringite were also detected in all SB mixtures, except M14, which had ettringite in abundance.

The sunflower bark mixtures showed a low thermal conductivity and it was dependent to the dry density and the presence of sunflower bark. Globally, the thermal conductivity of sunflower bark mixtures was between 0.1263 and 0.1428 W/m.K and the dry densities ranged from 717 to 774 kg/m^3. The dynamic vapour sorption indicated that SB mixtures present excellent moisture adsorption and desorption capacity. At 90 % RH, the moisture content for all SB mixtures varied from 50 to 56 %.

Furthermore, it was also found that wetting and drying cycles negatively affect the mechanical properties of sunflower bark mixtures. The flexural strength reduced by 47.96-75.46 % while the compressive strength decreased by 12.50-72.09 %. This significant reduction in strength depended on the amount of sunflower bark and is due to high porosity and weak interface between sunflower bark and the binding matrix.

In short, the aforementioned findings show that sunflower bark and wood fly ash can be associated to produce lightweight bio-based prefabricated building elements, with mechanical and hygrothermal properties as those of currently available bio-based building insulation materials.

Chapter 7: Conclusion and perspectives

7.1 Conclusion

The main objective of this thesis was to study the variability of wood ashes and valorize them with sunflower particles in lightweight bio-based building materials. Thanks to the results obtained from various experimental analyses, including mechanical, morphological, microstructural, thermal, hygroscopic and durability, the following eco-friendly building materials were proposed:

- Thirty binders made based on four different batches of wood ash and mineral hydraulic additives, namely natural hydraulic lime and ordinary Portland cement;
- Six sunflower pith mortars designed for implementation by projection for building insulation from the exterior;
- Six sunflower bark mixtures intended to produce prefabricated building elements (lightweight bricks, blocs, etc.).

It is worth mentioning that it was essential to review the existing works dedicated to materials comparable or similar to the biomass by-products before establishing the experimental program.

Chapter 1 summarised the literature discussing the role of supplementary cementitious materials (SCMs), namely coal fly ash, silica fume, ground granulated blast slag, limestone powder and metakaolin on the hydration, mechanical properties, durability of cement-based materials and their environmental and economic benefits. It was noticed that the influence of SCMs on the performance of cement-based materials might depend on several factors, including the nature and origin of an SCM, replacement ratios, physical and chemical properties. The application of SCMs at suitable replacement levels has been reported to improve some properties of cement-based materials. On the other hand, most studies agree that adding a high SCMs content (> 50 %) significantly reduces the mechanical properties and durability of cement-based materials. Globally, the compressive strength decreases with an increasing amount of SCMs in the mixture.

Moreover, SCMs used at a similar replacement level can act differently due to a significant disparity in their physical and chemical properties. It was noted that the influence of SCMs on the hydration of cement-based materials highly depends on the SCMs content, fineness and synergic effect of the SCMs reactivity mechanisms. Concerning the environmental and economic aspects, using SCMs in cement-based materials provides numerous benefits, such as fair use and conservation of natural resources, efficient waste management, reduction of energy consumption, production cost, and carbon dioxide emissions.

Then, a literature review on the applications of wood ashes and sunflower particles in building materials was made in Chapter 2. This chapter focused on the supply of wood ashes, their applications, physical and chemical properties and their influence on the mechanical properties of cement-based and bio-based materials. In the section related to bio-based particles, we have presented the history of bio-based building insulation materials and the evolution of thermal regulations in France. Afterwards, the sunflower crop history, supply, applications of its by-products and their impact on the mechanical, thermal, hygroscopic properties and durability of bio-based concretes have been discussed.

Wood ashes can have angular and spherical particles. The chemical composition of wood ashes varies from ash to ash. This disparity is due to several factors, such as feedstock type, treatment applied to feedstock, thermal technology, temperature, combustion techniques, conditioning, etc. The environmental assessment revealed that wood ash might contain hazardous elements such as zinc, lead, copper, mercury, etc., which is the main factor limiting their recycling.

On the other hand, extensive research has been carried out on the suitability of these biomass by-products in construction materials. Generally, the mechanical performance and durability of building materials decrease with increasing wood ash proportion. In contrast, many studies have proved that when wood ashes are used at lower content (< 30 %), they can densify the microstructure, improve the compressive strength, flexural strength, elasticity modulus, reduce the permeability and alkali-silica reactions expansion. Apart from that, we have noticed that less attention has been given to the valorization of wood ashes in bio-based materials.

Since the presentation of hemp concrete in 1986, the applications and research of bio-based building materials have expanded considerably. Currently, a wide range of plant particles is used to produce bio-based materials. Sunflower is one of these emerging particles. Owing to their low bulk density and high porosity, the sunflower particles present excellent thermal, acoustic and hygroscopic properties.

The sunflower-based materials exhibit close properties to those of hemp concrete, which is the most popular bio-based building material. The compressive strength of bio-based mortars/concretes ranges between 0.1 and 4 MPa, while elastic modulus varies from 1.5-160 MPa. This lower strength has been ascribed to the chemical compounds in plant particles that interfere with the hydration of the mineral binder. On the other hand, the thermal conductivity of bio-based materials ranges from 0.055 to 0.35 W/m.K. The latter also has high water

absorption, storage and diffusion capacity. Based on the literature surveyed, bio-based materials' mechanical performance and durability need to be improved.

As the demand for bio-based building materials is expected to continue increasing, it is essential to find new sources of raw materials for these eco-friendly materials to satisfy market demand. In addition, their production cost must also be reduced to compete with traditional building insulation materials.

Chapter 3 discussed about the raw materials and their characterization results. The raw materials collected included eight different biomass ashes and sunflower particles. The biomass ashes were heterogeneous in terms of physical and chemical properties. Some of the wood ashes analysed were coarser than others. The bulk density ranged from 374 to 631 kg/m^3 for wood fly ash, whereas for the wood bottom ash, it was 1035 kg/m^3. The skeletal density of ashes varied between 2.0 and 4.5 g/cm^3. The moisture content of the wood ashes was below 2 %. Concerning the chemical composition, the wood ashes appeared to be rich in calcium oxide, silica and potassium oxide. The loss on ignition was slightly higher in the two evaluated ashes than in OPC.

On the other hand, sunflower pith and bark particles presented different physical and chemical properties. The sunflower pith (SP) particles were finer, lighter and more porous than sunflower bark (SB) particles. The average bulk density of SP and SB was 20.6 and 155.2 kg/m^3, respectively. The skeletal densities were 732-1029 kg/m^3 for SP and 1170-1542 kg/m^3 for SB. The water absorption capacity of SP was significantly higher than SB. After 5 min of immersion, the water intake for SP was 1305 %, while for SB, it was 155 %. The thermal conductivity (λ) of sunflower pith was equal to 0.0390 W/m.K and 0.0583 W/m.K for sunflower bark.

Chapter 4 presented the characterization results of thirty potential binding matrices elaborated based on four batches of wood ashes and small NHL or OPC contents as mineral additives. The water demand for the wood ashes evaluated depended on the type of wood ash, conditioning, particle size distribution and porosity. The ashes received in a wet state required more mixing water than those delivered in a dry condition.

The water-to-wood ash ratios selected were 0.50 for WFA8 and WFA9, and 0.7 for WFA3 and WBA. Based on the quantities of ashes collected and the results of preliminary analyses, four batches of wood ashes were selected to be used to prepare the binding matrices. The Vicat test revealed a delayed setting of the wood fly ash WFA8 pastes. Nevertheless, adding 5, 10 and

20 % NHL or OPC contents remarkably improved the setting of the wood ash pastes. Concerning the WFA8-NHL pastes, the initial and final setting time dropped simultaneously from 25 to 12.5 hours and 56 to 24 hours. In the case of WFA8-OPC pastes, the initial setting time was reduced from 25 to 4.5 hours, whereas the final setting time diminished from 56 to 30 hours. The accelerated hardening observed after adding NHL or OPC is attributed to the hydration reactions of these hydraulic binders.

Moreover, the mechanical tests indicated that the wood ash pastes developed in this study had close flexural (R_f) and compressive (R_c) strengths as those of building materials with identical wood ash content found in the literature. The wood ash pastes incorporated with NHL had lower R_f and R_c than those containing OPC. The flexural and compressive strengths of the wood ash paste samples typically increased with the increase in NHL or OPC contents, bulk density, mass and curing age. In contrast, unexcepted behaviour has been noticed among WBA pastes, where the trend in R_f and R_c declined with an increment in curing time. This was ascribed to the particle size distribution (coarse particles, irregular particle shape) of WBA, inadequate compaction, evaporation of mixing water during the curing, increased porosity, lack and insufficient hydration products.

Using 5, 10 and 20 % NHL or OPC improved the mechanical performance of the wood ash pastes, except WBA pastes. The highest flexural and compressive strength values were obtained from the wood ash pastes containing 20 % NHL or OPC at 28 days. The main findings of this chapter are summarised in Table 7-1.

Table 7-1. Minimum and maximum flexural strength, compressive strength, bulk density and mass values obtained from the wood ash pastes studied.

Mix notation	Flexural strength (MPa) at 28 days	Compressive strength (MPa) at 28 days	Bulk density (kg/m^3)	Mass (g)
NHL100	0.85	2.69	1205-1218	312-322
WFA3-NHL pastes	0.38-0.44	0.92-2.59	972-1210	245-322
WBA-NHL pastes	0.02-0.15	0.05-0.24	917-1212	243-318
WFA8-NHL pastes	0.65-1.12	0.77-1.82	1218-1407	309-361
WFA9-NHL pastes	0.57-0.70	0.72-0.96	1148-1388	309-359
OPC100	3.14	29*	1677-1773	444-471
WFA3-OPC pastes	0.32-0.71	1.65-3.87	986-1261	241-336
WBA-OPC pastes	0.07-0.22	0.13-2.56	895-1272	232-319
WFA8-OPC pastes	0.89-2.72	1.40-5.49	1110-1442	296-355
WFA9-OPC pastes	0.65-2.11	0.62-4.01	1126-1453	299-372

*Note: *: Detection limit of the apparatus. Normally, the 28-day Rc of the cement used is 32.5 MPa.*

In Chapter 5, six different sunflower pith mortars were elaborated for implementation by projection process. These lightweight bio-based mortars were prepared using two low-carbon binding matrices composed of 80-90 % wood fly ash WFA8 and 10-20 % ordinary Portland cement. The sunflower pith (SP) particles were used as aggregates at ratios of 5, 10 and 15 % by mass of binder. The SP mortars proposed in this study had the mechanical, microstructural, hygrothermal properties and durability comparable to those of currently available bio-based building materials. It was noted that sunflower pith particles considerably reduced the bulk density, flexural strength, compressive strength, elastic modulus and thermal conductivity (λ), as shown in Table 7-2.

Table 7-2. Minimum and maximum average flexural strength, compressive strength, thermal conductivity and bulk density values obtained from the sunflower pith mortars.

Mix notation	Flexural strength (MPa)	Compressive strength (MPa)	Elastic modulus (MPa)	Thermal conductivity (W/m.K)	Bulk density (kg/m^3)
M0	0.33-1.17	0.48-1.82	10.77-69.27	n.t.	1147-1238
M1	1.31-2.77	3.72-7.04	202.94-415.93	n.t.	1305-1425
M2	0.27-0.54	0.28-0.53	6.76-14.33	n.t.	676-846
M3	0.15-0.40	0.21-0.49	3.73-11.22	n.t.	522-742
M4	0.08-0.21	0.11-0.26	1.28-4.58	n.t.	402-572
M8	0.76-1.94	1.30-4.05	46.74-196.63	0.272-0.304	1207-1343
M9	0.24-0.63	0.29-0.62	7.70-28.24	0.106-0.110	658-834
M10	0.16-0.41	0.23-0.53	4.86-18.08	n.t.	527-612
M11	0.08-0.27	0.11-0.40	1.39-8.69	0.074-0.073	412-507

Note: n.t.: not tested.

Moreover, the sunflower pith mortars exhibited a less dense, more porous microstructure and the interfacial zone between sunflower pith and wood ash binder appeared to be weak at 28 days. At a similar age, the microstructural analyses found some hydration products, such as C-S-H, ettringite, and portlandite in SP mortars but, the latter were not as abundant as those usually observed in cement-based materials. The amount of portlandite was remarkably lower than calcite. Besides that, the SP mortars also contained other crystalline phases, including albite, alite, dolomite, sylvite, syngenite, etc.

The presence of sunflower pith particles delayed the setting, increased the porosity and made the bio-based mortars more flexible. The hygroscopic properties of the bio-based mortars were also improved. The sorption isotherms showed that, at 90 % RH, the sunflower pith mortars had a moisture content ranging from 15 to 52 %, while for the reference pastes M0, M1 and M8, it was 7, 25 and 30 %, respectively.

Chapter 6 presented the results obtained from the characterization of six different sunflower bark mixtures intended for prefabricated building elements. These lightweight bio-based mixtures were developed using two low-carbon binding matrices consisting of 80-90 % wood fly ash WFA8 and 10-20 % ordinary Portland cement. The sunflower bark (SB) particles were added as aggregates at ratios of 20, 25 and 30 % by mass of binder. At the desired curing ages, the SB mortars' mechanical, microstructural, thermal, hygroscopic, and durability properties were investigated.

Like the SP mortars, the mechanical, thermal, hygroscopic properties and durability performance of sunflower bark mixtures were also close to those of available bio-based building materials. The inclusion of sunflower bark particles improved the thermal insulation efficiency of the material as the thermal conductivity (λ) decreased significantly. Other than that, they also lowered the bulk density, flexural strength, compressive strength and elastic modulus, as can be seen in Table 7-3. The wetting and drying cycles did not significantly alter the mechanical performance of SB mortars. SB mortars' low flexural and compressive strengths were attributed to the water-soluble extractives from sunflower bark particles, which interfered with the hydration reactions.

Table 7-3. Minimum and maximum average flexural strength, compressive strength, thermal conductivity and bulk density values obtained from the sunflower bark mixtures.

Mix notation	Flexural strength (MPa)	Compressive strength (MPa)	Elastic modulus (MPa)	Thermal conductivity (W/m.K)	Bulk density (kg/m^3)
M0	0.33-1.17	0.48-1.82	10.77-69.27	n.t.	1147-1238
M1	1.31-2.77	3.72-7.04	202.94-415.93	n.t.	1305-1425
M5	0.39-0.45	0.48-0.54	25.69-29.05	n.t.	707-816
M6	0.40-0.51	0.54-0.71	29.82-44.81	n.t.	707-859
M7	0.40-0.59	0.65-0.85	35.11-44.70	n.t.	707-836
M8	0.76-1.94	1.30-4.05	46.74-196.63	0.272-0.304	1207-1343
M12	0.37-0.66	0.47-0.76	24.77-34.51	0.126-0.143	731-844
M13	0.38-0.45	0.47-0.72	20.38-30.89	n.t.	677-819
M14	0.40-0.49	0.55-0.78	24.79-31.37	0.124-0.132	677-799

Note: n.t.: not tested.

Furthermore, compared with SP mortars, the SB mortars hardened faster. The microstructural analyses revealed the presence of hydration products, including ettringite and portlandite. The samples also contained crystalline compounds, such as albite, alite, calcite, quartz, sylvite, syngenite, dolomite, etc. The amount of calcite was considerably higher than that of portlandite at 28 days. As noted previously on SP mortars, the SB mortars also presented a less dense and porous microstructure, and the bonding between sunflower bark and wood ash binder was weak. The incorporation of sunflower bark noticeably improved the hygroscopic properties of the bio-based mixtures. The sorption isotherms indicated that, at 90 % RH, the sunflower bark mixtures exhibited a moisture content of 50-56 %, while for the reference pastes M0, M1 and M8, it was 7, 25 and 30 %, respectively.

In summary, the sunflower pith mortars and sunflower bark mixtures developed in this study presented the mechanical, thermal and hygroscopic properties equivalent and, in some cases, better than those of currently available bio-based building materials. Therefore, this study has proven the suitability of wood fly ash, sunflower pith and bark particles in bio-based building materials. This approach could make bio-based building materials more affordable and sustainable. Wood fly ash is available at a lower cost compared to lime-based and cement-based binders. In addition, the fact that sunflower is one of the most widely cultivated crops in France and Europe implies that its by-products are also in ample supply.

7.2 Perspectives

This research work contributed to the existing knowledge on bio-based building materials and also provides a solid foundation for future research works on bio-based mortars/concretes where biomass ashes will be used as the main component of the binding matrix. Besides that, the areas for further research were also highlighted. For instance, more research should be undertaken on the interfacial zone between the wood ash-based binding matrix and sunflower particles. Except that, the durability (carbonation, resistance to microbial growth, etc.) of building materials made of wood ash and sunflower particles is another important subject that should be addressed more thoroughly.

Moreover, it would be interesting to optimise the binding matrices proposed in this study and then apply the optimised formulation to different batches of wood biomass ashes. This could enable the development of numerical models to predict the mechanical performance of wood biomass ash-based binders. The optimised binding matrix could then be combined with other batches of sunflower and plant particles to produce lightweight bio-based building materials. In addition, it would also be of interest to consider pairing wood biomass ashes with other industrial by-products to produce low-carbon and affordable alternative binding matrices for bio-based building materials.

Furthermore, to make bio-based mortars/concretes more sustainable, it is crucial to find production methods that require less water consumption. Due to time constraints, the environmental assessment of the biomass ashes was not performed. Thus, leachability research should be conducted to ensure the safety of the proposed binders and bio-based mortars. Besides that, it would also be fascinating to use the binding matrices, sunflower pith and bark mortars developed in this research at a full-scale construction to examine their performances in actual building structures.

References

Abbas, M.S., (2021). Caractérisations multi-physiques des mortiers biosourcés isolants et modélisation de leurs impacts sur les transferts hygrothermiques à l'échelle des parois. Application aux bétons de moelles végétales. Thèse de doctorat de l'Université de Lyon, 166p.

Abbas, M.S., Gourdon, E., Glé, P., McGregor, F., Ferroukhi, M.Y., Fabbri, A., (2021). Relationship between hygrothermal and acoustical behavior of hemp and sunflower composites. Building and Environment, 188, 107462. https://doi.org/10.1016/j.buildenv.2020.107462.

Abbas, M.S., McGregor, F., Fabbri, A., Ferroukhi, M.Y., (2020). The use of pith in the formulation of lightweight bio-based composites: Impact on mechanical and hygrothermal properties. Construction and Building Materials, 259, 120573. https://doi.org/10.1016/j.conbuildmat.2020.120573.

Abdullahi, M., (2006). Characteristics of Wood ASH/OPC Concrete. Leonardo Electronic Journal of Practices and Technologies, pp. 9–16.

Aggarwal, L.K., Singh, J., (1990). Effect of plant fibre extractives on properties of cement. Cement and Concrete Composites, 12, pp. 103-108. https://doi.org/10.1016/0958-9465(90)90047-2.

Ahmad, M.R., Chen, B., (2018). Effect of silica fume and basalt fiber on the mechanical properties and microstructure of magnesium phosphate cement (MPC) mortar. Construction and Building Materials 190, pp. 466-478. https://doi.org/10.1016/j.conbuildmat.2018.09.143.

Ahmad, M.R., Chen, B., Farasat Ali Shah, S., (2019). Investigate the influence of expanded clay aggregate and silica fume on the properties of lightweight concrete. Construction and Building Materials, 220, pp. 253-266. https://doi.org/10.1016/j.conbuildmat.2019.05.171.

Aïtcin, P.-C., (2016). Supplementary cementitious materials and blended cements, in: Science and Technology of Concrete Admixtures. Woodhead Publishing, pp. 53-73. https://doi.org/10.1016/B978-0-08-100693-1.00004-7.

Al Menhosh, A., Wang, Y., Wang, Y. Augusthus-Nelson, L., (2018). Long term durability properties of concrete modified with metakaolin and polymer admixture. Construction and Building Materials, 172, pp. 41-51. https://doi.org/10.1016/j.conbuildmat.2018.03.215.

Alaskar, A., Hooton, R.D., (2020). Effect of binder fineness and composition on length change of high-performance concrete. Construction and Building Materials, 237, 117537. https://doi.org/10.1016/j.conbuildmat.2019.117537.

Alengaram, U.J., Mahmud, H., Jumaat, M.Z., (2011). Enhancement and prediction of modulus of elasticity of palm kernel shell concrete. Materials & Design 32, 2143–2148. https://doi.org/10.1016/j.matdes.2010.11.035.

Alyousef, R., Benjeddou, O., Soussi, C., Khadimallah, M.A., Mustafa Mohamed, A., (2019). Effects of Incorporation of Marble Powder Obtained by Recycling Waste Sludge and Limestone Powder on Rheology, Compressive Strength, and Durability of Self-Compacting

Concrete. Advances in Materials Science and Engineering, pp. 1-15. https://doi.org/10.1155/2019/4609353.

Amziane, S., (2016). Overview on bio-based building material made with plant aggregate. RILEM Technical Letters 8, 1, pp. 31-38.

Amziane, S., Arnaud, L., (2013). Bio-aggregate-based building materials: applications to hemp concretes, Civil engineering and geomechanics series. ISTE Ltd, John Wiley & Sons, Inc., London: Hoboken, NJ. 323p.

Amziane, S., Collet, F., (2017). Bio-aggregates Based Building Materials: State-of-the-Art Report of the RILEM Technical Committee 236-BBM, RILEM State-of-the-Art Reports. Springer Netherlands, Dordrecht. https://doi.org/10.1007/978-94-024-1031-0.

Anjos, M.A.S., Camões, A., Campos, P., Azeredo, G.A., Ferreira, R.L.S., (2020). Effect of high-volume fly ash and metakaolin with and without hydrated lime on the properties of self-compacting concrete. Building Engineering, 27, 100985. https://doi.org/10.1016/j.jobe.2019.100985

Antoni, M., Rossen, J., Martirena, F., Scrivener, K., (2012). Cement substitution by a combination of metakaolin and limestone. Cement and Concrete Research 42, pp. 1579-1589. https://doi.org/10.1016/j.cemconres.2012.09.006.

Antonio-Cisneros, C.M., Elizalde-Gonzalez, M.P., (2010). Characterization of Manihot residues and preparation of activated carbon. biomass and bioenergy 7, 34, pp. 389-395. https://doi.org/10.1016/j.biombioe.2009.12.001.

Arizzi, A., Cultrone, G., Brümmer, M., Viles, H., (2015). A chemical, morphological and mineralogical study on the interaction between hemp hurds and aerial and natural hydraulic lime particles: Implications for mortar manufacturing. Construction and Building Materials 75, pp. 375-384. https://doi.org/10.1016/j.conbuildmat.2014.11.026.

Arnaud, L., Gourlay, E., (2012). Experimental study of parameters influencing mechanical properties of hemp concretes. Construction and Building Materials, 28, pp. 50-56. https://doi.org/10.1016/j.conbuildmat.2011.07.052.

Arufe, S., Hellouin de Menibus, A., Leblanc, N., Lenormand, H., (2021). Physico-chemical characterisation of plant particles with potential to produce biobased building materials. Industrial Crops and Products, 171, 113901. https://doi.org/10.1016/j.indcrop.2021.113901.

Arvaniti, E.C., Juenger, M.C.G., Bernal, S.A., Duchesne, J., Courard, L., Leroy, S., Provis, J.L., Klemm, A., De Belie, N., (2015a). Determination of particle size, surface area, and shape of supplementary cementitious materials by different techniques. Materials and Structures, 48, pp. 3687-3701. https://doi.org/10.1617/s11527-014-0431-3.

Arvaniti, E.C., Juenger, M.C.G., Bernal, S.A., Duchesne, J., Courard, L., Leroy, S., Provis, J.L., Klemm, A., De Belie, N., (2015b). Physical characterization methods for supplementary cementitious materials. Materials and Structures, 48, pp. 3675-3686. https://doi.org/10.1617/s11527-014-0430-4.

Avet, F., Snellings, R., Alujas Diaz, A., Ben Haha, M., Scrivener, K., (2016). Development of a new rapid, relevant and reliable (R3) test method to evaluate the pozzolanic reactivity of calcined kaolinitic clays. Cement and Concrete Research 85, p. 1-11. https://doi.org/10.1016/j.cemconres.2016.02.015.

Baecher, C., Dutreix, N., Buick, R., Rimbaud, A., (2012). Etude sur le secteur et les filières de production des matériaux et produits bio-sourcés utilisés dans la construction (à l'exception du bois). Nomadéis.

Bajpai, R., Choudhary, K., Srivastava, A., Sangwan, K.S., Singh, M., (2020). *Environmental impact assessment of fly ash and silica fume based geopolymer concrete*. Cleaner Production, 254, 120147. https://doi.org/10.1016/j.jclepro.2020.120147.

Balek, V., Fusek, J., Kříž, J., Murat, M., (1995). Differences in the thermal behaviour of natural quartz before and after mechanical grinding as observed by emanation thermal analysis. Thermochimica Acta, 262, pp. 209-214. https://doi.org/10.1016/0040-6031(95)02350-B.

Baquerizo, L.G., Matschei, T., Scrivener, K.L., Saeidpour, M., Wadsö, L., (2015). Hydration states of AFm cement phases. Cement and Concrete Research, 73, pp. 143-157. https://doi.org/10.1016/j.cemconres.2015.02.011.

Barbieri, V., Lassinantti Gualtieri, M., Siligardi, C., (2020). Wheat husk: A renewable resource for bio-based building materials. Construction and Building Materials, 251, 118909. https://doi.org/10.1016/j.conbuildmat.2020.118909.

Behnood, A., Van Tittelboom, K., De Belie, N., (2016). Methods for measuring pH in concrete: A review. Construction and Building Materials, 105, pp. 176-188. https://doi.org/10.1016/j.conbuildmat.2015.12.032.

Benmahiddine, F., Bennai, F., Cherif, R., Belarbi, R., Tahakourt, A., Abahri, K., (2020). Experimental investigation on the influence of immersion/drying cycles on the hygrothermal and mechanical properties of hemp concrete. Building Engineering, 32, 101758. https://doi.org/10.1016/j.jobe.2020.101758.

Berglund, D.R., (2007). Sunflower production A-1331 (EB-25 Revised). North Dakota State University, 128p.

Berra, M., Mangialardi, T., Paolini, A.E., (2015). Reuse of woody biomass fly ash in cement-based materials. Construction and Building Materials, 76, pp. 286-296. https://doi.org/10.1016/j.conbuildmat.2014.11.052.

Bhojaraju, C., Mousavi, S.S., Brial, V., DiMare, M., Ouellet-Plamondon, C.M., (2021). Fresh and hardened properties of GGBS-contained cementitious composites using graphene and graphene oxide. Construction and Building Materials, 300, 123902. https://doi.org/10.1016/j.conbuildmat.2021.123902.

Bilba, K., Arsene, M.-A., Ouensanga, A., (2003). Sugar cane bagasse fibre reinforced cement composites. Part I. Influence of the botanical components of bagasse on the setting of bagasse/cement composite. Cement and Concrete Composites, 25, pp. 91-96. https://doi.org/10.1016/S0958-9465(02)00003-3.

Bondar, D., Basheer, M., Nanukuttan, S., (2019). Suitability of alkali activated slag/fly ash (AA-GGBS/FA) concretes for chloride environments: Characterisation based on mix design and compliance testing. Construction and Building Materials, 216, pp. 612-621. https://doi.org/10.1016/j.conbuildmat.2019.05.043.

Boulday, D., Marcovecchio, F., (2016). Valorisation des cendres issues de la combustion de biomasse. Revue des gisements et des procédés associés. CEDEN and LDAR, Etude RECORD n°14-0913/1A, 92p.

Bourchy, A., Barnes, L., Bessette, L., Chalencon, F., Joron, A., Torrenti, J.M., (2019). Optimization of concrete mix design to account for strength and hydration heat in massive concrete structures. Cement and Concrete Composites, 103, pp. 233-241. https://doi.org/10.1016/j.cemconcomp.2019.05.005.

Bourdot, A., Magniont, C., Lagouin, M., Niyigena, C., Evon, P., Amziane, S., (2019). Impact of bio-aggregates properties on the chemical interactions with mineral binder, application to vegetal Concrete. Journal of Advanced Concrete Technology, 17(9), pp. 542-558.

Boutin, M.-P., Flamin, C., Quinton, S., Gosse, G., (2006). Analyse du cycle de vie de : 1. Compounds thermoplastiques chargés fibres de chanvre et 2. Mur en béton chanvre banché sur ossature en bois. INRA de Lille, Editor Interchanvre.org, 102p.

Bozsaky, D., (2010). The historical development of thermal insulation materials. Periodica Polytechnica Architecture, 41, pp. 49-56. https://doi.org/10.3311/pp.ar.2010-2.02.

Brandt, A.M., (2008). Fibre reinforced cement-based (FRC) composites after over 40 years of development in building and civil engineering. Composite Structures, pp. 86, 3-9. https://doi.org/10.1016/j.compstruct.2008.03.006.

Brewer, C.E., Chuang, V.J., Masiello, C.A., Gonnermann, H., Gao, X., Dugan, B., Driver, L.E., Panzacchi, P., Zygourakis, K., Davies, C.A., (2014). New approaches to measuring biochar density and porosity. Biomass and Bioenergy, 66, pp. 176-185. https://doi.org/10.1016/j.biombioe.2014.03.059.

Brouard, Y., Belayachi, N., Hoxha, D., Ranganathan, N., Méo, S., (2018). Mechanical and hygrothermal behavior of clay – Sunflower (Helianthus annuus) and rape straw (Brassica napus) plaster bio-composites for building insulation. Construction and Building Materials, 161, 196-207pp. https://doi.org/10.1016/j.conbuildmat.2017.11.140.

Bucher, R., Diederich, P., Escadeillas, G., Cyr, M., (2017). Service life of metakaolin-based concrete exposed to carbonation. Cement and Concrete Research, 99, 18-29pp. https://doi.org/10.1016/j.cemconres.2017.04.013.

Cai, R., Tian, Z., Ye, H., He, Z., Tang, S., (2021). The role of metakaolin in pore structure evolution of Portland cement pastes revealed by an impedance approach. Cement and Concrete Composites, 119, 103999. https://doi.org/10.1016/j.cemconcomp.2021.103999.

Caldas, L.R., Da Gloria, M.Y.R., Pittau, F., Andreola, V.M., Habert, G., Toledo Filho, R.D., (2021). Environmental impact assessment of wood bio-concretes: Evaluation of the influence

of different supplementary cementitious materials. Construction and Building Materials, 268, 121146. https://doi.org/10.1016/j.conbuildmat.2020.121146.

Callebaut, K., Elsen, J., Balen, K.V., Viaene, W., (2001). Nineteenth century hydraulic restoration mortars in the Saint Michael's Church (Leuven, Belgium) Natural hydraulic lime or cement?. Cement and Concrete Research, 31, pp. 397-403. https://doi.org/10.1016/S0008-8846(00)00499-3.

Carević, I., Baričević, A., Štirmer, N., Šantek Bajto, J., (2020). Correlation between physical and chemical properties of wood biomass ash and cement composites performances. Construction and Building Materials 256, 119450. https://doi.org/10.1016/j.conbuildmat.2020.119450

Castel, A., Foster, S.J., (2015). Bond strength between blended slag and Class F fly ash geopolymer concrete with steel reinforcement. Cement and Concrete Research 72, pp. 48-53. https://doi.org/10.1016/j.cemconres.2015.02.016.

Celik, K., Hay, R., Hargis, C.W., Moon, J., (2019). Effect of volcanic ash pozzolan or limestone replacement on hydration of Portland cement. Construction and Building Materials, 197, pp. 803-812. https://doi.org/10.1016/j.conbuildmat.2018.11.193.

Cérézo, V., (2005). Propriétés mécaniques, thermiques et acoustiques d'un matériau à base de particules végétales : approche expérimentale et modélisation théorique. Thèse de doctorat de l'Institut National des Sciences Appliquées de Lyon, 244p.

Chabannes, M., Bénézet, J.-C., Clerc, L., Garcia-Diaz, E., (2014). Use of raw rice husk as natural aggregate in a lightweight insulating concrete: An innovative application. Construction and Building Materials, 70, pp. 428-438. https://doi.org/10.1016/j.conbuildmat.2014.07.025.

Chabannes, M., Nozahic, V., Amziane, S., (2015). Design and multi-physical properties of a new insulating concrete using sunflower stem aggregates and eco-friendly binders. Materials and Structures, 48, pp. 1815-1829. https://doi.org/10.1617/s11527-014-0276-9.

Chabriac, P.A., Gourdon, E., Gle, P., Fabbri, A., Lenormand, H., (2016). Agricultural by-products for building insulation: Acoustical characterization and modeling to predict micro-structural parameters. Construction and Building Materials, 112, pp. 158-167. https://doi.org/10.1016/j.conbuildmat.2016.02.162.

Chang, C.-F., Chen, J.-W., (2006). The experimental investigation of concrete carbonation depth. Cement and Concrete Research, 36, pp. 1760-1767. https://doi.org/10.1016/j.cemconres.2004.07.025.

Cheah, C.B., Ramli, M., (2011). The implementation of wood waste ash as a partial cement replacement material in the production of structural grade concrete and mortar: An overview. Resources, Conservation and Recycling, 55, pp. 669-685. https://doi.org/10.1016/j.resconrec.2011.02.002.

Chen, Y.X., Wu, F., Yu, Q., Brouwers, H.J.H., (2020). Bio-based ultra-lightweight concrete applying miscanthus fibers: Acoustic absorption and thermal insulation. Cement and Concrete Composites, 114, 103829. https://doi.org/10.1016/j.cemconcomp.2020.103829.

Cheng, S., Shui, Z., Sun, T., Yu, R., Zhang, G., Ding, S., (2017). Effects of fly ash, blast furnace slag and metakaolin on mechanical properties and durability of coral sand concrete. Applied Clay Science, 141, pp. 111-117. https://doi.org/10.1016/j.clay.2017.02.026.

Chowdhury, S., Maniar, A., Suganya, O.M., (2015). Strength development in concrete with wood ash blended cement and use of soft computing models to predict strength parameters.Advanced Research 6, pp. 907-913. https://doi.org/10.1016/j.jare.2014.08.006.

Cizer, Ö., Rodriguez-Navarro, C., Ruiz-Agudo, E., Elsen, J., Van Gemert, D., Van Balen, K., (2012). Phase and morphology evolution of calcium carbonate precipitated by carbonation of hydrated lime. J Mater Sci 47, pp. 6151-6165. https://doi.org/10.1007/s10853-012-6535-7.

Collet, F., Chamoin, J., Pretot, S., Lanos, C., (2013). Comparison of the hygric behaviour of three hemp concretes. Energy and Buildings, 62, pp. 294-303. https://doi.org/10.1016/j.enbuild.2013.03.010.

Collet, F., Pretot, S., (2014). Thermal conductivity of hemp concretes: Variation with formulation, density and water content. Construction and Building Materials 65, pp. 612–619. https://doi.org/10.1016/j.conbuildmat.2014.05.039.

Conseil de l'Union Européenne, (2003). DÉCISION DU CONSEIL du 19 décembre 2002 établissant des critères et des procédures d'admission des déchets dans les décharges, conformément à l'article 16 et à l'annexe II de la directive 1999/31/CE (2003/33/CE).

Czech, T., Marchewicz, A., Sobczyk, A.T., Krupa, A., Jaworek, A., Śliwiński, Ł., Rosiak, D., (2020). Heavy metals partitioning in fly ashes between various stages of electrostatic precipitator after combustion of different types of coal. Process Safety and Environmental Protection, 133, pp. 18-31. https://doi.org/10.1016/j.psep.2019.10.033.

Da Silva Andrade, D., Da Silva Rêgo, J.H., Cesar Morais, P., Frías Rojas, M., (2018). Chemical and mechanical characterization of ternary cement pastes containing metakaolin and nanosilica. Construction and Building Materials, 159, pp. 18-26. https://doi.org/10.1016/j.conbuildmat.2017.10.123.

Dahl, O., Nurmesniemi, H., Pöykiö, R., Watkins, G., (2010). Heavy metal concentrations in bottom ash and fly ash fractions from a large-sized (246MW) fluidized bed boiler with respect to their Finnish forest fertilizer limit values. Fuel Processing Technology, 91, pp. 1634-1639. https://doi.org/10.1016/j.fuproc.2010.06.012.

De Bruijn, P., Johansson, P., (2013). Moisture fixation and thermal properties of lime–hemp concrete. Construction and Building Materials, 47, pp. 1235-1242. https://doi.org/10.1016/j.conbuildmat.2013.06.006.

De Bruijn, P.B., Jeppsson, K.-H., Sandin, K., Nilsson, C., (2009). Mechanical properties of lime–hemp concrete containing shives and fibres. Biosystems Engineering 103, pp. 474-479. https://doi.org/10.1016/j.biosystemseng.2009.02.005.

De Weerdt, K., Haha, M.B., Le Saout, G., Kjellsen, K.O., Justnes, H., Lothenbach, B., (2011). Hydration mechanisms of ternary Portland cements containing limestone powder and fly ash. Cement and Concrete Research 41, 279-291. https://doi.org/10.1016/j.cemconres.2010.11.014.

Delannoy, G., Marceau, S., Glé, P., Gourlay, E., Guéguen-Minerbe, M., Amziane, S., Farcas, F., (2020). Durability of hemp concretes exposed to accelerated environmental aging. Construction and Building Materials, 252, 119043. https://doi.org/10.1016/j.conbuildmat.2020.119043.

Demirboğa, R., (2003). Influence of mineral admixtures on thermal conductivity and compressive strength of mortar. Energy and Buildings, 35, pp. 189-192. https://doi.org/10.1016/S0378-7788(02)00052-X.

Dutreix, N., Baecher, C., Laulan, G., Lacoste, T., Gandara, A., (2020). Les matériaux de construction biosourcés dans la commande publique. Editor : DGALN - Direction générale de l'aménagement, du logement et de la nature / DHUP - Direction de l'urbanisme, de l'habitat et des paysages. Nomadéis, 36p.

Diquélou, Y., Gourlay, E., Arnaud, L., Kurek, B., (2015). Impact of hemp shiv on cement setting and hardening: Influence of the extracted components from the aggregates and study of the interfaces with the inorganic matrix. Cement and Concrete Composites, 55, pp. 112-121. https://doi.org/10.1016/j.cemconcomp.2014.09.004.

Doudart de la Grée, G.C.H., Yu, Q.L., Brouwers, H.J.H., (2017). Assessing the effect of CaSO4 content on the hydration kinetics, microstructure and mechanical properties of cements containing sugars. Construction and Building Materials 143, pp. 48-60. https://doi.org/10.1016/j.conbuildmat.2017.03.067.

Du, Y., Yang, W., Ge, Y., Wang, S., Liu, P., (2021). Thermal conductivity of cement paste containing waste glass powder, metakaolin and limestone filler as supplementary cementitious material. Journal of Cleaner Production, 287, 125018. https://doi.org/10.1016/j.jclepro.2020.125018.

Dubois, S., Evrard, A., Lebeau, F., (2012). Hygrothermal modelling of Lime-Hemp concrete used as building material and indoor climate buffering characterization. Presented at the International Conference of Agricultural engineering (CIGR-Ageng), p. 6.

Dupre, B., (2014). Le végétal en construction - Bâtir durable avec des ressources de proximité. La construction responsable. Editor : techniques de l'ingénieur, https://doi.org/10.51257/a-v1-c8104.

Dutreix, N., Baecher, C., Pianu, B., Marx, I., Habasque, M., (2017). Etude sur le secteur et les filières de production des matériaux et produits biosourcés utilisés dans la construction (à l'exception du bois). Etat des lieux économiques du secteur et des filières. Nomadéis, 97p.

Elahi, A., Basheer, P.A.M., Nanukuttan, S.V., Khan, Q.U.Z., (2010). Mechanical and durability properties of high-performance concretes containing supplementary cementitious materials. Construction and Building Materials, 24, pp. 292-299. https://doi.org/10.1016/j.conbuildmat.2009.08.045.

Elchalakani, M., Aly, T., Abu-Aisheh, E., (2014). Sustainable concrete with high volume GGBFS to build Masdar City in the UAE. Case Studies in Construction Materials, 1, pp. 10-24. https://doi.org/10.1016/j.cscm.2013.11.001.

Elfordy, S., Lucas, F., Tancret, F., Scudeller, Y., Goudet, L., (2008). Mechanical and thermal properties of lime and hemp concrete ("hempcrete") manufactured by a projection process. Construction and Building Materials, 22, pp. 2116-2123. https://doi.org/10.1016/j.conbuildmat.2007.07.016.

Elinwa, A.U., Ejeh, S.P., (2004). Effects of the Incorporation of Sawdust Waste Incineration Fly Ash in Cement Pastes and Mortars. Asian Architecture and Building Engineering, 3, pp. 1-7. https://doi.org/10.3130/jaabe.3.1.

ElNemr, A., (2020). Generating water/binder ratio -to- strength curves for cement mortar used in Masnory walls. Construction and Building Materials, 233, 117249. https://doi.org/10.1016/j.conbuildmat.2019.117249.

Elyamany, H.E., Abd Elmoaty, A.E.M., Elshaboury, A.M., (2018). Setting time and 7-day strength of geopolymer mortar with various binders. Construction and Building Materials 187, pp. 974-983. https://doi.org/10.1016/j.conbuildmat.2018.08.025.

Esteves, T.C., Rajamma, R., Soares, D., Silva, A.S., Ferreira, V.M., Labrincha, J.A., (2012). Use of biomass fly ash for mitigation of alkali-silica reaction of cement mortars. Construction and Building Materials 26, 687–693. https://doi.org/10.1016/j.conbuildmat.2011.06.075.

Etiégni, L., Campbell, A.G., (1991). Physical and chemical characteristics of wood ash. Bioresource Technology, 37, pp. 173-178. https://doi.org/10.1016/0960-8524(91)90207-Z

European parliament and council, (2010). Directive 2010/75/EU of the European Parliament and of the Council of 24 November 2010 on industrial emissions (integrated pollution prevention and control) (DIRECTIVES).

Fernández-Pereira, C., de la Casa, J.A., Gómez-Barea, A., Arroyo, F., Leiva, C., Luna, Y., (2011). Application of biomass gasification fly ash for brick manufacturing. Fuel, 90, pp. 220-232. https://doi.org/10.1016/j.fuel.2010.07.057.

Ferraz, E., Andrejkovičová, S., Hajjaji, W., Velosa, A.L., Silva, A.S., Rocha, F., (2015). Pozzolanic activity of metakaolins by the French standard of the modified Chapelle test: A direct methology. Acta Geodynamica et Geomaterialia pp. 289-298. https://doi.org/10.13168/AGG.2015.0026.

Floissac, L., Valkhoff, H., Angerand, S., (2016). Analyse de la chaine de valeur dans le domaine de la production, fabrication, commercialisation et de la mise en œuvre de matériaux biosourcés. BioEconomics project, LRA - Laboratoire de Recherche en Architecture de Toulouse. 67p. available on https://lra.toulouse.archi.fr/.

Florentin, Y., Pearlmutter, D., Givoni, B., Gal, E., (2017). A life-cycle energy and carbon analysis of hemp-lime bio-composite building materials. Energy and Buildings, 156, 293-305pp. https://doi.org/10.1016/j.enbuild.2017.09.097

Földvári, M., (2011). Handbook of thermogravimetric system of minerals and its use in geological practice, Occasional papers of the Geological Institute of Hungary. Editor: Geological Institute of Hungary, Budapest., 180p.

Fořt, J., Šál, J., Ševčík, R., Doleželová, M., Keppert, M., Jerman, M., Záleská, M., Stehel, V., Černý, R., (2021). Biomass fly ash as an alternative to coal fly ash in blended cements: Functional aspects. Construction and Building Materials, 271, 121544. https://doi.org/10.1016/j.conbuildmat.2020.121544.

Frías Rojas, M., (2006). Study of hydrated phases present in a MK–lime system cured at 60 °C and 60 months of reaction. Cement and Concrete Research, 36, pp. 827-831. https://doi.org/10.1016/j.cemconres.2006.01.001.

Fu, C., Ye, H., Zhu, K., Fang, D., Zhou, J., (2020). Alkali cation effects on chloride binding of alkali-activated fly ash and metakaolin geopolymers. Cement and Concrete Composites, 114, 103721. https://doi.org/10.1016/j.cemconcomp.2020.103721.

Garcia, M. da L., Sousa-Coutinho, J., (2013). Strength and durability of cement with forest waste bottom ash. Construction and Building Materials, 41, pp. 897-910. https://doi.org/10.1016/j.conbuildmat.2012.11.081.

Glé, P., Lecompte, T., Hellouin de Ménibus, A., Lenormand, H., Arufe, S., Chateau, C., Fierro, V., Celzard, A., (2021). Densities of hemp shiv for building: From multiscale characterisation to application. Industrial Crops and Products, 164, 113390. https://doi.org/10.1016/j.indcrop.2021.113390.

Gomes, C.E.M., Ferreira, O.P., Fernandes, M.R., (2005). Influence of vinyl acetate-versatic vinylester copolymer on the microstructural characteristics of cement pastes. Materials Research, 8, pp. 51-56.

Gómez-Barea, A., Vilches, L.F., Leiva, C., Campoy, M., Fernández-Pereira, C., (2009). Plant optimisation and ash recycling in fluidised bed waste gasification. Chemical Engineering Journal, 146, pp. 227-236. https://doi.org/10.1016/j.cej.2008.05.039.

Gong, J., Zhang, W., (2019). The effects of pozzolanic powder on foam concrete pore structure and frost resistance. Construction and Building Materials, 208, pp. 135-143. https://doi.org/10.1016/j.conbuildmat.2019.02.021.

Gori, M., Bergfeldt, B., Pfrang-Stotz, G., Reichelt, J., Sirini, P., (2011). Effect of short-term natural weathering on MSWI and wood waste bottom ash leaching behaviour. Hazardous Materials, 189, pp. 435-443. https://doi.org/10.1016/j.jhazmat.2011.02.045.

Gourlay, E., Glé, P., Marceau, S., Foy, C., Moscardelli, S., (2017). Effect of water content on the acoustical and thermal properties of hemp concretes. Construction and Building Materials, 139, pp. 513-523. https://doi.org/10.1016/j.conbuildmat.2016.11.018.

Govin, A., Peschard, A., Guyonnet, R., (2006). Modification of cement hydration at early ages by natural and heated wood. Cement and Concrete Composites, 28, pp. 12-20. https://doi.org/10.1016/j.cemconcomp.2005.09.002.

Grilo, J., Faria, P., Veiga, R., Santos Silva, A., Silva, V., Velosa, A., (2014). New natural hydraulic lime mortars – Physical and microstructural properties in different curing conditions. Construction and Building Materials, 54, pp. 378-384. https://doi.org/10.1016/j.conbuildmat.2013.12.078.

Hany, E., Fouad, N., Abdel-Wahab, M., Sadek, E., (2020). Compressive strength of mortars incorporating alkali-activated materials as partial or full replacement of cement. Construction and Building Materials 261, 120518. https://doi.org/10.1016/j.conbuildmat.2020.120518.

Haque, M.N., Kayyali, O.A., (1995). Free and water-soluble chloride in concrete. Cement and Concrete Research, 25, pp. 531-542. https://doi.org/10.1016/0008-8846(95)00042-B.

Harbi, R., Derabla, R., Nafa, Z., (2017). Improvement of the properties of a mortar with 5% of kaolin fillers in sand combined with metakaolin, brick waste and glass powder in cement. Construction and Building Materials, 152, pp. 632-641. https://doi.org/10.1016/j.conbuildmat.2017.07.062.

Hart, J., D'Amico, B., Pomponi, F., (2021). Whole-life embodied carbon in multistory buildings: Steel, concrete, and timber structures. Industrial Ecology, 25, pp. 403-418. https://doi.org/DOI: 10.1111/jiec.13139.

Hassan, H.S., Abdel-Gawwad, H.A., Vásquez-García, S.R., Israde-Alcántara, I., Flores-Ramirez, N., Rico, J.L., Mohammed, M.S., (2019). Cleaner production of one-part white geopolymer cement using pre-treated wood biomass ash and diatomite. Cleaner Production, 209, pp. 1420-1428. https://doi.org/10.1016/j.jclepro.2018.11.137.

He, R., Ma, H., Hafiz, R.B., Fu, C., Jin, X., He, J., (2018). Determining porosity and pore network connectivity of cement-based materials by a modified non-contact electrical resistivity measurement: Experiment and theory. Materials & Design 156, 82–92. https://doi.org/10.1016/j.matdes.2018.06.04.

He, Z., Zhu, X., Wang, J., Mu, M., Wang, Y., (2019). Comparison of CO2 emissions from OPC and recycled cement production. Construction and Building Materials 211, 965–973. https://doi.org/10.1016/j.conbuildmat.2019.03.289.

Helsel, M.A., Ferraris, C.F., Bentz, D., (2016). Comparative study of methods to measure the density of Cementious powders. Testing and Evaluation, 44, pp. 1-13. DOI: 10.1520/JTE20150148.

Hu, L., He, Z., (2020). A fresh perspective on effect of metakaolin and limestone powder on sulfate resistance of cement-based materials. Construction and Building Materials, 262, 119847. https://doi.org/10.1016/j.conbuildmat.2020.119847.

Hu, X., Shi, C., Shi, Z., Tong, B., Wang, D., (2017). Early age shrinkage and heat of hydration of cement-fly ash-slag ternary blends. Construction and Building Materials, 153, pp. 857-865. https://doi.org/10.1016/j.conbuildmat.2017.07.138

Huang, W., Kazemi-Kamyab, H., Sun, W., Scrivener, K., (2017). Effect of cement substitution by limestone on the hydration and microstructural development of ultra-high-performance concrete (UHPC). Cement and Concrete Composites, 77, pp. 86-101. https://doi.org/10.1016/j.cemconcomp.2016.12.009.

Hussain, M., Levacher, D., Leblanc, N., Zmamou, H., Djeran-Maigre, I., Razakamanantsoa, A., Saouti, L., (2022). Reuse of harbour and river dredged sediments in adobe bricks. Cleaner Materials 3, 100046. https://doi.org/10.1016/j.clema.2022.100046.

IEA Bioenergy, (2018). IEA Bioenergy Task 32-Deliverable D7-Options for increased use of ash from biomass combustion and co-firing. IEA Bioenergy, 61p.

Illikainen, M., Tanskanen, P., Kinnunen, P., Körkkö, M., Peltosaari, O., Wigren, V., Österbacka, J., Talling, B., Niinimäki, J., (2014). Reactivity and self-hardening of fly ash from the fluidized bed combustion of wood and peat. Fuel, 135, pp. 69-75. https://doi.org/10.1016/j.fuel.2014.06.029.

Indukuri, C.S.R., Nerella, R., Madduru, S.R.C., (2019). Effect of graphene oxide on microstructure and strengthened properties of fly ash and silica fume-based cement composites. Construction and Building Materials, 229, 116863. https://doi.org/10.1016/j.conbuildmat.2019.116863.

International Energy Agency IEA, (2018). Technology Roadmap - Low-Carbon Transition in the Cement Industry. International Energy Agency IEA, 66p.

Ip, K., Miller, A., (2012). Life cycle greenhouse gas emissions of hemp–lime wall constructions in the UK. Resources, Conservation and Recycling, 69, pp. 1-9. https://doi.org/10.1016/j.resconrec.2012.09.001.

Ipavec, A., Vuk, T., Gabrovšek, R., Kaučič, V., (2013). Chloride binding into hydrated blended cements: The influence of limestone and alkalinity. Cement and Concrete Research, 48, pp. 74-85. https://doi.org/10.1016/j.cemconres.2013.02.010.

Iqbal Khan, M., Mourad, S.M., Charif, A., (2017). Utilization of Supplementary Cementitious Materials in HPC: From rheology to pore structure. KSCE of Civil Engineering 21, pp. 889-899. https://doi.org/10.1007/s12205-016-1781-x.

Islam, G.M.S., Rahman, M.H., Kazi, N., (2017). Waste glass powder as partial replacement of cement for sustainable concrete practice. International Journal of Sustainable Built Environment, 6, pp. 37-44. https://doi.org/10.1016/j.ijsbe.2016.10.005.

Jami, T., Karade, S.R., Singh, L.P., (2019). A review of the properties of hemp concrete for green building applications. Cleaner Production, 239, 117852. https://doi.org/10.1016/j.jclepro.2019.117852.

Jelle, B.P., (2011). Traditional, state-of-the-art, and future thermal building insulation materials and solutions – Properties, requirements and possibilities. Energy and Buildings, 43, pp. 2549-2563. https://doi.org/10.1016/j.enbuild.2011.05.015.

Jiang, C., Jin, C., Wang, Y., Yan, S., Chen, D., (2018). Effect of heat curing treatment on the drying shrinkage behavior and microstructure characteristics of mortar incorporating different content ground granulated blast-furnace slag. Construction and Building Materials, 186, pp. 379-387. https://doi.org/10.1016/j.conbuildmat.2018.07.079.

Jiang, Y., Lawrence, M., Hussain, A., Ansell, M., Walker, P., (2019). Comparative moisture and heat sorption properties of fibre and shiv derived from hemp and flax. Cellulose, 26, pp. 823-843. https://doi.org/10.1007/s10570-018-2145-0.

Jianming, Y., Luming, W., Cheng, J., Dong, S., (2020). Effect of fly ash on the corrosion resistance of magnesium potassium phosphate cement paste in sulfate solution. Construction and Building Materials, 237, 117639. https://doi.org/10.1016/j.conbuildmat.2019.117639.

Jones, D., Brischke, C., (2017). Performance of Bio-based Building Materials. Woodhead publishing, 652p.

Juenger, M., Provis, J.L., Elsen, J., Matthes, W., Hooton, R.D., Duchesne, J., Courard, L., He, H., Michel, F., Snellings, R., Belie, N.D., (2012). Supplementary cementitious materials for concrete: Characterization needs. MRS Online Proceedings Library, 1488, pp. 8-22. https://doi.org/10.1557/opl.2012.1536.

Juenger, M.C.G., Siddique, R., (2015). *Recent advances in understanding the role of supplementary cementitious materials in concrete*. Cement and Concrete Research, 78, 71-80pp. https://doi.org/10.1016/j.cemconres.2015.03.018.

Kadri, E.-H., Kenai, S., Ezziane, K., Siddique, R., De Schutter, G., (2011). Influence of metakaolin and silica fume on the heat of hydration and compressive strength development of mortar. Applied Clay Science, 53, pp. 704-708. https://doi.org/10.1016/j.clay.2011.06.008.

Kang, S.-H., Jeong, Y., Tan, K.H., Moon, J., (2019a). High-volume use of limestone in ultra-high-performance fiber-reinforced concrete for reducing cement content and autogenous shrinkage. Construction and Building Materials, 213, pp. 292-305. https://doi.org/10.1016/j.conbuildmat.2019.04.091.

Kang, S.-H., Kwon, Y.-H., Hong, S.-G., Chun, S., Moon, J., (2019b). Hydrated lime activation on byproducts for eco-friendly production of structural mortars. Cleaner Production, 231, 1389-1398pp. https://doi.org/10.1016/j.jclepro.2019.05.313.

Kang, S.-H., Kwon, Y.-H., Moon, J., (2020). Controlling the hydration and carbonation in lime-based materials: Advantage of slow carbonation in CO2 curable construction materials. Construction and Building Materials, 249, 118749. https://doi.org/10.1016/j.conbuildmat.2020.118749.

Kayali, O., Sharfuddin Ahmed, M., (2013). Assessment of high-volume replacement fly ash concrete – Concept of performance index. Construction and Building Materials, 39, pp. 71-76. https://doi.org/10.1016/j.conbuildmat.2012.05.009.

Khayat, K.H., 1998. Viscosity-enhancing admixtures for cement-based materials - An overview. Cement and Concrete Composites 20, 171–188. https://doi.org/10.1016/S0958-9465(98)80006-1.

Kinnane, O., Reilly, A., Grimes, J., Pavia, S., Walker, R., (2016). Acoustic absorption of hemp-lime construction. Construction and Building Materials, 122, pp. 674-682. https://doi.org/10.1016/j.conbuildmat.2016.06.106.

Klimesch, D.S., Ray, A., (1997). The use of DTA/TGA to study the effects of ground quartz with different surface areas in autoclaved cement: quartz pastes. Use of the semi-isothermal thermogravimetric technique. Thermochimica Acta, 306, pp. 159-165. https://doi.org/10.1016/S0040-6031(97)00279-7.

Kocak, Y., (2020). Effects of metakaolin on the hydration development of Portland–composite cement. Building Engineering 31, 101419. https://doi.org/10.1016/j.jobe.2020.101419.

Kula, I., Olgun, A., Erdogan, Y., Sevinc, V., (2001). Effects of colemanite waste, cool bottom ash, and fly ash on the properties of cement. Cement and Concrete Research, 31, pp. 491-494. DOI:10.1016/S0008-8846(00)00486-5.

Laborel-Préneron, A., Magniont, C., Aubert, J.-E., (2018a). Hygrothermal properties of unfired earth bricks: Effect of barley straw, hemp shiv and corn cob addition. Energy and Buildings, 178, pp. 265-278. https://doi.org/10.1016/j.enbuild.2018.08.021.

Laborel-Préneron, A., Magniont, C., Aubert, J.-E., (2018b). Characterization of Barley Straw, Hemp Shiv and Corn Cob as Resources for Bioaggregate Based Building Materials. Waste Biomass Valor, 9, pp. 1095-1112. https://doi.org/10.1007/s12649-017-9895-z.

Lagouin, M., (2020). Caractérisation et optimisation multiphysiques d'une paroi bicouche bio et géosourcée. Thèse de doctorat de l'Université de Toulouse, 279p.

Lagouin, M., Magniont, C., Sénéchal, P., Moonen, P., Aubert, J.-E., Laborel-préneron, A., (2019). Influence of types of binder and plant aggregates on hygrothermal and mechanical properties of vegetal concretes. Construction and Building Materials, 222, 852-871pp. https://doi.org/10.1016/j.conbuildmat.2019.06.004.

Leemann, A., Winnefeld, F., 2007. The effect of viscosity modifying agents on mortar and concrete. Cement and Concrete Composites 29, 341–349. https://doi.org/10.1016/j.cemconcomp.2007.01.004

Lenormand, H., Mahieu, A., Leblanc, N., Vivet, A., (2014). Nouvelles agroressources pour panneaux de particules 100% biosourcés. In Conférence Matériaux 2014 - Colloque Ecomatériaux, pp. 1-10.

Lessard, J.-M., Omran, A., Tagnit-Hamou, A., Gagne, R., (2017a). Feasibility of using biomass fly and bottom ashes in dry-cast concrete production. Construction and Building Materials, 132, pp. 565-577. https://doi.org/10.1016/j.conbuildmat.2016.12.009.

Lessard, J.-M., Omran, A., Tagnit-Hamou, A., Gagne, R., (2017b). Feasibility of Using Biomass Fly and Bottom Ashes to Produce RCC and PCC. Materials Civil Engineering. 29, 04016267. https://doi.org/10.1061/(ASCE)MT.1943-5533.0001796.

Li, C., Jiang, L., (2020). Utilization of limestone powder as an activator for early-age strength improvement of slag concrete. Construction and Building Materials, 253, 119257. https://doi.org/10.1016/j.conbuildmat.2020.119257.

Li, C., Jiang, L., Li, S., (2020a). Effect of limestone powder addition on threshold chloride concentration for steel corrosion in reinforced concrete. Cement and Concrete Research, 131, 106018. https://doi.org/10.1016/j.cemconres.2020.106018.

Li, C., Xiao, K., (2021). Chloride threshold, modelling of corrosion rate and pore structure of concrete with metakaolin addition. Construction and Building Materials, 305, 124666. https://doi.org/10.1016/j.conbuildmat.2021.124666.

Li, P.P., Brouwers, H.J.H., Chen, W., Yu, Q., (2020b). Optimization and characterization of high-volume limestone powder in sustainable ultra-high-performance concrete. Construction and Building Materials, 242, 118112. https://doi.org/10.1016/j.conbuildmat.2020.118112.

Li, Z., (2016). Drying shrinkage prediction of paste containing meta-kaolin and ultrafine fly ash for developing ultra-high performance concrete. Materials Today Communications, 6, pp. 74-80. https://doi.org/10.1016/j.mtcomm.2016.01.001.

Li, Z., (2011). Advanced Concrete Technology. Editor: John Wiley & Sons, Inc., Hoboken, New Jersey, 521p.

Li, Z., Lu, D., Gao, X., (2020c). Analysis of correlation between hydration heat release and compressive strength for blended cement pastes. Construction and Building Materials, 260, 120436. https://doi.org/10.1016/j.conbuildmat.2020.120436.

Ling, Y., Wang, K., Fu, C., (2019). Shrinkage behavior of fly ash based geopolymer pastes with and without shrinkage reducing admixture. Cement and Concrete Composites 98, pp. 74-82. https://doi.org/10.1016/j.cemconcomp.2019.02.007.

Liu, J., Ou, Z., Mo, J., Wang, Y., Wu, H., (2017). The effect of SCMs and SAP on the autogenous shrinkage and hydration process of RPC. Construction and Building Materials 155, pp. 239-249. https://doi.org/10.1016/j.conbuildmat.2017.08.061.

Liu, S., Zhang, T., Guo, Y., Wei, J., Yu, Q., (2018). Effects of SCMs particles on the compressive strength of micro-structurally designed cement paste: Inherent characteristic effect, particle size refinement effect, and hydration effect. Powder Technology, 330, pp. 1-11. https://doi.org/10.1016/j.powtec.2018.01.087.

Lopez Fernandez, R., (2009). Calcined Clayey Soils as a Potential Replacement for Cement in Developing Countries. Thèse de doctorat de la faculté des sciences et techniques de l'ingénieur, et l'école polytechnique fédérale de Lausanne, 178p.

Lothenbach, B., Rentsch, D., Wieland, E., (2014). Hydration of a silica fume blended low-alkali shotcrete cement. Physics and Chemistry of the Earth, Parts A/B/C, 70-71, pp. 3-16. https://doi.org/10.1016/j.pce.2013.09.007.

Lothenbach, B., Scrivener, K., Hooton, R.D., (2011). Supplementary cementitious materials. Cement and Concrete Research, 41, pp. 1244-1256. https://doi.org/10.1016/j.cemconres.2010.12.001.

Magniont, C., (2010). Contribution à la formulation et à la caractérisation d'un écomatériau de construction à base d'agroressources. Thèse de doctorat de l'Université de Toulouse, 343p.

Magniont, C., Escadeillas, G., Coutand, M., Oms-Multon, C., (2012). Use of plant aggregates in building ecomaterials. European Journal of Environmental and Civil Engineering 16, s17–s33. https://doi.org/10.1080/19648189.2012.682452

Mahieu, A., Alix, S., Leblanc, N., (2019). Properties of particleboards made of agricultural by-products with a classical binder or self-bound. Industrial Crops and Products, 130, pp. 371-379. https://doi.org/10.1016/j.indcrop.2018.12.094.

Mantellato, S., Palacios, M., Flatt, R.J., (2015). Reliable specific surface area measurements on anhydrous cements. Cement and Concrete Research, 67, pp. 286-291. https://doi.org/10.1016/j.cemconres.2014.10.009.

Marceau, S., Glé, P., Gueguen, M., Gourlay, E., Moscardelli, S., Nour, I., Amziane, S., (2015). Assessment of the durability of bio-based insulating materials. Presented at the First International Conference on Bio-based Building Materials, AJCE - Special Issue, Clermont-Ferrand, France, p. 5.

Maschio, S., Tonello, G., Piani, L., Furlani, E., (2011). Fly and bottom ashes from biomass combustion as cement replacing components in mortars production: Rheological behaviour of the pastes and materials compression strength. Chemosphere, 85, pp. 666-671. https://doi.org/10.1016/j.chemosphere.2011.06.070.

Mazhoud, B., Collet, F., Pretot, S., Chamoin, J., (2016). Hygric and thermal properties of hemp-lime plasters. Building and Environment, 96, pp. 206-216. https://doi.org/10.1016/j.buildenv.2015.11.013.

Mazhoud, B., Collet, F., Prétot, S., Lanos, C., (2021). Effect of hemp content and clay stabilization on hygric and thermal properties of hemp-clay composites. Construction and Building Materials, 300, 123878. https://doi.org/10.1016/j.conbuildmat.2021.123878.

Mazhoud, B., Collet, F., Pretot, S., Lanos, C., (2017). Mechanical properties of hemp-clay and hemp stabilized clay composites. Construction and Building Materials, 155, pp. 1126-1137. https://doi.org/10.1016/j.conbuildmat.2017.08.121.

Meddah, M.S., Ismail, M.A., El-Gamal, S., Fitriani, H., (2018). Performances evaluation of binary concrete designed with silica fume and metakaolin. Construction and Building Materials, 166, pp. 400-412. https://doi.org/10.1016/j.conbuildmat.2018.01.138.

Medjigbodo, G., Rozière, E., Charrier, K., Izoret, L., Loukili, A., (2018). Hydration, shrinkage, and durability of ternary binders containing Portland cement, limestone filler and metakaolin. Construction and Building Materials, 183, pp. 114-126. https://doi.org/10.1016/j.conbuildmat.2018.06.138.

Megat Johari, M.A., Brooks, J.J., Kabir, S., Rivard, P., (2011). Influence of supplementary cementitious materials on engineering properties of high strength concrete. Construction and Building Materials, 25, pp. 2639-2648. https://doi.org/10.1016/j.conbuildmat.2010.12.013.

Mehta, P.K., (2002). Greening of the Concrete Industry for Sustainable Development, 31, pp. 601-605. https://doi.org/10.1016/j.cemconcomp.2008.12.010.

Mehta, P.K., Monteiro, P.J.M., (2006). Concrete: microstructure, properties, and materials, Third Edition, McGraw-Hill, New York.

Miller, D.P., Mosleni, A.A., (1991). Wood cement composites: effect of model compounds on hydration characteristics and tensile strength. Wood and fiber science, 23, pp.472-482.

Milovanović, B., Štirmer, N., Carević, I., Baričević, A., (2019). Wood biomass ash as a raw material in concrete industry. JCE 71, pp. 505-14. https://doi.org/10.14256/JCE.2546.2018.

Mindess, S. (Ed.), (2019). Developments in the formulation and reinforcement of concrete, Second edition. ed, Woodhead Publishing series in civil and structural engineering. Woodhead Publishing, Duxford, United Kingdom is an imprint of Elsevier.

Mironyuk, I., Tatarchuk, T., Paliychuk, N., Heviuk, I., Horpynko, A., Yarema, O., Mykytyn, I., (2021). Effect of surface-modified fly ash on compressive strength of cement mortar. Materials Today: Proceedings, 35, pp. 534-537. https://doi.org/10.1016/j.matpr.2019.10.016.

Mivière, J.-M., (2008). Les Cendres des chaudières automatiques au bois et leurs possibilités de valorisation-Les cahiers du Bois énergie : Fascicule 1.

Modolo, R.C.E., Ferreira, V.M., Tarelho, L.A., Labrincha, J.A., Senff, L., Silva, L., (2013). Mortar formulations with bottom ash from biomass combustion. Construction and Building Materials 45, 275–281. https://doi.org/10.1016/j.conbuildmat.2013.03.093.

Moghaddam, F., Sirivivatnanon, V., Vessalas, K., (2019). The effect of fly ash fineness on heat of hydration, microstructure, flow and compressive strength of blended cement pastes. Case Studies in Construction Materials, 10, e00218. https://doi.org/10.1016/j.cscm.2019.e00218

Mohan, D., Pittman, C.U., Steele, P.H., (2006). Pyrolysis of Wood/Biomass for Bio-oil: A Critical Review. Energy Fuels, 20, pp. 848-889. https://doi.org/10.1021/ef0502397

Moon, G.D., Oh, S., Jung, S.H., Choi, Y.C., (2017). Effects of the fineness of limestone powder and cement on the hydration and strength development of PLC concrete. Construction and Building Materials, 135, pp. 129-136. https://doi.org/10.1016/j.conbuildmat.2016.12.189.

Muduli, R., Mukharjee, B.B., (2019). Effect of incorporation of metakaolin and recycled coarse aggregate on properties of concrete. Cleaner Production, 209, pp. 398-414. https://doi.org/10.1016/j.jclepro.2018.10.221.

Munjal, P., Hau, K.K., Hon Arthur, C.C., (2021). Effect of GGBS and curing conditions on strength and microstructure properties of oil well cement slurry. Building Engineering, 40, 102331. https://doi.org/10.1016/j.jobe.2021.102331.

Naik, T.R., 2002. Greener Concrete Using Recycled Materials. Concrete international, 24, pp. 45-49.

Nawaz, M.A., Ali, B., Qureshi, L.A., Usman Aslam, H.M., Hussain, I., Masood, B., Raza, S.S., (2020). Effect of sulfate activator on mechanical and durability properties of concrete incorporating low calcium fly ash. Case Studies in Construction Materials, 13, e00407. https://doi.org/10.1016/j.cscm.2020.e00407.

Ndahirwa, D., Zmamou, H., Lenormand, H., Leblanc, N., (2022). The role of supplementary cementitious materials in hydration, durability and shrinkage of cement-based materials, their environmental and economic benefits: A review. Cleaner Materials, 5, 100123. https://doi.org/10.1016/j.clema.2022.100123.

Nežerka, V., Bílý, P., Hrbek, V., Fládr, J., (2019). Impact of silica fume, fly ash, and metakaolin on the thickness and strength of the ITZ in concrete. Cement and Concrete Composites, 103, pp. 252-262. https://doi.org/10.1016/j.cemconcomp.2019.05.012.

Nguyen, H.G.T., Horn, J.C., Bleakney, M., Siderius, D.W., Espinal, L., (2019). Understanding Material Characteristics through Signature Traits from Helium Pycnometry. Langmuir, 35, 2115–2122. https://doi.org/10.1021/acs.langmuir.8b03731.

Nguyen, T.T., Picandet, V., Carre, P., Lecompte, T., Amziane, S., Baley, C., (2010). Effect of compaction on mechanical and thermal properties of hemp concrete. European Journal of Environmental and Civil Engineering, 14, pp. 545-560. https://doi.org/10.1080/19648189.2010.9693246.

Ni, C., Wu, Q., Yu, Z., Shen, X., (2021). Hydration of Portland cement paste mixed with densified silica fume: From the point of view of fineness. Construction and Building Materials, 272, 121906. https://doi.org/10.1016/j.conbuildmat.2020.121906.

Nogueira, R., Ferreira Pinto, A.P., Gomes, A., (2018). Design and behavior of traditional lime-based plasters and renders. Review and critical appraisal of strengths and weaknesses. Cement and Concrete Composites, 89, pp. 192-204. https://doi.org/10.1016/j.cemconcomp.2018.03.005.

Nozahic, V., (2012). Vers une nouvelle démarche de conception des bétons de végétaux lignocellulosiques basée sur la compréhension et l'amélioration de l'interface liant / végétal : application à des granulats de chenevotte et de tige de tournesol associés à un liant ponce / chaux. Thèse de doctorat de l'Université Blaise Pascal - Clermont II, 334p.

Nozahic, V., Amziane, S., (2012). Influence of sunflower aggregates surface treatments on physical properties and adhesion with a mineral binder. Composites Part A: Applied Science and Manufacturing, 43, pp. 1837-1849. https://doi.org/10.1016/j.compositesa.2012.07.011.

Nozahic, V., Amziane, S., Torrent, G., Saïdi, K., De Baynast, H., (2012). Design of green concrete made of plant-derived aggregates and a pumice–lime binder. Cement and Concrete Composites 34, pp. 231-241. https://doi.org/10.1016/j.cemconcomp.2011.09.002.

Obernberger, I., Biedermann, F., Widmann, W., Riedl, R., (1997). Concentrations of inorganic elements in biomass fuels and recovery in the different ash fractions. Biomass and Bioenergy 12, 211–224. https://doi.org/DOI: 10.1016/S0961-9534(96)00051-7.

Obernberger, I., Supancic, K., (2009). Possibilities of ash utilisation from biomass combustion plants, in: Proceedings of the 17th European Biomass Conference & Exhibition. Hamburg.

Ohenoja, K., Rissanen, J., Kinnunen, P., Illikainen, M., (2020). Direct carbonation of peat-wood fly ash for carbon capture and utilization in construction application. CO_2 Utilization, 40, 101203. https://doi.org/10.1016/j.jcou.2020.101203.

Ohenoja, K., Tanskanen, P., Wigren, V., Kinnunen, P., Körkkö, M., Peltosaari, O., Österbacka, J., Illikainen, M., (2016). Self-hardening of fly ashes from a bubbling fluidized bed combustion of peat, forest industry residuals, and wastes. Fuel, 165, pp. 440-446. https://doi.org/10.1016/j.fuel.2015.10.093.

Omran, A., Soliman, N., Xie, A., Davidenko, T., Tagnit-Hamou, A., (2018). Field trials with concrete incorporating biomass-fly ash. Construction and Building Materials, 186, pp. 660-669. https://doi.org/10.1016/j.conbuildmat.2018.07.084.

Özbay, E., Erdemir, M., Durmuş, H.İ., (2016). Utilization and efficiency of ground granulated blast furnace slag on concrete properties – A review. Construction and Building Materials, 105, pp. 423-434. https://doi.org/10.1016/j.conbuildmat.2015.12.153.

Pacewska, B., Wilińska, I., (2013). Hydration of Cement Composites Containing Large Amount of Waste Materials. Procedia Engineering, 57, pp. 53-62. https://doi.org/10.1016/j.proeng.2013.04.009.

Palacios, A., Cong, L., Navarro, M.E., Ding, Y., Barreneche, C., (2019). Thermal conductivity measurement techniques for characterizing thermal energy storage materials – A review. Renewable and Sustainable Energy Reviews, 108, pp. 32-52. https://doi.org/10.1016/j.rser.2019.03.020.

Panesar, D.K., Zhang, R., (2020). Performance comparison of cement replacing materials in concrete: Limestone fillers and supplementary cementing materials – A review. Construction and Building Materials, 251, 118866. https://doi.org/10.1016/j.conbuildmat.2020.118866.

Papadakis, V.G., (2000). Effect of supplementary cementing materials on concrete resistance against carbonation and chloride ingress. Cement and Concrete Research, 30, pp. 291-299. https://doi.org/10.1016/S0008-8846(99)00249-5.

Park, J.-H., (2020). Exploration of the potential capacity of fly ash and bottom ash derived from wood pellet-based thermal power plant for heavy metal removal. Science of the Total Environment, 740, 140205. https://doi.org/10.1016/j.scitotenv.2020.140205.

Pavlík, V., Užáková, M., (2016). Effect of curing conditions on the properties of lime, lime–metakaolin and lime–zeolite mortars. Construction and Building Materials, 102, pp. 14-25. https://doi.org/10.1016/j.conbuildmat.2015.10.128.

Pichon, P.Q., Naumovic, J.-M., (2018). Béton et mortier de chanvre 59.

Puerta-Falla, G., Balonis, M., Le Saout, G., Falzone, G., Zhang, C., Neithalath, N., Sant, G., (2015). Elucidating the Role of the Aluminous Source on Limestone Reactivity in Cementitious Materials. American Ceramic society, 98, pp. 4076-4089. https://doi.org/10.1111/jace.13806.

Qin, L., Gao, X., Chen, T., (2019). Influence of mineral admixtures on carbonation curing of cement paste. Construction and Building Materials, 212, pp. 653-662. https://doi.org/10.1016/j.conbuildmat.2019.04.033.

Qin, Z., Ma, C., Zheng, Z., Long, G., Chen, B., (2020). Effects of metakaolin on properties and microstructure of magnesium phosphate cement. Construction and Building Materials, 234, 117353. https://doi.org/10.1016/j.conbuildmat.2019.117353.

Rafieizonooz, M., Mirza, J., Salim, M.R., Hussin, M.W., Khankhaje, E., (2016). Investigation of coal bottom ash and fly ash in concrete as replacement for sand and cement. Construction and Building Materials, 116, pp. 15-24. https://doi.org/10.1016/j.conbuildmat.2016.04.080.

Ragland, K.W., Aerts, D.J., Baker, A.J., (1991). Properties of wood for combustion analysis. Bioresource Technology, 37, pp. 161-168. https://doi.org/10.1016/0960-8524(91)90205-X.

Ragoug, R., Metalssi, O.O., Barberon, F., Torrenti, J.-M., Roussel, N., Divet, L., d'Espinose de Lacaillerie, J.-B., (2019). Durability of cement pastes exposed to external sulfate attack and

leaching: Physical and chemical aspects. Cement and Concrete Research, 116, pp. 134-145. https://doi.org/10.1016/j.cemconres.2018.11.006.

Rahim, M., Douzane, O., Tran Le, A.D., Langlet, T., (2016). Effect of moisture and temperature on thermal properties of three bio-based materials. Construction and Building Materials, 111, pp. 119-127. https://doi.org/10.1016/j.conbuildmat.2016.02.061.

Rahim, M., Douzane, O., Tran Le, A.D., Promis, G., Laidoudi, B., Crigny, A., Dupre, B., Langlet, T., (2015). Characterization of flax lime and hemp lime concretes: Hygric properties and moisture buffer capacity. Energy and Buildings, 88, pp. 91-99. https://doi.org/10.1016/j.enbuild.2014.11.043.

Rajamma, R., Ball, R.J., Tarelho, L.A.C., Allen, G.C., Labrincha, J.A., Ferreira, V.M., (2009). Characterisation and use of biomass fly ash in cement-based materials. Hazardous Materials, 172, pp. 1049-1060. https://doi.org/10.1016/j.jhazmat.2009.07.109.

Ramezanianpour, A.A., Bahrami Jovein, H., (2012). Influence of metakaolin as supplementary cementing material on strength and durability of concretes. Construction and Building Materials, 30, pp. 470-479. https://doi.org/10.1016/j.conbuildmat.2011.12.050.

Reddy, L.S.I., Vijayalakshmi, M.M., Praveenkumar, T.R., (2020). Thermal Conductivity and Strength Properties of Nanosilica and GGBS Incorporated Concrete Specimens. Silicon, 14, pp. 145-151. https://doi.org/10.1007/s12633-020-00813-7.

Rezvani, M., Proske, T., (2017). Influence of chemical-mineralogical properties of limestone on the shrinkage behaviour of cement paste and concrete made of limestone-rich cements. Construction and Building Materials, 157, pp. 818-828. https://doi.org/10.1016/j.conbuildmat.2017.09.101.

Rode, C., Peuhkuri, R.H., Mortensen, L.H., Hansen, K.K., Time, B., Gustavsen, A., Ojanen, T., Ahonen, J., Svennberg, K., Arfvidsson, J., Harderup, L.-E., (2005). Moisture Buffering of Building Materials. Technical University of Denmark, Department of Civil Engineering. BYG Report No. R-127.

Rong, Z.D., Sun, W., Xiao, H.J., Wang, W., (2014). Effect of silica fume and fly ash on hydration and microstructure evolution of cement-based composites at low water–binder ratios. Construction and Building Materials, 51, pp. 446-450. https://doi.org/10.1016/j.conbuildmat.2013.11.023.

Sabathier, V., Louvel, S., Correa, G., Magniont, C., Evon, P., Labonne, L., (2017). Incidence of the water-soluble compounds contained into lavender and sunflower bioaggregates on the hardening process of mineral binders. Presented at the ICBBM 2017, Academic Journal of Civil Engineering, pp. 62-68. https://doi.org/10.26168/icbbm2017.7.

Salimi, J., Ramezanianpour, A.M., Moradi, M.J., (2020). Studying the effect of low reactivity metakaolin on free and restrained shrinkage of high-performance concrete. Building Engineering, 28, 101053. https://doi.org/10.1016/j.jobe.2019.101053.

Saluja, S., Kaur, K., Goyal, S., Bhattacharjee, B., (2019). Assessing the effect of GGBS content and aggregate characteristics on drying shrinkage of roller compacted concrete. Construction and Building Materials, 201, pp. 72-80. https://doi.org/10.1016/j.conbuildmat.2018.12.179.

Samad, S., Shah, A., (2017). Role of binary cement including Supplementary Cementitious Material (SCM), in production of environmentally sustainable concrete: A critical review. International Journal of Sustainable Built Environment, 6, pp. 663-674. https://doi.org/10.1016/j.ijsbe.2017.07.003.

Samtani, M., Dollimore, D., Alexander, K.S., (2002). Comparison of dolomite decomposition kinetics with related carbonates and the effect of procedural variables on its kinetic parameters. Thermochimica Acta, 392-393, pp. 135-145. https://doi.org/10.1016/S0040-6031(02)00094-1.

Sassoni, E., Manzi, S., Motori, A., Montecchi, M., Canti, M., (2015). Experimental study on the physical–mechanical durability of innovative hemp-based composites for the building industry. Energy and Buildings, 104, pp. 316-322. https://doi.org/10.1016/j.enbuild.2015.07.022.

Schankoski, R.A., Pilar, R., Prudêncio, L.R., Ferron, R.D., (2017). Evaluation of fresh cement pastes containing quarry by-product powders. Construction and Building Materials 133, pp. 234-242. https://doi.org/10.1016/j.conbuildmat.2016.12.056.

Schneider, M., Romer, M., Tschudin, M., Bolio, H., (2011). Sustainable cement production-present and future. Cement and Concrete Research, 41, pp. 642-650. https://doi.org/10.1016/j.cemconres.2011.03.019.

Scrivener, K., Avet, F., Maraghechi, H., Zunino, F., Ston, J., Hanpongpun, W., Favier, A., (2019). Impacting factors and properties of limestone calcined clay cements (LC^3). Green Materials 7, pp. 3-14. https://doi.org/10.1680/jgrma.18.00029.

Seifi, S., Sebaibi, N., Levacher, D., Boutouil, M., (2019). Mechanical performance of a dry mortar without cement, based on paper fly ash and blast furnace slag. Building Engineering, 22, pp. 113-121. https://doi.org/10.1016/j.jobe.2018.11.004.

Shafigh, P., Nomeli, M.A., Alengaram, U.J., Mahmud, H.B., Jumaat, M.Z., (2016). Engineering properties of lightweight aggregate concrete containing limestone powder and high-volume fly ash. Cleaner Production 135, pp. 148-157. https://doi.org/10.1016/j.jclepro.2016.06.082.

Shaikh, F.U.A., Supit, S.W.M., Sarker, P.K., (2014). A study on the effect of nano silica on compressive strength of high-volume fly ash mortars and concretes. Materials & Design, 60, pp. 433-442. https://doi.org/10.1016/j.matdes.2014.04.025.

Shariq, M., Prasad, J., Abbas, H., (2016). Creep and drying shrinkage of concrete containing GGBFS. Cement and Concrete Composites, 68, pp.35-45. https://doi.org/10.1016/j.cemconcomp.2016.02.004.

Shariq, M., Prasad, J., Masood, A., (2010). Effect of GGBFS on time dependent compressive strength of concrete. Construction and Building Materials, 24, pp. 1469-1478. https://doi.org/10.1016/j.conbuildmat.2010.01.007.

Shen, L., Li, Q., Ge, W., Xu, S., (2020). The mechanical property and frost resistance of roller compacted concrete by mixing silica fume and limestone powder: Experimental study. Construction and Building Materials, 239, 117882. https://doi.org/10.1016/j.conbuildmat.2019.117882.

Sheridan, J., Sonebi, M., Taylor, S., Amziane, S., 2020a. The effect of a polyacrylic acid viscosity modifying agent on the mechanical, thermal and transport properties of hemp and rapeseed straw concrete. Construction and Building Materials 235, 117536. https://doi.org/10.1016/j.conbuildmat.2019.117536.

Sheridan, J., Sonebi, M., Taylor, S., Amziane, S., 2020b. The effect of long term weathering on hemp and rapeseed concrete. Cement and Concrete Research 131, 106014. https://doi.org/10.1016/j.cemconres.2020.106014.

Shi, C., Wang, D., Wu, L., Wu, Z., (2015). The hydration and microstructure of ultra high-strength concrete with cement–silica fume–slag binder. Cement and Concrete Composites 61, pp. 44-52. https://doi.org/10.1016/j.cemconcomp.2015.04.013.

Shi, Z., Lothenbach, B., Geiker, M.R., Kaufmann, J., Leemann, A., Ferreiro, S., Skibsted, J., (2016). Experimental studies and thermodynamic modeling of the carbonation of Portland cement, metakaolin and limestone mortars. Cement and Concrete Research 88, pp. 60-72. https://doi.org/10.1016/j.cemconres.2016.06.006.

Shon, C.-S., Abdigaliyev, A., Bagitova, S., Chung, C.-W., Kim, D., (2018). Determination of air-void system and modified frost resistance number for freeze-thaw resistance evaluation of ternary blended concrete made of ordinary Portland cement/silica fume/class F fly ash. Cold Regions Science and Technology 155, pp. 127-136. https://doi.org/10.1016/j.coldregions.2018.08.003.

Siddique, R., (2012). Utilization of wood ash in concrete manufacturing. Resources, Conservation and Recycling, 67, pp. 27-33. https://doi.org/10.1016/j.resconrec.2012.07.004.

Sigvardsen, N.M., Geiker, M.R., Ottosen, L.M., (2021a). Phase development and mechanical response of low-level cement replacements with wood ash and washed wood ash. Construction and Building Materials, 269, 121234. https://doi.org/10.1016/j.conbuildmat.2020.121234.

Sigvardsen, N.M., Geiker, M.R., Ottosen, L.M., (2021b). Reaction mechanisms of wood ash for use as a partial cement replacement. Construction and Building Materials, 286, 122889. https://doi.org/10.1016/j.conbuildmat.2021.122889.

Sigvardsen, N.M., Ottosen, L.M., (2019). Characterization of coal bio ash from wood pellets and low-alkali coal fly ash and use as partial cement replacement in mortar. Cement and Concrete Composites, 95, pp. 25-32. https://doi.org/10.1016/j.cemconcomp.2018.10.005.

Sing, K.S.W., Everett, D.H., Haul, R.A.W., Moscou, L., Pierotti, R.A., Rouquerol, J., Siemieniewska, T., (1984). Reporting physisorption data for gas/solid systems with special reference to the determination of surface area and porosity (Recommendations 1984). International Union of Pure and Applied Chemistry (IUPAC).

Singh, B., Rahman, M.R., Paswan, R., Bhattacharyya, S.K., (2016). Effect of activator concentration on the strength, ITZ and drying shrinkage of fly ash/slag geopolymer concrete. Construction and Building Materials, 118, pp. 171-179. https://doi.org/10.1016/j.conbuildmat.2016.05.008.

Singh, K., Risse, M., Das, K.C., Worley, J., (2009). Determination of Composition of Cellulose and Lignin Mixtures Using Thermogravimetric Analysis. Energy Resources Technology, 131, 022201. https://doi.org/10.1115/1.3120349.

Skibsted, J., Snellings, R., (2019). Reactivity of supplementary cementitious materials (SCMs) in cement blends. Cement and Concrete Research 124, 105799. https://doi.org/10.1016/j.cemconres.2019.105799.

Snellings, R., Chwast, J., Cizer, Ö., De Belie, N., Dhandapani, Y., Durdzinski, P., Elsen, J., Haufe, J., Hooton, D., Patapy, C., Santhanam, M., Scrivener, K., Snoeck, D., Steger, L., Tongbo, S., Vollpracht, A., Winnefeld, F., Lothenbach, B., (2018). RILEM TC-238 SCM recommendation on hydration stoppage by solvent exchange for the study of hydrate assemblages. Materials and Structures, 51, 172. https://doi.org/10.1617/s11527-018-1298-5.

Sobral, H.S., (2004). Vegetable Plants and their Fibres as Building Materials: Proceedings of the Second International RILEM Symposium. Taylor and Francis, Hoboken.

Sonebi, M., Wana, S., Amziane, S., Khatib, J., Pascal, U.B., Pascal, I., (2015). Investigation of the mechanical performance and weathering of hemp concrete. Presented at the First International Conference on Bio-based Building Materials, Academic Journal of Civil Engineering, Clermont-Ferrand, France, pp. 416-421. https://doi.org/10.26168/icbbm2015.64.

Steenari, B.-M., Lindqvist, O., (1997). Stabilisation of biofuel ashes for recycling to forest soil. Biomass and Bioenergy 13, pp. 39–50. https://doi.org/10.1016/S0961-9534(97)00024-X.

Stefanidis, S.D., Kalogiannis, K.G., Iliopoulou, E.F., Michailof, C.M., Pilavachi, P.A., Lappas, A.A., (2014). A study of lignocellulosic biomass pyrolysis via the pyrolysis of cellulose, hemicellulose and lignin. Analytical and Applied Pyrolysis 105, pp. 143-150. https://doi.org/10.1016/j.jaap.2013.10.013.

Stepkowska, E.T., Pérez-Rodríguez, J.L., Sayagués, M.J., Martínez-Blanes, J.M., (2003). Calcite, vaterite and aragonite forming on cement hydration from liquid and gaseous phase. Thermal Analysis and Calorimetry, 73, pp. 247-269. DOI: 10.1023/A:1025158213560.

Sun, S., Mathias, J.-D., Toussaint, E., Grédiac, M., (2013). Hygromechanical characterization of sunflower stems. Industrial Crops and Products 46, pp. 50–59. https://doi.org/10.1016/j.indcrop.2013.01.009.

Tang, J., Wei, S., Li, W., Ma, S., Ji, P., Shen, X., (2019). Synergistic effect of metakaolin and limestone on the hydration properties of Portland cement. Construction and Building Materials, 223, pp. 177–184. https://doi.org/10.1016/j.conbuildmat.2019.06.059.

Tennich, M., Kallel, A., Ben Ouezdou, M., (2015). Incorporation of fillers from marble and tile wastes in the composition of self-compacting concretes. Construction and Building Materials 91, pp. 65-70. https://doi.org/10.1016/j.conbuildmat.2015.04.052.

Thomas, M.D.A., Hooton, R.D., Scott, A., Zibara, H., (2012). The effect of supplementary cementitious materials on chloride binding in hardened cement paste. Cement and Concrete Research 42, pp. 1-7. https://doi.org/10.1016/j.cemconres.2011.01.001.

Tronet, P., Lecompte, T., Picandet, V., Baley, C., (2016). Study of lime hemp concrete (LHC) – Mix design, casting process and mechanical behaviour. Cement and Concrete Composites, 67, pp. 60-72. https://doi.org/10.1016/j.cemconcomp.2015.12.004.

Válek, J., van Halem, E., Viani, A., Pérez-Estébanez, M., Ševčík, R., Šašek, P., (2014). Determination of optimal burning temperature ranges for production of natural hydraulic limes. Construction and Building Materials 66, pp. 771-780. https://doi.org/10.1016/j.conbuildmat.2014.06.015.

Van Loo, S. and Koppejan, J. (Eds.), (2008). The handbook of biomass combustion and co-firing. Earthscan, London; Sterling, VA, 442p.

Vandenbossche, V., Rigal, L., Saiah, R., Perrin, B., (2012). New agro-materials with thermal insulation properties, in: 18th International Sunflower Conference, Mar Del Plata, Argentina. Presented at the 18th Conference on Sunflower, Mar Del Plata Argentina, p. 6.

Ventolà, L., Vendrell, M., Giraldez, P., Merino, L., (2011). Traditional organic additives improve lime mortars: New old materials for restoration and building natural stone fabrics. Construction and Building Materials 25, pp. 3313-3318. https://doi.org/10.1016/j.conbuildmat.2011.03.020

Viel, M., Collet, F., Lanos, C., (2018). Chemical and multi-physical characterization of agro-resources' by-product as a possible raw building material. Industrial crops, 120, pp. 214-237. https://doi.org/10.1016/j.indcrop.2018.04.025.

Villagrán-Zaccardi, Y.A., Egüez-Alava, H., De Buysser, K., Gruyaert, E., De Belie, N., (2017). Calibrated quantitative thermogravimetric analysis for the determination of portlandite and calcite content in hydrated cementitious systems. Materials and Structures, 50, 179. https://doi.org/10.1617/s11527-017-1046-2.

Vo, L.T.T., Navard, P., (2016). Treatments of plant biomass for cementitious building materials – A review. Construction and Building Materials 121, pp. 161-176. https://doi.org/10.1016/j.conbuildmat.2016.05.125.

Walker, R., (2013). A study of the properties of lime-hemp concrete with pozzolans. PhD Thesis University of Dublin, 278p.

Walker, R., Pavia, S., Mitchell, R., (2014). Mechanical properties and durability of hemp-lime concretes. Construction and Building Materials 9.

Wang, D., Shi, C., Farzadnia, N., Jia, H., Zeng, R., Wu, Y., Lao, L., (2019a). A quantitative study on physical and chemical effects of limestone powder on properties of cement pastes. Construction and Building Materials 204, pp. 58-69. https://doi.org/10.1016/j.conbuildmat.2019.01.154

Wang, D., Shi, C., Farzadnia, N., Shi, Z., Jia, H., Ou, Z., (2018). A review on use of limestone powder in cement-based materials: Mechanism, hydration and microstructures. Construction and Building Materials, 181, pp. 659-672. https://doi.org/10.1016/j.conbuildmat.2018.06.075

Wang, L., Cho, D.-W., Tsang, D.C.W., Cao, X., Hou, D., Shen, Z., Alessi, D.S., Ok, Y.S., Poon, C.S., (2019b). Green remediation of As and Pb contaminated soil using cement-free clay-based stabilization/solidification. Environment International, 126, pp. 336-345. https://doi.org/10.1016/j.envint.2019.02.057.

Wang, L., Lenormand, H., Zmamou, H., Leblanc, N., (2019c). Effect of Soluble Components from Plant Aggregates on the Setting of the Lime-Based Binder. Renewable Materials 7, pp. 903-913. https://doi.org/10.32604/jrm.2019.06788.

Wang, S., Miller, A., Llamazos, E., Fonseca, F., Baxter, L., (2008). Biomass fly ash in concrete: Mixture proportioning and mechanical properties. Fuel, 87, 365-371. https://doi.org/10.1016/j.fuel.2007.05.026.

Wang, X., Hou, P., Yu, J., Zhou, X., Cheng, X., (2020a). The effects of silica fume on C_3A hydration. Construction and Building Materials, 250, 118766. https://doi.org/10.1016/j.conbuildmat.2020.118766.

Wang, X., Huang, J., Dai, S., Ma, B., Jiang, Q., (2020b). Investigation of silica fume as foam cell stabilizer for foamed concrete. Construction and Building Materials, 237, 117514. https://doi.org/10.1016/j.conbuildmat.2019.117514.

Wianglor, K., Sinthupinyo, S., Piyaworapaiboon, M., Chaipanich, A., (2017). Effect of alkali-activated metakaolin cement on compressive strength of mortars. Applied Clay Science 141, pp. 272–279. https://doi.org/10.1016/j.clay.2017.01.025.

Woodson, R.D., (2011). Concrete portable handbook. Butterworth-Heinemann, Amsterdam, Boston, 463p.

Wu, B., Ye, G., (2017). Development of porosity of cement paste blended with supplementary cementitious materials after carbonation. Construction and Building Materials 10.

Wu, F., Yu, Q., Liu, C., (2021). Durability of thermal insulating bio-based lightweight concrete: Understanding of heat treatment on bio-aggregates. Construction and Building Materials, 269, 121800. https://doi.org/10.1016/j.conbuildmat.2020.121800.

Wu, L., Farzadnia, N., Shi, C., Zhang, Z., Wang, H., (2017). Autogenous shrinkage of high performance concrete: A review. Construction and Building Materials, 149, pp. 62-75. https://doi.org/10.1016/j.conbuildmat.2017.05.064.

Wu, Z., Shi, C., Khayat, K.H., (2016). Influence of silica fume content on microstructure development and bond to steel fiber in ultra-high strength cement-based materials (UHSC). Cement and Concrete Composites, 71, pp. 97-109. https://doi.org/10.1016/j.cemconcomp.2016.05.005.

Xing, P., Mason, P.E., Chilton, S., Lloyd, S., Jones, J.M., Williams, A., Nimmo, W., Pourkashanian, M., (2016). A comparative assessment of biomass ash preparation methods

using X-ray fluorescence and wet chemical analysis. Fuel, 182, pp. 161-165. https://doi.org/10.1016/j.fuel.2016.05.081.

Xu, G., Tian, Q., Miao, J., Liu, J., (2017). Early-age hydration and mechanical properties of high-volume slag and fly ash concrete at different curing temperatures. Construction and Building Materials, 149, pp. 367-377. https://doi.org/10.1016/j.conbuildmat.2017.05.080.

Xu, X., Lin, X., Pan, X., Ji, T., Liang, Y., Zhang, H., (2020). Influence of silica fume on the setting time and mechanical properties of a new magnesium phosphate cement. Construction and Building Materials, 235, 117544. https://doi.org/10.1016/j.conbuildmat.2019.117544.

Xu, Z., Gao, J., Zhao, Y., Li, S., Guo, Z., Luo, X., Chen, G., (2022). Promoting utilization rate of ground granulated blast furnace slag (GGBS): Incorporation of nanosilica to improve the properties of blended cement containing high volume GGBS. Cleaner Production, 332, 130096. https://doi.org/10.1016/j.jclepro.2021.130096.

Yang, G., Wu, T., Fu, C., Ye, H., (2021). Effects of activator dosage and silica fume on the properties of Na_2SO_4-activated high-volume fly ash. Construction and Building Materials, 278, 122346. https://doi.org/10.1016/j.conbuildmat.2021.122346.

Yang, K.-H., Jung, Y.-B., Cho, M.-S., Tae, S.-H., (2015). Effect of supplementary cementitious materials on reduction of CO_2 emissions from concrete. Cleaner Production, 103, pp. 774-783. https://doi.org/10.1016/j.jclepro.2014.03.018.

Yang, K.-H., Moon, G.-D., Jeon, Y.-S., (2016). Implementing ternary supplementary cementing binder for reduction of the heat of hydration of concrete. Cleaner Production, 112, pp. 845-852. https://doi.org/10.1016/j.jclepro.2015.06.022.

Yang, R., Yu, R., Shui, Z., Gao, X., Han, J., Lin, G., Qian, D., Liu, Z., He, Y., (2020). Environmental and economical friendly ultra-high performance-concrete incorporating appropriate quarry-stone powders. Cleaner Production, 260, 121112. https://doi.org/10.1016/j.jclepro.2020.121112.

Yang, T., Zhu, H., Zhang, Z., (2017). Influence of fly ash on the pore structure and shrinkage characteristics of metakaolin-based geopolymer pastes and mortars. Construction and Building Materials, 153, pp. 284-293. https://doi.org/10.1016/j.conbuildmat.2017.05.067.

Yin, Z.D., Pan, Z.L., Wang, C., Dong, Y.P., Ou, Y.X., (2007). Composition, structure and mechanical properties of several natural cellular materials 52, 6.

Yuan, B., Yu, Q.L., Dainese, E., Brouwers, H.J.H., (2017). Autogenous and drying shrinkage of sodium carbonate activated slag altered by limestone powder incorporation. Construction and Building Materials, 153, pp. 459-468. https://doi.org/10.1016/j.conbuildmat.2017.07.112.

Zajac, M., Rossberg, A., Le Saout, G., Lothenbach, B., (2014). Influence of limestone and anhydrite on the hydration of Portland cements. Cement and Concrete Composites 46, pp. 99-108. https://doi.org/10.1016/j.cemconcomp.2013.11.007.

Zhai, J., Burke, I.T., Stewart, D.I., (2021). Beneficial management of biomass combustion ashes. Renewable and Sustainable Energy Reviews, 151, 111555. https://doi.org/10.1016/j.rser.2021.111555.

Zhang, W., Hama, Y., Na, S.H., (2015). Drying shrinkage and microstructure characteristics of mortar incorporating ground granulated blast furnace slag and shrinkage reducing admixture. Construction and Building Materials, 93, pp. 267-277. https://doi.org/10.1016/j.conbuildmat.2015.05.103.

Zhang, W., Zakaria, M., Hama, Y., (2013). Influence of aggregate materials characteristics on the drying shrinkage properties of mortar and concrete. Construction and Building Materials 49, pp. 500-510. https://doi.org/10.1016/j.conbuildmat.2013.08.069.

Zhang, Y., Zhang, J., Luo, W., Wang, J., Shi, J., Zhuang, H., Wang, Y., (2019). Effect of compressive strength and chloride diffusion on life cycle CO_2 assessment of concrete containing supplementary cementitious materials. Cleaner Production, 218, pp. 450-458. https://doi.org/10.1016/j.jclepro.2019.01.335.

Zhang, Z., Zhang, B., Yan, P., (2016a). Hydration and microstructures of concrete containing raw or densified silica fume at different curing temperatures. Construction and Building Materials 121, 483–490. https://doi.org/10.1016/j.conbuildmat.2016.06.014.

Zhang, Z., Zhang, B., Yan, P., (2016b). Comparative study of effect of raw and densified silica fume in the paste, mortar and concrete. Construction and Building Materials, 105, pp. 82-93. https://doi.org/10.1016/j.conbuildmat.2015.12.045.

Zhao, D., Qian, X., Gu, X., Jajja, S.A., Yang, R., (2016). Measurement techniques for thermal conductivity and interfacial thermal conductance of bulk and thin film materials. Journal of Electronic Packaging, 138 (4), 040802. https://doi.org/10.1115/1.4034605.

Zhao, Y., Gong, J., Zhao, S., (2017). Experimental study on shrinkage of HPC containing fly ash and ground granulated blast-furnace slag. Construction and Building Materials, 155, pp. 145-153. https://doi.org/10.1016/j.conbuildmat.2017.07.020.

Zhu, Z., Chu, H., Guo, M., Shen, M., Jiang, L., Yu, L., (2020). Effect of silica fume and fly ash on the stability of bound chlorides in cement mortar during electrochemical chloride extraction. Construction and Building Materials, 256, 119481. https://doi.org/10.1016/j.conbuildmat.2020.119481.

Zmamou, H., (2015). Eco-conception de nouveaux agromatériaux à partir de cendre de chaudière biomasse. Relation structures-propriétés. Thèse de doctorat de l'Université de Rouen, 288p.

Standards references

Afnor, (2016). NF EN 196-1. Méthodes d'essais des ciments - Partie 1 : détermination des résistances [WWW Document]. Afnor EDITIONS. URL https://www.boutique.afnor.org/fr-fr/norme/nf-en-1961/methodes-dessais-des-ciments-partie-1-determination-des resistances/fa184622/57803 (accessed 12.8.22).

ASTM D3766-86 (2002). Standard Terminology Relating to Catalysts and Catalysis.

ASTM C136, (2003). Standard Test Method for Sieve Analysis of Fine and Coarse Aggregates.

ASTM C188-95, (2003). Standard Test Method for Density of Hydraulic Cement.

ASTM C204, (2003). Standard Test Method for Fineness of Hydraulic Cement by Air Permeability Apparatus.

ASTM C618, (2003). Standard Specification for Coal Fly Ash and Raw or Calcined Natural Pozzolan for Use in Concrete.

ISO 13320:2020, (2020). Particle size analysis - Laser diffraction methods.

NF EN 196-3, 2017. Methods of testing cement - Part 3: Determination of setting times and soundness. Afnor EDITIONS. URL https://www.boutique.afnor.org/Store/Preview/DisplayExtract?ProductID=79422&VersionID=14 (accessed 8.10.22).

SEBTP - Société d'édition du bâtiment et des travaux publics, (2012). Règles professionnelles d'exécution d'ouvrages en béton de chanvre. Enduits en mortier.

Webography

Abbott, T., (2014). Hempcrete Factsheet. The Limecrete Company. URL https://limecrete.co.uk/hempcrete-factsheet/ (accessed 11.18.22).

ADEME - Agence de l'environnement et de la maîtrise de l'énergie, (2014). Documentation des facteurs d'émissions de la Base Carbone. URL https://bilans-ges.ademe.fr/static/documents/%5BBase%20Carbone%5D%20Documentation%20g%C3%A9n%C3%A9rale%20v11.0.pdf (accessed 2.8.22).

Agreste, (2022). Cultures développées (hors fourrage, prairies, fruits, fleurs et vigne). Cultures industrielles. Chanvre papier : la production de 2006,2007,2008,2009 et 2012. URL https://agreste.agriculture.gouv.fr/agreste-saiku/?plugin=true&query=query/open/SAANR_DEVELOPPE_2#query/open/SAANR_DEVELOPPE_2 (accessed 8.4.22).

Baecher, C., Dutreix, N., Buick, R., Rimbaud, A., (2012). Etude sur le secteur et les filières de production des matériaux et produits bio-sourcés utilisés dans la construction (à l'exception du bois). Nomadéis. https://www.nomadeis.com/dl/2013/05/Rapport-final-NOMADEIS-MEDDE-phase-1.pdf.

CERADEL, (2022). Metakaolin argical M 1200S sac 15 kg. URL https://www.ceradel.fr/en/matieres-premieres-de-base/15949-metakaolin-argical-m-1200s-sac-15kg.html (accessed 2.5.22).

CIBE, (2021). Etat des lieux. URL https://cibe.fr/etat-des-lieux/ (accessed 6.14.22).

Ciments Vigier SA, (2014). Assortiment et prix, Ciments et liants hydrauliques.

Comores En Ligne, (2022). Ciment gris 1 tonne | Comores - Achat / Vente en ligne / e-commerce. URL https://www.comores-en-ligne.fr/catalogue/ciment-gris-1-tonne_188/ (accessed 2.5.22).

Construction Durable et Écomatériaux (CODEM), (2021). Guide de la rénovation de parois à l'aide de materiaux biosources. https://www.dispositif-rexbp.com/sites/default/files/2021-03/CODEM_Guide-renovation-parois-materiaux-biosources.pdf.

ECOCEM, (2011). Laitier moulu pour béton, mortier et coulis | Ecocem. https://www.batiproduits.com. URL https://www.batiproduits.com/fiche/produits/laitier-moulu-pour-beton-mortier-et-coulis-p69135228.html (accessed 2.5.22).

Ernst & Young s.r.l./S.E.N.C.R.L., (2015). FerroQuébec Inc. Empreinte carbone du silicium métal. URL https://archives.bape.gouv.qc.ca/sections/mandats/usine_silicium_port-cartier/documents/PR8.1.pdf (accessed 2.8.22).

European Commission, (2021). Statistical Factsheet-France.

Eurostat, (2022a). Productions végétales au taux d'humidité standard UE. URL https://ec.europa.eu/eurostat/databrowser/view/APRO_CPSH1__custom_2903478/default/bar?lang=fr (accessed 6.13.22).

Eurostat, (2022b). Crop production in EU standard humidity. URL https://ec.europa.eu/eurostat/databrowser/view/APRO_CPSH1__custom_2897770/default/table?lang=en (accessed 6.11.22).

Eurostat, (2019). Eurostat regional yearbook. Eurostat, Luxembourg.

Forest Research, (2022). Ash. Forest Research. URL https://www.forestresearch.gov.uk/tools-and-resources/fthr/biomass-energy-resources/technical-and-regulatory/emissions/ash/ (accessed 6.14.22).

Gilmour, (2018). Growing Sunflowers: Plant & Harvest Sunflowers. Gilmour. URL https://gilmour.com/growing-sunflowers (accessed 6.13.22).

Harmonie, (2017). 1974-2020 : l'évolution de la réglementation thermique. Isolation thermique. URL https://www.harmonie.fr/1974-2020-evolution-reglementation-thermique/ (accessed 4.5.22).

Hatfield, A. K., (2022). Cement Statistics and Information | U.S. Geological Survey. URL https://www.usgs.gov/centers/national-minerals-information-center/cement-statistics-and-information.

Kenzai, (2022). Métakaolin : matière première naturelle pouzzolanique pour préparation des bétons, mortiers. Kenzai. URL https://www.kenzai.fr/adjuvant-additif/1417-7193-metakaolin-pour-preparation-de-beton-mortier-et-ciment.html (accessed 2.5.22).

Lalanne, A., (2021). Retour sur la réglementation thermique de 2005 (RT 2005). Maîtrisez vos dépenses dès aujourd'hui. URL https://www.choisir.com/energie/articles/128018/retour-sur-la-reglementation-thermique-de-2005-rt-2005 (accessed 4.5.22).

Luoyang Minghong import and export trade Co., Ltd, (2022). Products display. URL https://www.supersilicafume.com/ (accessed 2.5.22).

Ministère de la Transition écologique, (2021a). Énergie dans les bâtiments. Ministère de la Transition écologique. URL https://www.ecologie.gouv.fr/energie-dans-batiments (accessed 4.8.22).

Ministère de la Transition écologique, (2021b). Des Assises de la forêt et du bois, pour une vision partagée de la forêt française. Ministère de la Transition écologique. URL

https://www.ecologie.gouv.fr/des-assises-foret-et-du-bois-vision-partagee-foret-francaise (accessed 3.24.22).

NOAA - Global Monitoring Laboratory, (2022). Trends in atmospheric carbon dioxide. URL https://gml.noaa.gov/ccgg/trends/global.html (accessed 5.9.22).

Ritchie, H., Roser, M., (2020). Agricultural Production. Published online at OurWorldInData.org. Retrieved from: 'https://ourworldindata.org/agricultural-production'.

Ritchie H. and Roser M., (2013). Land Use. Published online at OurWorldInData.org. Retrieved from: 'https://ourworldindata.org/land-use'.

Ritchie, H., Roser, M., Rosado, P., (2020). CO_2 and Greenhouse Gas Emissions. Published online at OurWorldInData.org. Retrieved from: 'https://ourworldindata.org/co2-and-other-greenhouse-gas-emissions'.

Roser, M., Ritchie, H., Ortiz-Ospina, E., (2013). World Population Growth. Published online at OurWorldInData.org. Retrieved from: 'https://ourworldindata.org/world-population-growth.

Tenerrdis, n.d. Biomass and Biogas. URL https://www.tenerrdis.fr/en/energy-fields/biomass-biogas/ (accessed 6.8.22).

TerresOléoPro, (2014). Tournesol. Helianthus annuus. URL https://www.terresoleopro.com/le-tournesol-une-nature-essentielle (accessed 6.11.22).

The World Bank, (2022). Agricultural land (% of land area) - France. URL https://data.worldbank.org/indicator/AG.LND.AGRI.ZS?locations=FR (accessed 6.11.22).

The World Bank, (2020). Overview. World Bank. URL https://www.worldbank.org/en/topic/urbandevelopment/overview (accessed 5.21.22).

Tout sur le béton, (2020). Le prix d'un sac de ciment. Tout sur le béton. URL https://www.toutsurlebeton.fr/guide-des-prix/le-prix-dun-sac-de-ciment/ (accessed 2.5.22).

Travaux-maçonnerie, 2019. Chaux hydraulique : prix et intérêt. Conseils et devis en maçonnerie. URL https://www.travaux-maconnerie.fr/chaux-hydraulique-prix-interet (accessed 2.5.22).

Tuffe, P.B., (2018). «Béton…l'addition s'il vous plait !! ». URL https://www.afgc.asso.fr/app/uploads/2010/02/AFGC-ADDITIONS-MINERALES-6-DEC-2018.pdf (accessed 2.8.22).

Van Oss, H. G., (2001). Cement Statistics and Information | U.S. Geological Survey. URL https://www.usgs.gov/centers/national-minerals-information-center/cement-statistics-and-information (accessed 12.30.21).